BIOSENSOR DESIGN UTILIZING PARTICLE-BOUND ENZYMES

Cassi Joanna Henderson

Queens’ College

Department of Chemical Engineering and Biotechnology

University of Cambridge

This thesis is submitted for the degree of Doctor of Philosophy

April 2019

To my mom

DECLARATION

I hereby declare that this dissertation is the result of my own work and includes nothing which is the outcome of work done in collaboration except as declared in the Preface and specified in the text. It is not substantially the same as any that I have submitted, in whole or in part, for a degree or diploma or other qualification to the University of Cambridge or to any other university or institution. It does not exceed the prescribed word limit of 65,000 words (including appendices, footnotes, tables and equations) and contains no more than 150 figures as specified by the Engineering Degree Committee.

Cassi J. Henderson

ABSTRACT

Biosensor design utilizing particle-bound enzymes

Cassi J. Henderson

There is a clear need for affordable point-of-care diagnostics, especially in vulnerable low- and middle-income countries where access to laboratory-based testing is limited. This thesis explores whether recombinant protein technology in combination with a low-cost support matrix could provide a basis for an inexpensive, simple, and robust production process for the bio-sensing element of a diagnostic that would be amenable to manufacture in resource constrained settings. Silica was selected as the solid support for this work, given its biocompatibility and wide-availability (including extraction from natural sources, like sand, as demonstrated here).

By employing an affinity binding sequence for silica in fusion with the central assay reagent protein targeting the analyte, simultaneous isolation and immobilisation onto silica carrier particles was achieved directly from lysate. In addition, the incorporation of a coloured fluorescent protein in the fusion enabled the protein production and immobilisation to be followed visually without significant laboratory equipment.

Diagnostic sensing activity was retained in the immobilised fusion proteins, even over two months at 20-22 °C in a dried state. A comparable limit of detection was achieved with immobilised reagents as with the soluble form. Taken together with the reduced downstream processing attained by a one-step purification and immobilisation approach, this supports the use of particle-bound reagents in the development of point-of-care tests.

To make use of the particle-bound reagents, a novel falling particle biosensor design was explored in this thesis, where the sedimentation of the silica particles was used to drive mixing in an otherwise stationary fluid compartment. The performance of this design was compared against two other formats commonly employed with bio-functionalised particles – (A) a simple suspension in a microcentrifuge tube and (B) a packed bed in a microfluidic channel. The falling particle device outperformed both formats.

Overall, this work has demonstrated that the integrated functionality of the fusion proteins could facilitate a production pathway from raw material to end diagnostic, highlighting the use of silica as a protein carrier and presenting a novel biosensor format for utilizing particle-bound enzymes.

ACKNOWLEDGEMENTS

This research would not have been possible without the support of a multitude of people, and to them I owe extensive thanks.

First and foremost, I would like to thank my supervisors Professor Lisa Hall and Dr. Ronan Daly for their guidance and encouragement, starting from our very first discussions about potential projects together. Their constructive feedback has been invaluable in the development of this research and their willingness to give so generously of their time is much appreciated.

I am grateful for the financial support I received from the Gates Cambridge Trust, without which this project would not have been possible, as well as the travel grants from Queens', the Shell Fund, and the Philosophical Society, which enabled me to communicate my research outside of Cambridge.

I would also like to express my gratitude towards the members of the Cambridge Analytical Biotechnology and the Fluids in Advanced Manufacturing groups, both past and present, for their support and companionship over the last few years. Special thanks go to Dr. Etienne Rognin for his patient instruction in fluid dynamics, to Dr. Christina Rodriguez Rivero for her guidance in imaging particle settling behaviour and to my research partners, Dushanth Seevaratnam, Dr. Neus Jornet-Martínez, Ziyan Zhao and Dr. David Bailey, for their advice in designing and troubleshooting experiments. Thanks are also due to the technical teams for facilitating my research and to the wider body of CEB and IfM for creating an inviting and collaborative atmosphere for research.

Finally, I am tremendously grateful for the network of family and friends, especially Jacob, who celebrated the successes, patiently listened to the frustrations, and shared many laughs along the way.

Thank you!

CONTENTS

List of Tables

List of Figures

NOMENCLATURE

ABBREVIATIONS AND ACRONYMS

6H	polyhistidine tag (6 histidines)
aa	amino acid residues
ABTS	2,2'-azino-bis(3-ethylbenzothiazoline-6-sulphonic acid)
ANOVA	analysis of variance
AR	Amplex™ UltraRed dye
AUC	area under the curve
BET	Brunauer-Emmett-Teller
BSA	bovine serum albumin
CB	St. Lucia, Caribbean (sand source)
CBM	cellulose binding module
CCD	charge-coupled device
CE	circle equivalent
CI	confidence interval
CMOS	complementary metal-oxide-semiconductor
DNA	deoxyribonucleic acid
DLVO	Derjaguin, Landau, Verwey and Overbeek
Enz	enzyme
ESC	enzyme surface coverage
FTIR	Fourier-transform infrared
GFP	green fluorescent protein
GH	Accra, Ghana (sand source)
HIV	human immunodeficiency virus
HK	Sharp Island, Hong Kong (sand source)
HRP	horseradish peroxidase
IB	inclusion bodies

IPTG	isopropyl β-D-1-thiogalactopyranoside
IVD	*in vitro* diagnostic
LAMP	loop-mediated isothermal amplification
LB	luria broth
LDA	laser diffraction analysis
LED	light emitting diode
LMICs	low- and middle-income countries
LOD	limit of detection
mCh	mCherry
micro-CT	micro computed tomography
MS	mass spectroscopy
MBP	magnetic binding protein
NAA	nucleic acid amplification
NCD	non-communicable diseases
Ni-NTA	nickel-charged affinity resin (nitrilotriacetic acid)
PBR	packed bed reactor
PBS	phosphate buffered saline
PCR	polymerase chain reaction
PDMS	polydimethylsiloxane
pI	isoelectric point
PIV	particle image velocimetry
PMMA	poly(methyl methacrylate)
PMT	photomultiplier tube
POCT	point-of-care test
PPP	purchasing power parity
PSA	prostate specific antigen
QCM(-D)	quartz crystal microbalance (with dissipation monitoring)

R5	silaffin tag
RGB	Red-Green-Blue channels
RNA	ribonucleic acid
SA	surface area
SBP	silica binding peptide/protein
SC	South Carolina, USA (sand source)
SD	standard deviation of the response
SDS-PAGE	sodium dodecyl sulphate polyacrylamide gel electrophoresis
SOx	sarcosine oxidase
ST	Santorini, Greece (sand source)
TEOS	tetraethyl orthosilicate
TGA	thermogravimetric analysis
TGP	thermal green protein
TMB	3,3’,5,5’-tetramethylbenzidine
TPI	total protein immobilised
UK	Southwold, UK (sand source)
WHO	World Health Organisation
WT	wild-type
XRF	x-ray fluorescence
YFP	yellow fluorescent protein

SYMBOLS

α	statistical significance level
A	absorbance
a	active area between QCM electrodes
b	slope of the linear regression
C	concentration of the protein added to QCM

d_i	particle diameter
D_s	substrate diffusivity
ε	millimolar extinction coefficient
F_0	frequency at the start of association/dissociation
F_{max}	frequency shift observed from F_0 to signal plateau
F_t	frequency at time t
f_0	resonant frequency
Δf	frequency change
g	gravitational acceleration
h	device height
hA	void volume of a packed bed reactor
I	fluorescence intensity of the sample
I_0	fluorescence intensity of the blank
$I_{standard}$	fluorescence intensity of the standard
k	parameter for Bonferonni correction
k_a	association constant
k_{cat}	enzyme turnover rate
k_d	dissociation constant
K_D	equilibrium dissociation constant
K_m	Michaelis constant
l	pathlength
m	mass
η_f	dynamic viscosity
ρ_f	density, fluid
ρ_q	density, quartz (for QCM)
ρ_s	density, silica particle
P_i	quantity of product produced by settled particle of diameter d_i

Q	volumetric flow rate through a packed bed
S_0	initial substrate concentration
θ_p	particle volume fraction
θ_v	void volume fraction
t_i	time of settling for particle of diameter d_i
$t_{inver.}$	time between inversions
u_p	relative velocity of the fluid to the falling particle
u_s	superficial velocity
μ_q	shear modulus, quartz (for QCM)
v	final volume of the assay
V	rate of product formation under kinetic control
V_{max}	maximum reaction rate
V_{max_SA}	max. reaction rate per unit surface area
Vol_{sb}	volume of particles in the settled bed
Vol_{void}	volume of the void in the settled bed
ϕ	substrate flux to the surface of the particle

DIMENSIONLESS GROUPS

Da	Damköhler number
Pe	Péclet number
Re_p	Reynolds number, particle
Re_{pb}	Reynolds number, packed bed

AMINO ACIDS WITH SYMBOLS

A	alanine	Ala
R	arginine	Arg
N	asparagine	Asn
D	aspartic acid	Asp
C	cysteine	Cys
Q	glutamine	Gln
E	glutamic acid	Glu
G	glycine	Gly
H	histidine	His
I	isoleucine	Ile
L	leucine	Leu
K	lysine	Lys
M	methionine	Met
F	phenylalanine	Phe
P	proline	Pro
S	serine	Ser
T	threonine	Thr
W	tryptophan	Trp
Y	tyrosine	Tyr
V	valine	Val

PREFACE

Work in this thesis was supported by a number of individuals, whose contributions are summarised below. Specific mentions are also made where appropriate in the main text.

Chapter 2: Dr. Shah Abbas and Dr. Si Chen designed the R5-tagged constructs as part of their doctoral work ($R5_n$-mCh-6H and mSOx-R5-6H, respectively) and provided glycerol stocks. Elizabeth Pumford designed and transformed the $R5_2$-mCh-mSOx-R5-6H construct and conducted preliminary experiments showing silica purification with R5-tagged proteins. Dr. David Bailey designed the constructs containing HRP and performed the transformation into hosts. Ziyan Zhao and Dushanth Seevaratnam performed the expression and purification of fusion proteins containing HRP. Dushanth Seevaratnam also performed sample collection for the study of fluorescence over the expression period, assisted in analysis of immobilisation process by SDS-PAGE gel, and facilitated DNA and amino acid sequencing of fusion proteins. Dr. Neus Jornet-Martínez provided guidance in the design of the fluorescence assay for sarcosine and in the development the extraction process of silica from sand and provided assistance in conducting QCM experiments. Dr. Sharel E and Dr. Changshin Jo provided support in performing and interpreting N_2 adsorption/desorption analysis. Dr. David Hopkinson and Dr. Andrew Cockburn assisted in powder size distribution measurements using Laser Diffraction Analysis, and Simon Crowhurst assisted with XRF analysis of sands and silica extracts. Dr. Kamran Yunus provided training and guidance on the confocal and optical morphology microscope.

Chapter 3: Dr. Christina Rodiguez Rivero provided guidance in the set-up of the rig for imaging particle settling behaviour. Dr. Etienne Rognin and Eric Bringley provided advice and guidance in the development of the mathematical model of product formation by particle-bound enzymes. Dr. Yao Du provided silica nanoparticles (produced and characterised for his doctoral research). Dr. Yao Du and Dr. Jacob Brubert provided assistance in generating MATLAB scripts for data processing.

Chapter 4: Tony Dennis provided assistance in micro-CT imaging and supported analysis of the results.

Chapter 5: Andrew Stretton and Sebastien Cosnefroy assisted in the design and construction of the electronics to enable PID-controlled heating for LAMP tests.

LIST OF PUBLICATIONS

Much of Chapter 2 and parts of Chapter 3 and Chapter 4 were included in the following publication.

- C.J. Henderson, E. Pumford, D.J. Seevaratnam, R. Daly, E.A.H. Hall. (2019) Gene to diagnostic : Self immobilising protein for silica microparticle biosensor , modelled with sarcosine oxidase. *Biomaterials, 193,* 58–70. doi:10.1016/j.biomaterials.2018.12.003.

References are made to the following works completed with collaborators but results are not included directly in this thesis.

- J.F. Engels, C.J. Henderson, R. Daly, R. Renneberg, E.A.H. Hall. (2018). A lateral flow channel immunoassay combining a particle binding zone geometry with nanoparticle labelling amplification. *Sensors Actuators B. Chem., 262,* 1–8. doi:10.1016/j.snb.2018.01.213.
- N. Jornet-Martínez, C.J. Henderson, P. Campins-Falco, R. Daly, E.A.H. Hall. (2019). Towards Sarcosine Determination in Urine for Prostatic Carcinoma Detection. *Sensors Actuators B. Chem., 287,* 380-389. doi:10.1016/j.snb.2019.02.061.

1 INTRODUCTION

1.1 The need for affordable *in vitro* diagnostics

Disease diagnosis is paramount for both individual case management of ill patients and for public health monitoring. For individual patients, diagnosis allows for the correct treatment to be given, hopefully improving prognosis. With respect to public health initiatives, widespread testing is necessary to accurately profile disease prevalence in order to measure the performance of prevention and treatment programs and inform future funding.

Accurate diagnosis of disease makes use of clinical observation of symptoms and signs as well as diagnostic tests and procedures. However, in its study on increasing access to diagnostics in low- and middle-income countries (LMICs), the World Health Organization (WHO) reports that diagnostic tests are not affordable in these vulnerable countries where the burden of disease is highest [1]. The absence of affordable medical diagnostics undermines the cornerstones of effective clinical decision-making [2]. Clinicians often don’t have enough information, so syndromic or presumptive treatment is particularly common.

The absence of diagnostic tests becomes particularly evident in the case of differentiation between viral and bacterial infections, a major cause of mortality in LMICs [3]. These infections present with similar febrile symptoms but require distinctly different treatments. Incorrect treatment not only hinders recovery of the individual but also is implicated in wider public health issues such as the rise of antibiotic resistance. The lack of diagnostics is leading to unnecessary or inappropriate use of antibiotics and has been cited as the “Achilles Heel” in combating antimicrobial resistance [4,5].

In LMICs, the conventional focus has been upon the control of communicable diseases, but chronic, non-communicable diseases (NCDs) account for more than half the burden of disease and the greatest global share of death and disability [6]. NCDs include cardiovascular disease, diabetes, cancers, degenerative and inflammatory conditions, affecting people of all ages, nationalities and classes. For many of these diseases, frequent monitoring and/or screening is key for improving survival, often assisted by diagnostic technologies. However, this beneficial monitoring is often lacking in LMICs. One illustrative example of the contrast with high income countries is the case of diabetes care in Mozambique; only 6 % of healthcare facilities could carry out a blood glucose analysis and personal monitoring with handheld blood glucometers is not available in general [7]. The contribution of NCDs to global deaths is predicted to rise over the next few decades [8,9], especially in LMICs. It is estimated that two thirds of new cancer diagnosis will occur in LMICs by the end of the next decade [10,11]. In cancer treatment, the need for early detection and triage is well established. For example, five year survival rates for localised prostate cancer (one of the leading causes of cancer death among men worldwide [12,13]) are nearly 100 %; however, this drops to ~ 30 % when the disease has become metastatic [14]. Unfortunately, early diagnosis programs are not affordable in LMICs, which acts as an impediment for surveillance and clinical management.

The rewards for versatile low-cost diagnostics could be considerable with respect to both communicable and non-communicable diseases. It has been proposed that low-cost *in vitro* diagnostics (IVDs) in clinical practice can, in general, facilitate decision-making to guide management of the patient pathway with improved cost effectiveness [15,16].

1.2 Design requirements for diagnostics for resource-limited settings

Traditional medical diagnostic testing is primarily done in centralised laboratory facilities with large and expensive analytical machines. However, access to laboratory testing facilities in LMICs is extremely limited [17]. Even where facilities exist, they are often under-resourced and under-staffed which lengthens sample processing times [18]. These turnaround times are too slow to influence the first response in patient treatment.

Point-of-care tests (POCT) offer an attractive alternative to laboratory based IVDs. POCTs are medical diagnostic tests that are performed outside the laboratory in close proximity to the patient and the delivery of care [19]. POCT tests have been developed that cover the range of IVDs – from immunoassay to small molecule to nucleic acid testing. Many of these detect the presence or quantity of the target substance using a biological component (e.g. proteins) in combination with physio-chemical transduction methods (electrochemical, optical, acoustic, thermometric, etc.) – i.e. biosensor. Often POCTs are performed by nurses or other personnel without training in laboratory techniques. These tests should not require sample preparation and should have the reagents stored in the device. POCTs can be used stand-alone or with a user-friendly, dedicated analytical instrument, providing an integrated sample-to-answer solution. Most importantly, they have a short turnaround time to enable result-informed therapeutic action in that visit [20].

These characteristics make POCTs especially amenable to healthcare in LMICs. Enabling care in the same visit as the diagnostic test is critical, as patients may have walked several hours to reach the clinic. If asked to return for their test results, many will fail to do so [18]. Sample-to-answer solutions are even more important because of low levels of training and high demand on healthcare workers’ time [21].

The environment of healthcare provision in LMICs imposes further constraints on any POCT (Figure 1.1). Especially in rural areas, healthcare is often provided in facilities with limited access to clean water and reliable electricity, if any at all [22]. Harsh environmental conditions such as extreme temperatures and dust make many technologies designed for controlled laboratory environments unreliable [23]. When they break down, technical support and repair options are extremely limited [24]. Often the supply chain is unreliable [25], and can lack cold-chain storage, which cuts into the shelf-life of sensitive reagents [26]. Finally, with significantly smaller governmental healthcare budgets in LMICs [27], cost remains a significant factor in accessibility.

Figure 1.1 A diagnostic testing lab in a rural health centre. Image taken in Nyaishozi, Tanzania.

In light of these challenges, the WHO has developed a framework for the design of POCTs, describing the ideal characteristics for use in resource-limited settings. POCTs should be A.S.S.U.R.E.D.: affordable, sensitive, specific, user-friendly, rapid & robust, equipment-free and deliverable to those in need [28]. These guidelines were developed in relation to tests for sexually transmitted infections, such as human immunodeficiency virus (HIV), but can be applied more broadly to POCTs intended for use in LMICs.

1.3 Potential for a local production approach

There have been numerous attempts to propose low-cost diagnostics for LMICs that meet the A.S.S.U.R.E.D criteria using a variety of platform technologies (e.g. microfluidics [26,29], paper diagnostics [30,31], nanotechnology enhanced lateral flow assays [32]), however they remain at a high cost when examined in the context of the local economy. As a result, many of the IVDs that are available in LMICs are the result of international donors supporting disease-specific initiatives. The enormous value of these initiatives is seen, for example, in HIV and malaria testing [23], but tests need to become self-sustaining [5], without charitable donor commitment. Furthermore, even in relatively well supported urban laboratories that have been equipped by investment from donors and non-governmental organisations, instrumentation sits idle since reagent and kit costs have rendered it beyond operating budgets [33].

A workshop held during the Geneva Health Forum 2016 considered how to increase access to quality diagnostics in LMICs using social innovation [34], centring production around local communities [35]. However, even basic raw materials to achieve this vision have to be imported at too high a cost due to a lack of agreement between currency exchange rates and Purchasing Power Parity (PPP). PPP is an approach that compares the currencies of two countries through the relative price of the same bundle of goods [36], allowing a comparison of costs adjusted for the in-country purchasing power of a unit of currency. For example, the polymerase for a nucleic acid diagnostic is at nearly the same cost price in the Philippines as in US and Europe (> 80 %), despite the average household income being 80-90 % lower [37]. As a result, the development of local enterprises and infrastructure for diagnostic technologies in LMICs is not competitive [23]. Often the locally produced product, even when marketed at an unsustainable small margin, would still be more expensive than the imported finished (unaffordable) product [38]. There is a need to consider a different approach that doesn't presume the use of expensive off-the-shelf reagents. Innovation is therefore required to empower LMICs, through local production, without subsidies or major infrastructure investment [39–41].

Specifically, enabling the local production of the required biological reagents (e.g. enzymes, antibodies) for POCTs could be significant step as this can be the largest proportion of the total cost of a device [42]. Production methods vary dependent on the biological reagents required, which vary with the type of diagnostic test. For example, immunoassays require antibodies specific to the pathogen antigen, small molecule assays require enzymes that act upon the target substrate, and nucleic acid assays require polymerases to amplify the DNA/RNA of interest in the sample. Antibodies are often harvested from the serum of host animals exposed to the antigen, a resource intensive process. Certain enzymes can also be derived from animal sources, while others can be extracted from plants; however, the seasonal and/or geographical nature of plant growth limits the utility of plants as a source. Production in microorganism hosts like *E. coli* is an increasingly popular approach especially with the advent of recombinant technology for the production of enzymes or other proteins not naturally produced by these organisms [43]. All of these production processes have typically required extensive know-how and large capital investment in equipment.

Recent reports have recognized the need for decentralised bio-manufacturing, especially in remote locations with limited infrastructure. Some have proposed microfluidic systems to automate the various steps of the process over a smaller footprint (e.g. [44,45]), while others have demonstrated magnetic nanoparticle-based systems for simplifying the purification step from crude cell lysate (e.g. [46–48]); however, these lab-on-chip and nanoparticle-based approaches have complex fabrication requirements. Alternatively, Pardee *et al.* have proposed portable, on-demand bio-manufacturing using cell-free production technology and demonstrated the approach for a range of proteins, including antimicrobial peptides, enzymes and antibody conjugates for vaccines, in a proof-of-concept study [40]. From a production perspective, cell-free expression has the advantage that encoding DNA sequences and corresponding expression parameters can be rapidly screened for utility in the absence of the cell wall. Freeze-dried cell extracts have also been incorporated into diagnostic platforms such that the bio-sensing protein is produced *in situ* [49,50]. While freeze-dried cell-free extracts potentially support distributed manufacturing with their lack of requirement for cold-chain distribution, the production of the extracts still requires much of the same specialised and costly equipment as classical protein production [51]. The challenges in extract production and the ensuing high cost of cell-free reagents remain as major barriers to the widespread implementation of this approach [52,53].

Despite classical production with microorganisms requiring significant capital and knowledge resources, molecular biology can be harnessed to bypass many of the normal steps in producing, isolating and integrating the biological element of the diagnostic device. The rise of “Garage Biotech” where do-it-yourself scientists, with limited experience, have successfully produced proteins without conventional laboratory resources [54] supports the applicability of a molecular biology approach for production in resource-limited settings without highly trained personnel.

With a molecular biology approach, protein engineering techniques can be used to integrate multiple functionalities into a single fusion protein produced by bacterial hosts. The protein providing the desired assay functionality can be genetically fused with peptide tags having specific affinity for low-cost materials that can act as the stationary phase in purification from the remainder of the material produced by the host organism. While the classical method of protein purification uses a peptide tag (poly-histidine, often referred to as His-tag), the necessary ligand modification of the resin surface to enable affinity with the His-tag makes this method expensive, estimated at $ 2 per mg of purified protein [55]. Alternative peptide tags have been developed that have affinity for cheaper purification matrix materials and don’t require additional modification steps. Peptide tags have been identified with affinity for organic materials (e.g. graphene oxide [56], carbon nanotubes [57], cellulose [58]), metals (e.g. Au [59–61], Ag [62,63], and oxides (e.g. TiO_2 [64,65], ZnO [66,67], Cu_2O [68], SiO_2 [69,70]). Given that purification costs are primarily associated with the price of the stationary phase [71], the support material should be low-cost and widely available in order to be amenable to local production of low-cost diagnostics. Silica (SiO_2) fits this description and has a history of use as a low-cost substrate for biosensor design given its biocompatibility [72–74]. In addition, it is easily extractable from local materials (e.g. sand [75,76], rice husk, bamboo leaves, sugarcane bagasse [77], iron slag [78]), making it a good choice as an initial platform for a local approach.

Not only is the inclusion of a peptide tag key for purification of the target protein, but it can also have a secondary function – immobilisation of the assay reagent without additional steps. Immobilisation has been shown to add retention of enzyme activity and increase enzyme thermal stability [79–81], critical features in the shelf-life of a diagnostic test. In addition, using the immobilised version of the enzyme in the diagnostic device eliminates several steps in the production process, e.g. the need to purify the target protein from the agent used to displace it from the affinity matrix and the need to remove the affinity tag. Simultaneous purification and immobilisation is proposed to reduce the total work effort and cost of the process [79,82].

Traditional methods of immobilisation to a support surface include entrapment within a gel/polymer matrix, adsorption-based methods via a range of intermolecular forces or covalent attachment using chemical reagents [83,84] (Figure 1.2). Entrapment is a classical strategy for enzyme immobilisation in catalysis and has been explored extensively, however, the limited rate of diffusion of the substrate to the entrapped enzyme can reduce the apparent activity of the enzyme. Alternatively, chemical surface modification can be used to unite the bio-sensing element with the solid support. Common covalent surface modification strategies include carbodiimide or glutaradehyde coupling, however, these require the target proteins and support materials to undergo multiple modification steps and require additional chemical reagents which would be unlikely to be locally sourced. In addition, chemical modification to achieve immobilisation can cause protein degradation or in the case of enzymes, block the active centre or result in the enzyme orientation being incorrect for reaction with its substrate [85]. Multi-point attachment and resulting rigidity can be another challenge [86]. Another common strategy to achieve surface immobilisation is coupling via high-affinity pairs, such as streptavidin/biotin or antibody/antigen couplings, where one component is fused with the bio-sensing element and the other onto the support material surface [56,87]. Although one-half of the pair could be expressed as a genetic fusion with the target protein, this strategy still requires attachment of the other half of the pair to the solid matrix, often using similar chemistry mentioned above. In general, these approaches require already purified proteins. Opting instead to use peptide tags that are incorporated with the functional assay protein during the production process but that bind directly with the target support material via intermolecular forces can reduce complexity and cost. In addition, using peptide tags can achieve oriented immobilisation that can result in less conformational changes than direct association of the protein and the substrate [88], and generally results in higher activities relative to random immobilisation [80].

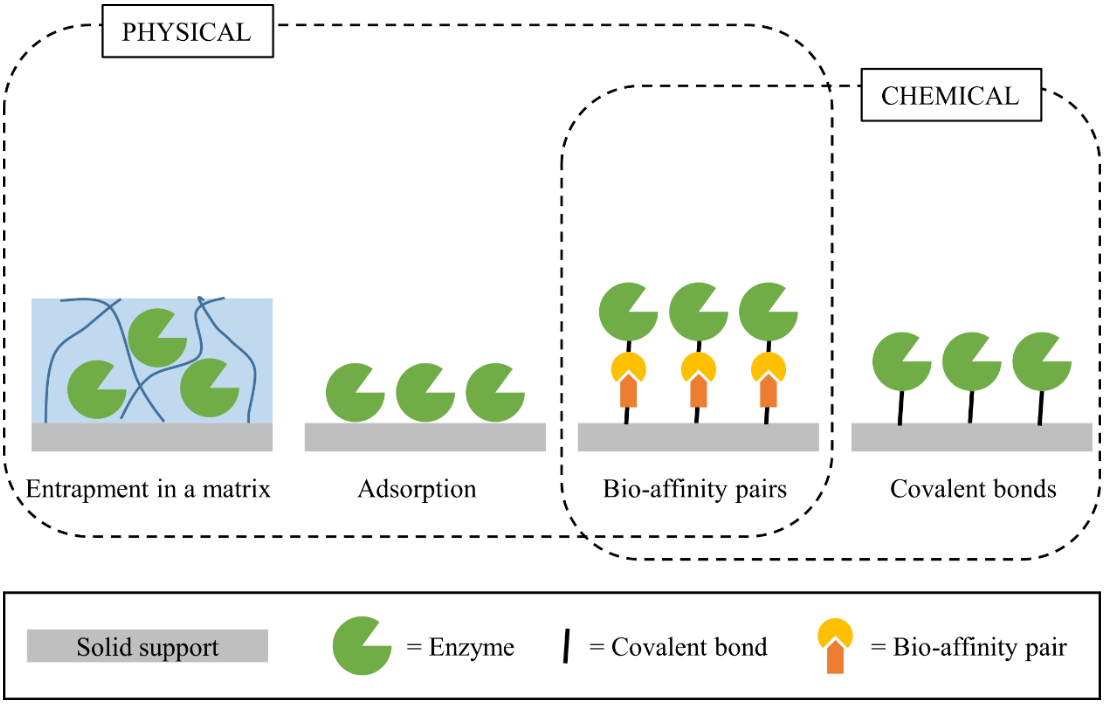

Figure 1.2 Common immobilisation strategies to join proteins with solid-support materials.

By designing the biological reagent through recombinant protein technology, additional functionality can be incorporated into the protein. Not only can the fusion protein contain the functional assay protein and a built-in purification and immobilisation tag, but also a ‘visualisation’ protein (e.g. fluorescent protein) can be incorporated (Figure 1.3). This element of the fusion could facilitate visual monitoring of the production and isolation without a laboratory infrastructure and provide a reference measurement in the final diagnostic. The integrated functionality in the fusion protein, which would normally be fulfilled through separate materials and/or procedures, could reduce production steps and facilitate an integrated pathway from raw material to end diagnostic.

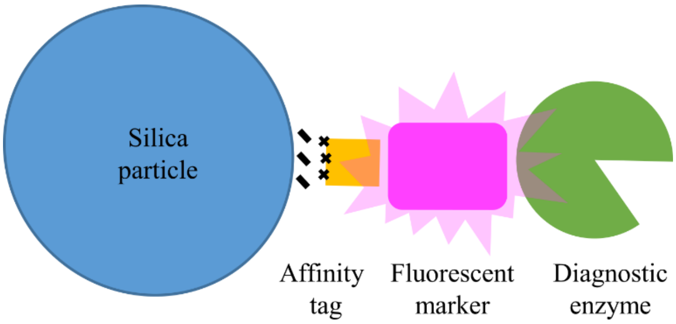

Figure 1.3 Schematic of the silica-immobilised fusion protein showing the three functional elements.

1.4 Research Aims

There is a clear need for versatile affordable POCTs with respect to both communicable and non-communicable diseases, especially in vulnerable LMICs where access to laboratory-based testing is limited. There have been numerous attempts to propose low-cost diagnostics for LMICs that meet the A.S.S.U.R.E.D criteria, however, there is a need to consider a different approach that doesn’t presume the use of expensive off-the-shelf reagents and looks to empower low-income countries, through local production, without subsidies or major infrastructure investment. Specifically, enabling the in-country production of the required biological reagents (e.g. enzymes, antibodies) for POCTs could be significant step.

The overall goal of the research was to explore whether recombinant protein technology in combination with a low-cost support matrix could provide a basis for an inexpensive, simple, and robust production process for the bio-sensing element of a diagnostic. The approach was to merge protein purification and immobilisation into a single step and integrate the resulting bio-functionalised particles directly into an assay format. This thesis is focused on the use of silica as the low-cost support matrix due to its abundance and biocompatibility.

In line with the above goal, the objectives of this work were as follows:

- To evaluate the potential of silica, including silica extracted from a natural resource, as the stationary phase for the purification and immobilisation of designer fusion proteins containing peptide affinity tags

- To investigate the retention of activity by the silica-immobilised proteins and to test their potential sensing capability

- To explore a novel design for a biosensor using bio-functionalised silica as the mobile phase in conjunction with theoretical modelling of the kinetic and mass transport rates for the bio-functionalised particles

- To compare the sensing performance of a range of simple, low-cost biosensor designs utilizing the bio-functionalised silica, including the novel design

2 SILICA-IMMOBILISED FUSION PROTEINS

2.1 Introduction

As described in Chapter 1, enabling the local production of the required biological reagents (e.g. enzymes, antibodies) could be a significant step towards affordable diagnostic testing. By designing fusion proteins through recombinant protein technology, additional functionality can be incorporated into the biological reagent, including a built-in purification and immobilisation peptide tag. Simultaneous purification and immobilisation bypasses many of the normal steps in isolating and integrating the biological element of the diagnostic device, but to be amenable to local production, the stationary phase must be a low-cost and widely available material. A material that fits this description is silica, or silicon dioxide (SiO_2).

Silica has a history as the stationary phase in purification techniques as silica gel is a commonly used resin in column chromatography because of its mechanical strength, easily controlled particle size and porosity, and low cost [89]. However, it has been primarily used as the backbone for functionalised analytical and preparative chromatography resins rather than used directly. The use of unmodified silica gel has previously been explored for both lab and for process-scale purification (e.g. for insulin-like growth factor-I and related proteins [90]) but examples are limited.

This chapter will look to evaluate the potential of unmodified silica as the stationary phase for the purification and immobilisation of designer proteins. Silica particles can be obtained via a range of synthesis processes (Section 2.1.1), including extraction from natural resources which could be available locally in LMICs. One such source, sand, will be investigated and the resulting product characterised and compared to industrially produced silica. The interaction between silica and proteins is mediated via a range of intermolecular forces and is influenced by both the surface composition of the silica and the amino acid residues of the protein (Section 2.1.2 and Section 2.1.3). Peptide tags with specific affinity for silica harness these interactions and can provide specific and oriented immobilisation when genetically appended to proteins of interest. There are a range of options for silica binding peptides/proteins (SBPs) (Section 2.1.4), one of which will be evaluated in this work. The peptide tags are appended to fusion proteins incorporating the bio-sensing element for the diagnostic. A model assay system (Section 2.1.5) will be used to investigate the retention of diagnostic activity by the silica-immobilised fusion proteins.

2.1.1 Sources of silica

Silica is the most abundant material in the earth's crust [91] where it exists in several crystalline phases (quartz is the most common). It can also exist in an amorphous form, as is the case for most synthetic production processes. At an industrial scale, silica is produced by either a gas phase process of pyrogenic flame hydrolysis resulting in fumed silica or by a wet process resulting in silica gel or precipitated silica. Silica gel is an amorphous form of SiO_2 with variable porosity and is made via a sol-gel reaction with sodium silicate and mineral acid, such as sulphuric or hydrochloric acids. The monomers polymerize first into particles and then into 3-dimensional networks, the properties of which can be adjusted based on reaction conditions (e.g. pH). Silica gel particles of various diameters and pore sizes are widely available. Precipitated silica is formed using similar reactants but under higher temperatures. As a result, precipitated silica has minimal porosity. Both types of silica are washed, dried and milled to the appropriate size range [92].

Another sol-gel technique, known as the Stöber process, is commonly used to fabricate silica nanoparticles where controllable and uniform size is desired [93]. Here, the precursor tetraethyl orthosilicate ($Si(OEt)_4$, TEOS) is hydrolysed in alcohol (typically methanol or ethanol) and ammonia is used as a catalyst. Biomimetic silica formation from monosilic acid (generally hydrolysed TEOS or tetramethoxysilane) follows a similar process but occurs under aqueous conditions where peptides with high affinity for silica act as the catalyst [94,95].

Silica can also be easily extracted from a variety of natural sources. Sand is often used as source as silica makes up a large fraction of the material (> 90 % in some sands) [75,76,96] but clay can also be used as a source [97]. Agricultural waste products, after an initial high-temperature sintering step to form ash, can be used to produce silica with varying degrees of success (rice husk > sugarcane bagasse > bamboo) [77]. Other waste products such as glass bottles [98] and iron slag [78] can also be used for silica extraction. Typically, silica extraction from sand and other sources follows a process of alkali treatment and subsequent acidification (Figure 2.1). The silica source can be combined with sodium hydroxide (NaOH) in either a dry or hydrothermal process, and NaOH reacts with SiO_2 in the source to form sodium silicate. The sodium silicate that forms is soluble in water and dissolves when the mixture is washed. Any remaining solid material is removed by filtration. Acidification of sodium silicate (Na_2SiO_3) in the filtrate with sulphuric acid (H_2SO_4) produces silicic acid which readily decomposes to silicon dioxide. Other strong acids such as hydrochloric acid (HCl) can also be used in this step (as done by Munasir *et al.* [75] and Arunmetha *et al.* [76]). Final wash steps and drying produces a precipitate. This process produces largely amorphous phase SiO_2, although Munasir *et al.* observed a small amount of crystalline phase in their production of silica nanoparticles from sands [75]. Provided the common acids and bases required for extraction of silica are accessible, the production of the support phase from locally-available natural resources could be advantageous for the in-country production of diagnostics, as it could remove dependence on an additional foreign-supplied reagent.

$$\mathbf{SiO_2 + 2NaOH \rightarrow Na_2SiO_3 + H_2O}$$

$$\mathbf{Na_2SiO_3 + H_2SO_4 \rightarrow SiO_2 + Na_2SO_4 + H_2O}$$

Figure 2.1 Reaction steps for the extraction of silica from sands

Whether extracted from natural sources or produced industrially, the utility of unmodified silica as the stationary phase for purification and immobilisation will depend on the binding affinity of proteins for the silica surface. This is influenced by the composition of the silica surface [99,100].

2.1.2 Composition of the silica surface

In amorphous SiO_2, silicon atoms are coordinated to oxygen atoms in a tetrahedral arrangement through siloxane bonds. The surface of the material contains these siloxane groups, usually considered to be hydrophobic [101], and unreacted hydroxyl groups called silanols (Si-OH). These have been shown to exist in various forms - isolate (single), geminal (silanediol), or vicinal (H-bonded), each with a distinct pK_a value (Figure 2.2). These groups determine the ionisation state of the silica surface in aqueous solution as a function of ionic strength and pH. Above pH ~3, these silanol groups start to become deprotonated, resulting in siloxide groups (SiO^-) and an increased negative charge on the surface [91]. For example, Puddu *et al.* have shown that the degree of ionization of 80 nm SiO_2 nanoparticles fabricated in a Stöber process increases from 9 % to 18 % to 50 % at pH 5, 7.4 and 8.5, respectively [102]. The degree of surface ionisation along with the area density of the silanol groups and the prevalence of different types (single, vicinal, germinal) all influence the surface properties of silica in aqueous environments.

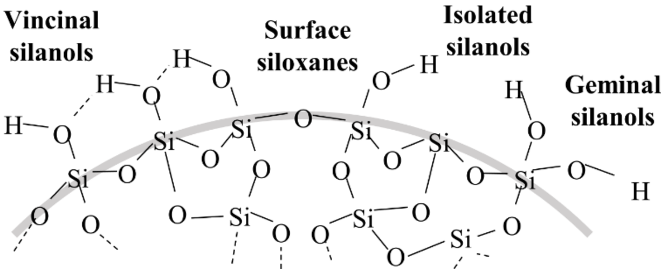

Figure 2.2 Types of silanol groups and siloxane bridges on the surface of amorphous silica.

The density and degree of ionization of the silanol groups depends on the synthetic origin and thermal history of the silica [102,103]. While the chemical composition is essentially the same (SiO_2), silica produced under hydrated processes like sol-gel have an approximately 4–fold higher density of silanol groups compared with fumed silica [104]. Similarly, the surfaces of biomimetic silica structures are highly hydroxylated while thermally grown films made under dry oxidation have low hydroxyl content [74]. Even among silica types produced with a wet process, differences in ionization state are observed [100]. For example, at pH 7.5 and 0.1 M ionic strength, silica sol is reported to have 0.21-0.56 siloxide groups/nm^2 [105–107] compared to 0.56-1.0 siloxide groups/nm^2 for precipitated silica [108,109]. The effect of silica type on binding affinity, and thus the effect of surface composition, is evident in the lack of convergence between peptide sequences selected from combinatorial libraries for their affinity for different silica types (e.g. biogenic silica [110], thermally grown silica [74], and quartz powder [111]).

However, binding interactions are complex and depend not only on surface properties but also on the binding environment and nature of the binder, in this case proteins.

2.1.3 Nature of the silica-protein interaction

Experimental and computational studies about the interaction at the interface between peptides and silica reported that several forces were implicated in the process (electrostatic and van der Waals forces, hydrogen bonds and hydrophobic interactions) [16,18,21,27,28]. While silica surface charge is dependent on the synthetic origin and thermal history of the silica, the surface charge of proteins is determined by their exposed amino acid residues. Although proteins often display multiple positive and negatively charged surface patches [112], their overall electrostatic nature is described by their isoelectric point (pI) or the pH at which the protein's net charge is zero [113].

The interaction between electrically charged bodies can generally be described by the Derjaguin, Landau, Verwey, and Overbeek (DLVO) theory [114–116]. The DLVO theory considers two types of forces: the electrical double-layer repulsion and the van der Waals attraction. (In the case of silica-silica interactions, this theory has been extended to include hydration forces to help explain the short range repulsions observed between silica surfaces [117,118].) The electrostatic interactions are on dependent the pH and ionic strength in the medium, and the degree to which they affect protein adsorption is dependent of the role electrostatics plays in adsorption [119]. For instance, increasing ionic strength (and thus increasing shielding of the surface charge [119]) increased the adsorption of bovine serum albumin (BSA) onto fused silica at high pH (pH > pI) where surface and protein had like charges, but had little effect at low pH (pH < pI) where they exhibited opposite charges [112]. In contrast, short-range interactions (e.g. hydrophobic) are largely independent of the ionic strength [112,117], provided changes in pH and ionic strength don't significantly affect protein conformational stability [119].

A neutral or basic pH the negative charge of the ionized silanols attracts positively charged species by electrostatic forces [74,91,100]. This includes basic side chains (e.g. lysine (Lys, K), arginine (Arg, R)) as well as the N-termini of peptide chains, all of which are protonated at neutral and basic pH ($pK_a > 7$). Under such conditions, protein adsorption on a silica surface is expected to be entropically driven by the release of water molecules and sodium ions on the surface [74,120].

While electrostatic forces are expected to dominate for cationic peptides containing these residues, adsorption was also observed at low pH (i.e. 3.0) [102], suggesting simultaneous H-bonding and van der Waals interactions are also important, especially when the surface is less charged. The importance of these interactions is supported by the adsorption of non-cationic peptides (containing serine (Ser, S) and aspartic acid (Asp, D) residues) onto silica surfaces [100]; however, these peptides show a preference for heat-treated silica (where there is a loss of hydroxyl groups) and have a higher minimum threshold concentration for adsorption [102]. The higher the theoretical pI of the peptide, the lower the threshold concentration, suggesting more positive peptides have a higher affinity to silica under physiological conditions.

Similar trends are also observed for the interaction of larger protein structures with silica [121]. For instance, Ghose *et al.* investigated the suitability of unmodified silica as a stationary phase for protein purification (without an affinity tag) and found a correlation between the mechanism of retention on silica (electrostatic vs. hydrophobic, or some combination) and the molecular properties of the proteins (pI and surface hydrophobicity) [89]. Both electrostatic and hydrophobic interactions were shown to be significant for those proteins that were cationic and hydrophobic in nature, while hydrophobic interactions were shown to be dominant for anionic but hydrophobic proteins. While this knowledge can be exploited for specific selection of target proteins, it does not lend itself to a widely applicable purification and immobilisation process. In addition, there is a risk of protein denaturation if the interaction with the surface is too strong [122].

Alternatively, a peptide tag with affinity for silica can be genetically appended to the target protein. This would enable a range of proteins to be amenable to purification on silica, rather than requiring specific characteristics to be present for good retention times (as explored in [89]). In addition, using peptide tags can achieve oriented immobilisation that can result in less conformational changes than direct association of the protein and the support [88], and generally results in higher activities relative to random immobilisation [80]. This might help preserve the function (e.g. enzymatic activity) of fusion proteins during immobilisation. There are a range of options for silica binding peptides/proteins (SBPs), a review of which will be presented in the next section in order to select a tag for inclusion in the fusion proteins.

2.1.4 Silica binding peptides

A variety of SBPs have been used in purification and/or immobilisation applications in conjunction with other functional proteins. Given the retention of functionality in the fusion protein is key for a diagnostic reagent, this review will focus on those proteins and peptides for which genetic fusion to target functional proteins has been demonstrated with retention of functionality. These peptides and their sequences can be found in Table 2.1.

Peptide sequences with affinity for silica (and for driving silica precipitation) have been identified from organisms in nature (e.g. L2 protein [122], CotB1 protein [123], R5 peptide [124]). L2 is a bacterial 50S ribosomal protein from *E. coli* [122] and CotB1 is a spore coat protein from *B. cereus* that mediates the accumulation of silica [123]. The R5 peptide is a synthetic subunit of the silaffin protein from the diatom *Cylindrotheca fusiformis* (one of seven highly homologous repeating units [124]). SBPs have also been identified synthetically from combinatorial phage or cell-surface display libraries [71,110,111,125] and created through intentional design [126]. The Car9 peptide was originally identified through cell-surface display technology for its affinity for graphitic materials [127]. The poly-arginine tag, with nine arginine residues (poly-Arg, R9), was originally designed as a tag for use with cation exchange chromatography resin given arginine was expected to bind strongly to a cation exchanger as the most basic amino acid [126]. Both Car9 and poly-Arg have been subsequently shown to have affinity for silica [71,128,129].

The interaction of SBPs with silica is thought to be primarily driven by electrostatic forces at physiological pH [102], where their positively charged residues (K and R) interact with the silanol/siloxide groups on the silica surface [102,121,130]. For the large SBPs, L2 and CotB1, regions rich in positive residues are thought to drive their interaction with silica (see Table 2.1 for sequences). Silica binding domains were found at both the N- and C-terminal regions of L2 (1-60 aa and 203-273 aa) [122] whereas the middle section is known to be the RNA binding domain [131]. These protein fragments demonstrated dissociation constant (k_d) values that were ~20 fold higher than the L2 protein in its entirety (when fused to the N-terminus of green fluorescent protein (GFP) in all cases) [122]. In the case of CotB1, its C-terminal region with five arginine and three serine residues, labelled CotB1p, is expected to drive the interaction with silica [123]. The shorter peptide tags (Car9, R5, poly-Arg) are also expected to have similar electrostatic interactions of their positive residues with the negative silanol groups.

While electrostatic forces are expected to dominate, simultaneous H-bonding, van der Waals and dipole-dipole interactions are also suggested to be involved, as discussed above in Section 2.1.3. For example, hydrophobic contacts between the central phenylalanine and siloxane groups were proposed in the interaction of the Car9 peptide with the silica surface [71].

Table 2.1 Silica binding tags and their use cases.

Tag name	Origin	Amino acid residues	Use case
L2	Bacterial 50S ribosomal protein of *E. coli*	Total length: 273 residues Silica-binding regions: N-terminal, 1-60: NAVVKCKPTSPGRRHVVKVVNPELHKGKPFAPLLEKNSKSGGRNNNGRITTRHIGGGHKQ C-terminal, 203-273: VLGKAGAARWRGVRPTVRGTAMNPVDHPHGGGEGRNFGKHPVTPWGVQTKGKKTRSNKRTDKFIVRRRSK	Surface immobilisation (silicon oxidized to silica for biosensor) [122] Purification [132] Purification under denaturing conditions [133]
CotB1	*B. cereus* spore coat protein that mediates the accumulation of silica	Total length: 171 residues Silica-binding regions: C-terminal (see below for residues)	Purification [123]
CotB1p	C-terminal region of CotB1	SGRARAQRASSRGR (14)	Purification [123]
Car9	Identified from combinatorial library, originally for carbonaceous materials	DSARGFKKPGKR (12)	Microcontact printing [134] Purification [71,129] Encapsulation/release of genetically appended cargo [135]
R5	Repeat unit from silaffin polypeptide of diatom *C. fusiformis*	SSKKSGSYSGSKGSKRRIL (19)	Co-precipitation with enzyme [94,136,137] Encapsulation/release of post-translationally added cargo [95] Encapsulation of genetically appended cargo [69,72,138,139] Purification followed by encapsulation [140]
poly-Arg	n/a	RRRRRRRRR (9)	Directed adsorption onto glass slide [128]

Unlike some affinity tags that require proper folding for binding interactions (e.g. maltose binding peptide), some SBPs (L2 and Car9) have been used for affinity purification on silica under denaturing conditions [129,133] as well as under native conditions [71,132]. In addition, the silica binding regions of the L2 were unable to be crystallized, suggesting a non-organized structure that interacts with large area of silica surface [122,132]. This lack of structure has also been predicted for other tags; modelling *in silico* of the R5 sequence gave highly varying models and was unable to predict a meaningful end to end distance, indicating that R5 in isolation is highly flexible [141]. Moreover, although Car9 was originally identified in a disulphide-constrained loop confirmation, a linear version has also been shown to have high affinity for silica [71]. Together this suggests that the mechanism of binding is generally independent of 3-dimensional structure for the SBPs.

SBPs have been genetically appended to a variety of functional target proteins for the purposes of affinity purification with silica gel, immobilisation on solid surfaces (e.g. glass) and/or encapsulation in the presence of silica precursors (See Table 2.1). In some cases, the overall pI of the protein may be < 7 after fusion, as in the case of CotB1p (pI of 12.6) with fluorescent proteins GFP and mCherry (mCh) (pIs of 5.3-6.8, respectively). However, good binding was still observed, which suggested that positive tags can interact with negative silica even when the overall charge of the fusion protein is negative [123]. This is encouraging for the peptide tag approach to be applicable to a variety of functional proteins with a range of pIs.

The SBPs were observed to retain their affinity for silica and/or silica precursors when fused as tags to either the N- or C-terminus of target proteins [71,122,128,129,132,140]. Nevertheless, the choice of terminus for the tag will largely depend on the protein of interest and how the position of the tag affects function [140]. Functional proteins joined with SBPs included fluorescent proteins (GFP, mCh, yellow fluorescent protein (YFP)) [122,123,129,140], enzymes (e.g. B-lactamase [129], luciferase [122], RNAase A [128]) and proteins with binding capacity for secondary coupling to other proteins (e.g. maltose binding protein [129], protein A [132], biotin acceptor protein/AviTag [133]). Functionality (e.g. fluorescence, enzymatic activity) was largely retained in the expressed fusion constructs. Where tested, functionality was retained after immobilisation of the fusion constructs on silica surfaces or after encapsulation, though a slight reduction was observed in some cases [122,128]. In general, the interaction of silica and proteins has the advantage of mild reaction conditions that enables good retention of activity [94,136].

When used for affinity purification purposes, CotB1/CotB1p, L2, Car9 and R5 were all shown to have comparable purity and yield to conventional affinity purification techniques, including the His-tag [55], under native conditions. The electrostatic interactions of SBPs could be disrupted to release the fusion proteins from the silica gel matrix. For example, L2 was released from the silica by ion exchange effect under high concentrations (2 M) of the divalent cation $MgCl_2$ [132], while Car9 and R5 were released by high concentrations of the amino acid lysine [71,129,140]. Several examples also included regions for site-specific cleavage between the SBP and the protein of interest in order to release target proteins from the affinity tags in the event that a protein with a (near) native sequence is required (e.g. with small ubiquitin-like modifier [123], tobacco etch virus and OmpT [71,129] protease-excisable linkers). However, these examples of affinity purification presumed removal of the target protein from the solid support was a prerequisite for the development of useful purification schemes, unlike the approach of simultaneous purification and immobilisation to be considered in this work.

After purification (either on silica gel or on nickel-charged affinity resin (Ni-NTA) using a classical His-tag approach), SBPs have also been used in ‘biomineralisation’ strategies to encapsulate proteins in a sol-gel like, ‘one-pot’ process at room temperature [135], especially R5 [94,136]. (R5 has also been used in co-precipitation as well as genetic fusion strategies, however, ~15 times greater concentration of R5 was needed with the co-precipitation approach [139]). SBPs have also been used to immobilise functional proteins on solid silica surfaces, mainly glass substrates via simple dropcasting [128] or, in one example, via a micro-contact printing process for controlling the pattern of the immobilised protein [134]. The enhanced binding (compared to without the tag) enabled retention during wash steps. This also enables the removal of any proteins bound through non-specific interactions during purification, which will be important for a diagnostic reagent.

Although all of the above SBPs have demonstrated affinity for silica, not all are equal when it comes to selection for inclusion in a fusion construct intended for the local production of the bio-sensing element for a POCT. For instance, the large size of L2 and CotB1 is a disadvantage for expression. Large tags require more metabolic energy during overproduction than small tags [142]; for example, higher expression levels were observed for CotB1p (14 aa) fused constructs compared to those fused with CotB1 (171 aa) [123]. Large tags also tend to drive the formation of inclusion bodies when expressed in *E. coli*, complicating the cell lysis step prior to purification/immobilisation step [123]. In addition, L2 is intrinsically expressed by *E. coli*, which could result in competition of the native form with the fusion construct for surface binding sites under low levels of induced expression [132].

In contrast, poly-Arg, Car9, CotB1p, and R5 are all short peptide extensions that are easily added to either terminal of the target functional protein. While poly-Arg does exhibit affinity for silica surfaces, the strength of the interaction was 1-2 orders of magnitude less than L2 and some slow release was observed, indicating it may not be suitable for the intended immobilisation application [122]. Compared to R5, Car9 fused to fluorescent proteins (sfGFP-Car9) resulted in an accelerated rate of silicic acid polycondensation without causing silica precipitation [135] (when used at the same concentrations as GFP-R5 by Nam *et al.* [139]). While this lack of entrapment in precipitated silica was deemed beneficial for applications requiring protein release, it may indicate a lower affinity for precipitated silica.

Although Car9 and R5 have a similar pI (11.1) and comparable numbers of basic residues (3 Lys / 2 Arg for Car9 versus 4 Lys / 2 Arg for R5), Car9 is lacking the RRIL motif which has been proposed to be involved in the silica precipitation process by clustering R5 segments through electrostatic interactions [143,144]. CotB1p also lacks this motif. Although the interactions with oligomeric silicate species are different to those on extended silica surfaces, Patwardan *et al.* noted a correlation between binding strength and precipitation activity for SBPs [100]. This prompts the selection of R5 for inclusion in fusion constructs intended for affinity purification and immobilisation. R5 has previously been used successfully for affinity purification [140], but direct use of the immobilised product has not yet been studied and will be investigated in this work. The functional elements to be fused with R5 are described in the next section.

2.1.5 Selection of fusion elements for visualisation and bio-sensing functionality

As discussed above, SBPs can be fused with a wide-range of functional proteins. In this work, the fluorescent protein mCherry (mCh) was used as a first model protein for preliminary studies of the interaction between the R5 fusion protein and the silica support material. mCh is a monomeric derivative of *Dicosoma sp.* DsRed (tetrameric) [145] and has been used in diverse applications. It has a fast maturation time [146] and has been shown to have a higher tolerance to fusions (as the termini lie outside the β-barrel) [147] and photostability against pressure [148] and pH [147,149], making it a good choice as a first model.

As mentioned in Chapter 1, the inclusion of a fluorescent protein in fusion construct could potentially facilitate visual monitoring of the protein production and immobilisation process without a laboratory infrastructure. In this capacity, a fluorescent protein in the red range, e.g. mCh, is preferred to the green range, e.g. GFP, as green fluorescence is more difficult to observe by eye in the yellow-coloured media used for culturing *E. coli*.

With respect to the functional enzyme (Enz) portion of the R5-mCh-Enz fusions, the enzymes sarcosine oxidase (SOx) and horse radish peroxidase (HRP) will be explored as first models. HRP in combination with an oxidase is the most used enzyme pair in bioassays; HRP detects the peroxide co-product which acts as a good measurand for the oxidase's substrate (sarcosine in the case of SOx). In the multi-enzyme cascade (Figure 2.3A) combining the two proteins, SOx catalyses the oxidation of sarcosine, yielding glycine, formaldehyde and hydrogen peroxide. Subsequently, in the presence of HRP, hydrogen peroxide (H_2O_2) reacts with a chromogenic agent to product a colorimetric or fluorimetric response. For applications requiring a very low limit of detection, the high-sensitivity of the fluorescence approach is generally preferred [30]. It should be noted that this scheme requires HRP to have activity in excess of SOx in the assay, so that the conversion of sarcosine is the limiting step. Alternatively, the peroxide co-product could be detected electrochemically without HRP, using an approach similar to the first-generation glucose biosensors [150] (Figure 2.3B). Such measurements are carried out on an electrode (commonly platinum) at moderate anodic potential [151]. Although it is possible to detect peroxide directly, this approach is reliant on the concentration of dissolved oxygen in the bulk solution. To overcome this limitation, most oxidase-based electrochemical biosensors make use of artificial electron acceptors, known as mediators (e.g. ferrocene), to shuttle electrons from the active site of the enzyme to the electrode. When held at a constant potential, the current at the electrode correlates with the substrate concentration. Both approaches have been successfully incorporated into biosensors for a range of oxidase enzymes, including SOx [152–156].

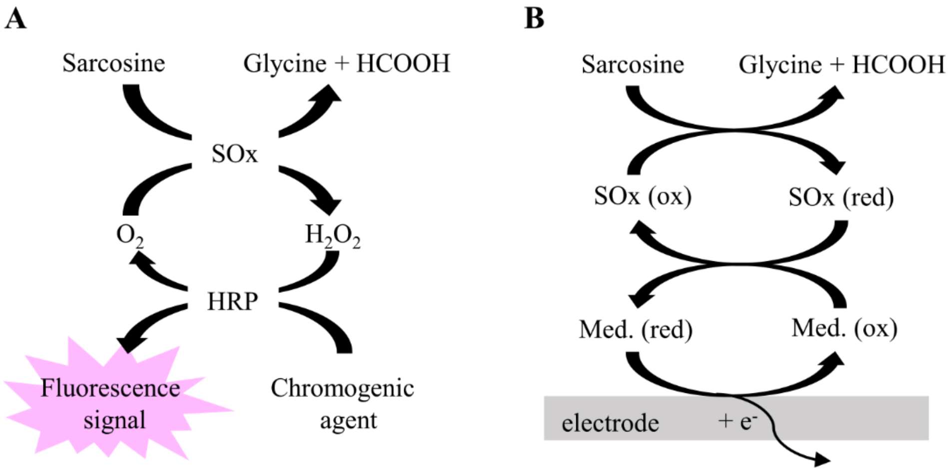

Figure 2.3 Reaction schemes for the detection of sarcosine with sarcosine oxidase by (A) fluorimetric detection using horse radish peroxidase and a chromogenic agent or by (B) electrochemical detection in the presence of a mediator (Med.).

Given colorimetric and fluorimetric signals have been noted for their utility in POCTs for LMICs [21], a fluorimetric signal will be explored in the first instance. This approach also offers the potential advantage of using the visualisation protein (e.g. mCh) incorporated in the fusion construct as internal reference in the diagnostic. Moreover, sarcosine levels in urine have recently been studied as a potential marker of early-stage prostate cancer, when the level rises over 5 µM [157,158], giving the model system potential NCD relevance.

2.2 Experimental

2.2.1 Materials

Materials sourced from Sigma-Aldrich: sarcosine, horseradish peroxidase (HRP, Type 1, P8125), isopropyl β-D-1-thiogalactopyranoside (IPTG), sodium chloride (NaCl), sodium phosphate dibasic (Na_2HPO_4), potassium phosphate monobasic (KH_2PO_4), sodium hydroxide (NaOH), lysozyme (from chicken egg white), Triton X-100, sulfuric acid (H_2SO_4 95 %), bovine serum albumin (BSA), 2,2'-azino-bis(3-ethylbenzothiazoline-6-sulphonic acid) (ABTS), Coomaisse Brilliant Blue, phosphoric acid, L-ascorbic acid, glucose, glycine, silica gel 150 250-500 µm, benzonase nuclease, imidazole, 2-mercaptoethanol, calcium chloride ($CaCl_2$). Materials sourced from Melford Laboratories: LB agar (L1706), LB media (L1704), kanamycin (K0126), carbenicillin. Materials sourced from Acros Organics: potassium chloride (KCl), uric acid, L-alanine, L-proline, creatinine. Materials sourced from alternate suppliers: Amplex^{TM} UltraRed (Invitrogen), commercial silica gel 60 (<63 µm / mesh <230 (Fluka), 6-35 µm (Fisher

Scientific), 40-63 µm (Merck), 63-210 µm (YMC), 200-500 µm (Macherey Nagel)), glycerol (Fisher Scientific), hydrogen peroxide (30 % w/v in H_2O, Fisher Bioreagents), dopamine salt (LKT laboratories Inc.), N-methyl-L-alanine (Alfa Asear), 5-aminolevulinic acid (Cayman Chemical Company).

2.2.2 Extraction of SiO_2 from sand

Sand was identified as natural resource from which silica is commonly extracted and which could be available locally to enable an in-country production process. The protocol for silica extraction from sand followed previously published methods with some changes [75,77] (Figure 2.6). Small amounts of sand (< 5 g) and NaOH were combine and crushed. The mixture was transferred into a Pyrex glass test tube and heated over a flame for 3-5 min. After cooling, water was added and it was filtered through filter paper QL100 (Fisherbrand). H_2SO_4 (95 %, 0.25-1 mL) was added carefully, drop by drop, to the filtrate. The white precipitate was collected, centrifuged (13 k rpm for 1 min) (Biofuge pico, Heraeus Instruments) and washed with water three times (1 mL). The white precipitate was dried at room temperature for 5+ days, collected and ground manually to a powder.

2.2.3 Characterisation of extracted silica

Original sands and dried precipitates were imaged by light microscopy (Optiphot 2 EFD-3, Nikon) and analysed by attenuated total reflectance - Fourier-transform infrared spectroscopy (ATR-FTIR, SpectrumOne, Perkin Elmer). N_2 gas adsorption/desorption studies were used to characterise porosity (3Flex, Micromeritics), ~100 mg tested. Thermogravimetric analysis (TGA, Pyris, Perkin Elmer) results were obtained with a heating rate of 10 ^{0}C/min from 30 ^{0}C to 850 ^{0}C in air and nitrogen.

Both laser diffraction analysis (LDA, Mastersizer 3000, Malvern Instruments) and image analysis using light microscopy (Morphologi G3, Malvern Instruments) were used to investigate particle size. Under light microscopy analysis, greyscale thresholding was used to define particles from surroundings and circle equivalent (CE) diameter calculated for the resulting shape. Filters were applied (CE diameter < 1.80 µm, elongation > 0.6, circularity < 0.7) to remove noise related to contaminants (e.g. dust fibres) and greyscale variation in the background. Calculations for these parameters can be found in the equipment manual. For LDA measurements, a refractive index of 1.45 and an absorption index of 0.01 were used. LDA measurements were also used to calculate silica surface area (SA) per kg of silica particles using surface areas and volumes as determined for spheres with smooth sphere equivalent diameters from the volume distribution collected by LDA.

Silica extracts and sands were analysed by x-ray fluorescence (XRF, Avaatech) for their relative elemental compositions, under the following conditions: 30 s collection time for 50 kV and 15 s for 30 kV and 10 kV with irradiation of the surface in a sample window of 12 mm × 5 mm and a step of 2 mm. Post-processing of the XRF spectra using the Canberra WinAxil software with standard software settings and spectrum fit models was used to obtain element area counts. The element area counts for chlorine (Cl), potassium (K), tin (Sn), and silver (Ag) were removed from analysis as components of the system (detector, sample tray, etc.) raise artificial peaks. A one-way analysis of variance (ANOVA) was conducted with a $\alpha = 0.05$, followed by multiple pairwise two-tailed t-tests for those elements showing a significant difference by the overall F-test ($F_{value} > F_{crit}$). The t-tests were conducted with a Bonferonni correction, namely $\alpha_{adjusted} = \alpha/k$, where k is the number of comparisons made. In the case of the two extracted silica variants compared together with the commercial silica gel 60, k = 3.

Densities of silica extracts and commercially available silica were obtained using a pycnometer. In brief, the weight of the pycnometer alone was measured (m_b), then silica or sand sample added and the weight taken again (m_{b+s}). The remaining volume of the pycnometer was filled with ultra-high purity water and the weight taken again ($m_{b+s+H2O}$). The pycnometer was emptied and water added to full and the weight taken (m_{b+H2O}). The silica density, ρ_s, was calculated by Eq. (2.1), where the density of water, ρ_f, was adjusted for temperature based on reference tables.

$$\boldsymbol{\rho_s = \frac{m_{b+s} - m_b}{\frac{(m_{b+H2O} - m_b) - (m_{b+s+H20} - m_{b+s})}{\rho_f}} = \frac{m_{sample}}{volume_{sample}}} \tag{2.1}$$

2.2.4 Recombinant protein expression

Fusion protein design and transformation into hosts was completed by previous members of the Cambridge Analytical Biotechnology group and glycerol stocks were provided (60 % (v/v) glycerol stored at -80 ^{0}C). Their methods are recorded in brief in Appendix A. Constructs for mCh-6H, R5-mCh-6H and R5$_3$-mCh-6H were designed and provided by Dr. Shah Abbas [141], for mSOx-R5-6H and mSOx-6H by Dr. Si Chen [159], for R5$_2$-mCh-mSOx-R5-6H by Elizabeth Pumford, and for 6H-R5-mCh-HRP and HRP-mCh-R5-

6H by Dr. David Bailey and Ziyan Zhao. The DNA and amino acid sequences for the proteins can be found in [37]. All the provided constructs in *E. coli* strains were grown and induced to express proteins which were purified and analysed as described below.

2.2.4.1 mCh-6H, R5-mCh-6H, $R5_3$-mCh-6H, and $R5_2$-mCh-mSOx-R5-6H

One Shot® BL21(DE3) *E.coli* competent cells (Novagen, F-ompT hsdSB (rBmB-) gal dcm (DE3)) were used for expression of recombinant proteins. Before inducing the expression of proteins, BL21 (DE3) *E. coli* containing expression vector pET-24a (+) with the insert were grown overnight in a starter culture of 20 mL lysogeny broth (LB) media with kanamycin. The culture was then scaled up to 200 mL by inoculating fresh LB media, containing 50 µg/mL kanamycin, with 10 % inoculum (20 mL) from starter culture. It was grown at 37 °C with shaking (225 rpm) to mid-log growth phase ($OD_{600} \approx 0.6$) (not more than 0.8) and induced with 1 mM IPTG at 37 °C with shaking for 4-5 h. Induced cells with expressed proteins were separated into 50 mL aliquots and were centrifuged at 4.3 k rpm and 4 °C for 30 min using a centrifuge (Megafuge 1.0R, Heraeus Instruments), and the resulting pellets were stored at 4 °C or -20 °C.

For lysis, 5 mL of lysozyme (1 mg/mL) in H_2O was added to each cell pellet and incubated on ice for 30 min, followed by probe sonication (30 cycles, 10 s on / 5 s off). The resultant lysate was split into 1 mL aliquots and centrifuged at 13 k rpm for 30 min in a microcentrifuge (Biofuge pico, Heraeus Instruments). The supernatant was either purified on nickel resin for reference following manufacturer's instructions (Section 2.2.5) or immobilised directly onto silica (Section 2.2.6) .

2.2.4.2 HRP-mCh-R5-6H and 6H-R5-mCh-HRP

HRP expression, purification and reactivation was done in collaboration with Ziyan Zhao and Dushanth Seevaratnam. The HRP-mCh-R5-6H was expressed in the BL21 Rosetta II *E. coli* cells and the 6H-R5-mCh-HRP was expressed in *E. coli* pLysS. pTTQ18 (Addgene 69122) was used as the expression vector. The cells were grown in 5 mL LB media supplemented with carbencillin overnight at 37 °C for 12-16 hours. The starting culture was diluted 1:100 in 200 mL LB media with carbencillin and incubated at 37 °C with shaking at 225 rpm until an OD_{600} of 0.6 - 0.8 was reached. The inoculated culture was then supplemented with 2 mM 5-aminolevulinic acid and 1 mM $CaCl_2$ and induced with 1 mM IPTG. The culture was incubated further at 30 °C with shaking at 225 rpm for 8 hours.

The cells were harvested by centrifuge at 6 k rpm for 20 min. The supernatant was discarded and the cell pellet was re-suspended in 35 mL buffer A (300 mM NaCl, 2.7 mM KCl, 10 mM phosphate buffer solution pH 7.5, 10 mM 2-Mercaptoethanol, 0.1 % protease inhibitor cocktail, 20 % glycerol) supplemented with 20 mM imidazole and 2 % Triton X-100 per 200 mL of cell culture. The lysis was achieved by freezing the re-suspended solution at -80 °C for 15 min. Lysozyme was added to a final concentration of 5 mg/mL after the solution was thawed. Another two repeats of freeze and thaw were carried out. The lysed solution was supplemented with 250 units of benzonase nuclease and was incubated on ice for 1 hour, before centrifugation at 13.5 k rpm for 45 min. The supernatant was collected for protein purification (see Section 2.2.5).

The purified protein was desalted using a desalting column to exchange the elution buffer with the desired protein storage buffer (10 mM sodium phosphate buffer, pH 7.5). Reactivation of the protein was achieved by reconstitution with 6 µM of hemin following published method [160], either before or after immobilisation on silica. The hemin solution was added drop by drop from a 1 mM stock solution in 0.1 M KOH. In the case of activation prior to immobilisation, the activated protein was desalted again after incubation with hemin for 1 hour at 4 °C. Post-immobilisation activated protein was desalted via repeated centrifuge at 4 k rpm for 3 min, followed by replacing the supernatant with protein storage buffer. The final desalted immobilised activated protein was suspended in protein storage buffer at a ratio of 20 µL of buffer per 1 mg of silica.

2.2.5 Protein purification

Protein purification was performed using Nickel His-Bind Resin (Novagen). The purification columns were prepared as recommended by the manufacturer. The column was first washed by 5X bed volume of equilibration buffer (20 mM sodium phosphate, 500 mM NaCl, 20 mM imidazole, pH 7.8), followed by loading the supernatant of the cell suspension. The impurities were removed by washing with 3X bed volume of binding buffer (buffer A with 20 mM imidazole), 5X bed volume of wash buffer (buffer A with 50 mM imidazole). The target protein was then eluted with 5X bed volume of elution buffer (buffer A with 250 mM imidazole).

The purified proteins were confirmed using size analyses of denatured proteins on sodium dodecyl sulfate polyacrylamide gel electrophoresis (SDS-PAGE, 8 % SDS) in collaboration with Dushanth Seevaratnam and Ziyan Zhao. The presence of the R5-

silaffin tag was confirmed by protein sequencing using liquid chromatography coupled mass spectroscopy. The yield for R5-mCh-6H was 200 mg/L culture, for R5$_2$-mCh-mSOx-R5-6H was 220 mg/L, for HRP-mCh-R5-6H was 6 mg/L and for 6H-R5-mCh-HRP was 3 mg/L after Ni-purification.

2.2.6 Immobilisation of R5-proteins onto silica particles and characterisation

All functional proteins were analysed for their fluorescence and binding affinity to silica after Ni-purification and/or from crude lysate.

A suspension of silica particles (10 mg/mL, 5 mg in 0.5 mL) was prepared in buffered saline (100 mM Na_2HPO_4, 150 mM NaCl, pH 7.5). The mixture was sonicated for 1 h (water bath FB15056, Fisher Scientific) and a volume of either purified protein or lysate was added, as specified in the text where relevant. The final concentration of the Ni-purified proteins was between 0.05-0.5 mg/mL. After mixing by vortex (VariMix, SciEquip), the suspension was rotated (SB1 tube rotator, Stuart Science) for 1 h and left at room temperature to precipitate. The particles became pink and the supernatant colourless. The protein-modified silica was centrifuged at 13 k rpm for 5 min. The particles were washed several times with water and no leaching of the protein from the particles to the solution was observed, as measured by fluorescence. This immobilisation process was completed with a range of commercial silica particles as well as extracted silica. The selectivity of R5$_2$-mCh-mSOx-R5-6H for silica against other materials such as alumina, calcium carbonate, and cellulose was tested following the same protocol.

The percentage of R5-protein immobilised was calculated by measuring the fluorescence intensity characteristic of mCh, i.e. excitation 587 nm / emission 607 nm (Cary Eclipse Fluorescence Spectrophotometer, Varian) of the supernatant at the beginning and end of the immobilisation.

A Bradford assay was used to determine the total protein immobilisation. In brief, 20 µL of supernatant following the first spin-down after incubation was added to 100 µL Bradford reagent (Coomassie Brilliant Blue in phosphoric acid) in a well plate. Absorbance at 595 nm was measured with a UV spectrophotometer and compared with a standard curve made with bovine serum albumin (BSA) (Figure 2.4). Elution of the proteins off silica was achieved by incubation in 0.5-1 M lysine for 30-120 min.

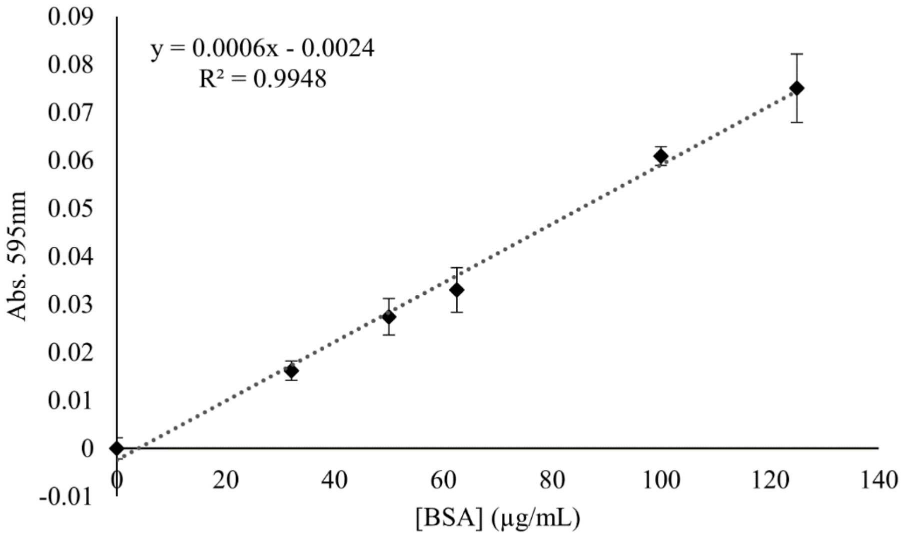

Figure 2.4 Standard curve for Bradford assay, showing linear relationship of Abs. 595 nm (blank subtracted) with BSA concentrations from 0 to 125 µg/mL.

Absorbance (Infinite M200, Tecan) and fluorescence readings were taken of both functionalised particles and soluble proteins to identify any changes in absorbance or fluorescence spectra as a result of R5-peptide fusions or immobilisation. Confocal microscopy images were obtained using Leica TCS SP2 spectral confocal microscopy. Z-stack images were taken for multiple particles and intensity profiles for emission 609 nm analysed across particle cross-sections.

A quartz crystal microbalance (QCM, openQCM) was used to estimate binding coefficients for the fusion proteins with silica in collaboration with Dr. Neus Jornet-Martínez. The gold chips were first cleaned with piranha solution for 20 min. They were then immersed into 5 mM (3-mercaptopropyl)trimethoxysilane solution in ethanol overnight. Under these conditions, the thiol group is expected to interact with the gold surface [161] and the remaining alkoxy side groups are expected to undergo self-condensation and hydrolysis reactions to form siloxane bridges and silanol groups [162–164], forming a layer on the surface of the chip. The modified chip was rinsed with acetonitrile and dried before use. Measurements were conducted at 10 MHz and a flow rate of 3.6 mL/h. Buffer (phosphate buffered saline, pH 7.4, PBS) was flown through the system (~ 60 min), followed by the Ni-purified proteins in buffer (10 and 5 µg/mL of R5-mCh-6H and mCh-6H), then buffer again, each time until the frequency stabilised. Plots of frequency over time were used to determine the equilibrium dissociation constant K_D as measure of protein's affinity for a surface. K_D (M) is the ratio of the dissociation rate constant, k_d (s^{-1}), to the association rate constant, k_a ($M^{-1}s^{-1}$), i.e. $K_D = k_d / k_a$. The association portion of the frequency over time curves were fitted to a function for exponential growth (Eq. (2.2)) and the dissociation portion to an exponential decay (Eq. (2.3)) using Origin Pro9.1 software, following convention for protein affinity isotherms with QCM [141,165,166].

$$\boldsymbol{F_t = \frac{k_a F_{max} C}{k_a C + k_d}\left(e^{-((k_a C + k_d)\times(t-t_0))} - 1\right) + F_0} \tag{2.2}$$

$$\boldsymbol{F_t = F_0 e^{-k_d(t-t_0)}} \tag{2.3}$$

Where F_t is frequency at time t, F_0 is frequency at the start of association/dissociation, t_0 is the time at the start of association/dissociation, C is concentration of the protein, and F_{max} is the frequency shift observed from F_0 to the plateau. The mass of protein (Δm) adsorbed onto the surface of the chip was calculated using the Sauerbrey equation (Eq. (2.4)(2.4)(2.4)(2.4)) [167,168]:

$$\boldsymbol{\Delta f = -\frac{2f_0^2}{a\sqrt{\rho_q \mu_q}}\Delta m} \tag{2.4}$$

where Δf is the frequency change, f_0 is the resonant frequency of the chip, ρ_q is the density of quartz (2.648 g/cm^3), μ_q is the shear modulus of quartz (2.947×10^{11} g/cm/s^2) and a is the active area between the electrodes.

2.2.7 Determination of sarcosine and H_2O_2

Sarcosine or H_2O_2 was detected by functional R5 proteins (R5$_2$-mCh-mSOx-R5-6H and/or HRP-mCh-R5-6H or 6H-R5-mCH-HRP, respectively) in combination with the dye Amplex^{TM} UltraRed (AR) for both soluble and immobilised proteins. There are a variety of chromogenic substrates to choose from with HRP, but AR is reported to have stability across a range of pH by the manufacturer and is the dye typically included in commercially available enzyme kits for sarcosine detection in plasma/serum.

For the detection of sarcosine in well plates with Ni-purified protein in solution, 10 µL of Ni-purified R5$_2$-mCh-mSOx-R5-6H (1.9 mg/mL) was added to 0-10 µL volumes of sarcosine solution (100 µM), 10 µL of wild-type (WT) HRP (0.4 mg/mL) and 10 µL of AR (1 mM). For the detection of H_2O_2, 4.8 µg of Ni-purified HRP-mCh-R5-6H or 6H-R5-mCh-HRP (40 µL of 0.12 mg/mL or 80 µL of 0.06 mg/mL, respectively) was added to 10 µL of AR (1 mM) and final concentration of 0-168 µM H_2O_2. The final volume in each well was adjusted to 100 µL with water. The fluorescence was measured, after reaction for 20 min at room temperature (in the dark), at ex. 530 nm / em. 582 nm, photomultiplier tube (PMT) voltage 800 V, excitation slit 5 nm. Emission slit was 10 nm for mSOx, 5 nm for HRP. The fluorescence intensity of the sample (I) with respect to the blank (I_0) was plotted against the concentration of substrate (sarcosine or H_2O_2). A similar protocol was conducted with silica-immobilised protein for the detection of sarcosine, replacing soluble protein with 1 mg of R5$_2$-mCh-mSOx-R5-6H on silica extracted from SC sand (~90 µg protein / mg silica). Figure 2.5 shows the calibration curve for the AR assay using WT HRP following the protocol described above (100 µL total volume).

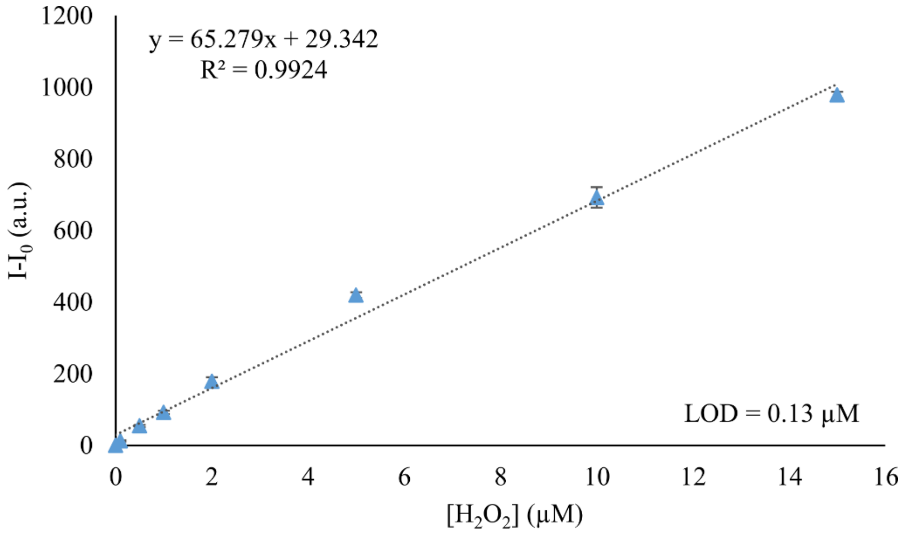

Figure 2.5 Calibration curve for the detection of H_2O_2 with AR dye at 100 µM using WT HRP (0.04 mg/mL) and the indicated concentration of H_2O_2. Ex. 530 nm / ex. 580 nm, slits 5 nm, PMT voltage 800 V, blank subtracted.

Endpoint assays for sarcosine were conducted in well plates, 50 µL each assay with 50 µM AR, 0.04 mg/mL WT HRP, 3.75 mg silica-immobilised R5$_2$-mCh-mSOx-R5-6H and various final concentrations of sarcosine.

For any calibration curves, the limit of detection (LOD) was determined based on the slope of the linear regression (b) and the standard deviation of the blank response (SD) using the following formula:

$$\boldsymbol{LOD = (3.3 \times SD)/b} \qquad (2.5)$$

For evaluating the effect pore size of commercial silica gel particles on activity, detection of 10 µM sarcosine was performed using the AR assay as described above. Quantity of silica added was adjusted based on immobilisation efficiency in order to maintain equivalent enzyme concentration. The microcentrifuge tubes were rotated for 60 min before fluorescence intensity was measured at ex. 530 nm / em. 582 nm, PMT voltage 800 V, excitation/emission slits at 5 nm.

2.2.8 Determination of specific activity

For the fusion proteins to potentially have utility as biosensors, they must show activity in the presence of the target substrate. Trinder's colorimetric assay was adapted to measure specific activity of sarcosine oxidase. 4-aminoantipyrine (50 µL, 4.7 mM), phenol (50 µL, 20 mM), sarcosine (50 µL, 2 M), HRP (50 µL, 0.4 mg/mL) was added to 300 µL of 10 mM sodium phosphate buffer (pH 7.5). After 5 min, 10 µL of enzyme was added to the mix (either R5$_2$-mCh-mSOx-R5-6H, in solution (1.9 mg/mL) or immobilised on silica (0.1 mg silica, ~90 µg protein/mg silica), or WT sarcosine oxidase (0.5 mg/mL)). After 5 min, 2.5 mL of ethanol was added to stop the reaction and the absorbance was registered at 480 nm.

Specific activity for HRP constructs was measured using a colorimetric assay with indicator ABTS (2,2'-Azinobis [3-ethylbenzothiazoline-6-sulfonic acid]-diammonium salt). The enzyme (in solution or immobilised, 0.25 mg) was added to ABTS solution (4.83 mM final) to a total volume of 295 µL and allowed to equilibrate for 5 min. Then, 5 µL of hydrogen peroxide solution was added and the absorbance at 405 nm was measured every 5 s over 2 min.

For both assays of specific activity, total protein immobilised on the silica was measured by Bradford assay, as described above. Change in absorbance over time was converted to Units of activity per mg total protein using Eq. (2.6) derived from the Beer Lambert law.

$$\boldsymbol{U/mg = \frac{\Delta A}{\varepsilon l x} \times \frac{v}{m}} \tag{2.6}$$

Where ΔA is rate of change of absorbance over time, l is pathlength of the cell, v is the final volume of the assay, m is the mass of protein added to the reaction mix and ε is the millimolar extinction coefficient (17.14 for quinoneimine dye at 480 nm and 36.8 for ABTS at 405 nm). The variable x is a multiplier for depending on the ratio of moles of substrate to product, e.g. two moles of H_2O_2 produces a mole of quinoneimine dye. Pathlength, l, for the well plate was determined by the difference in absorbance of water at 977 nm and 900 nm for an equivalent volume (Eq. (2.7)), where 0.18 is a reference value for this difference in a 1 mL cuvette. Pathlength values of 0.624 cm and 0.912 cm were used for 200 and 300 µL samples, respectively.

$$\boldsymbol{l = \frac{A_{977} - A_{900}}{0.18}} \tag{2.7}$$

2.2.9 Determination of selectivity and pH effect

Selectivity is an important component in a biosensor to avoid false positive signal from other interfering substances that may be present in the sample. The selectivity of fusion constructs was evaluated by the generation of AR fluorescence in the presence of potential interferents. The AR assay was conducted following the protocol described above for well plate assays of sarcosine/H_2O_2 but with the following changes.

For the selectivity of sarcosine oxidase, stock solutions of potential interfering substances N-methyl-L-alanine, L-alanine, glycine, L-proline, and creatinine were prepared at concentration of 1 mM. The solutions were diluted to final concentrations of 10 µM in the assay. L-alanine and creatinine were also tested at final concentrations of 10 mM and 20 mM, respectively, to compare with expected levels in urine [169,170]. Either 1 mg of $R5_2$-mCh-mSOx-R5-6H on silica extracted from SC sand in 10 µL buffer (~90 µg protein/mg silica), 10 µL of crude lysate or 10 µL of 0.1 mg/mL WT SOx was added to potential interferents along with 5 µL of AR (1 mM) and 10 µL of WT HRP (0.4 mg/mL).

For the selectivity of HRP, stock solutions were prepared of dopamine HCL, L-ascorbic acid, glucose and uric acid, and diluted to final concentration of 50 µM in the assay. Either 0.5 mg of immobilised 6H-R5-mCh-HRP on SC extract in 5 µL buffer (10 µg protein/mg silica) or 10 µL of 0.01 U/mL WT HRP was added to potential interferents along with 5 µL of AR (1 mM).

For both SOx and HRP, the effect of pH was evaluated using the same protocol as the selectivity well plate assay but using buffers of various pH (determined by Jenway 3510). In all cases, fluorescence was measured at 20 min with an emission slit of 5 nm for SOx and 10 nm for HRP. A standard ($I_{standard}$) of sarcosine (10 µM) or H_2O_2 (50 µM) and a blank (I_0), all at pH 7.5, were used as a references to calculate relative responses.

2.3 Results and Discussion

2.3.1 Silica extraction and characterisation

As mentioned above, sand can be a good natural source for silica (silica content > 90 % for some sands). Silica extraction from sands followed an alkali treatment and subsequent acidification process, adapted from published examples of silica extraction from sand [75,77], as outlined in Figure 2.6. Here, the sand is mixed with NaOH in a dry process and heated under flame. After filtration, acidification and wash steps, the resulting precipitate is dried at room temperature (~20 ^{o}C).

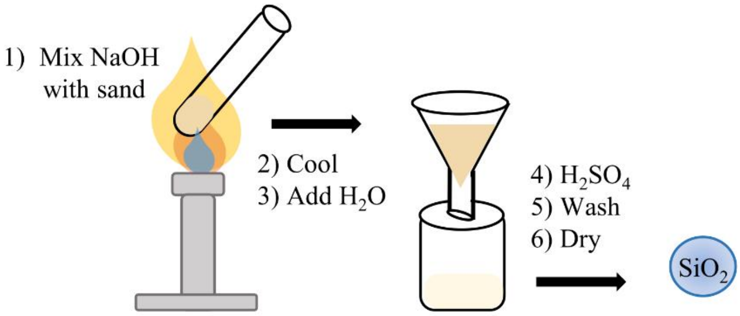

Figure 2.6 Schematic illustration of the extraction process of silica (SiO_2) from sand.

A variety of beach sands from diverse locations (Table 2.2 and Figure 2.7A) were used to evaluated the performance of the extraction process across a range of sand compositions. Sand is a class of material defined by size, rather than by composition; The Unified Soil Classification System defines sands as those soils containing 50 % of their material larger than No. 200 sieve (> 74 µm in diameter) where > 50 % of this is smaller than No. 4 sieve (< 4.76 mm diameter)[171]. The composition of sand varies significantly as it is dependent on the local rock sources and conditions, so the variability in yield from the extraction process was unsurprising. Not all sands tested had sufficient yields of silica from this process. For example, no silica was able to be extracted from sand obtained from the Caribbean (CB) and yields from Hong Kong (HK) and Santorini (ST) sands were < 1 % weight. In contrast, yields of 11.5 ± 1.4% and 4.7 ± 0.9% weight were obtained for beach sands from South Carolina (SC) and Ghana (GH), respectively. Yield could potentially be increased with more control over the heating step, e.g. use of a hotplate rather than flame, or reduction in initial grain size through milling [76]. Nonetheless, yields from SC and GH were sufficient to carry forward for additional characterisation (below) and evaluation of binding capacity for fusion proteins (Section 2.3.2 and 2.3.3).

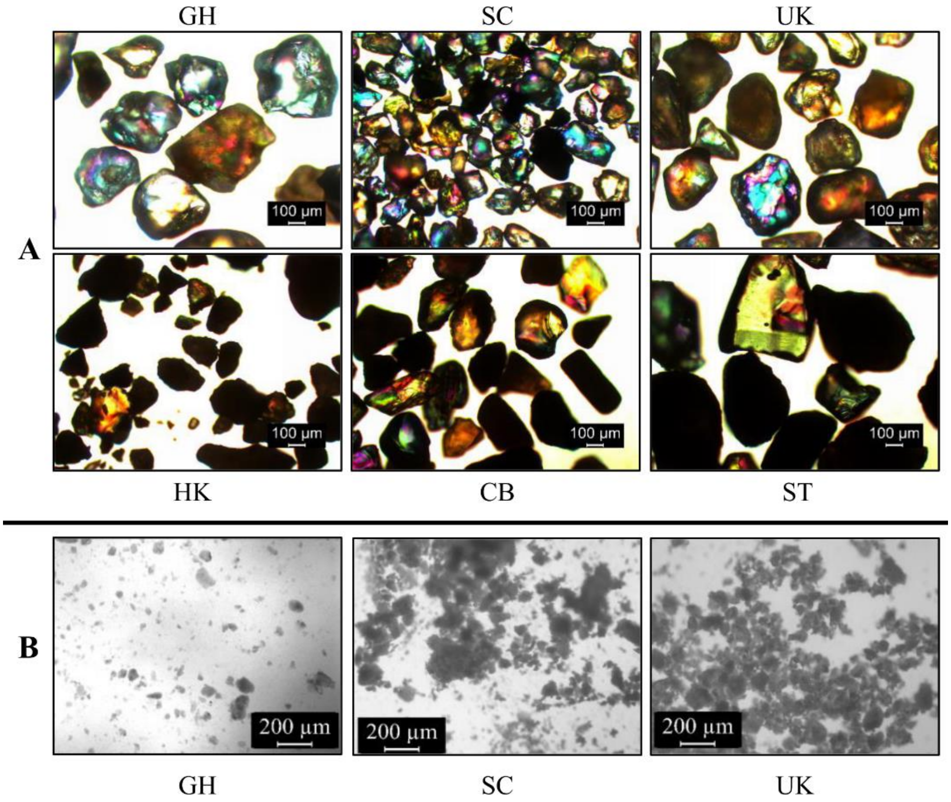

Figure 2.7 Bright field optical microscope images for both (A) the sands and (B) the resulting precipitates (from GH, SC, and UK sands).

Table 2.2 Sand sources and corresponding silica yields after extraction

Sand source location	Abbreviation	Silica % yield (w/w)
South Carolina, U.S.A.	SC	11.5 ± 1.4 %
Accra, Ghana	GH	4.7 ± 0.9 %
Southwold, U.K.	UK	~1 %
Sharp Island, Hong Kong	HK	< 1 %
St. Lucia, Caribbean	CB	n/a
Santorini, Greece	ST	< 1 %

The variability in yield across the sand sources is likely related to their variability in overall silica content, as shown by XRF analysis. Although elemental counts derived from XRF spectra (Figure 2.8) are dependent not only on the concentration of the element but also on matrix effects, physical properties, sample geometry and the hardware settings of the scanner [172,173], intersample variability in a single element can be used for a relative comparison between samples (Figure 2.9). Analysis of XRF results showed that sands from ST, HK, and CB had relatively less silica (Si) as compared to the sands from SC, GH and UK, with HK exhibiting the lowest counts. $CaCO_3$ is another common component in sands from broken shells and differences in sand composition were also observed for calcium (Ca); HK and CB sands show relatively higher counts for calcium (Ca) than GH, SC, UK or ST sands, with SC and UK showing the lowest counts. Other variances in composition were also visible between the sand variants with this analysis technique. HK sand also shows the highest counts for strontium (Sr) and rubidium (Rb). CB and ST sands show higher levels of iron (Fe), zinc (Zn), and cobalt (Co). ST also shows higher levels of aluminium (Al), barium (Ba) and titanium (Ti). The remaining elements showed limited variance across the sands.

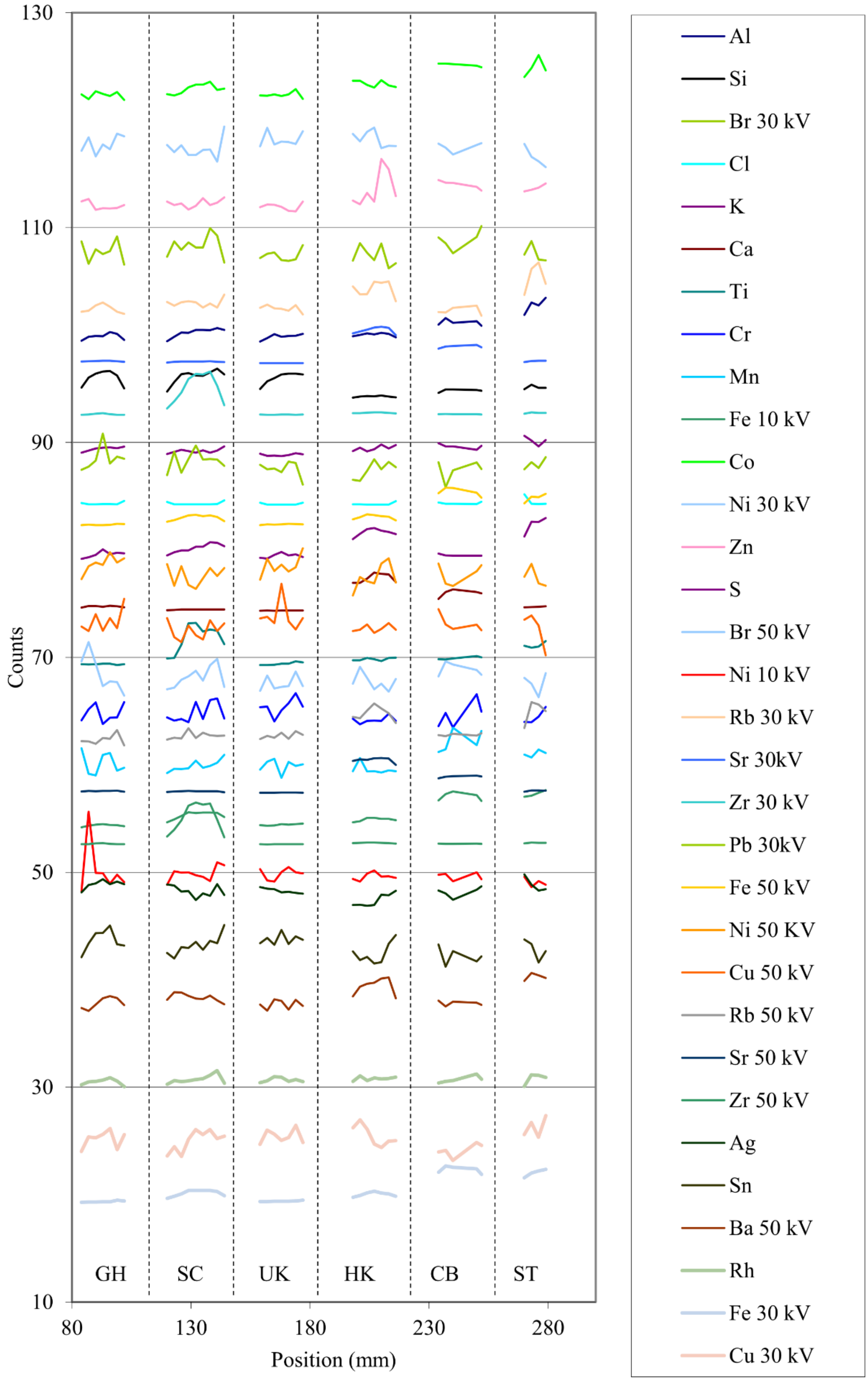

Figure 2.8 Normalized and offset elemental intensities from XRF plotted across sample position for sand sources.

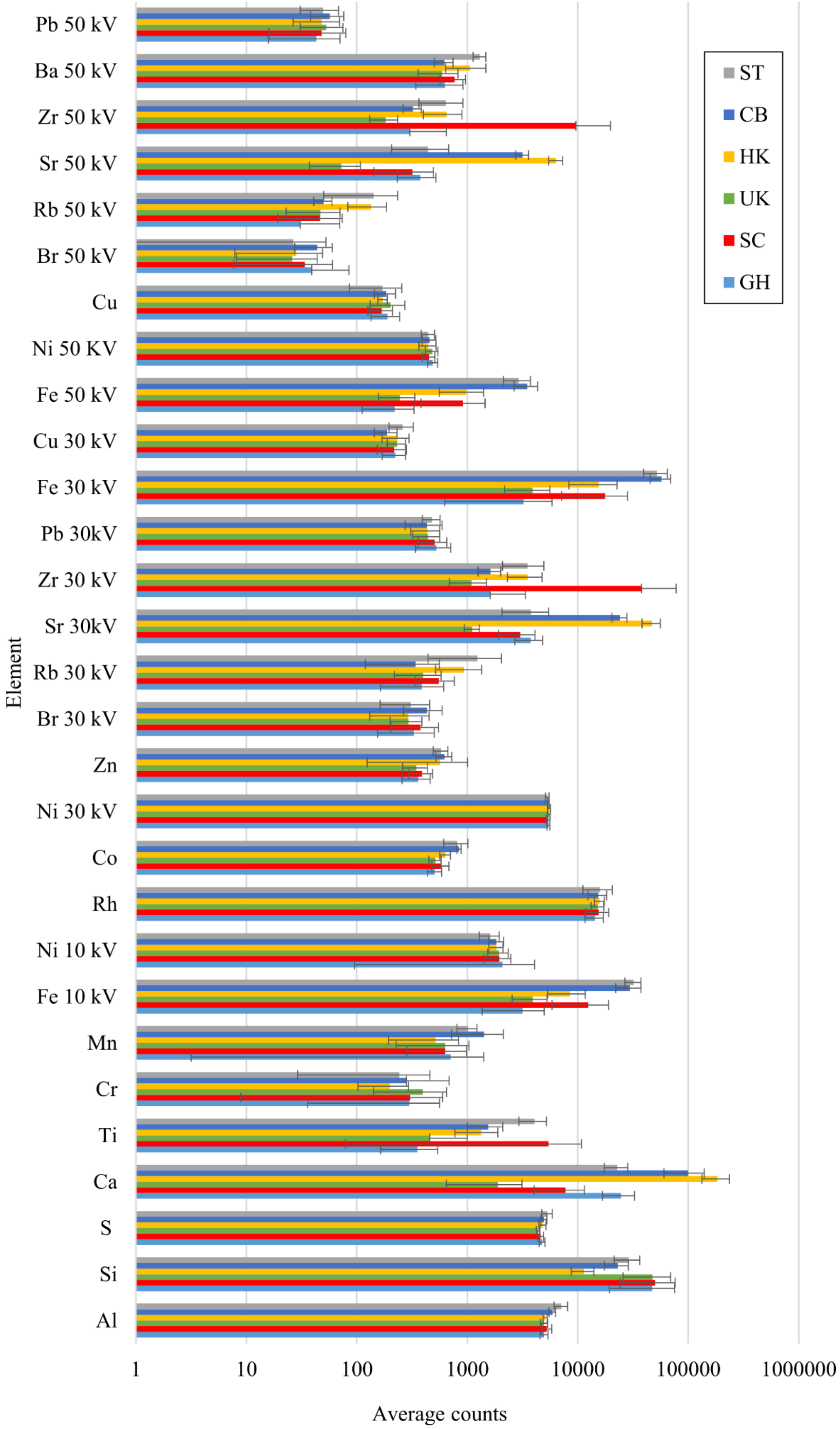

Figure 2.9 Mean element intensity counts across individual samples for sand sources.

For those sand sources with sufficient silica content to yield a precipitate (SC, GH, UK), the FTIR spectra of these extracted products show characteristic symmetric and asymmetric stretching modes for Si-O-Si (804-805 cm^{-1} and 1079-1088 cm^{-1}, respectively) and the symmetric Si-OH mode (952-953 cm^{-1}), which overlay with commercially available silica gel (Figure 2.10). Similar features are observed in the corresponding unprocessed sands, albeit at a lower % transmission. Comparing the relative intensities of the symmetric vibrations indicates that the silica extracts have slightly higher ratio of Si-OH groups relative to the Si-O-Si groups compared with commercial silica gel (Figure 2.10C and Table 2.3). Given the area density of silanol groups on the silica surface can influence binding affinity [100], this may have an effect on binding capacity of the silica and will be discussed further in Section 2.3.4.

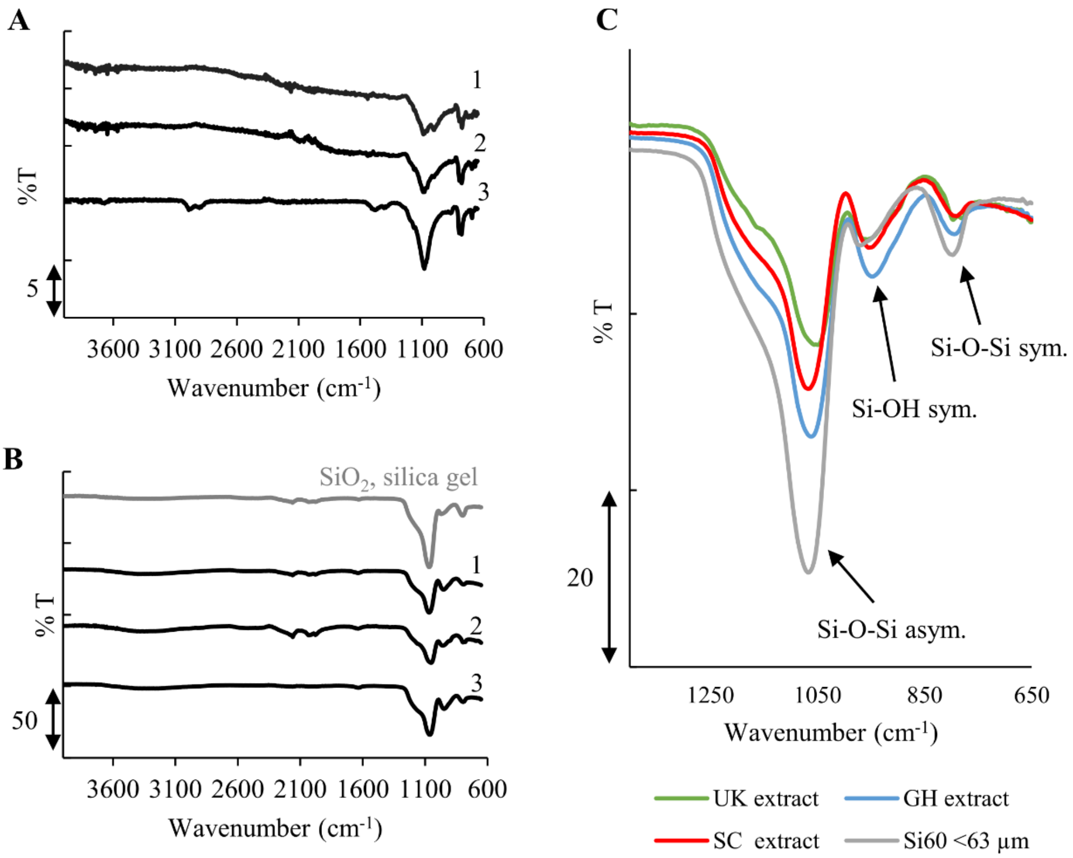

Figure 2.10 Fourier-transform infrared (FTIR) spectra of (A) sands and (B) extracted silica, with sand from (1) South Carolina, U.S.A. (2) Southwold, U.K. (3) Accra, Ghana. Curves are offset. Results are also shown in (B) for commercial silica gel 60 <63 µm. (C) Magnified region of (B) showing peaks of characteristic peaks for SiO_2, highlighting the difference in the ratio of Si-OH and Si-O-Si symmetric stretching modes between extracted silica and commercial silica gel.

Table 2.3 Ratio of the peaks for symmetric stretching of Si-OH (950 cm^{-1}) over Si-O-Si (800 cm^{-1}).

Silica type	Ratio Si-OH / Si-O-Si groups (950/800)
Silica gel 60 <63 µm	0.84
UK extract	1.27
GH extract	1.44
SC extract	1.43

Given their higher yields, SC and GH sand sources were selected for further characterisation including size, porosity and density. Figure 2.11 shows the heterogeneous size distribution of the precipitate and Table 2.4 lists the density of sands and extracts alongside commercial silica gel variants (60 and 150 refer to pore size in Å). Size distributions of commercial silica with discrete size classes (Figure 2.39) are shown later in Section 2.3.4 with respect to the effect of particle size on fusion protein binding.

Table 2.4 Characterisation of sand and silica

Source	Type	Particle size range (µm)	Density (g/cm^3)
Commercial	silica 60	<63	1.87
Commercial	silica 60	6-35	2.07
Commercial	silica 60	40-63	2.04
Commercial	silica 60	63-210	1.96
Commercial	silica 60	200-500	2.03
Commercial	silica 150	200-500	2.05
SC	silica extract	See Figure 2.11	2.18
GH	silica extract	See Figure 2.11	2.02
SC	sand	100-500	2.75
GH	sand	300-700	2.66

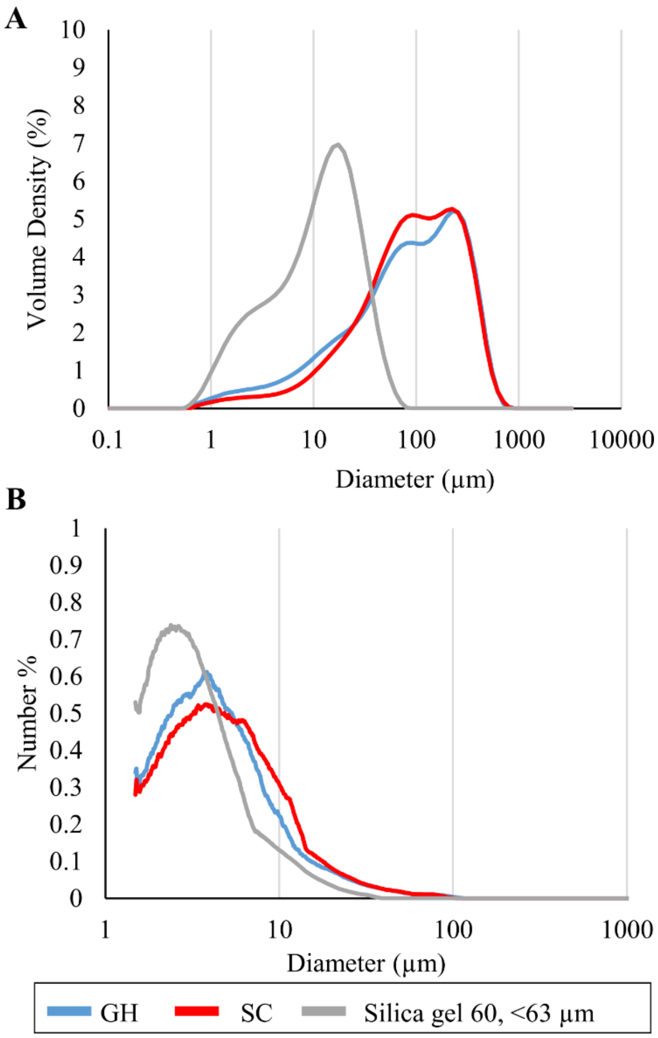

Figure 2.11 Particle size distribution of the silica extract from SC and GH and of commercial silica gel 60 <63 µm as measured by (A) laser diffraction and (B) microscopy. Resolution limit for microscopy was diameter of 1.8 µm.

Despite the similarity in FTIR spectra (Figure 2.10), the N_2 gas adsorption/desorption isotherms (Figure 2.12) suggest that the silica precipitated from sand-processing is nonporous or macroporous (> 50 nm pore diameter) and undergoes a nearly reversible multilayer adsorption (type II isotherm). In contrast the commercial silica gels demonstrate mesoporous (type IV isotherm) behaviour, which is typical of mono-layer/multilayer adsorption followed by capillary condensation in the mesopores. This is also consistent with the higher density for silica extracted than commercial silica gel (Table 2.4). Figure 2.12E also shows that N_2 adsorption on unprocessed sand is very low.

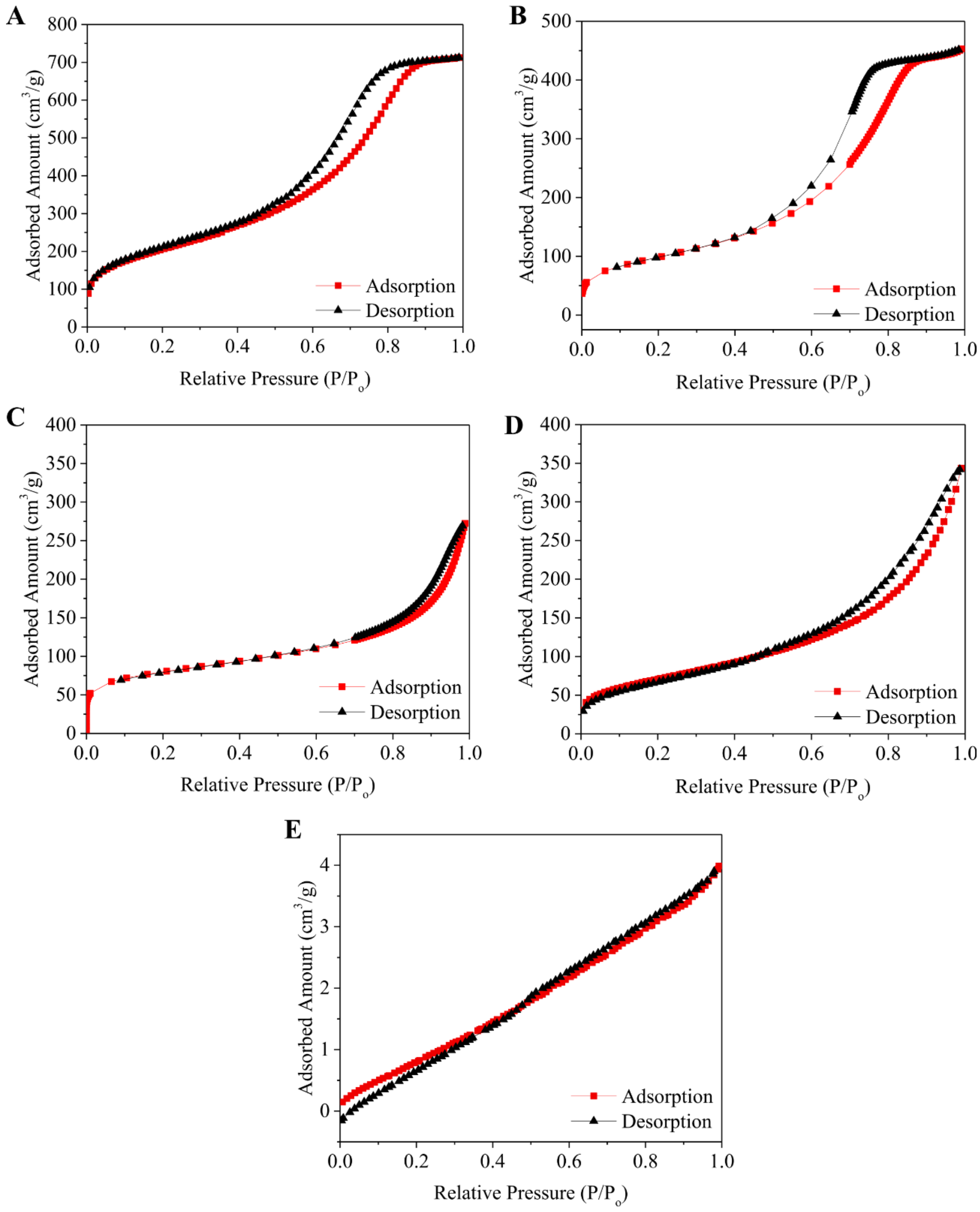

Figure 2.12 N_2 isotherms for commercial silica 60 (A) <63 µm and (B) 63-210 µm in diameter, for silica extracted from sand from (C) SC and (D) GH and for (E) sand, SC.

During the extraction process, it is expected that the NaOH primarily reacts with SiO_2 to form sodium silicate, however, there may be some side reactions occurring with other components present in the sand. Although the FTIR spectra primarily shows the presence of SiO_2 (Figure 2.10), other components from these side reactions may also be present in low concentration in the extracted silica. Comparative thermogravimetric analysis (TGA) against a reference material, e.g. commercial silica gel, can be used to identify if this is the case (Figure 2.13 and Table 2.5). TGA is a method of materials characterization through analysis of characteristic decomposition patterns. Some weight loss is expected for silica gel due to the loss of water. Indeed, the pattern of weight loss for the commercial silica gel follows the expected shifts where the first loss between 50-150 ^{0}C is attributed to physically absorbed water, the second loss between 150-400 ^{0}C to strongly held water, and the final loss between 400-900 ^{0}C attributed to the condensation of silanol groups on the surface [174] (Figure 2.13). A similar pattern is observed for the both extracted silica variants, but with additional overall weight loss. This suggests that there may be components other than silica present in the extracts. Minimal difference in weight loss was observed between heating in air or in nitrogen, which suggests that the mass loss from organic matter is small and the other components may be inorganic.

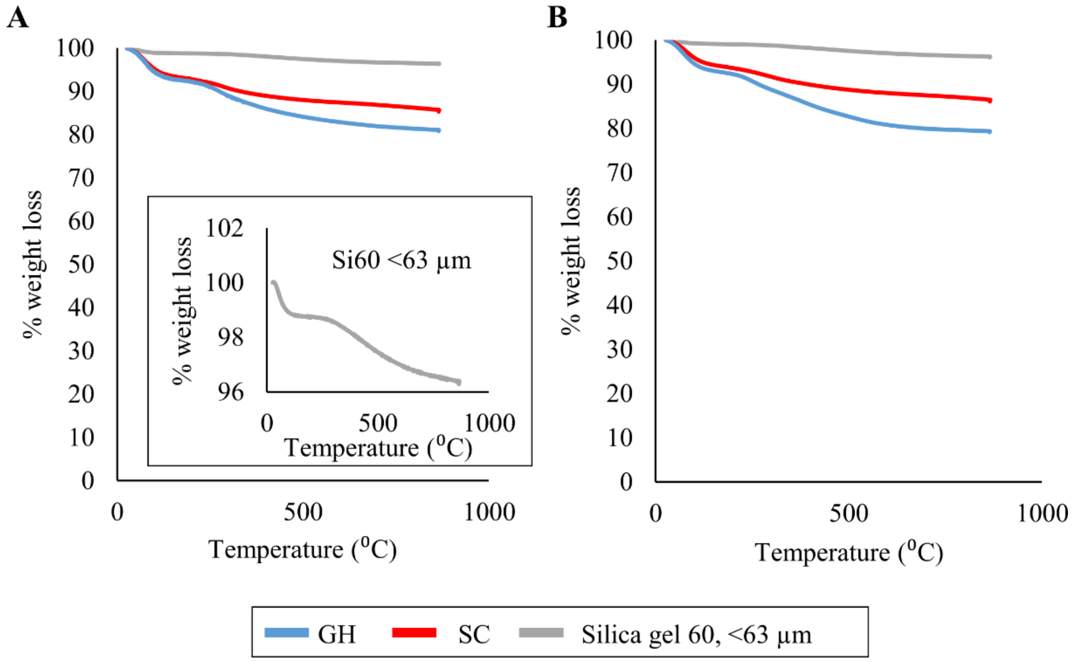

Figure 2.13 TGA of commercial silica gel and extracted silica in (A) air and (B) nitrogen.

Table 2.5 Weight loss of silica variants during TGA in air and nitrogen.

Silica type	Air	Nitrogen
Silica gel 60, <63 µm	3.7 %	3.9 %
SC extract	14.7 %	13.9 %
GH extract	19.3 %	20.8 %

To identify potential differences in inorganic components in the extracts, element counts from XRF analysis of extracted silica variants were tested for statistically significant differences using a one-way ANOVA with α of 0.05 followed by multiple pairwise two-tailed t-tests with a Bonferonni correction of α_{altered} of 0.017. The extracted silica variants were compared to each other and to commercial silica gel 60 (<63 µm) as a reference. This analysis showed that the two extracted silica variants have more sulphur (S) than the commercial silica gel, which is likely a residue from the final acidic precipitation step, with GH extract showing higher levels than SC. This could potentially be removed with further wash steps as done by Lazaar *et al.* for Cl^- ions after HCl precipitation [96].

Statistically significant differences are also observed in other elements. Both silica extracts show lower counts for calcium (Ca) and aluminium (Al) than commercial silica gel, but no difference to each other. SC shows higher counts for titanium (Ti), but lower counts for silicon (Si) and rhodium (Rh) when compared to either GH or commercial silica gel. SC extract also shows higher counts for iron (Fe) than the other two at 10 kV and 30 kV. Fe counts at 30 kV are also higher for GH as compared to commercial silica gel. However, Fe counts at 50 kV show SC is only significantly different from GH extract and neither different from commercial silica 60. This pattern at 50 kV is also observed for Ba counts. While some elements are counted in more than one energy band in order to make the deconvolution most effective, one energy band is usually recommended for each element. For Fe, the 10 kV band is recommended, while for Ba, the 50 kV band is recommended. GH shows higher counts for zinc (Zn) than either SC or commercial silica gel. It also shows higher counts for bromium (Br), but lower counts for zirconium (Zr) and nickel (Ni) when compared to commercial silica 60 but only in the 30 kV energy, not at the 50 kV. However, the 30 kV energy band is recommended for these elements so the differences are likely significant between the materials. There were no statistically significant differences between samples for the other elements analysed here.

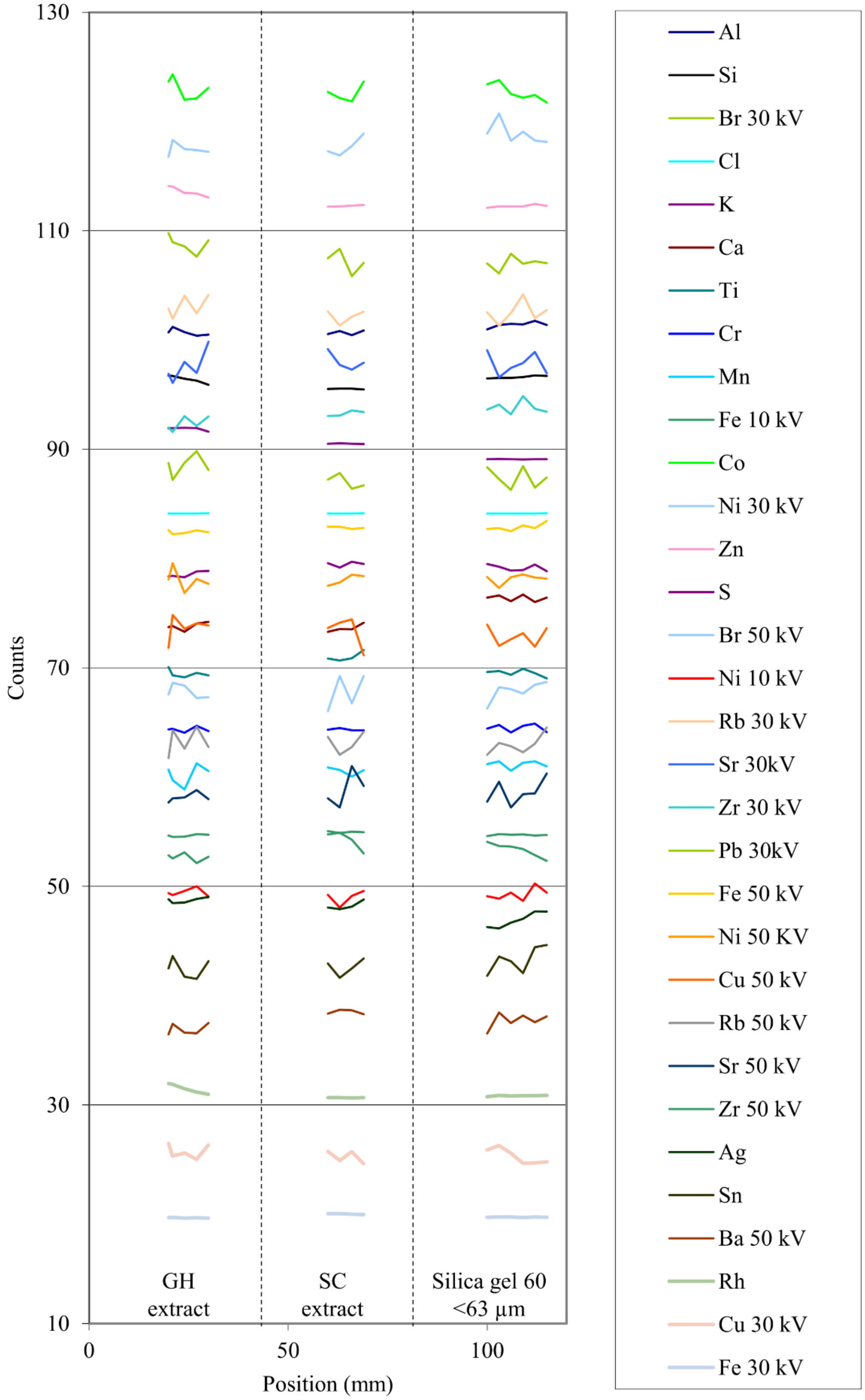

Figure 2.14 Normalized and offset elemental intensities from XRF plotted across sample position for silica extracted from SC and GH sands and for commercial silica gel 60, <63 µm.

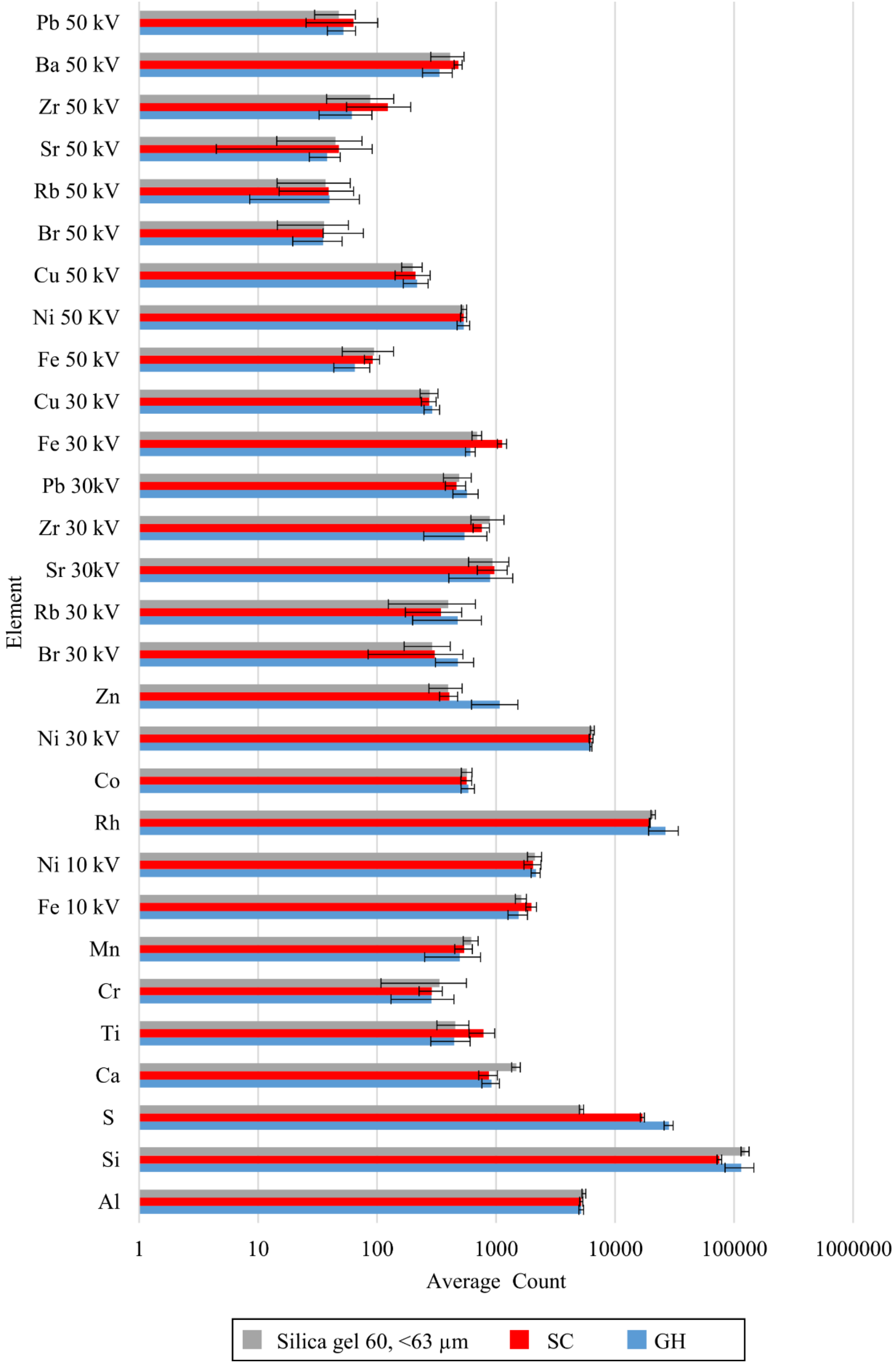

Figure 2.15 Mean element intensity counts across individual samples for silica extracted from SC and GH sands and for commercial silica gel 60, <63 µm.

Some of these variances reflect variances in the sand sources (Ti, Fe, Zr), however, the majority are uncorrelated. XRF analysis does not provide a quantitative measure, however, the FTIR results confirm the precipitate is primarily silica and suggest that these are likely trace elements. If significant variance is observed in the purification and immobilisation ability of the silica extracts, explored in Section 2.3.2 and 2.3.3, then future work may need to consider the role of these trace elements and/or ways to remove them (e.g. pre-treatment of sand with HCl [76], increased time soaking the precipitate in acid [75] or additional wash steps [96]).

In general, the results discussed above indicate that the implementation of a local production process including silica extraction will require analysis of the available sand to determine if silica content is high enough to yield silica extract with the simple method explored here. Of those sands tested in this work, SC sand had the highest yield with 11.5 ± 1.4%. The presence of silica in the extracted products was confirmed by both FTIR and XRF. Although extracted silica was shown to have a different porosity and density to commercially available silica gel 60 particles and may have some traces of other elements, the utility of the extracted silica to a local manufacturing process for diagnostics will ultimately depend on its performance with respect to integrated purification and immobilisation of fusion proteins. This will be explored in the next section.

2.3.2 Proof-of-concept: Immobilisation of R5-tagged mCherry on silica particles

To test the feasibility of immobilisation onto particulate silica through the R5-tag, the fluorescent protein mCh was used as a first model in fusion constructs.

As discussed in Section 2.1.3, general protein adsorption on silica is a combination of both electrostatic interactions of the ionized silanol groups with positively charged residues on the surface of the protein and weaker interactions of H-bonding, van der Waals interactions and structural flexibility [89,100,102]. However, the R5 peptide in the fusion protein is expected to provide an affinity site for silica, thereby incorporating a more selective immobilisation capability for the protein without requiring additional chemical coupling reagents. R5 belongs to the proteins involved in silica precipitation in diatoms that are rich in arginine and lysine (silaffins [70,124,175,176]). These positively charged residues interact with the negative charge of silica surface that results from deprotonated hydroxyl groups on the surface (-$SiO^{-,}$ at $pK_a > 3$-4) [102,177]. By adding the 19-amino acid R5 sequence (SSKKSGSYSGSKGSKRRIL) to mCh the estimated pI for the protein shifts positive by ~1 unit for each R5 peptide unit added [140,178]. Table 2.6 shows the estimated pI for the fusion sequences used in this work. It should be noted that pI is only an average indication of charge on macromolecules and significantly positively charged regions might exist on proteins even when overall charge is negative, as is likely the case for R5-mCh-6H. These regions can still exhibit good binding to silica even with the overall charge of the fusion is negative, as previously shown for other SBPs [123,140]. Thus, the addition of the R5-tag should increase the affinity of the fusion protein for binding to silica.

Table 2.6 Theoretical pI for fusion sequences (calculated using ExPASy online tool [178]**).**

Sequence	pI
R5	11.22
mCh-6H	5.85
R5-mCh-6H	6.64
$R5_3$-mCh-6H	9.27

Although the intended process for use in local production is direct immobilisation of proteins from crude lysate onto silica, R5-mCh-6H and mCh-6H were purified via a conventional Ni-column for preliminary studies. Figure 2.16 shows the immobilisation efficiency on both commercial silica gel and extracted silica (SC) for R5-mCh-6H and mCh-6H. Greater than 90 % immobilisation, as measured by built-in fluorescence, was observed on either silica substrate for R5-mCh-6H. (Although silica is present in sand, the sand variants showed little to no immobilisation of R5-proteins (less than 1 %).) Good efficiency of adsorption at this low concentration (0.05 mg/mL) correlates with electrostatic interaction as the driving mechanism (as observed for the cationic peptide sequence investigated by Puddu *et al.* [102]). However, the improvement in immobilisation efficiency compared to the control without the R5 tag (mCh-6H) is small (~10 %). The interaction of mCh with silica without the R5-tag is unsurprising; fluorescent proteins, especially those in the red family, have been reported to have susceptibility to adsorption on silica [179]. Yang *et al.* observed some acceleration of the sol-gel gelation process with green-fluorescent protein (GFP) alone without the Car9 tag; however without the Car9 tag, GFP leaked out much faster at higher pH [135], indicating possibly more hydrophobic interactions involved in its binding [100,102]. This may also be the case for the interaction of mCh and particulate silica.

The small difference in immobilisation efficiency of mCh with and without the R5-tag is in line with previous *in situ* observations of binding behaviour for these constructs on silica surfaces using a quartz crystal microbalance with dissipation monitoring (QCM-D) [141]. Here the chip was functionalised by dipping it in the reaction mix for silica polymerisation following the Stöber method (a solvent mixture of 15 % aqueous 2-propanol solution containing 2 % NH_4OH, as a catalyst, with a mixture of organosilanes (octyltriethoxysilane and Bis[3-(trimethoxysilyl)-propyl]amine), followed by dipping in a mixture with tetraethylorthosilicate. Under these conditions the silanes are expected to undergo self-condensation and hydrolysis to form a silica layer on the chip. Only a slight difference in the change in frequency (ΔF) caused by the adsorption of the protein was observed between mCh-6H and R5-mCh-6H. However, increasing the number of R5 tags (to $R5_3$-mCh-6H) was observed to significantly increase ΔF. This indicates that the R5 peptide tag can increase affinity of a target protein for silica surfaces. Increasing the number of R5 tags has also be shown in increase the efficiency of immobilisation for larger target proteins (unpublished results from D. J. Seevaratnam, Dept. Chemical Engineering and Biotechnology, U. of Cambridge). Nevertheless, in the presence of the $R5_3$-tag, mCh fluorescence was reduced, possibly due to interactions of the longer tag inhibiting chromophore maturation. The solubility of mCh was also reduced, resulting in the formation of inclusion bodies (IBs) [141]. Together, this suggests that the increase in immobilisation efficiency must be balanced against other undesirable effects, and that appending more than three R5-tags is likely to be a disadvantage for protein production and retention of functionality.

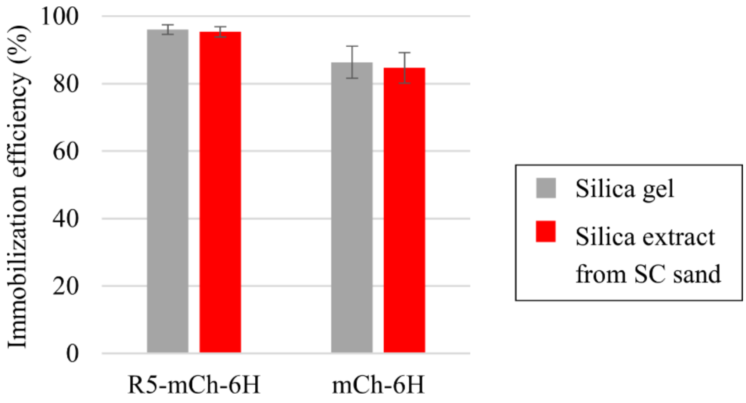

Figure 2.16 Immobilisation efficiency of R5-mCh-6H and mCh-6H (0.05 mg/mL) on silica gel 60 (<63 µm) powder (grey) and extracted silica (red) (5 mg), as measured by mCh fluorescence.

The effect of the addition of the R5-tag was also observed when comparing the interaction of the proteins with a silane-modified gold surface using a QCM (example curve shown in Figure 2.17). While there may be some unreacted alkoxygroups present, the silanol and siloxane groups formed through hydrolysis and self-condensation of the organosilane used to functionalise the gold chip provide a silica-like surface [163,164]. This functionalised surface is likely similar to the modified chip used in the previously described QCM experiments, although the thickness of the layer and the surface density of silanol groups may be different. Interaction of the R5-tagged proteins with these surfaces can provide an estimate of their binding affinities with silica particle surfaces.

Without the R5-tag, the quantity of the mCh-6H immobilised at saturation on the silane-modified chip was four times less than that of R5-mCh-6H (100 ng for R5-mCh-6H compared with 24 ng for mCh-6H calculated by the Sauerbrey equation, Eq. (2.4)(2.4)(2.4)(2.4) [167,168]). This fits with reported observations that, when added at the same concentration, a higher percentage of peptide is adsorbed for those peptide-silica interactions dominated by electrostatic interactions than for those of hydrophobic interactions [102], again indicating the electrostatic nature of the interaction of R5 with the silica surface compared to more hydrophobic interactions in the case of the fluorescent protein alone. Equilibrium dissociation constants (K_D) previously obtained for mCh-6H and R5-mCh-6H using QCM-D also show an increase in binding affinity with the addition of the R5-tag (1.34×10^{-6} M and 0.427×10^{-6} M, respectively) [141]. A similar K_D was obtained for R5-mCh-6H by fitting to the frequency plots obtained in this work ($0.34 \pm 0.03 \times 10^{-6}$ M). This K_D is similar to those reported for other silica binding tags in the literature (e.g. 1×10^{-6} M for Car9 with silica particles [71]) and for the interaction of His-targeted proteins and Ni-NTA-coated surfaces [180], which suggests the R5-peptide may be able to function as an affinity tag for purification where silica is the stationary phase.

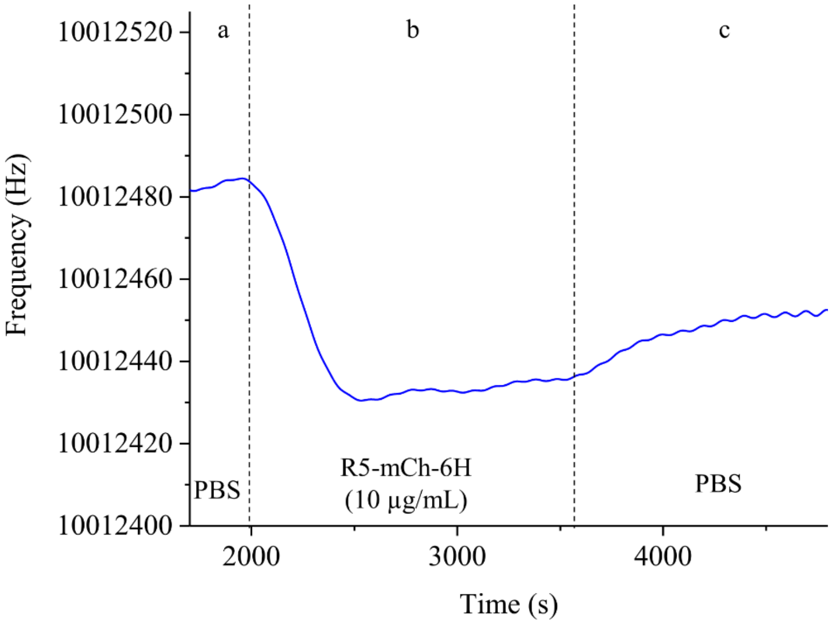

Figure 2.17 QCM frequency over time, showing (a) stabilisation in buffer, (b) introduction of R5-mCh-6H at 10 mg/mL, and (c) return to buffer.

Although the increase in binding affinity was small with the addition of a single R5-tag, the results of R5-mCh-6H and mCh-6H adsorbed on to silica thin layer chromatography plate clearly demonstrate the benefit of oriented attachment over general adsorption. R5-mCh-6H maintained > 60 % of its fluorescence over one month at room temperature while mCh-6H lost the majority of its fluorescence within a day [181]. This stability will be important given the intention to use the fusion constructs in their immobilised state, rather than elute them from the stationary phase (as is classically done in protein purification).

For the R5-peptide to function as a combined purification and immobilisation tag for silica, the fusion construct should remain bound during wash steps. No significant leaching (< 5 %) was observed over several washes of the silica nor after a one-hour incubation as shown in Figure 2.18 for of R5-mCh-6H (as measured by fluorescence). For analysis of the bound fraction, R5-mCh-6H was eluted off the silica by incubation in concentrated lysine solution (1 M), as demonstrated previously for the Car9 tag [71,129] and for R5 tag [140]. Arginine has also been shown to be effective as an eluting agent for proteins bound to silica, as demonstrated for the release Car9-fused cargo proteins in silica sol-gels [135] and for the purification process using silica with un-tagged proteins [89]. The R5-tagged protein can also be eluted by using a buffer with acidic pH, as shown previously for R5-mCh constructs [181]. This protein release behaviour adheres to the current understanding that the molecular interaction between the R5 tag and silica is dominated by electrostatic interactions. At acidic pH, the hydroxyl groups are protonated or partially protonated (-SiOH, pKa ~3-4) and the negative charge on the silica surface decreases; hence, the R5-tagged protein is partially released from the silica under such conditions. In the case of lysine or arginine, at neutral or basic pH the protonated amines ($-NH_3^+$) interact with the negative charge on silica surface ($-SiO^-$). This competition between the positively charged R5 peptide and free amino acid for the ionized silanol groups, or binding sites, on the silica surface produces the release of the R5-tagged protein.

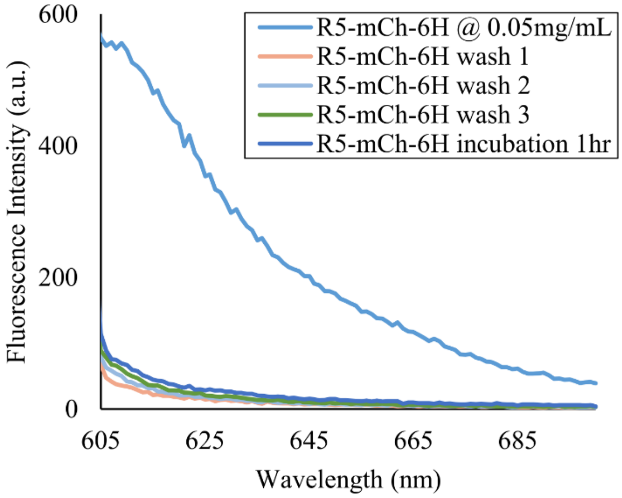

Figure 2.18 Release of proteins after incubation in H_2O, as measured by fluorescence intensity of the supernatant.

Despite encouraging immobilisation results, correlation with protein activity needs to be established. In this proof-of-concept, the mCh fluorescence serves as an initial marker of immobilised protein activity. Fluorescent lifetimes of mCh-6H and R5-mCh-6H are similar and are comparable with the reported lifetime for mCh (1.46 ns) [182] (Table 2.7), and therefore suggest that the secondary structure (and the chromophore) is retained. Olmez *et al.* observed retention of fluorescence characteristics of a C-terminal R5-tagged mCh, but the N-terminal variant was untested given an observed shift in the excitation-emission maxima of N-terminal tagged GFP [140]. No shift with R5 as an N-terminal tag was observed here. Figure 2.19A and Table 2.8 show that the soluble and immobilised R5-mCh-6H protein exhibited nearly identical red fluorescence to mCh-6H with excitation/emission peaks at 587/608 nm. Spectral analysis of individual silica particles with confocal microscopy confirmed an emission peak around 608 nm (Figure 2.19B). For all of the above, no significant difference was observed when extracted silica was used as the stationary phase in place of commercial silica gel.

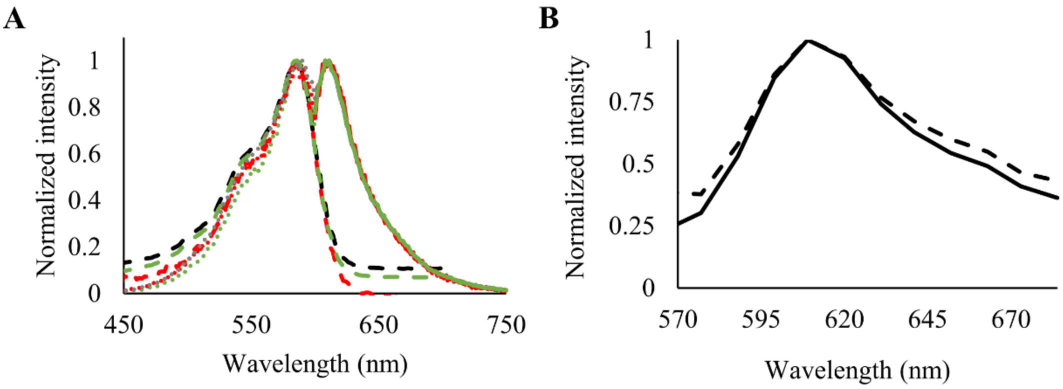

Figure 2.19 (A) Emission (solid), excitation (dots) and adsorption (dash) spectra comparing mCh-6H in solution (green) to R5-mCh-6H in solution (black) to R5-mCh-6H immobilised on silica extracted from sand (red). (B) Confocal spectral analysis for immobilised R5-mCh-6H (n=10) showing retention of mCherry emission peak around 608 nm on either commercial silica gel 60 <63 µm (solid) or extracted silica (SC, dash). Resolution is limited by the discrete emission bands of the confocal microscope.

Table 2.7 Fluorescence lifetime values (ns) for constructs. Measured in solution and immobilised on silica (commercial or extracted from sand).

Constructs	Free in solution	Immobilised on silica	Immobilised on sand extract
mCh-6H	1.61	1.58	1.60
R5-mCh-6H	1.68	1.55	1.55

Table 2.8 Peak fluorescence (max. λem) values for mCh constructs. Measured in solution and immobilised on silica (commercial Si60 <63 µm or extracted from sand), excitation 587 nm.

Construct	Condition	Max. λ_{em} (nm)
mCh-6H	Ni purified	608
	immobilised – Si60	608
	immobilised - SC	608
R5-mCh-6H	Ni purified	608
	immobilised – Si60	608
	immobilised - SC	608

These results with R5-mCh-6H demonstrate successful immobilisation and retention of fluorescence with this approach and prompted the progression towards the inclusion of functional enzymes in the fusion construct. Moreover, it was decided to retain mCh in subsequent fusion constructs, as mCh expression in *E.coli* produces a pink culture that allows for simple visual monitoring of the successful production of the protein. For example, Figure 2.20 demonstrates the increase in the inbuilt fusion protein fluorescence, as a function of protein expression after induction for $R5_3$-mCh-6H. It can be followed semi-quantitatively (visual colour matching – Figure 2.20B) or checked against a colour card (Figure 2.20C), depending on available resources. The inclusion of mCh also allows for visual tracking of the success of the subsequent purification and immobilisation process as the functionalised silica becomes pink in colour as the R5-mCh-6H becomes adsorbed and the supernatant becomes colourless. Together this could enable in-country production and purification of the fusion proteins by making the process suitable for use in a laboratory with minimal infrastructure.

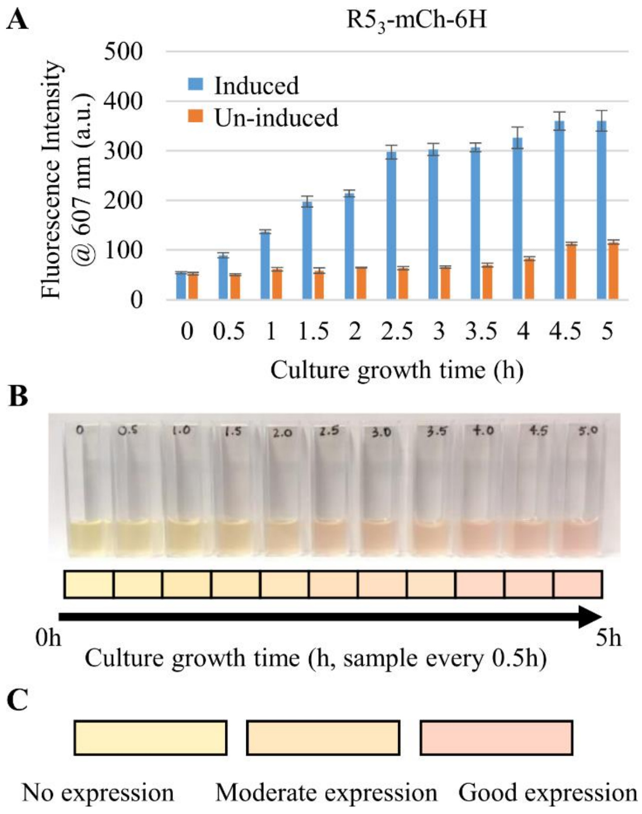

Figure 2.20 (A) Fluorescence intensity at ex. 587 nm / em. 607 nm for the (blue) induced and (orange) un-induced culture over growth period for 5 h at 37 ^{0}C for $R5_3$-mCh-6H and (B) corresponding cuvette samples to show visual change in colour. Expression levels can be checked semi-quantitatively against a colour card (C).

2.3.3 Silica immobilisation with functional R5-mCh-Enzyme proteins

As discussed in Section 2.1.5, mSOX and HRP were used as first models of functional enzyme units in R5-mCh-Enz fusions. These enzymes can be used in conjunction for the detection of sarcosine (Figure 2.3), a potential biomarker for prostate cancer [183], as a first example of a gene-to-diagnostic production process potentially amenable to resource-limited settings.

The increase in the inbuilt fusion protein fluorescence, as a function of protein expression after induction, was also observed for R5-mCh-Enz fusions, as demonstrated for the fusion containing mSOx (R5$_2$-mCh-mSOx-R5-6H) in Figure 2.21. A slight delay in the growth curve was observed as compared to R5$_3$-mCh-6H (Figure 2.20), which could be due to the increased size of the SOx construct, as an increase in peptide length is associated with more metabolic energy requirements during expression [123,142]. Tracking these expression patterns visually for each construct could be used to help identify the correct expression time for each construct under the conditions of each local production facility.

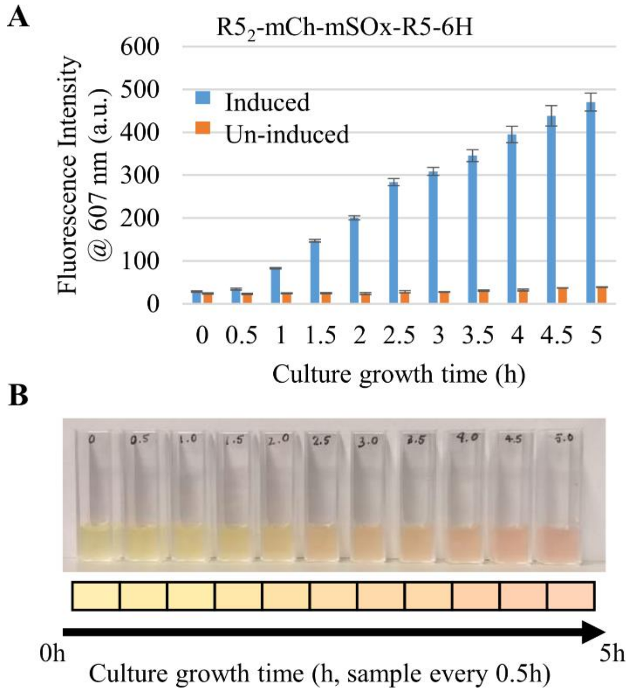

Figure 2.21 (A) Fluorescence intensity at ex. 587 nm / em. 607 nm for the (blue) induced and (orange) un-induced culture over growth period at 37 ^{0}C for R5$_2$-mCh-mSOx-R5-6H and (B) corresponding cuvette samples to show visual change in colour.

R5-mCh constructs with HRP were also expressed under similar conditions. Despite being widely used in bioassays, either as a label or to detect peroxide as co-product, recombinant HRP is a difficult protein to express [160,184–186]. (Many commercially available peroxidases remain largely an isoenzyme mixture from plant extracts, requiring normal downstream processing purification and isolation steps.) Recombinant HRP has a tendency to form IBs with low yield of active protein [186]. However, both HRP-mCh-R5-6H and 6H-R5-mCh-HRP (type C HRP) were transformed and expressed in *E. coli* without IB formation. This is possibly the result of the R5 sequence and the change in pI of the protein improving its solubility (Table 2.9). The protein could therefore be isolated from the soluble cell fraction.

Table 2.9 Theoretical pI for fusion sequences with functional proteins (calculated using ExPASy online tool).

Sequence	**pI**
mSOx	5.34
R5$_2$-mCh-mSOx-6H	6.55
HRP	6.30
6H-R5-mCh-HRP	6.58
HRP-mCh-R5-6H	6.58

Again, fusion proteins were purified via a conventional Ni-column for preliminary studies of binding affinity for silica. Good immobilisation efficiency (> 85 %) was observed for the R5-mCh-Enz constructs on both extracted silica and commercial silica gel (Figure 2.22A). It was previously shown that mSOx-R5-6H also exhibited > 90 % immobilisation efficiency on silica gel but SOx-6H showed only 32.3 ± 2.6 % (as measured by Bradford assay) [37,181]. Thus, it is expected that the R5 sequence is primarily responsible for the affinity for silica in these fusion proteins rather than mCh.

As expected, when immobilisation was done with proteins pre-purified on Ni-resin, total (measured by the Bradford total protein assay) and selective (measured via the built-in mCh fluorescence) protein immobilisation were similar (Figure 2.22B). However, immobilisation of the R5-tagged proteins onto the silica from crude cell lysate results in 30-50 % uptake of total protein, but this corresponds to 85-95 % selective uptake of the R5-mCh-Enz fusion proteins (as shown for R5$_2$-mCh-mSOx-R5-6H on SC extract) (Figure 2.22B). This is consistent with selective immobilisation via the R5 tag and demonstrates the potential for a reliable immobilisation process directly from lysate. R5-tagged HRP constructs could be also be isolated directly from the cell lysate with silica.

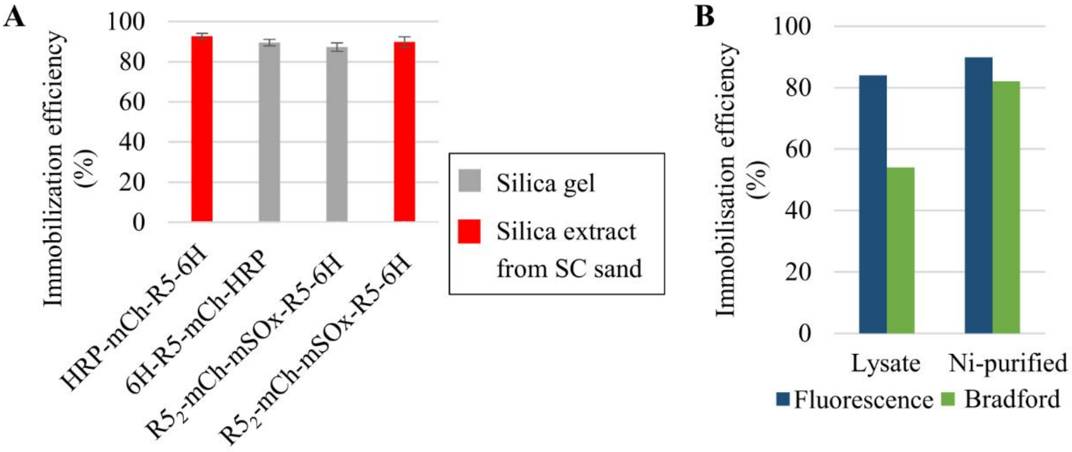

Figure 2.22 Immobilisation efficiency of the (A) Ni-purified R5-mCh-Enz proteins on silica gel 60 <63 µm (grey) and extracted silica (red) (5 mg), as measured by mCh fluorescence. (R5$_2$-mCh-mSOx-R5-6H 0.4 mg/mL, HRP-mCh-R5-6H 0.12 mg/mL, 6H-R5-mCh-HRP 0.06 mg/mL). (B) Immobilisation efficiency of R5$_2$-mCh-mSOx-R5-6H on silica extracted from SC sand when added as Ni-pure or from lysate (30 µL lysate/mg silica, ~5 mg/mL protein), assessed by (dark blue) fluorescence for target protein amount or by (green) Bradford assay for total protein.

The immobilisation process from lysate to R5-mCh-Enz on silica can be followed step by step in the SDS-PAGE gel shown in Figure 2.23. The R5 protein band (R5$_2$-mCh-mSOx-R5-6H at 73 kDa), visible in the crude lysate (Lane 1), almost completely disappears from the supernatant (Lane 2) in contact with the silica, as the silica turns pink. The identity of the protein on the silica was confirmed in the eluent after elution in non-physiological conditions from the silica (Lane 3). While there is some decrease in purity compared to the His-tag approach (Lane 4), no wash steps were conducted on the silica prior to elution. Other purification approaches on silica matrices with SBPs observed similar purity to His-tag approaches after washing in buffers containing NaCl (0.5-2 M) and detergents such as Tween-20 or Triton X-100 (0.5 %) to reduce non-specific interactions [122,129,132], showing that higher purity could be achieved if deemed necessary. However, the addition of the detergents can also reduce the target protein loading [123] and add cost and complexity to the process. In addition, in many cases diagnostic products can function without high levels of purity [40]. Thus, the utility of the end product with minimal wash steps was explored throughout this work.

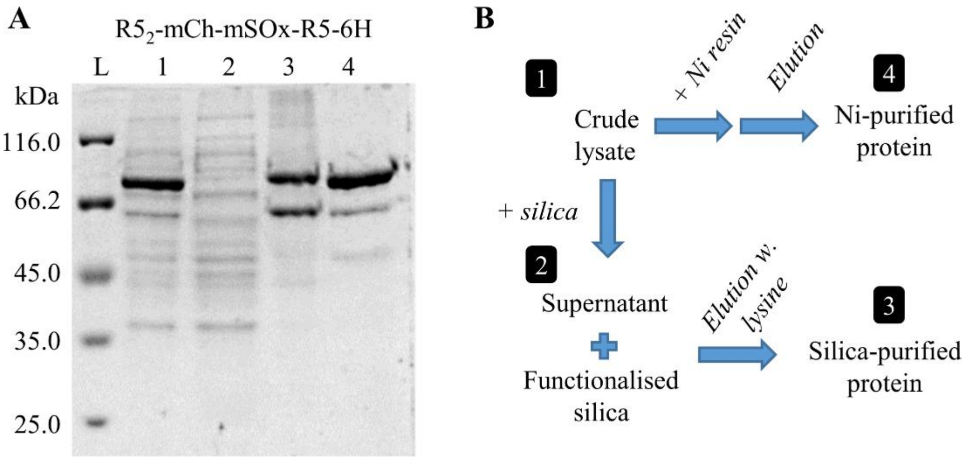

Figure 2.23 Immobilisation process from crude lysate as shown by (A) SDS page gel for R5$_2$-mCh-mSOx-R5-6H, showing in lane (1) crude lysate, (2) supernatant after immobilisation of silica, (3) eluent off silica and (4) eluent from Ni-resin. Purification pathway shown in (B). The band corresponding with the R5$_2$-mCh-mSOx-R5-6H (73 kDa) is significantly diminished in the supernatant after immobilisation on silica and reappears in the eluate from the silica, along with a small amount of other proteins. L indicates molecular weight 'Ladder'. The lower molecular weight band seen in the purified proteins indicates that the mCherry has undergone a partial hydrolysis of its chromophore acylimine bond [141] **during SDS-PAGE analysis.**

Even from lysate, the immobilisation process is quick; Most of the immobilisation happens within five minutes, as shown for R5$_2$-mCh-mSOx-R5-6H immobilised from lysate at concentration of 45 µg of total protein per mg of silica (Figure 2.24). This is similar to rates observed in the literature for other SBPs; for instance, 85 % of both CotB1 and CotB1p-tagged constructs were immobilised within the first minute of incubation, reaching a plateau at ~95 % at 15 min [123]. These rates support the strong affinity of the R5-tag for silica.

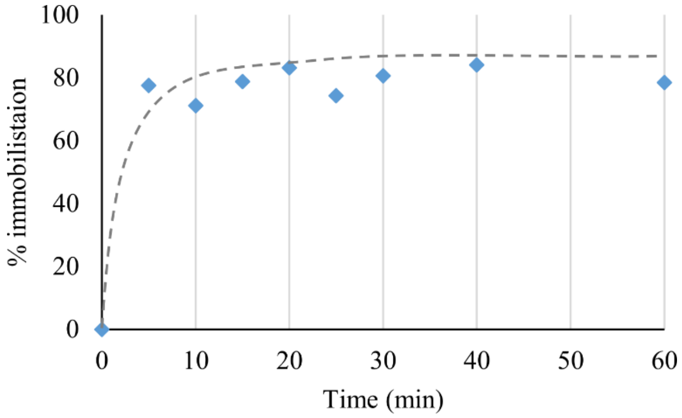

Figure 2.24 Immobilisation over time of R5$_2$-mCh-mSOx-R5-6H from crude lysate on silica extracted from sand (SC).

Specific immobilisation (as measured by mCh fluorescence) of R5-tagged proteins from lysate on silica was twice that of other substrates tested (alumina, calcium carbonate, and cellulose, Figure 2.25), demonstrating the selective affinity of the R5 sequence for silica. As discussed, the silica-protein interaction is expected to be primarily driven by electrostatic forces at physiological pH [102], where the positively charged residues (K and R) interact with negative surface of the silica. Zeta-potential is a relative indicator for the surface potential of the particle (one of the major forces mediating particle-protein interactions [86,187]) and can be used to compare the materials investigated here.

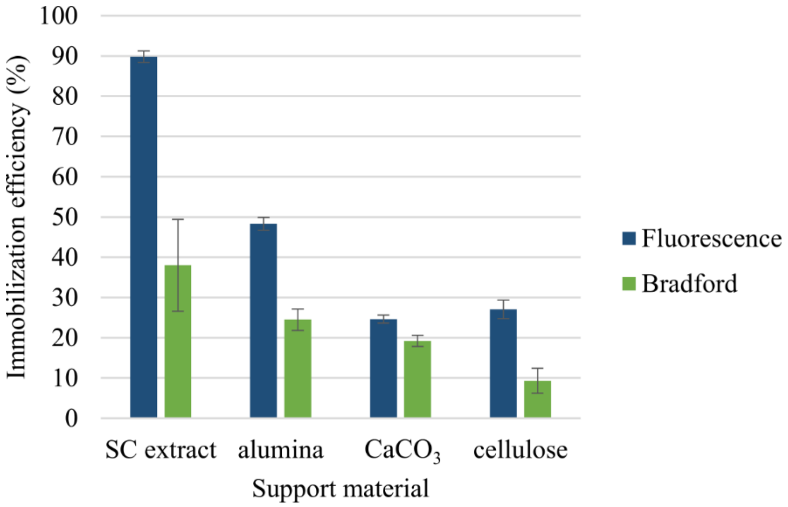

Figure 2.25 Immobilisation efficiency of R5$_2$-mCh-mSOx-R5-6H from crude lysate on various support materials, assessed by (dark blue) fluorescence for target protein amount or (green) by Bradford assay for total protein.

Like silica, alumina has hydroxyl groups on its surface, whose protonation and deprotonation is dependent on the environment [188]. However, at pH 7.5, silica has been shown to have a zeta-potential of approximately -30 mV, while alumina's is +30 mV [189]. This makes alumina positively charged at pH 7 [190], so the specific immobilisation of the fusion construct observed (as indicated by fluorescence) could be due to surface accessible negative amino acid residues in other parts of the fusion construct rather than through the R5 tag. In contrast, at pH 7.5 cellulose has been shown to have a slight negative surface charge, approximately -12 mV [191]. Unmodified cellulose is known for its low unspecific protein absorption [192], which is also observed in Figure 2.25, however, the increased specific adsorption of the R5$_2$-mCh-mSOx-R5-6H observed here may be a result of this slight negative charge electrostatically interacting with the positive amino acid residues of the R5 sequence. Finally, calcium carbonate particles have been shown to be close to neutral at pH 7.5 [193], indicating hydrophobic interactions may be the driving force for protein binding to this material. Minimal difference is observed between the specific and non-specific protein adsorption for this substrate material.

With the differences in surface charge across these materials, it is likely that there is some variance in which proteins adsorb generally from the lysate, as shown by the range of total protein adsorption results (measured by Bradford assay). The lysate contains many other proteins from the expression cell line, which are expected to be largely negatively charged [128], as well as the lysozyme from the lysis technique. These proteins will vary in their spatial surface potential distribution and total charge at a given pH [194], and this will affect their interaction with the substrate surface. For example, lysozyme is positively charged while bovine serum albumin (BSA) is negatively charged at pH 7, resulting in more lysozyme immobilised on negative surfaces and vice versa for BSA [190]. Nevertheless, the target protein is the dominant protein binding to the surface of the silica, as shown by the SDS-PAGE results above (Figure 2.23). Having demonstrated that the R5-tag can function as a tag for affinity purification of the R5-mCh-Enz fusions on silica, the next step is to ensure the retention of functionality in the fusion constructs.

2.3.4 Functionality of R5-mCh-Enzyme proteins

The retention of enzymatic activity in the fusion constructs is essential for their utility as diagnostic reagents. However, both fusion of additional peptide sequences and immobilisation on silica have the potential to disturb native protein folding and correspondingly the characteristics of fluorescence and enzyme subunits. Fusion proteins were first evaluated for fluorescence, as an initial marker of correct protein folding, and subsequently for enzymatic activity, selectivity, performance in a range of pH environments and stability.

2.3.4.1 Fluorescence

The inbuilt fluorescence of mCh was checked against the reference standard (mCh-6H) to provide an indication of any changes in protein folding as a result of the incorporation of enzyme units into the fusion. Fluorescent lifetimes between 1.45-1.68 ns were measured in all the cases (Table 2.10), again comparable with the reported lifetime for mCherry (1.46 ns) [182]. The fluorescence spectra for each of the R5-mCh fusions also exhibited nearly identical red fluorescence with the mCh-6H standard (Figure 2.19), as shown for HRP-mCh-R5-6H and R5$_2$-mCh-mSOx-R5-6H in Figure 2.26. Silica-immobilised versions of these constructs exhibited identical fluorescence spectra to their solution counterparts, including the small shift observed for R5$_2$-mCh-mSOx-R5-6H in lysate. These results provide an indication that the protein is folded properly both after the fusion and after immobilisation on silica.

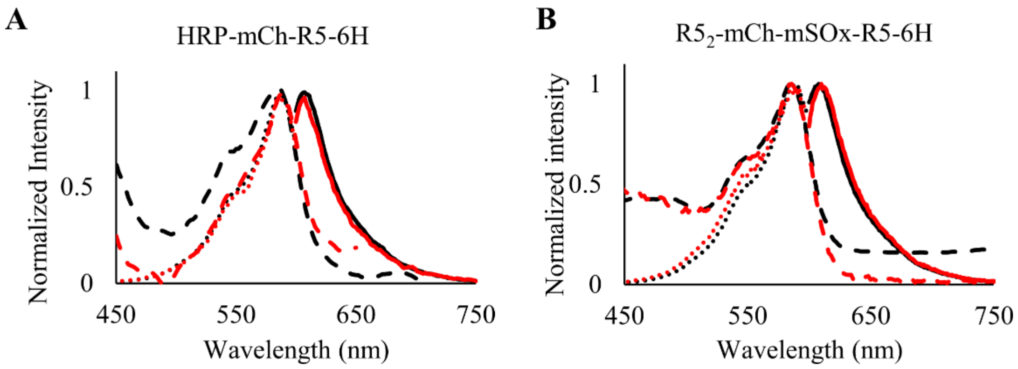

Figure 2.26 Characterization of the free (black) and immobilised (red) R5-mCh proteins. Emission (solid), excitation (dots) and adsorption (dash) spectra for (A) HRP-mCh-R5-6H and (B) R5$_2$-mCh-mSOx-R5-6H immobilised on extracted silica.

Table 2.10 Fluorescence lifetime values (ns) for R5-mCh-Enz constructs. Measured in solution and immobilised on silica (commercial silica gel 60 <63 µm or extracted from sand).

Constructs	Free in solution	Immobilised on silica	Immobilised on sand extract
R5$_2$-mCh-mSOx-R5-6H	1.60	1.59	1.55
HRP-mCh-R5-6H	1.42	1.52	1.45
6H-R5-mCh-HRP	1.65	1.53	1.51

Table 2.11 Peak fluorescence (max. λ_{em}) values for R5-mCh-Enz constructs. Measured in solution and immobilised on silica (commercial Si60 <63 µm or extracted from sand (SC)), excitation 587 nm. Reference max. λ_{em} for mCh-6H = 608 nm.

Construct	Condition	Max. λ_{em} (nm)
$R5_2$-mCh-mSOx-R5-6H	Ni purified	608
	lysate	605
	immobilised – Si60	605
	immobilised - SC	605
HRP-mCh-R5-6H	Ni purified	608
	immobilised – Si60	608
	immobilised - SC	608
6H-R5-mCh-HRP	Ni purified	607
	immobilised – Si60	607
	immobilised - SC	607

2.3.4.2 Enzyme activity

Given fluorescence measurements showed no change after fusion or immobilisation, the next step was to evaluate the effect of these on enzyme activity. Specific activity of an enzyme is defined as the amount of substrate the enzyme converts (reactions catalysed), per mg protein in the enzyme preparation, per unit of time. Table 2.12 shows the specific activity for sarcosine and H_2O_2 for WT and R5-mCh-Enz fusion constructs of SOx and HRP, respectively.

A similar order of magnitude of specific activity was observed for Ni-purified $R5_2$-mCh-mSOx-R5-6H as compared to the WT SOx. Although, the apparent activity of the immobilised $R5_2$-mCh-mSOx-R5-6H is lower than that of the Ni-purified, the total protein here also includes some non-specific adsorption (See Lane 3 of the SDS-PAGE gel in Figure 2.23A). Notably, more specific activity is retained by this R5-immobilised SOx than by SOx immobilised on silica particles via chemical coupling with an NH_2 activated surface (~0.4 U/mg) or via the classical glutaraldehyde coupling method for protein crosslinking (~0.09 U/mg) [181]. Despite some reduction in activity, previous work in the Cambridge Analytical Biotechnology group has shown that K_m for the silica-$R5_2$-mCh-mSOx-R5-6H was 16.5 ± 0.9 mM (compared with 16.5 ± 0.4 mM, 16.3 ± 0.3 mM, and 16.1 ± 0.4 mM for $R5_2$-mCh-mSOx-R5-6H, R5-mSOx-6H and mSOx-6H, respectively, in solution) [37,159], which suggests that there has been minimal conformational impact on the sarcosine binding site due to the protein fusion or immobilisation.

Table 2.12 Specific activity for R5-mCh-Enz constructs and WT variants. Measured in solution and immobilised on silica (commercial or extracted from sand). SOx was measured for sarcosine and HRP for hydrogen peroxide.

Construct	Condition	U/mg protein
WT SOx	in solution	4.75 ± 0.30
$R5_2$-mCh-mSOx-R5-6H	Ni purified	7.06 ± 1.54
	crude lysate	0.50 ± 0.01
	immobilised – Si60	3.80 ± 0.22
	immobilised - SC	3.07 ± 0.20
HRP-mCh-R5-6H	Ni purified	0.142 ± 0.008
	immobilised – Si60	0.029 ± 0.010
	immobilised - SC	0.033 ± 0.0088
	immobilised pre-activation	0.037 ± 0.0061
6H-R5-mCh-HRP	Ni purified	0.229 ± 0.012
	immobilised – Si60	0.097 ± 0.028
	immobilised – SC	0.053 ± 0.0088
	immobilised pre-activation	0.020 ± 0.0023
WT HRP	in solution	386.0 ± 4.0

The HRP constructs required re-folding with heme to activate the enzyme. After incubation with heme, a K_m of 3.8 mM and 1.6 mM was measured for soluble 6H-R5-mCh-HRP and HRP-mCh-R5-6H, respectively. These are consistent with the range of values reported in the literature for different HRP isoenzyme preparations [195], compared with a K_m of 8 µM for the commercially available mixture of acidic and basic isoenzymes.

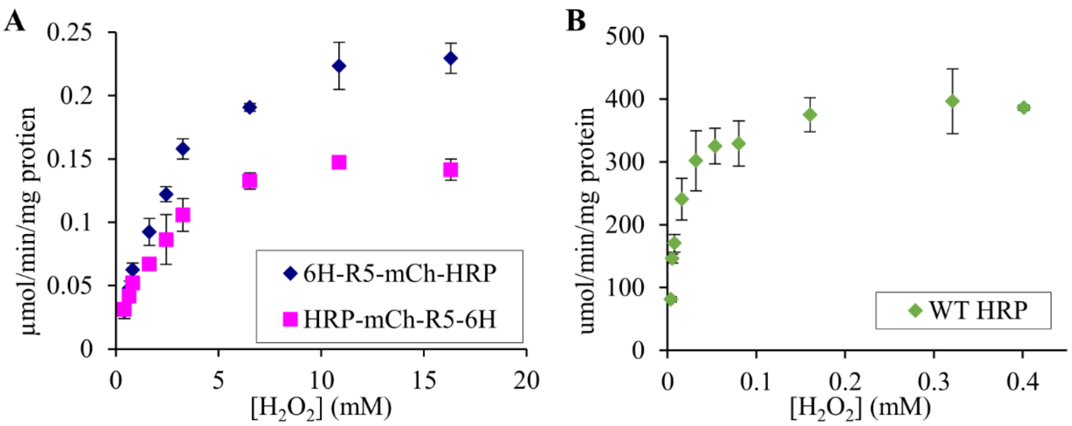

Figure 2.27 Reaction rate versus substrate concentration for (A) HRP-mCh-R5-6H and 6H-R5-mCh-HRP constructs (Type C) and (B) WT HRP (mix of isomerases), showing K_m of 1.62 mM, 3.8 mM and 8 µM, respectively.

Figure 2.28B shows that the response curve for both the N- and C-terminal recombinant HRP are similar, as are their specific activities (Table 2.12), with the C-terminal variant only showing a slight increase in activity of the Ni-purified protein. No significant difference was observed in the specific activity of HRP-mCh-R5-6H if activation with heme occurred before or after the protein was immobilised on silica, however, a decrease was observed in the specific activity of 6H-R5-mCh-HRP if activation was done after immobilisation (Table 2.12). In addition, the immobilisation of the Ni-purified protein was less efficient when it occurred prior to reactivation; only 60 % of total protein was immobilised as compared to > 75 % total protein when it followed activation. Although the constructs retained some activity, both the soluble and immobilised versions only showed minimal activity when compared to the commercially available WT HRP. Nevertheless, silica-immobilised HRP was shown to work in tandem with R5$_2$-mCh-mSOx-R5-6H (see Chapter 4). However, their low activity may ultimately limit their use in a diagnostic platform.

To have potential as a quantitative diagnostic, the fusion constructs must demonstrate a response correlated with substrate concentration; Figure 2.28 shows the calibration curves for the fusion constructs in solution. R5$_2$-mCh-mSOx-R5-6H was used in conjunction with WT HRP to test its performance independently of the low activity of the HRP fusion proteins. While it is possible to elute the R5-mCh-Enz proteins off the silica, as would be done in a classical protein purification with Ni-resin and has been done with various silica-affinity tags, the functionalised silica can also be used directly in bioassays without any further processing. This eliminates the need for the elution step using costly L-lysine or other eluting agents as well as reducing post-purification cleaning and concentrating steps that are often necessary.

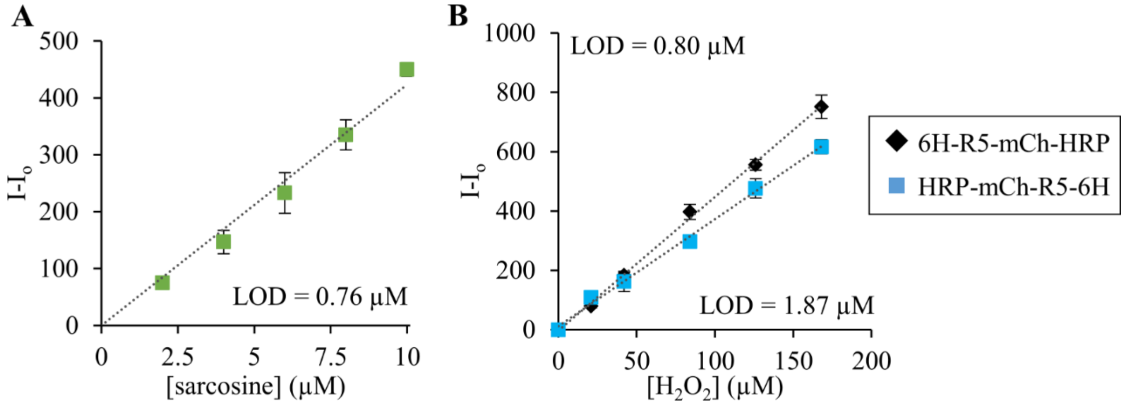

Figure 2.28 Calibration curves for free proteins in solution for (A) R5$_2$-mCh-mSOx-R5-6H and (B) HRP constructs, fluorescence intensity (ex. 530 nm / em. 582 nm) plotted against concentration. The isolated HRP showed a linear response to H_2O_2 in the range 0-200 µM, while mSOx is linear in the range of 0-10 µM when used with WT HRP.

Direct use is shown for R5$_2$-mCh-mSOx-R5-6H, collected on silica from the lysate (Figure 2.29). Here a linear relationship is observed between sarcosine and the fluorescence intensity of the reporter dye AR at 20 min over a range relevant to the detection of prostate cancer (0-10 µM) [157,158] with a limit of detection (LOD) similar to the soluble protein. In this example, R5$_2$-mCh-mSOx-R5-6H on silica extracted from sand had been stored dry for three months at 4 °C, suggesting the potential long-term stability of the reagent. This will be explored further in Section 2.3.4.5.

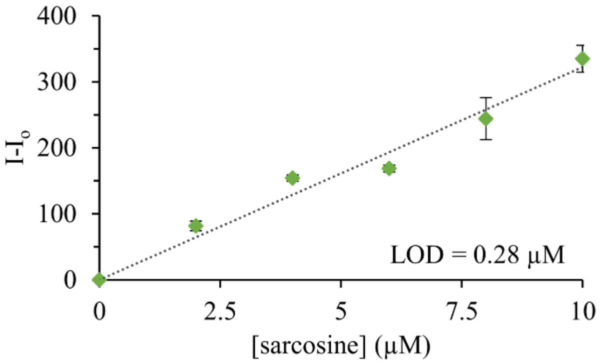

Figure 2.29 AR fluorescence (ex. 530 nm /em. 580 nm) with respect to final concentration of sarcosine in an assay using R5$_2$-mCh-mSOx-R5-6H on silica extracted from sand after 3 months of dry storage at 4 °C.

While these results showcase intensity of signal after 20 min which is still within the linear region of signal development, an end-point assay can also be designed that uses a smaller sample. For example, with 50 µL total sample and increased amount of silica-enzyme, consumption is achieved within circa 40 mins, again producing a linear relationship with sarcosine concentration (Figure 2.30). This assay can be extremely sensitive and valuable where only very small samples are available. While these results are promising, more characterisation of these fusion reagents, including selectivity, optimum pH and stability, is necessary to determine if they are fit for purpose and how such assays might be optimised.

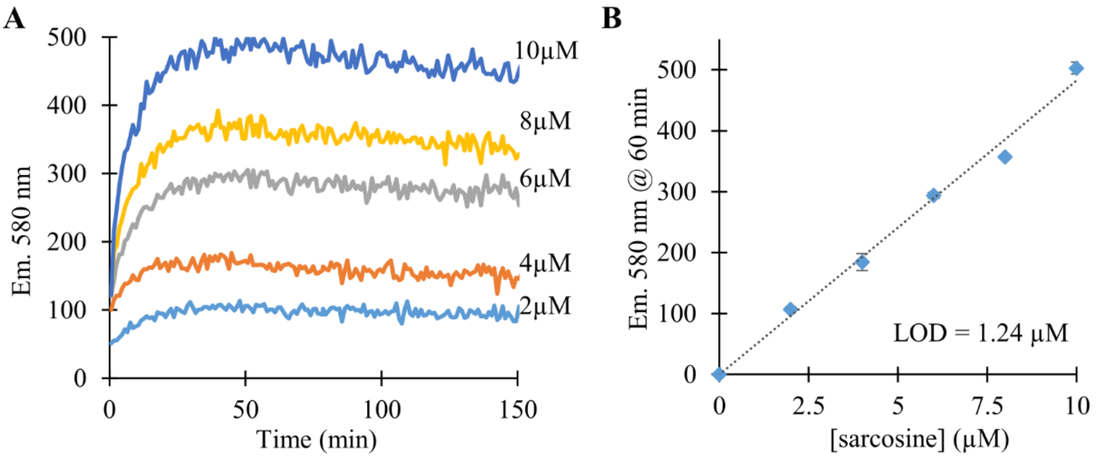

Figure 2.30 Endpoint assay for 50 µL sample showing (A) consumption of sarcosine with time, with completion by ~40 min. (ex. 530 nm / em. 580 nm) and (B) fluorescence intensity at 60 min showing a linear relationship of intensity with sarcosine concentration.

2.3.4.3 Selectivity

To function as a biosensor, the fusion proteins must not only have activity but also selectivity for their substrate to avoid false positive signals from other substances. Recombinant variants were compared against the commercially available reagent for their selectivity against known cross-reactants and potential interferents that may be present in a urine sample, given the potential application of the sarcosine assay (Figure 2.31).

Substrates known to show reactivity with SOx include other secondary amine substrates (N-methyl-L- or D-alanine and L- or D-proline [196,197]). Glycine, which is the downstream product of the oxidative demethylation of sarcosine catalysed by SOx, has also been shown to be a substrate for SOx with low activity. Both glycine and proline show little reactivity with either recombinant or WT SOx at 10 µM (Figure 2.31). In contrast, N-methyl-L-alanine results in 50-60 % relative fluorescence for R5$_2$-mCh-mSOx-R5-6H compared with 10 % cross reactivity with the WT SOx. Similar turnover rates for N-methyl-L-alanine compared to sarcosine have previously been reported for mSOx [197]. However, the concentration of N-methyl-L-alanine in urine samples is not well characterised in the literature, so it is difficult to determine the effect this change would have on sarcosine detection in urine (the target sample matrix).

Alanine, on the other hand, is present in urine. The concentration of alanine in urine is approximately 1000 fold higher than sarcosine [170,198], so 10 mM final concentration of L-alanine was also tested, but minimal cross-reactivity was observed. This suggests that an enzymatic approach could be a good alternative for selective measurements of sarcosine in urine. Creatinine is another potential interferent also present in urine. Males 40+ years of age (the group most likely to be tested for prostate cancer) have a mean urinary creatinine concentration of 150 mg/mL or 13.2 mM [169]. Hence, creatinine was tested at a final concentration of 20 mM (2000X [sarcosine]), but minimal cross-reactivity was observed.

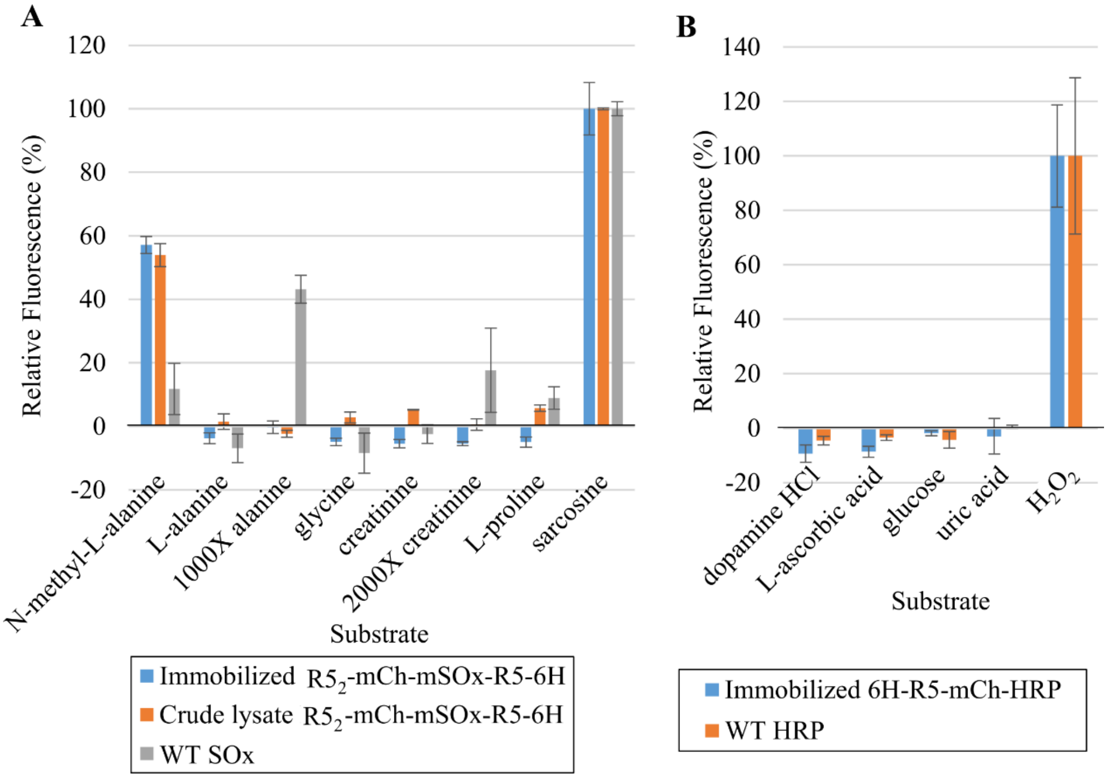

Figure 2.31 Selectivity of (A) $R5_2$-mCh-mSOx-R5-6H and WT SOx and (B) 6H-R5-mCh-HRP and WT HRP. Fluorescence intensity (ex. 530 nm/ em. 580 nm) recorded at 20 min after addition of the substrate. In the case of sarcosine oxidase, substrate final concentrations were 10 µM unless otherwise noted. For HRP, substrate concentrations were 50 µM.

The selectivity of one of the recombinant HRP (6H-R5-mCh-HRP) and WT HRP was evaluated against dopamine, L-ascorbic acid, glucose and uric acid [199], with minimal cross reactivity observed for either variant (Figure 2.31B). For both, HRP and SOx, those substrates that appear to give negative signals are likely to have some direct interaction with the AR dye that is reducing the background fluorescence [200].

2.3.4.4 Effect of pH on activity

Enzymes are known to be affected by pH so this effect was evaluated for recombinant and WT variants of SOx and HRP to determine their optimum pH for the detection of sarcosine and hydrogen peroxide, respectively. The reported optimal pH is 8.0-9.0 for WT SOx of *Bacillus sp.* origin [201,202] (the mSOx sequence used here is of *Bacillus sp.* origin). Both immobilised and crude lysate R5$_2$-mCh-mSOx-R5-6H show greater retention of activity in the lower pH range than WT SOx (obtained commercially). In contrast, the reported optimal pH by the supplier is 6.0-6.5 for WT HRP. Experimentally, WT HRP showed similar activity across the range of 5.0-7.5, consistent with its composition of a mixture of basic and acidic isoenzymes. In comparison, the optimal pH of immobilised 6H-R5-mCh-HRP (type C HRP) is shifted to higher pH range, 7.0-8.0, which matches better with the optimal pH of R5$_2$-mCh-mSOx-R5-6H.

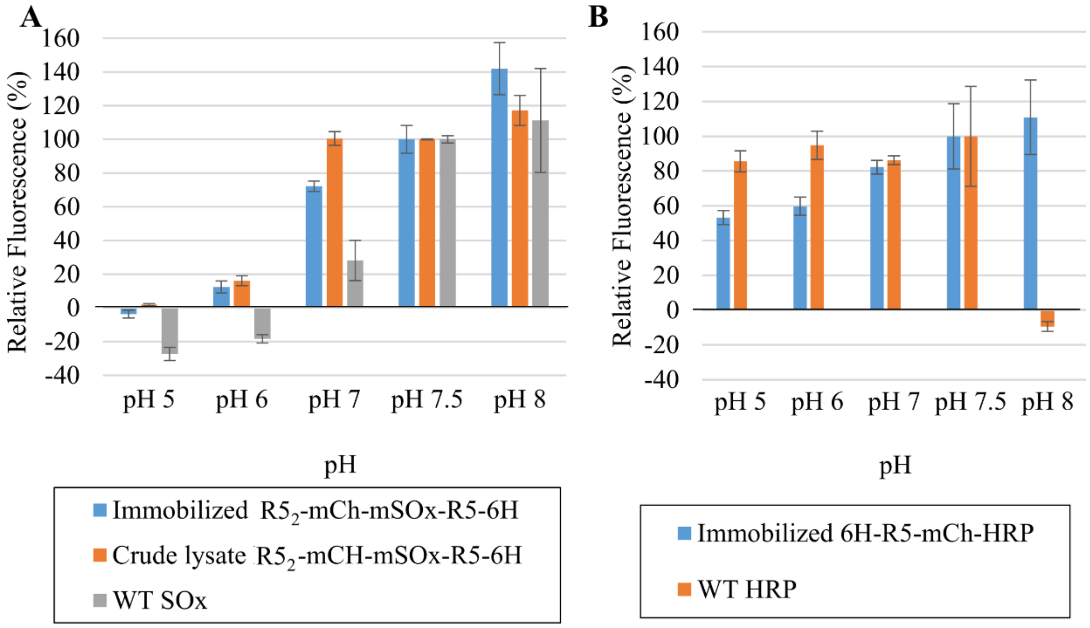

Figure 2.32 Effect of pH on the detection of sarcosine and H_2O_2 with (A) R5$_2$-mCh-mSOx-R5-6H and (B) 6H-R5-mCh-HRP, respectively. Fluorescence intensity (ex. 530 nm/ em. 580 nm) recorded at 20 min after addition of the substrate. In the case of sarcosine oxidase, substrate final concentrations were 10 µM. For HRP, substrate concentrations were 50 µM.

2.3.4.5 Stability of bio-recognition element

Given the intended use of the constructs is in POCTs in resource-limited settings where storage at -20 ^{0}C or even 4 ^{0}C may be unavailable, the stability of the fusion constructs was evaluated after storage at 20-22 ^{0}C (room temperature in the lab, RT) and at 37 ^{0}C (the expected room temperature in some target locations).

The free 6H-R5-mCh-HRP retained 60-80 % of its activity for more than two weeks, even at room temperature (the WT enzyme lost 90 % of its activity in 4 days, Figure 2.33). Given the specific activity of HRP constructs with R5-mCh was several orders of magnitude lower than the WT (Table 2.12), further improvements are needed to the protein design and hence, the stability of these constructs were not explored in depth.

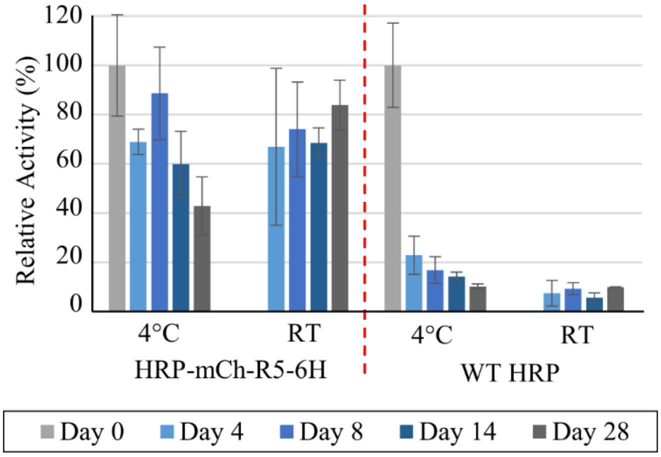

Figure 2.33 Stability of the WT HRP and the HRP-mCh-R5-6H over 4 weeks at 4 °C and ambient temperature, based on ABTS measurements of reaction rate.

Preliminary studies showed that for R5$_2$-mCh-mSOx-R5-6H on silica > 95 % of the activity remained after two months of storage at room temperature, compared with < 20 % for the protein in solution [37]. However, this activity was benchmarked after the drying process so further investigation was required. Both wet (in buffer) and dry storage states were investigated with regard to the stability of R5$_2$-mCh-mSOx-R5-6H on silica. The WT SOx control was stored in the lyophilized form provided commercially and rehydrated just prior to use at each time point.

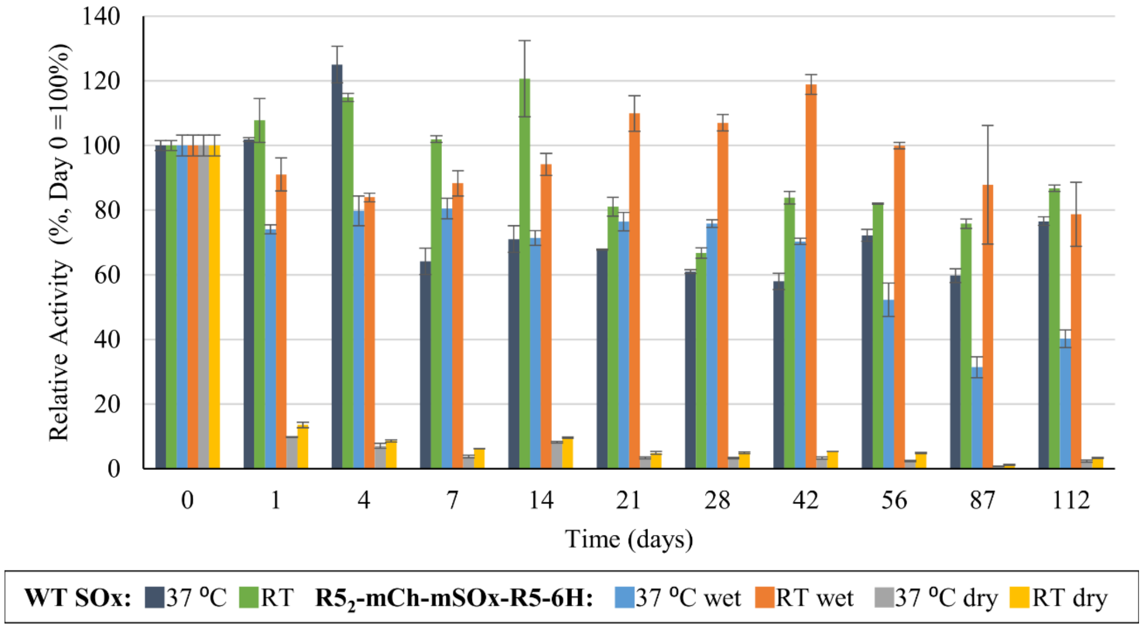

Figure 2.34 Relative enzymatic activity of WT SOx in a lyophilized form and R5$_2$-mCh-mSOx-R5-6H on silica overtime, in both wet and dry storage states at 20-22 ^{0}C (RT) and 37 ^{0}C, as measured by Trinder's assay.

The drying process for R5$_2$-mCh-mSOx-R5-6H on silica resulted in a significant loss of activity, over 85 % loss as compared to activity just after immobilisation (Figure 2.34). Addition of sugars or other stabilizing agents during the drying process or using lyophilization could help retain more of the initial activity [203] and should be further investigated as part of any future developments of this process. However, once dry (and after the significant drop in activity occurs), there is little difference between storage at 20-22 ^{0}C versus 37 ^{0}C. This suggests the dry form would not require storage at a specific temperature. When stored at 4 ^{0}C, the dry storage state maintains ~90 % for up to 3 months, but some decline in activity is seen after this point (Figure 2.35). This decline is observed for both commercial silica gel and silica extracted from sand.

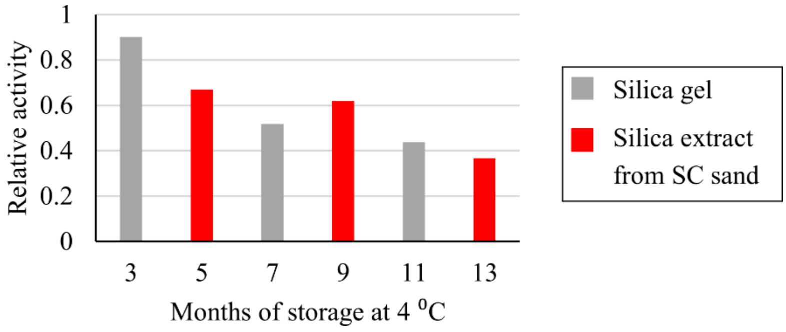

Figure 2.35 Relative activity of R5$_2$-mCh-mSOx-R5-6H on silica overtime in a dry storage state at 4 ^{0}C.

The wet storage states were kept in microcentrifuge tubes, however, significant evaporation occurred over the length of the study, especially for the 37 ^{0}C storage state (which was dry by the end of the 16-week study). This effect was compensated for in the activity results by a control study of evaporation at both temperatures (Figure 2.36). Storage at room temperature maintained more activity (80 % after 16 weeks) as compared to storage at 37 ^{0}C (~40 % at 16 weeks). A similar trend was observed for the lyophilized WT SOx. While wet storage states provided greater activity retention as compared to dry, aggregation of the particles was observed for the wet storage states. This aggregation could be driven by interactions of the protein immobilised on the surface, and may affect the dispersion of these functionalised particles in a sample, limiting their ability to consume substrate throughout the sample.

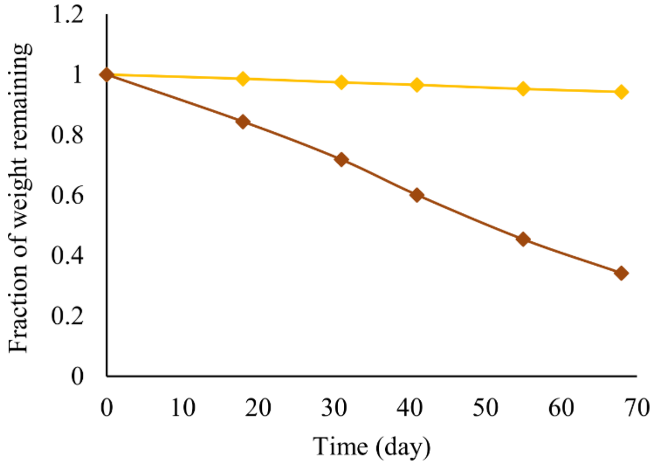

Figure 2.36 Percent weight loss due to dehydration overtime for 500 µL samples stored at 20-22 ^{o}C (yellow) and 37 ^{o}C (red).

The mCh portion of the fusion construct serves as a built-in visual marker for both the protein production and immobilisation processes. It was hypothesized that it could also serve as a marker of quality assurance for the stability of the protein and indicate retention of enzymatic activity. mCh retained more of its fluorescence when stored at 20-22 ^{0}C (room temperature) than when stored at 37 ^{0}C in either storage condition (Figure 2.37). While dry storage samples at room temperature visually appeared white, they regained their pink colour upon rehydration in the initial weeks of storage. After two weeks, all storage states apart from wet storage at room temperature lost over 50 % of their fluorescence intensity.

Although a loss of fluorescence and activity was observed for all storage states over time, there is no direct correlation between the two. For example, fluorescence retention is comparable at day 1 for the wet and dry storage states at room temperature (after rehydration of the dry state), but < 20 % activity is retained after drying. In contrast, wet storage at 37 ^{0}C results in the retention of ~ 75 % enzymatic activity, but < 30 % fluorescence activity. The lack of correlation between fluorescence intensity and activity suggests that mCh may not be well-suited as an internal quality assurance measure of enzymatic activity. Nevertheless, it still has utility as a visual indicator for monitoring of the earlier steps of the production process (see Figure 2.20 and Figure 2.21).

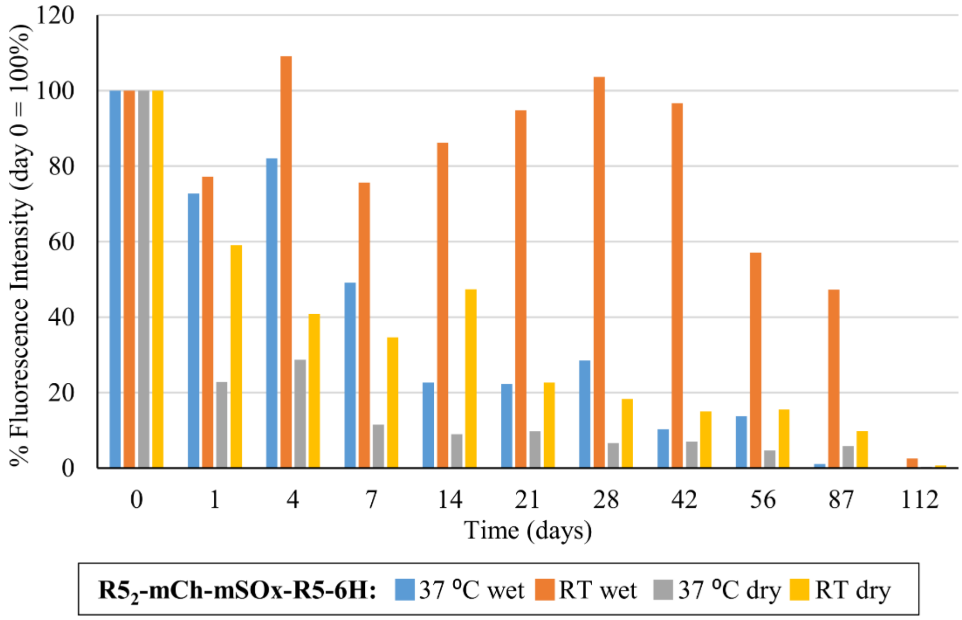

Figure 2.37 Relative fluorescence activity of $R5_2$-mCh-mSOx-R5-6H on silica overtime in both wet and dry storage states at 20-22 ^{0}C (RT) and 37 ^{0}C, ex. 587 nm / em. 607 nm.

In summary, R5-mCh-Enz fusions retained enzyme activity in both their soluble and immobilised forms. Although the drying process should be improved to prevent loss of activity, the dry reagent retained activity for over two months at room temperature. This is an advantage compared to the soluble reagents. Given a similar limit of detection can be achieved with immobilised reagents as with soluble protein, as shown for $R5_2$-mCh-mSOx-R5-6H (Figure 2.29 and Figure 2.28, respectively), this suggests directly immobilised reagents could be used in the development of POCTs. In light of this, it is important to investigate how particle characteristics affect the interaction of the of R5 peptide with silica in order to select the optimum stationary phase for both purification and immobilisation.

2.3.5 Effect of particle characteristics on immobilisation efficiency

Silica particle characteristics including diameter, pore size and silica type have previously been shown to affect the interaction of SBPs [99,100,129]. The effect of each of these was investigated for R5-tag mediated immobilisation directly from lysate with R5$_2$-mCh-mSOx-R5-6H.

2.3.5.1 Effect of particle diameter

Z-stacks acquired through confocal microscopy of the immobilised R5-mCh-Enz fusion proteins suggest that immobilisation is largely on the surface of the irregular silica particles; slices through the centre of the particles show a reduction in fluorescence in the middle of their intensity plots (Figure 2.38 shows this for R5$_2$-mCh-mSOx-R5-6H on silica extracted from SC). This would suggest that immobilisation efficiency should decrease with an increase in particle diameter.

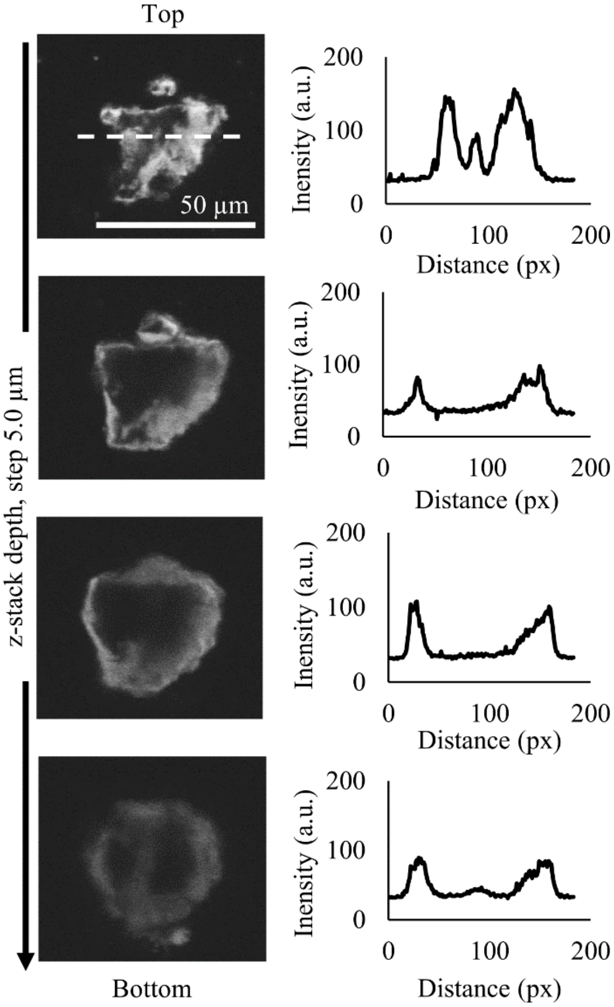

Figure 2.38 Confocal microscopy z-stack images of R5$_2$-mCh-mSOx-R5-6H immobilised on extracted silica showing emission at 609 nm and corresponding intensity plots along the position indicated by the dashed line.

To investigate this effect, commercial silica gel of discrete size classes but of the same pore size (60 Å) were tested. The size distribution of each of these classes is shown in Figure 2.39; Figure 2.40 shows the resulting fluorescent particles after immobilisation for each of the size classes.

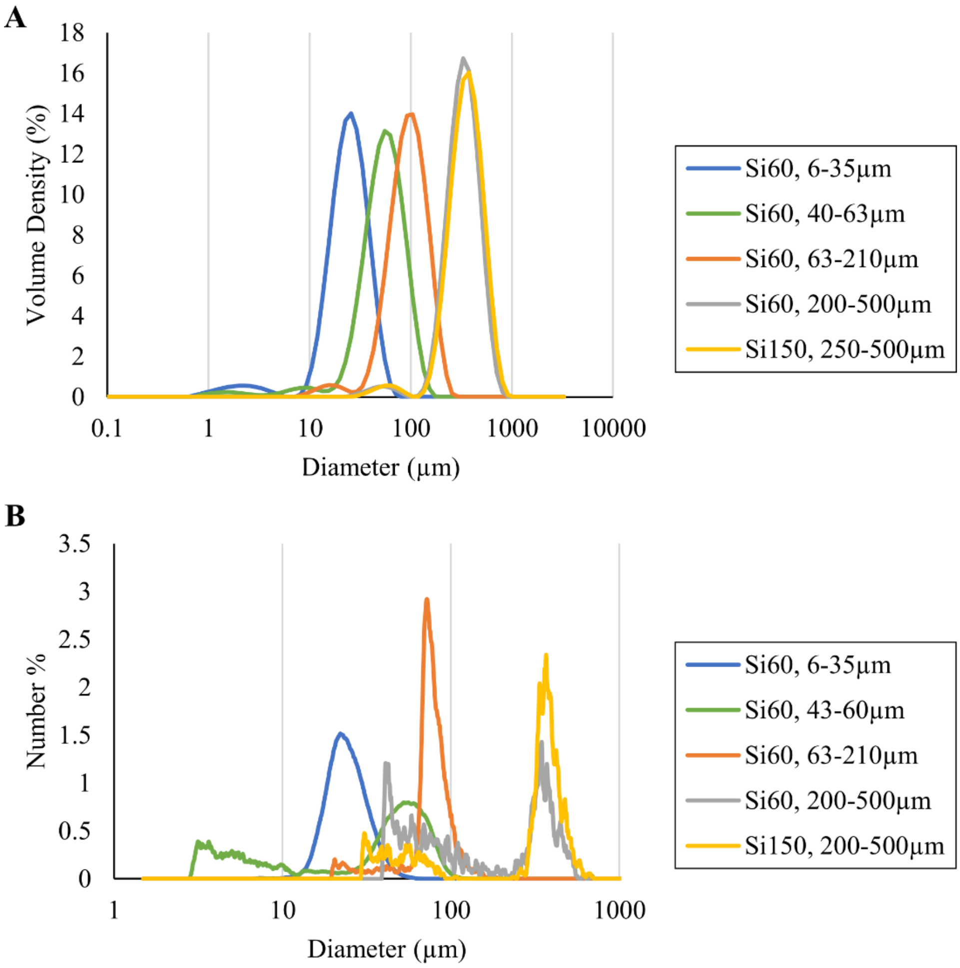

Figure 2.39 Particle size distribution of the commercially sourced silica gel 60 as measured by (A) laser diffraction and (B) microscopy.

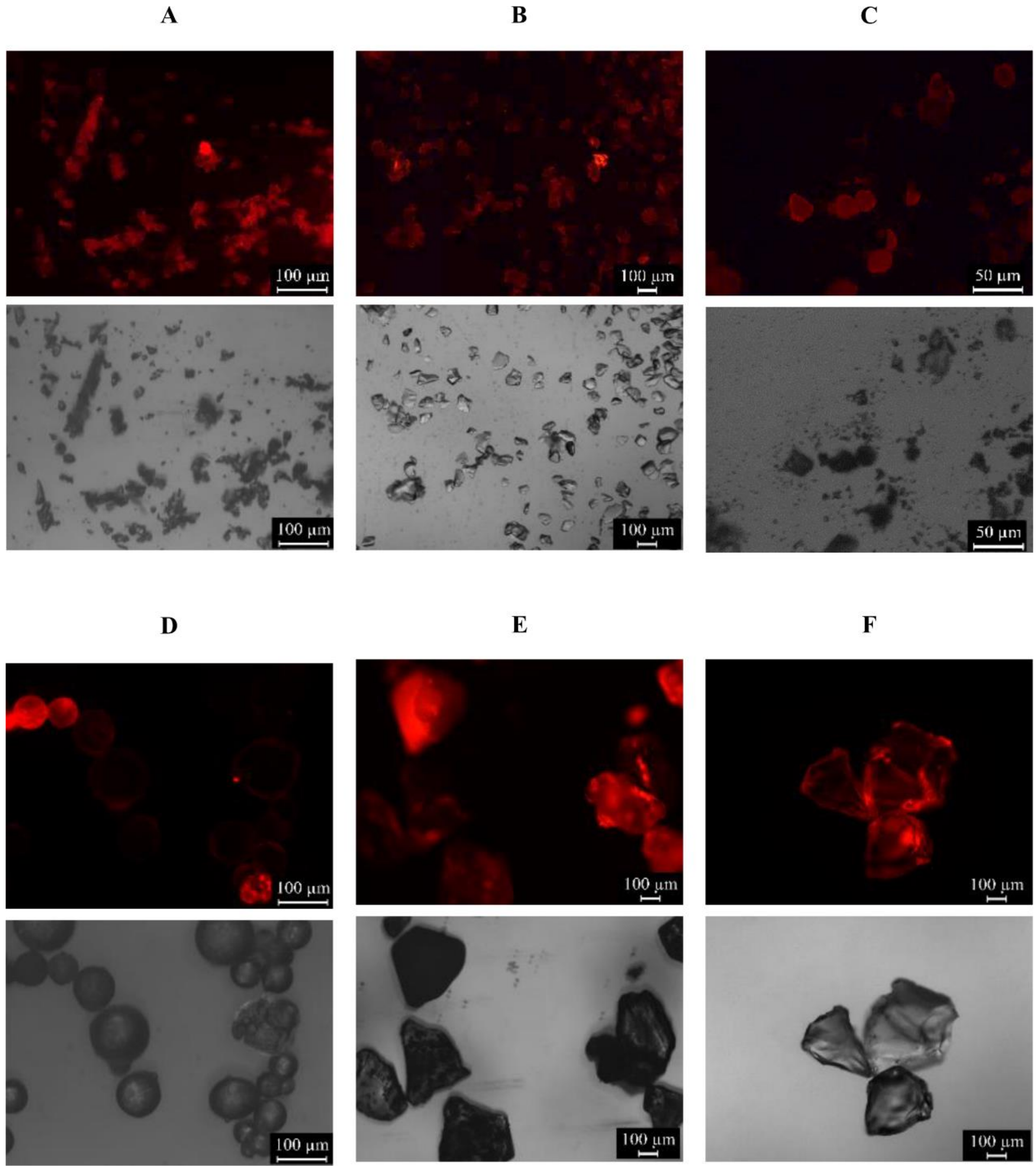

Figure 2.40 (top) Fluorescence and (bottom) corresponding light microscope images of (A) silica gel 60 <63 µm, (B) silica gel 60, 6-35 µm (C) silica gel 60 40-63 µm, (D) silica gel 60, 63-210 µm, (E) silica gel 60, 200-500 µm and (F) silica gel 150, 250-500 µm.

Figure 2.41 shows that as particle size increased, immobilisation efficiency decreased (where the same volume of crude lysate was added per weight of silica) (Figure 2.41). As particle diameter increases, the surface area to volume ratio decreases significantly, resulting in a reduced surface area for each 5 mg aliquot of silica. An estimated total surface area per unit mass (SA) can be calculated based on the sphere-equivalent diameters of the distributions determined by laser diffraction analysis (Table 2.13). As expected, the relative decrease in immobilisation efficiency follows closely with the decrease in total SA (Figure 2.41B). This trend was also observed in the Car9-tag purification of a GFP variant [129]. Thus, the decrease in immobilisation efficiency for the larger size classes is likely due to this decrease in available surface area. If this is the case, increasing the weight of larger silica added to same protein concentration, should improve immobilisation efficiency. This was observed for the silica variants with larger diameters (Figure 2.41C), and indicates that protein concentration may be above saturation for available surface area of these size classes at 5 mg of silica.

Table 2.13 Median diameter from imaging results and total surface area (SA) calculated for spherical equivalent diameters of the size distribution by LDA.

Silica size class (µm)	Median diameter (µm)	SA (m^2/kg silica)
<63	11	579
6-35	25	201
40-63	39	100
63-210	73	43
200-500	285	11

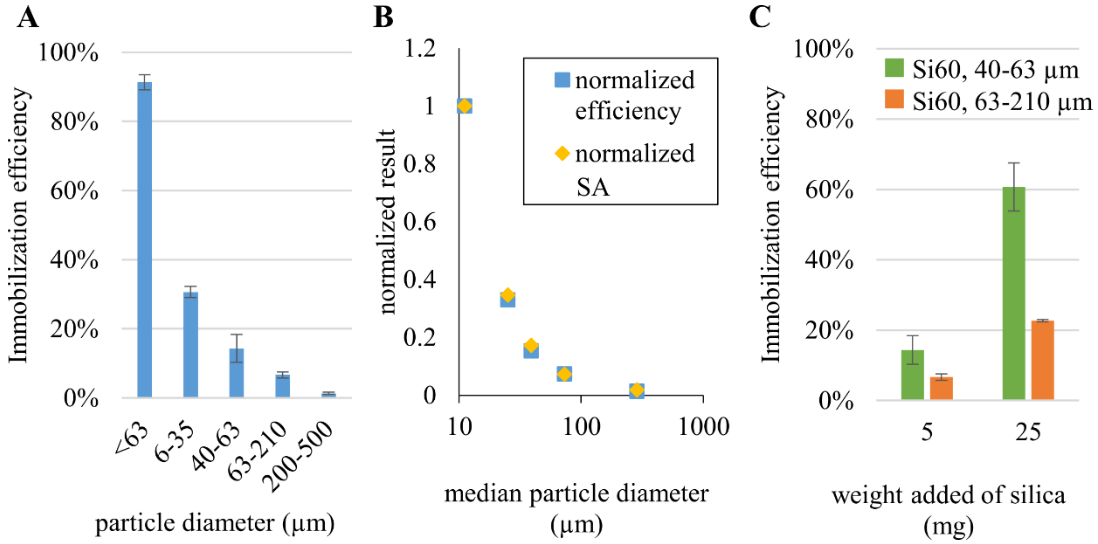

Figure 2.41 Immobilisation efficiency across (A) various silica gel 60 size classes. 75 µL of crude lysate for R5$_2$-mCh-mSOx-R5-6H (estimated 6.6 mg/mL) added to 5 mg of each silica type in 500 µL buffer. (B) Immobilisation efficiency and silica surface area (SA) normalized to silica gel 60 <63 µm. (C) Immobilisation efficiency across weight of silica 60 added for particle diameter size classes of 40-63 µm and 63-210 µm.

2.3.5.2 Effect of pore diameter

The results above suggest that the protein is immobilised largely on the surface for commercial silica gel with pore size 60 Å and extracted silica (observed to be non-pourous/macroporous, Figure 2.12). However, increasing the average pore size of commercial silica gel from 60 Å to 150 Å increases the immobilisation efficiency for the same size class of particles (Figure 2.42). This suggests that at 150 Å average pore diameter some of the protein is immobilising inside the pores. A similar increase in binding capacity when switching from 60 Å to 150 Å was observed by Soto-Rodruiguez *et al.* in their study of the use of the SBP Car9 as tag for affinity purification of proteins [129]. Correspondingly, pore sizes of 50-100 Å are typically used in biocatalyst materials to keep the entrapped enzymes from leaching into the surrounding fluid [204]. This difference in immobilisation between the pore sizes is in line with the expected size of the proteins, as the unit cell of mSOx alone is reported as 71 × 69.7 × 72.9 $Å^3$ (RCSB Protein Data Bank 3QSE for crystal structure for the complex of substrate-reduced mSOx with sarcosine). mCh is reported to have unit cell of 48.8 × 42.9 × 61 $Å^3$ (RCSB Protein Data Bank 2H5Q for crystal structure of mCherry) and the dimensions of the native HRP (MW: ~ 44 kDa) in a neutral buffer solution were predicted to be 62 × 43 × 12 $Å^3$ by a scanning tunnelling microscopy study [205]. Hence, for commercial silica gels of 60 Å and the extracted silica variants showing non-porous behaviour, immobilisation is expected to be primarily on the surface.

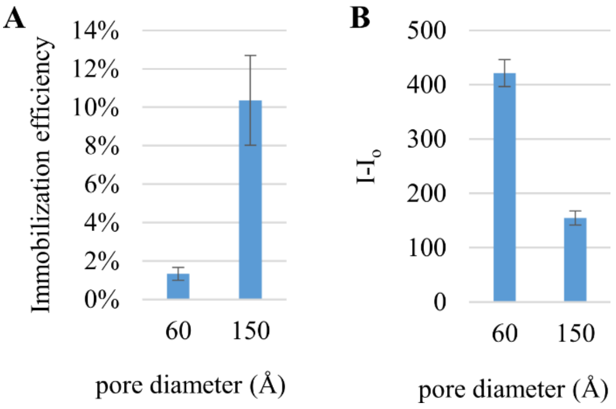

Figure 2.42 (A) Immobilisation efficiency across silica gel 200-500 µm particle diameter with two different average pore diameters. 75 µL of crude lysate for $R5_2$-mCh-mSOx-R5-6H (estimated 6.6 mg/mL) added to 5 mg of each silica type in 500 µL buffer. (B) Activity of silica of 200-500 µm particle diameter with different average pore diameter in the presence of 10 µM sarcosine

Although immobilisation efficiency increased with an increase in pore diameter, less fluorescent product was generated by functionalised 150 Å pore silica than by 60 Å pore silica when total enzyme (mSOx) added to the reaction was kept constant (based on immobilisation rates) (Figure 2.42B). A similar decrease was observed in the apparent activity of the immobilised enzyme with the increase in pore size, with 0.041 ± 0.008 U/mg and 0.152 ± 0.054 U/mg for 150 Å and 60 Å pore size, respectively, after dehydration (as determined by Trinder's assay). This suggests that the enzymes immobilised in the pores are not as accessible for the reaction with sarcosine, and hence primarily surface immobilisation is desirable.

2.3.5.3 Effect of silica type

The binding affinity of proteins for the silica surface in known to be influenced by the composition of the silica surface [99,100]. Surface composition includes the degree of surface ionisation, the area density of the silanol groups and the prevalence of different types (single, vicinal, germinal), and is known to depend on the synthetic origin and thermal history of the silica [102,103]. The extracted silica was compared against commercial silica gel to determine the effects of the extraction process used here.

No difference in immobilisation efficiency from lysate was observed between both extracted silica variants; however, a decrease in efficiency was observed for commercial silica gel 60 when immobilisation was performed under the same conditions (30 µL of lysate (~5 mg/mL protein) per 1 mg of silica) (Figure 2.43A). Although similar levels of immobilisation were observed for extracted silica and commercial silica gel using Ni-purified constructs (Figure 2.22), these were at lower total protein concentration than found in the lysate. Figure 2.43C shows that by decreasing the volume of lysate added to silica gel 60 <63 µm, immobilisation efficiency increases. This indicates that at 30 µL of lysate per 1 mg silica, the silica gel surface is likely saturated. In contrast, extracted silica saturates with a higher volume of lysate per mg of silica (Figure 2.43B).

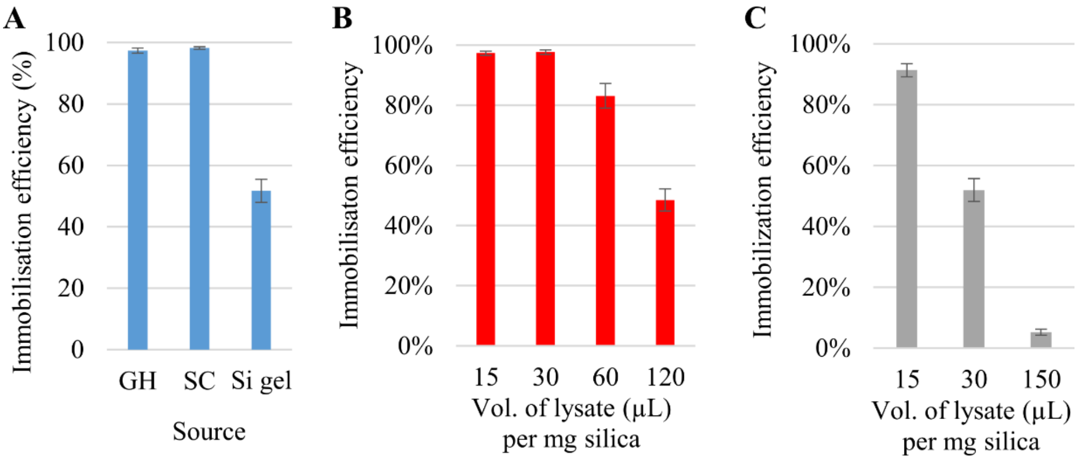

Figure 2.43 Immobilisation efficiency of R5$_2$-mCh-mSOx-R5 -6H from lysate on (A) extracts from GH and SC sands and on commercial silica gel 60 <63 µm, as measured by mCh fluorescence. Vol. of lysate per mg of silica required to observe saturation for (B) SC extract and (C) silica gel 60 <63 µm.

Although an increase in particle size was shown to reduce immobilisation capacity (Figure 2.41), extracted silica has a distribution shifted towards the larger particles (Figure 2.11). This suggests the difference observed in binding capacity between the extracted silica and silica gel 60 is not due to particle size. Instead, it is likely due to the differences in silica surface composition, including density of silanol groups and their ionisation, the degree of which varies across types of silica [105–109]. An increase in ionized silanol groups on the surface would result in a more negative surface charge, which would be expected to provide more binding sites for the R5-sequenece. This is likely the case here as the silica extracts were observed to have slightly higher ratios of Si-OH groups relative to the Si-O-Si groups as compared to commercial silica gel when analysed by FTIR (Figure 2.10). Therefore, silica extract not only supports R5 peptide mediated binding but is preferred over commercial silica gels when high surface loading is desired.

2.4 Summary

This chapter explored the feasibility of a simple protein production and purification process that could enable in-country manufacture of functional proteins for affordable diagnostics. The strategy was to design fusion proteins combining the R5 peptide and a fluorescent protein with the target bio-sensing protein for the diagnostic assay and to use silica as the low-cost support matrix. Figure 2.44 provides a summary of this ‘gene to device’ pathway, including extraction of silica from sand.

Silica was investigated as an abundant and low-cost support material for the proteins. It was extracted easily from beach sand with simple alkali treatment and subsequent acidification. Not all sands tested were sufficient sources of silica but of those that were, SC sand had the highest yield with 11.5 ± 1.4%. The precipitate from sand processing was shown to be nonporous or macroporous and of a heterogeneous size distribution, and the presence of silica was confirmed by both FTIR and XRF. While the material may have some traces of other elements, it showed good immobilisation of R5-tagged proteins, making applicable to the local production process. Moreover, it was shown to have a higher binding capacity than commercial silica gel 60.

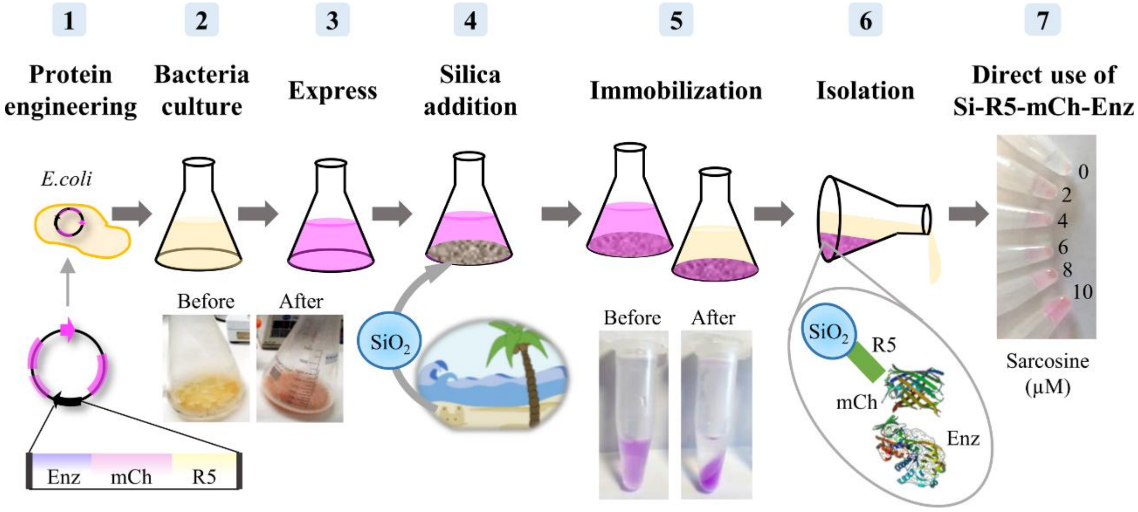

Figure 2.44 Schematic illustration of a "gene to device" pathway; 1) Protein engineering to obtain R5-mCh-Enz, 2) Bacterial culture growth, 3) Protein expression, 4) Addition of silica (extracted from sand) to lysate, 5) Protein purification/immobilisation/stabilisation on silica, before and after examples in microcentrifuge tubes shown, 6) Isolation of silica-R5-mCh-Enz, 7) Direct use of the silica-R5-mCh-Enz in biosensor platforms, as shown by silica-R5$_2$-mCh-mSOx-R5-6H for the detection of sarcosine. (mCh structure 2HQ5 and mSOx 3QSE from RCSB Protein Data Bank).

A proof of concept was demonstrated with R5-mCh-6H. Good rates of immobilisation were observed and the binding affinity of the R5 tag for silica was shown to be similar to the affinity of His-tagged proteins and Ni-NTA-coated surfaces used in the classical method of protein purification. Fluorescence lifetime and maximum λ_{em} values suggest that the chromophore structure of mCh was maintained after the fusion and after immobilisation.

Fusion proteins were created with two functional enzymes, HRP and mSOx. Together, these enzymes can be used to detect sarcosine, a potential biomarker for prostate cancer [158,183]. The fluorescent protein mCh was retained in the fusion construct as a tool for simple visual monitoring of both the successful production of the protein and its subsequent immobilisation, with the hope that this will help make the process suitable for use in a laboratory with minimal infrastructure. The HRP fusion proteins only showed minimal activity when compared to the commercially available WT HRP, but the R5-tag addition avoided HRP’s tendency form inclusion bodies during recombinant production. R5_2-mCh-mSOx-R5-6H showed comparable specific activity to WT SOx.

With R5_2-mCh-mSOx-R5-6H, the potential for a quick, reliable and specific immobilisation process directly from crude lysate without additional coupling agents was demonstrated. Immobilisation was found to be largely on the surface of both the extracted silica and commercial silica gel 60 for fusion proteins of this size. Although increasing pore diameter to 150 Å resulted in an increase in immobilisation efficiency, indicating that that immobilisation does occur in larger pores, less apparent activity per unit enzyme suggested that those enzymes were not as accessible for the reaction with sarcosine in the solution; hence, surface immobilisation is desirable.

While R5-mCh proteins could be eluted off the silica, as would be done in a classical protein purification, the functionalised silica can also be used directly in bioassays, removing steps and further simplifying the process. This is a new approach with SBPs as previous approaches have either shown their utility as a purification tag for later elution or their immobilisation/encapsulation ability after elution from column purification. Although there was a significant loss of activity during drying, which requires further process improvements, once dried, the reagent was shown to be stable for over two months. This indicates a potential advantage of immobilised reagents. In addition, by using solid components instead of liquid solutions in the biosensor, the time and laborious work of solution preparation can be reduced. This could result in increased portability and increased simplicity of the assay meaning it can be used by non-specialized personnel in remote areas. An assay format that takes advantage of the particulate nature of the reagent will be explored in Chapter 3.

3 EXPLORATION OF A FALLING PARTICLE BIOSENSOR

3.1 Introduction

3.1.1 POCT formats utilizing particle-bound enzymes

In Chapter 2 it was shown that the silica-immobilised R5-mCh-Enz proteins can be used directly for sensing target substrates in solution. While immobilisation can add stability and particle-based reagents could simplify assay preparation steps, immobilised enzymes experience different mass transport limitations to soluble enzymes, which can affect their apparent activity. Particles, even in stirred solution, are usually surrounded by a diffusion layer, such that the enzyme at the surface experiences a different local concentration than it would experience in the bulk; this surface concentration is typically lower with respect to substrate and higher with respect to product. The thickness of this layer varies with particle size and the relative movement between the solute and particle phase. For some immobilisation strategies (e.g. encapsulation), internal mass transport processes within the pores of the support material must be considered in addition to external mass transport to the surface; however, for silica-immobilised R5-mCh-Enz constructs, pore diffusion can be ignored as primarily surface immobilisation was observed (Chapter 2). A variety of strategies have been explored in the past to successfully utilize immobilised enzymes in POCTs by optimising the transport phenomena of substrates and products.

Classical diagnostic platforms have typically used the immobilised protein as the stationary phase, where the sample diffuses transversally or laterally into the protein layer. Examples include sample-fill into a glucose test strip, where the enzyme is deposited in a matrix of preservative agents, or lateral flow immunoassays, where the antibodies are immobilised directly to the nitrocellulose paper. Of those utilizing particle-bound enzymes, a packed particle bed is the most reported format. Packed beds of functionalised beads have been employed in microfluidic devices for both lateral flow immunoassays (as shown in a recent publication with collaborators [206] and by others in the literature [207–212]) and for small molecule assays (e.g. [213–216]). Although microfluidic channels are typically touted for their improved surface area to volume ratio compared to other systems, the use of particles in the channel provides further improvement of the surface area to volume ratios (as compared to bio-sensing elements immobilised directly to channel surfaces) and diffusion distances are significantly reduced in the narrow pores through a particle bed [206–208,217]. There is also some evidence to suggest that flow through a packed particle bed promotes improved mixing in microfluidic channels which typically face mixing challenges due to laminar flow rates [213]. However, maintaining these particles in place during microfluidic flow is often accomplished through mechanical structures such as weirs or pillars which require complex fabrication steps.

The particle format also allows other biosensor configurations to be explored. In contrast to a packed particle bed, where the fluid sample passes the stationary particles, a design can be considered where the bio-functionalised particles are moved throughout the sample in which they are suspended. ‘Stationary’ fluid concepts are attractive for POCT design because they do not require continuous fluid actuation to be integrated in the system. Within ‘stationary’ fluid compartments, particle movement can be used to homogenise reagents, increase particle-fluid interactions and help overcome diffusion limitations.

‘Stationary’ fluid concepts have often used magnetic particles as they can be conveniently manipulated by magnetic fields [218]. For example, magnetic particles have been transferred through various processing solutions separated by air gaps in a capillary tube by an external magnet for analyte capture. This is in contrast to the typical approach where magnetic particles are held stationary during fluid movement, akin to packed bed (e.g. [219]). The movement of the magnetic particles through pre-loaded solutions in a capillary tube has been used for both nucleic acid and protein extraction from clinical samples [220–222]. This approach to nucleic acid extraction has also been coupled with subsequent amplification of the extracts for the detection of infectious diseases [223–225]. In addition, magnetic particles have a tendency to form chains and other structures, due to magnetic dipole-dipole interactions between the particles, which can be used for chaotic mixing at the microscale [226].

Alternatively, the movement of the particles can be driven by simple gravitational force, i.e. particle sedimentation in a fluid-filled chamber (as shown in Figure 3.1). Particle sedimentation, and therefore interaction of the immobilised enzyme with the sample, is controlled by the density and size of the particles as well as the internal shape and dimensions of the chamber. This falling particle biosensor approach achieves dispersion of the particles throughout the fluid for a period of time, a feature that is often beneficial with respect to the reaction rate for large scale bioreactors using immobilised enzymes [227]. In addition, sedimentation allows for the removal of the silica particles from the region for fluorescent signal analysis, potentially improving the signal to noise ratio by removing background noise due to light scattering by the particles. Moreover, this approach requires no additional external components nor the use of expensive magnetic particles, making it amenable to use with the R5-mCh-Enz functionalised silica particles developed in Chapter 2. Despite the potential advantages of such an approach, no examples of POCT formats using the particle-bound enzyme as the mobile phase closely resemble the falling particle design proposed here. As such, an initial exploration of this format is presented in this chapter. Its performance against other assay formats utilizing particle-bound enzymes will be considered in Chapter 4.

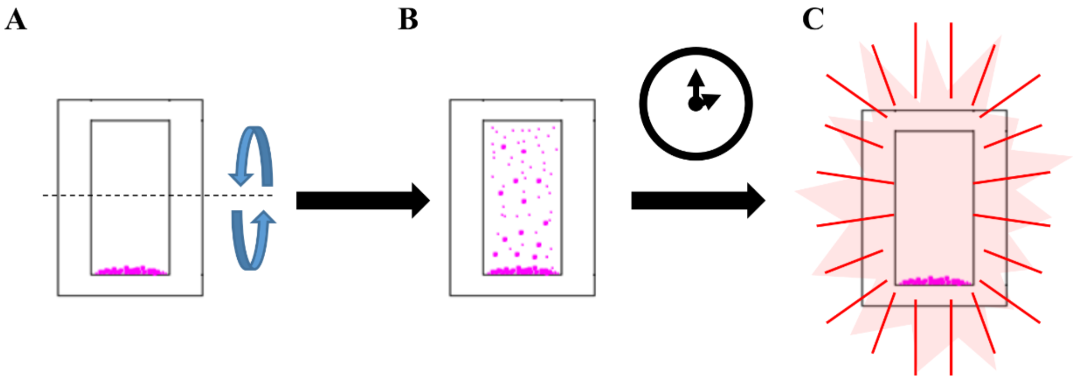

Figure 3.1 Schematic of a falling particle biosensor format, where (A) inversion and (B) subsequent sedimentation is used to pass the particles though the sample. After sedimentation, (C) fluorescent signal from the solution can be measured. Particles are shown in pink to represent R5-mCh-Enz immobilised on the surface.

To design an effective biosensor using the falling particle approach, it will be necessary to understand the interplay between the kinetics of the immobilised enzyme and the mass transport of the substrate to the particle surface, as this will ultimate determine product formation and thus, signal development.

3.1.1 Design parameters for a falling particle biosensor

Various characteristics of the falling particle biosensor design play a role in determining the rates of enzyme kinetics and mass transport in such a system. The kinetic reaction rate is a result of inherent enzyme characteristics. Enzyme behaviour, especially for those reactions involving a single substrate, is classically described by Michaelis-Menten kinetics [227,228], which mathematically describes the rate of product formation by the set of reactions in Figure 3.2.

$$E + S \underset{k_{-1}}{\overset{k_{+1}}{\rightleftarrows}} ES \xrightarrow{k_{+2}} E + P$$

Figure 3.2 Reaction sequence for a one-substrate reaction.

In the first step, the substrate (S) binds reversibly to the enzyme (E) forming an enzyme substrate complex (ES). This complex is then assumed to react irreversibly to generate product (P) and release the enzyme. The reaction rates are determined by the substrate binding (k_{+1}/k_{-1}) and catalytic conversion (k_{+2}). The assumption of irreversibility is generally valid when [S] >> [P], such as in the initial stages of reaction (where square brackets denote concentration). By making the steady-state assumption that the rate of formation of ES equals the rate of ES disappearance and subsequent product formation, the rate of production formation, V, can be described by:

$$\boldsymbol{V = \frac{[S]V_{max}}{K_m + [S]}} \tag{3.1}$$

where V_{max} is the maximum rate of reaction of the enzyme when it is under substrate saturated conditions and is a measure of enzyme specific activity. Practically, K_m is the concentration of substrate which permits the enzyme to achieve one-half V_{max}, but is also an inverse measure of affinity of the enzyme for the substrate. K_m is described by:

$$\boldsymbol{K_m = \frac{k_{-1} + k_{+2}}{k_{+1}}} \tag{3.2}$$

Clearly, both V_{max} and K_m are important parameters with respect to rate of product formation. K_m is a characteristic dependent on the relationship between enzyme and substrate (i.e. target analyte). V_{max} is a rate per unit of enzyme, which means that the activity for each particle will be dependent on the enzyme surface coverage (ESC, mg enzyme / m^2 silica surface) and particle surface area (as determined by particle size). When $[S] >> K_m$, the rate of product formation is independent of substrate concentration; however, when $[S] < K_m$, product formation exhibits first order kinetics with respect to [S]. In the case of an immobilised enzyme, the concentration of substrate at the particle surface will be determined by mass transport processes.

The rate of mass transport of the substrate is determined not only by substrate concentration and by substrate diffusivity, which is a function of substrate size and polarity, but also by fluid viscosity and by flow around the particle. In the case of the falling particle approach, the relative flow experienced at the particle surface is determined by the settling behaviour of the particles per inversion of the device and the number of inversions. Although there are no examples of POCTs that move particle-bound enzymes through the sample via particle settling, particle sedimentation has been extensively studied in many disciplines, ranging from geologists investigating the formation of river beds [229] to chemical engineers looking at the design and operation of chemical process equipment such as fluidized bed reactors [230,231].

It is well known that the settling behaviour of particles is affected by their inherent characteristics, such as size, shape and density, as well as the characteristics of the fluid in which they are suspended, such as viscosity and density. Stokes, in his classical work, presented an expression for particle settling velocity by equating the effective weight of a spherical particle to the viscous resistance of the fluid, also called the drag force [232]. Since then, extensive work has combined theoretical and experimental approaches to develop relationships that encompass particle-fluid systems beyond a single sphere in a viscous fluid. For example, the ratio of the principal axis lengths defining a particle’s shape was found to be a significant factor on settling velocity [233]. Particle volume fraction also has an effect; as particle fraction increases, the interparticle interactions become increasingly important. The motion of an individual particle is affected by the relative positions and velocities of nearby particles. Clusters, or small groups of closely spaced particles, have been shown to fall together and their velocity well approximated by the velocity of a sphere with an effective radius similar to that of the cluster [234].

When the number of particles becomes large, clusters become clouds of particles, and their behaviour changes. A cloud of particles can be regarded as an effective fluid drop, and thus described by the sedimentation of a heavy fluid in a lighter fluid (as solved by Hadamard and Rybezynski). Again, the cloud has a greater settling velocity than an individual particle. Within the cloud, the particles experience a degree of circulation and some are observed to ‘leak’ from the cloud and form a vertical tail [235].

For both clusters and clouds, the hydrodynamic interaction between particles has a cooperative effect, increasing velocity relative to Stokes velocity. However, this assumes infinite fluid in the direction of settling (or an experimental vessel long enough that the influence of the bottom wall is small). However, for particles uniformly dispersed in a viscous fluid in a vessel with vertical side walls and fixed bottom, the mean velocity of the particles is found to be hindered, decreasing as particle concentration is increased [236]. The presence of a fixed bottom on the vessel requires the fluid to move upward to compensate for the settling of the particles, such that the average velocity in the whole suspension is zero. This correlation has been extended from uniform spheres to multi-sized distributions of both large and small particles [237,238]. In addition, for multi-sized distributions, as the settling progresses, the faster falling large particles move away from the others, changing the concentrations of particles throughout the settling suspension [229]. It is clear that the settling behaviour of bio-functionalised silica explored here will be complex, especially for the silica extracted from sand given its wide distribution of particle size. Hence, experimental observations will be key to defining the relative velocity experienced by the particles, to then inform the understanding of reaction rate control.

In summary, there are many parameters for consideration in the initial exploration of a falling particle format presented in this chapter. Figure 3.3 shows these parameters grouped according to the processes in which they are involved. Both mass transport and kinetic rates are also affected by temperature, as it affects fluid viscosity and enzyme specific activity, however, temperature will be kept constant for initial exploration of the system.

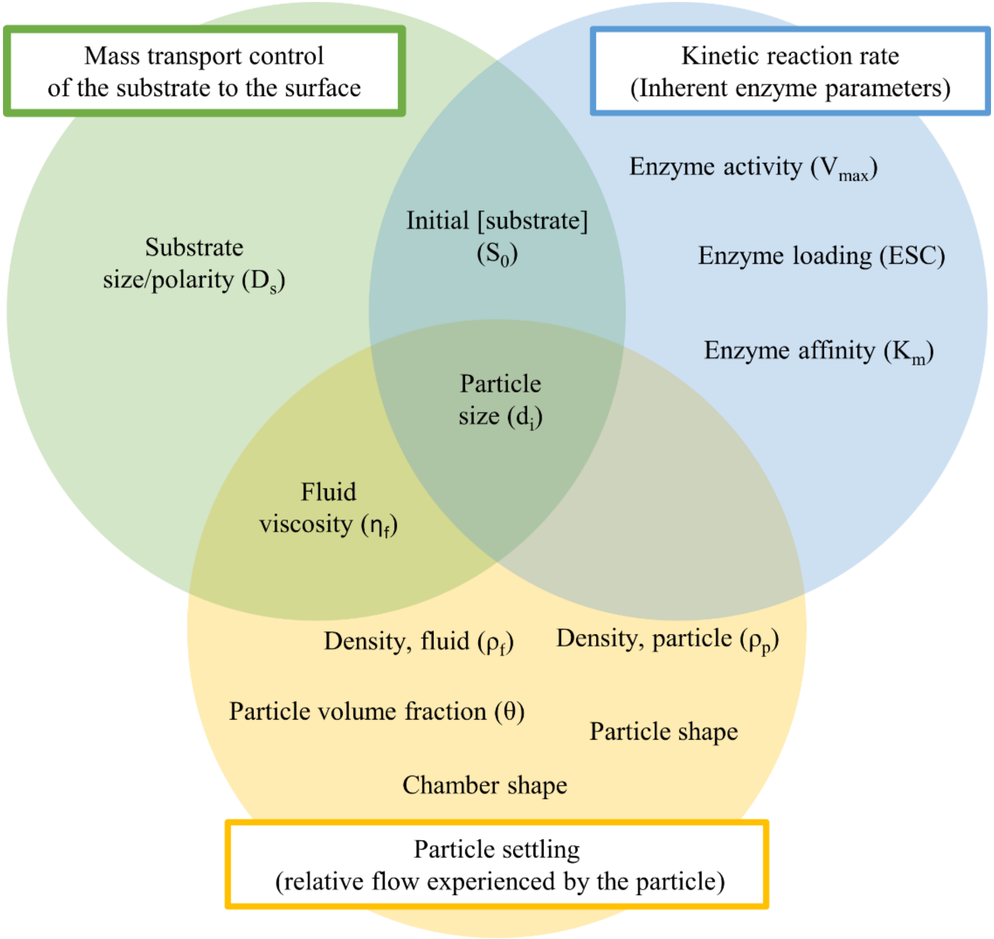

Figure 3.3 Parameters with a possible effect on the rate of product formation in an falling particle biosensor.

To determine the process controlling the rate of substrate conversion by enzymes on a falling particle, first it will be necessary to assess the relative flow around the particles and degree of turbulence in the device through detailed analyses of particle settling behaviour (Section 3.3.1 and 3.3.2). Next, this information will be used in conjunction with experimentally determined enzymatic parameters from Chapter 2 and reaction conditions (e.g. substrate concentration) to assess relative theoretical reaction rates under the regimes of kinetic and mass transport control (Section 3.3.3). Finally, these relative rates will be used to predict product formation by a range of silica types. These predictions will be compared to experimental results to determine validity of a relative reaction rate model and the ensuing design implications for a falling particle biosensor (Section 3.3.4).

3.2 Experimental

3.2.1 Materials

Materials were sourced as described in Chapter 2, with the addition of the following: poly(methyl methacrylate) (PMMA, Engineering Design Plastics, UK), PCR plate seal (Adhesive PCR Plate Seal, Thermo Scientific).

Silica nanoparticles made via Stöber synthesis [93] by a former member of the Cambridge Analytical Biotechnology group, Dr. Yao Du, were also tested [239]. These nanoparticles have a mean dry diameter of 245 ± 49.0 nm as measured by Scanning Electron Microscopy and subsequent image analysis by ImageJ [240].

3.2.2 Falling particle biosensor construction and use

Falling particle chambers were produced by laser cutting 2 mm thick PMMA and sealing both sides with PCR plate seal. Three different designs were explored: a system with a parallel sides, as shown in Figure 3.1, and two with central constrictions, or waists, of different widths. These are introduced in detail in Section 3.3.1 and shown in Figure 3.7. Total volumes were 320 / 240 / 200 µL for the parallel sided / standard waist / narrow waist designs, respectively. The sealed device containing bio-functionalised silica in solution was inverted for mixing, either by flipping about a central horizontal axis (flip) or by rotation in plane (tilt), each time allowing the particles to settle to the bottom (schematic of inversion techniques in Figure 3.12). Time between inversions was 60 s unless otherwise specified.

3.2.3 Particle image velocimetry analysis

Particle settling patterns were observed by obtaining shadows of particles using backlit illumination (experimental setup in Figure 3.4). For illumination, a 100 W light-emitting diode (LED) array with a light diffuser was placed behind the 'device' and aligned to the camera. The resulting shadow was captured by a high-speed camera (Phantom v130) with a 12X lens and accessories (Navitar). Videos were captured at 50 fps. Fixtures were designed to hold the device and to allow either inversion technique (i.e. rotation in plane or flipping about a horizontal axis through the middle of the device). Devices were filled with range of silica sizes suspended in buffer and sealed. Silica variants were presented and characterised in Chapter 2. Silica concentration in the device was 5 mg/mL unless otherwise noted. (For the volumes encased by the devices this is similar to the amount of silica added for each sarcosine assay - 0.875 mg). All silica was functionalised with $R5_2$-mCh-mSOx-R5-6H from lysate following the immobilisation protocol described in Chapter 2. Sample videos are provided on a USB drive across the range of silica types and inversion techniques, with details recorded in Appendix B.

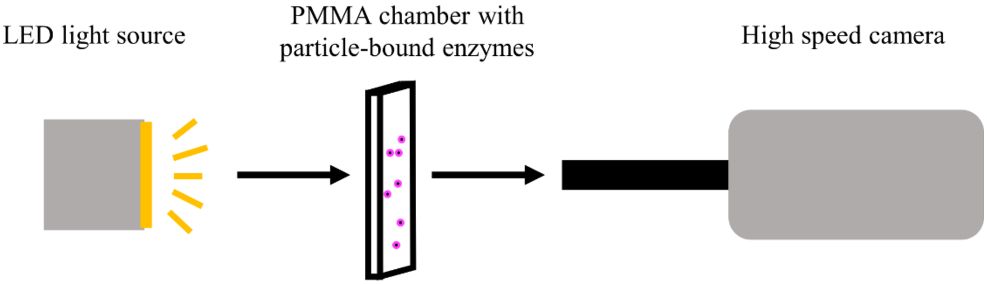

Figure 3.4 Schematic of experimental set-up for visualisation of particle settling patterns.

Frames from the videos captured by this setup were converted to greyscale and colour inverted using MATLAB [241] (See Appendix C for details). These inverted video frames were translated into virtual stacks using ImageJ and Z-projections of the maximum pixel value were used to create image overlays. Image overlays were then analysed using set level image thresholding to determine percentage of particle passage through the total volume using ratio of white to black pixels, where white pixels indicated particle passage.

Particle image velocimetry (PIV) analysis of particle settling patterns was performed using PIVLab v1.41 in MATLAB [242], using Fast Fourier Transform window deformation and four successive passes of pixel area (64, 32, 16 and 8) with 50 % step overlap, for each pair of images (pairings done 1-2, 3-4, etc.). Images were calibrated using an internal reference of chamber height (18.32 mm) and time step determined by frame rate (e.g. 20 ms for 50 fps). No observed velocities are reported for particles $r < 10$ µm due to limitations of camera resolution (1 pixel ≈ 20 µm).

3.2.4 Modelling product formation by the particle-bound enzymes

A mathematical model was developed to estimate the product formation for each particle size class while falling at a given velocity. The model combines the principles of enzyme kinetics for immobilised enzymes and corresponding equations [227] with a model for mass transfer of the substrate to the particle's surface based on Fick's law of diffusion [243]. Where the system was under mass transport control (diffusive or convective process) rather than kinetic control, the concentration of substrate at the surface was assumed to be zero and substrate flux to the surface was equated with product formation.

Given the immobilisation of the R5-mCh-Enz fusion proteins was shown to be largely on the surface of the particles (Chapter 2), the model does not consider internal diffusion of the substrate into the pores. Rather it considers only external diffusion processes where the transport of the substrates towards the surface and products away is in series with the catalytic conversion of substrates to products occurring at the surface. This surface where the enzyme is immobilised is assumed to be equally accessible by the substrate and to be a flat impervious support, given the relative scale of protein to particle. (The equivalent diameter of the fusion protein is on the order of 5-10 nm (see Chapter 2) while particle diameter > 1 µm; similar assumptions have been made regarding particle curvature in models of silica-protein interactions [100]). Total surface area per unit weight of silica particles (SA, m^2 / kg silica) was determined using the distribution of sphere equivalent diameters measured by LDA and calculating surface areas and volumes for spheres accordingly. Total protein immobilised per weight of silica (TPI, µg protein / mg silica) was determined experimentally with a Bradford assay (as described in Chapter 2). TPI divided by SA was used to estimate enzyme surface coverage (ESC, mg protein / m^2 silica). Values for TPI, SA, and ESC can be found in Table 3.1 for each of the silica variants explored here. As discussed in Chapter 2, silica extract was shown to support a higher binding capacity per weight of silica (TPI), so a sample with high loading was also included.

Table 3.1 Model inputs for each size class of silica for total protein immobilised per weight of silica (TPI), silica surface area (SA), and enzyme surface coverage (ESC) for immobilisation of R5$_2$-mCh-mSOx-R5-6H.

Silica size class (µm)	TPI (µg protein / mg silica)	SA (m^2 / kg silica)	ESC (mg protein / m^2 silica)
6-35	14.8	201	74
40-63	7.4	100	74
63-210	3.3	43	77
<63 µm	43	579	74
SC extract	43	150	286
SC extract, high loading	86	150	573

The product formation of immobilised enzymes is either controlled primarily by the diffusion of the substrate to the enzyme on the particle surface or by the catalytic activity of the immobilised enzyme (as determined by inherent characteristics of the enzyme and loading capacity of the substrate). The ratio of catalytic control to mass transport control is often characterised by the dimensionless Damköhler number, Da [227,244]. To determine Da for the falling particle system, it is necessary to first calculate the rates of product formation under each regime.

When the system is under kinetic control, enzyme behaviour is assumed to follow Michaelis-Menten kinetics (Eq. (3.1)) with an absence of product inhibition and of portioning or electrostatic effects (sarcosine is not a highly charged substrate). Steady state is assumed (ignore variation in S_0 with time). In addition, the target concentrations for detection (< 10 µM) are significantly less than the K_m for $R5_2$-mCh-mSOx-R5-6H (16.5 ± 0.9 mM [37]). Eq. (3.1) can be re-written such that it is with respect to particle surface area, Eq. (3.3), and can be used to calculate the rate of product formation per particle (units of mol/s).

$$\boldsymbol{V = 4\pi r_i^2 S_0 \left(\frac{V_{max\_SA}}{K_m}\right)} \tag{3.3}$$

where S_0 is the initial concentration of the substrate, r_i is the radius of the particle, and V_{max_SA} and K_m are experimentally determined enzyme parameters. This assumes $S_0 < K_m$, as is true for this case. The surface area term ($4\pi r^2$) assumes spherical geometry. V_{max_SA} is the maximum rate of reaction catalysed by unit of area, as calculated by:

$$\boldsymbol{V_{max\_SA} = V_{max} \times ESC} \tag{3.4}$$

where ESC is the enzyme surface coverage described above. Both V_{max} and ESC are determined experimentally (with values reported in Table 2.12 and Table 3.1, respectively).

Alternatively, when the system is under mass transport control, the conversion of substrate to product is expected to be instantaneous once the substrate reaches the surface-bound enzyme. Hence, the flux of the substrate to the surface is equal to rate of product formation. This flux is controlled by either a diffusion or convection process, depending on the flow experienced by the particle. The ratio of advection of a physical quantity by the flow over diffusion rate driven by a concentration gradient is given by the Péclet number (Pe), as described by:

$$\boldsymbol{Pe} = \frac{\boldsymbol{u_i} * \mathbf{a}}{\boldsymbol{D_s}} \tag{3.5}$$

where a is the characteristic length, D_s is the substrate diffusivity, and u_i is the relative velocity of the fluid regarding the particle of radius r_i. For D_s, the reported diffusivity of glycine, 1.1 × 10^{-9} m^2/s, was used as glycine is an amino acid of similar size and polarity to sarcosine [245]. Radius was used as the characteristic length, following convention for spherical particles [246]. By attaching the frame of reference to the particle, u_i can be set equal to the terminal velocity of the particle during fall. After the particles have settled, their velocity can be approximated as a zero velocity case.

The expected terminal velocity was calculated for each size class of particle of diameter d_i, combining theory on particle sedimentation and experimental observation. Only the steady-state situation in which velocity is constant was considered given the period of time required for the particles to reach their terminal settling velocity is very short (e.g. < 10 ms for particles 500 µm in diameter). To do this, the predicted settling velocity was first calculated based on the relationship developed by Song Zhiyao *et al.* for natural sediment particles, where the constants are derived from experimental data to account for the shape and roundness of such particles [247].

$$\boldsymbol{u_p} = \frac{\boldsymbol{\eta_f}}{\boldsymbol{\rho_f d}} \boldsymbol{d_*^3} \left[\mathbf{38.1} + \mathbf{0.93} \boldsymbol{d_*^{12/7}}\right]^{-7/8} \tag{3.6}$$

where u_p is the settling velocity for a single particle, η_f is the dynamic viscosity of the fluid and d_* is a dimensionless particle parameter as calculated by:

$$\boldsymbol{d_*} = \boldsymbol{d} \left(\frac{\Delta \boldsymbol{g}}{\left(\eta_f / \rho_f\right)^2} \right)^{1/3} \tag{3.7}$$

where g is the gravitational acceleration and $\Delta = \rho_S / \rho_f - 1$, and ρ_s and ρ_f represent the density of the particles and the density of the fluid, respectively.

This velocity was used to calculate the particle Reynolds number, Re_p.

$$\boldsymbol{Re_p} = \frac{\boldsymbol{\rho_f} * \boldsymbol{u_p} * \boldsymbol{d_i}}{\boldsymbol{\eta_f}} \tag{3.8}$$

where ρ_f is the density of the fluid, η_f is the dynamic viscosity of the fluid, u_p is the velocity of the particle and d_i is the diameter class of the particle [248].

This was in turn used to calculate the hindered settling velocities, u_h, due to particle fraction based on the Law of Richardson and Zaki [236] which describes the dependency of the settling velocity on the particle fraction:

$$\boldsymbol{u_h = u_p \times \left(1 - \theta_p\right)^n} \tag{3.9}$$

where θ is the volume fraction of particles in the suspension and n is an exponent dependent on Re_p (Table 3.2). A particle velocity u_i was selected for each diameter d_i, switching from the velocity predicted for natural sediment, u_p, to hindered settling velocity, u_h, for a particle fraction of 0.2 at d_i = ~20 µm, to 0.3 particle fraction at d_i = ~200 µm and to particle fraction 0.4 at d_i = ~300 µm based on experimental observations (Figure 3.9). This velocity function was smoothed using adjacent averaging of 150 pts.

Table 3.2 Corresponding n for specified ranges of Re_p.

Re_p	**0-0.2**	**0.2-1**	**1-500**	**>500**
n	4.6	4.4($Re^{-0.03}$)	4.4($Re^{-0.1}$)	2.4

For Pe << 1, diffusion still dominates and thus, the effect of flow on the chemical reaction is limited. Assuming a spherical particle in dilute suspension under flow with low Reynold’s number and expressing the mass transport problem in the frame of reference attached to the sphere, steady state flux under diffusion can be approximated by:

$$\boldsymbol{\phi_{diffusion} = 4\pi r_i D_s \frac{C_\infty - C_p}{1 - \frac{r_i}{b}}} \tag{3.10}$$

where r_i is the radius of the particle, C_∞ is the concentration of the substrate in the bulk, C_p is the concentration of the substrate at the surface of the particle, and b is the distance from the centre of the particle to the bulk. C_p is assumed to be zero as the substrate is expected to be consumed by the enzyme immediately upon arrival in the case of mass transport controlled system. C_∞ is the initial concentration of the substrate, S_0, and b >> r_i as the bulk is infinitely far away under low flow rates. Eq. (3.10) simplifies to:

$$\boldsymbol{\phi_{diffusion} = 4\pi r_i D_s S_0} \tag{3.11}$$

If Eq. (3.11) is divided by surface area of the particle, this matches the simple model often used to represent external diffusion with the assumptions of a boundary layer thickness equal to radius and $C_p = 0$ [86,227].

Alternatively, when $Pe >> 1$, the effect of flow must be accounted for. Eq. (3.12) approximates flux under convection (for $Re_p < 10$).

$$\boldsymbol{\phi_{convection}} \sim \boldsymbol{Pe} \times \boldsymbol{\phi_{diffusion}} = \boldsymbol{4\pi {r_i}^2 u_i (C_\infty - C_p)} \tag{3.12}$$

Again, C_p can be approximated as zero and C_∞ is the initial concentration of the substrate, S_0. Eq. (3.12) becomes:

$$\boldsymbol{\phi_{convection}} = \boldsymbol{4\pi {r_i}^2 u_i S_0} \tag{3.13}$$

Both relationships for substrate flux (Eq. (3.11) and Eq. (3.13)) were multiplied by a factor of 1000 L/m^3 to convert units to mol/s. At the transition between diffusive and convective regimes, these process are likely to be additive rather than a discrete switch between the two regimes, as described by:

$$\boldsymbol{\phi_{diffusion}} + \boldsymbol{\phi_{convection}} = \boldsymbol{4\pi r_i D_s S_0} + \boldsymbol{4\pi {r_i}^2 u_i S_0} = \boldsymbol{4\pi r_i S_0 (D_s + r_i u_i)} \tag{3.14}$$

Dividing Eq. (3.3) and Eq. (3.14), the relative ratio of kinetic controlled product formation to mass transport, or the Damköhler number for the system, Da, is described by:

$$\boldsymbol{Da} = \frac{\boldsymbol{V}}{\boldsymbol{\phi_{diffusion}} + \boldsymbol{\phi_{convection}}} = \frac{\boldsymbol{4\pi r_i^2 S_0 \left(\frac{V_{max\_SA}}{K_m}\right)}}{\boldsymbol{4\pi r_i S_0 (D_s + r_i u_i)}} = \frac{\boldsymbol{r_i V_{max\_SA}}}{\boldsymbol{K_m (D_s + r_i u_i)}} \tag{3.15}$$

When $Da << 1$, the system is under kinetic control and the rate of product formation is described by Eq. (3.3). When $Da > 1$, the system is expected to be under mass transport control and Eq. (3.14) describes the flux of substrate to the surface (and correspondingly, the rate of product formation).

To determine the product formation by individual particles during one inversion, either rate of product formation (kinetic or mass transport controlled) can be multiplied by the total time of inversion ($t_{inver.}$, e.g. 60 s). This approach assumes that particles continue reacting at the same rate after they have reached the base of the device. This assumption will be discussed further in Section 3.3.3.4.

In order to predict product formation by a known mass of particles of a certain distribution (e.g. 5 mg), the predicted amount of product formed per particle of diameter d_i can be multiplied by the number of particles at each d_i. (Particle number distributions were collected by imaging on a morphology microscope, see Figure 2.11 and Figure 2.39). A summation of the resulting product formed by each particle size class across the distribution of sizes gives the expected reaction rate over one inversion for the specified mass and size distribution of silica. These predictions can be compared to experimental results. A summary of the variables used in this model is provided in Table 3.3.

Table 3.3 Variables used as model inputs.

Constant	Variable	Value	Units
Device height	h	18.32	mm
Substrate diffusivity	D_s	1.10×10^{-5}	cm^2/s
Initial substrate concentration	S_0	0-10	µM
Density, fluid	ρ_f	1000	kg/m^3
Density, particle	ρ_s	1860-2180	kg/m^3
Dynamic viscosity	η_f	0.001	Pa s
Gravitational acceleration	g	9.81	m/s^2
Particle volume fraction	θ_p	0.2-0.4	
Particle diameter	d_i	1-1000	µm
Michaelis constant	K_m	1.65×10^{-2}	M
Total protein immobilised	TPI	See Table 3.1	µg total protein/mg silica
Silica surface area	SA	See Table 3.1	m^2/kg silica
Enzyme surface coverage	ESC	See Table 3.1	mg total protein/m^2 silica surface area
Maximum reaction rate	V_{max}	0.3	U/mg or µmol substrate/min/mg enzyme (for dried R5$_2$-mCh-mSOx-R5-6H)
Max. reaction rate per unit surface area	V_{max_SA}	See Eq. (3.4)	mol substrate/s/m^2 silica surface area
Time of between inversions	$t_{inver.}$	60	s

3.2.5 Experimental comparison to model predictions

Falling particle sensors were constructed as described above in Section 3.2.2 and rate of product formation in the device experimentally determined by the fluorescent signal from 2-enzyme coupled assay for sarcosine (as presented in Chapter 2). Both silica extracted from SC sand and a range of sizes of commercial silica gel 60 were functionalised with R5$_2$-mCh-mSOx-R5-6H from crude lysate following the protocol described in Chapter 2. The silica was suspended in buffer (4.17 mg/mL silica, protein loading per 1 mg silica specified in Table 3.1) and loaded into the device with dye AR (4.17 µM), WT HRP (0.016 mg/mL) and sarcosine (0-10 µM). After a number of inversions and subsequent particle settling, the device was laid on fluorescence flatbed scanner (FFEI) with 505 nm

LED for excitation and a CCD RGB linear sensor for detection (Figure 3.5) and fluorescence intensity was recorded. The spectra for the LED and CCD sensor, as specified in the equipment manual, can be found in Appendix D. Final concentration of sarcosine and number of inversions are specified in the text for each assay.

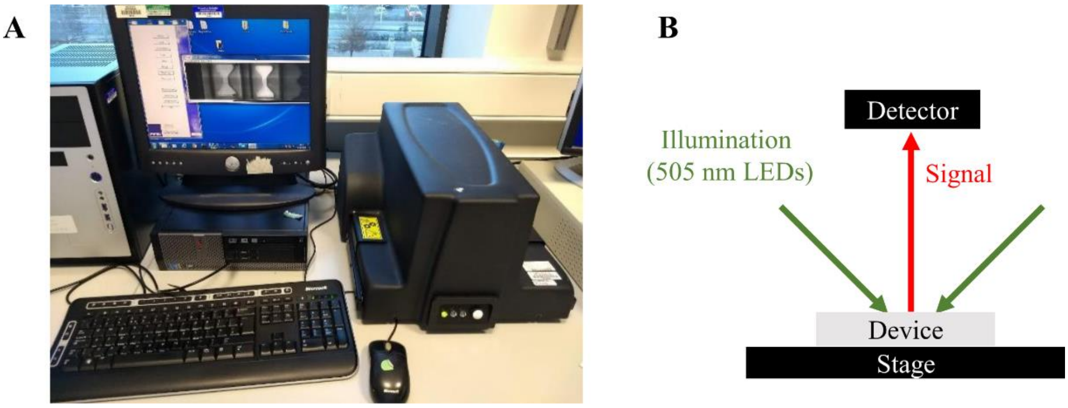

Figure 3.5 (A) Custom, flatbed fluorescence scanner, with (B) a diagram of signal detection elements housed within the scanner.

The fluorescence images were analysed for grey scale intensity of the red channel in the chamber area using ImageJ software. Selection of one particular colour component for quantification has been known to give better sensitivity [249] and the red channel has the most overlap with the emission spectra of the AR dye (as reported by the manufacturer). Fluorescent signal was determined by measuring the average intensity in the device. Figure 2.4 shows the calibration curves of fluorescence intensity for known concentrations of H_2O_2 in the presence of WT HRP following the protocol outlined above (200 µL total volume), as measured in both the falling particle chamber using the fluorescence flatbed scanner and in well plates using the fluorimeter (ex. 530 nm / em. 580 nm, slits 5 nm, PMT 800V). A similar LOD was observed with either measurement technique.

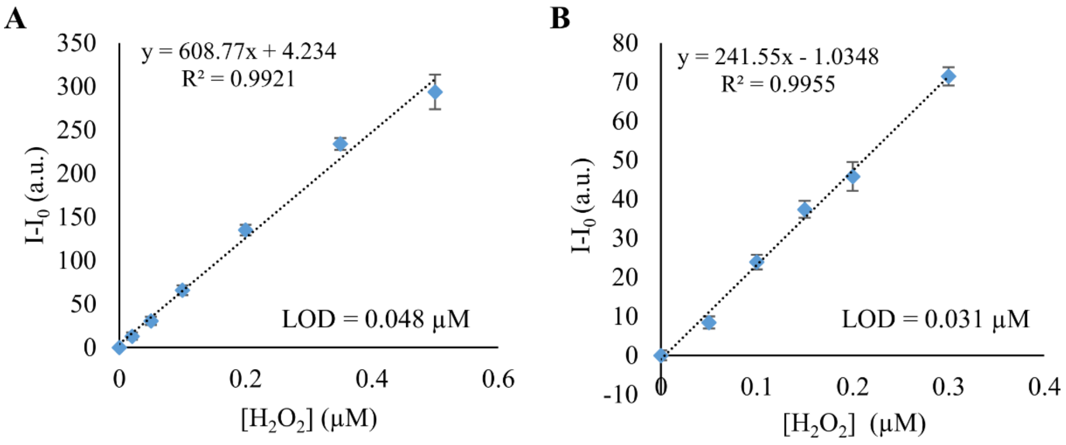

Figure 3.6 Standard curve for AR assay, showing linear relationship of fluorescence intensity (blank subtracted) with H_2O_2 concentrations as indicated, as measured by (A) fluorimeter and (B) fluorescence scanner.

3.3 Results and Discussion

3.3.1 Design of a falling particle biosensor

Ultimately, the falling particle devices are intended for use as low-cost diagnostics so they should be able to be constructed with low-cost materials and using simple manufacturing equipment. Devices were cut from PMMA using a benchtop laser cutter, potentially allowing for a wide range of chamber shapes. To explore the feasibility of a design utilizing particle sedimentation, three chamber designs were explored (Figure 3.7A-C). In addition to the parallel sided design presented in Figure 3.1, two designs with central constrictions or ‘waists’ were explored, with increasing degree of constriction; baffled tubes with similar constrictions have been shown to exhibit efficient mixing in oscillatory flow reactors [250] and mixing may be advantageous for increasing signal production as it can reduce mass transport limitations [227,243]. The overall aspect ratio was preserved across the designs in order to provide consistency in the settling time, as determined by the height, and in the depth of the settled particle bed prior to inversion, as determined by the width at the top/base and silica volume. However, a better understanding of the reaction dynamics of the system may prompt further optimisation of the chamber shape in the future.

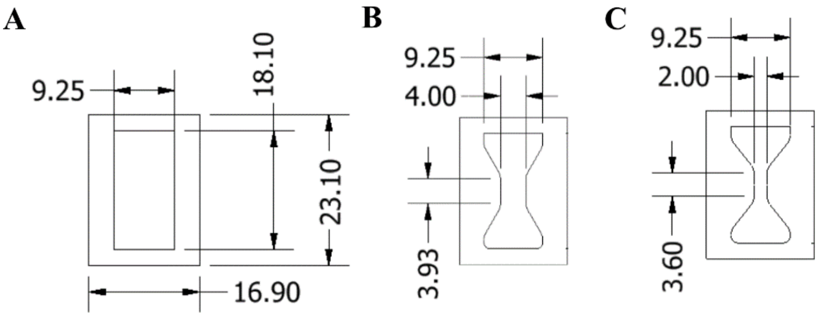

Figure 3.7 Dimensions of the chip designs for the (A) parallel sided, (B) standard waist and (C) narrow waist design. All dimensions are in mm. Actual physical dimensions of the chamber varied slightly as laser cutting results in some melting.

After the chambers were cut from PMMA, the seals were adhered by hand to each side but considering the intended application of the devices, it was envisioned that they could eventually be applied by a desktop laminator for consistency and increased throughput while keeping simplicity of manufacture. PMMA with a thickness of 2 mm resulted in a robust device that still could allow for sealing with a desktop laminator in the future, while 1 mm thick PMMA showed increased susceptibility to accidental flexing, and in some cases fracture, which compromised the seal and resulted in leakage. 200-300 µL was selected as the initial target volume range for the devices such that they would be large enough to handle without requiring significant sample volumes. Although urine, the target clinical sample for a prostate cancer test [183], is typically collected in greater volume than a finger prick of blood used for some POCTs, larger sample volumes likely require larger reagent volumes which would increase total assay cost.

For initial studies of particle settling behaviour, bio-functionalised silica extracted from sand was suspended in buffer within each sealed chamber. To initiate the movement of the particles, the device was inverted and the particles are allowed to sediment/settle for 60 seconds (the majority of the particle mass was observed to settle within this time). The settling patterns of the bio-functionalised silica extracted from sand suspended in the PMMA / adhesive tape chambers can be seen visually in Figure 3.8 for the (A) parallel sided (B) standard waist, and (C) narrow waist designs, flipped about a central horizontal axis. For all three designs, immediately following inversion of the device, plumes of closely grouped particles are observed. As these plumes contact the bottom wall of the chamber they create additional fluid displacement in the system. The larger particles are too heavy to become entrained in this fluid displacement and continue their fall undisturbed but some smaller particles are redistributed in the fluid as a result. After the fall of the largest particles within the first 6-7 s, the smaller particles continue to fall in a more laminar fashion. As discussed above, the relative velocity of the particles with respect to their surrounding fluid may influence the rate of product formation by the immobilised enzyme as it can affect the diffusion of the substrate to the particle surface. Particle image velocimetry (PIV) analysis was used to estimate the falling speeds of the particles and thus determine the degree of turbulence within the system and the possible effect on reaction rate.

PIV is a common technique to visualise flows within a fluid and measure velocities of those flows. Typically, the fluid is seeded with small particles, selected such that they are of a similar density to the fluid. These neutrally buoyant particles are assumed to follow the fluid dynamics of the system, becoming entrained in any fluid movement; hence, their motion can be used to calculate the speed and direction of the flow. In contrast, the particles of extracted silica in the system described here are generally of a larger size and of a higher density than the fluid; thus, they cannot be expected to follow fluid patterns. Rather, as previously mentioned, their movement causes additional fluid displacement in the system. However, conducting PIV on the videos of particle settling in the devices can provide estimates of particle velocity during their fall after inversion, making PIV analysis a useful tool for an initial understanding of the particle behaviour in the falling particle biosensor.

Factors affecting the settling velocity of sediment particles through fluids are well known (e.g. particle size, shape and density; fluid density, fluid viscosity). Theoretically, particle settling velocity is determined by equating the effective weight of a particle to the viscous resistance of the fluid or drag force, as first presented by Stokes for a sphere in viscous fluids with very small Reynolds number [232]. The drag coefficient is an intricate function of the flow conditions, as described by the Reynolds number, as well as the particle shape [230,235]. In the system described here, the particles are polydisperse, non-spherical and suspended in a fluid of low viscosity, so it is likely that a relationship beyond that of Stokes’ Law will be needed to describe their settling velocity.

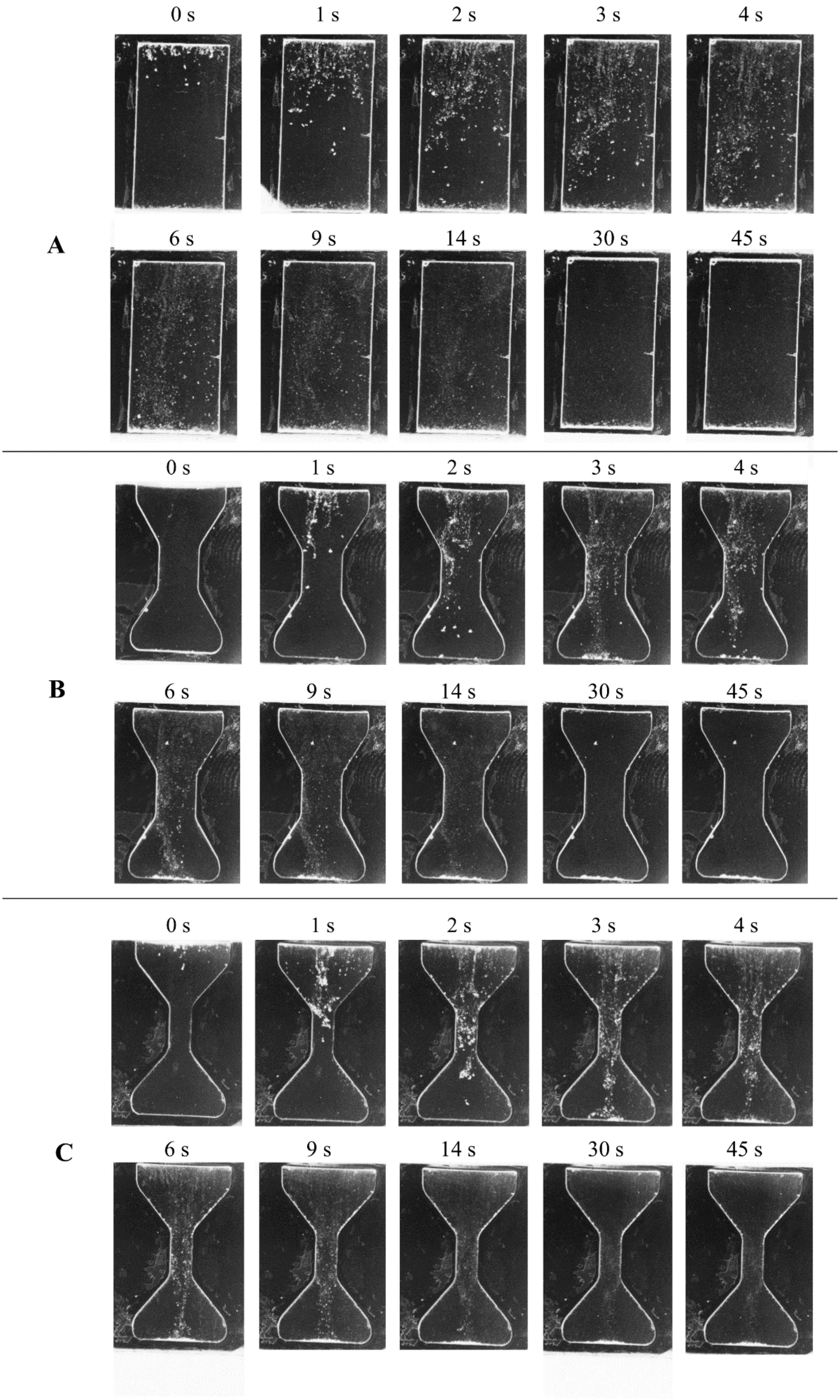

Figure 3.8 Colour-inverted stills of particle sedimentation for selected time points after flipping for the (A) parallel sided, (B) standard waist and (C) narrow waist design.

Those particles settling in the initial plumes with effective radii in the range of 100-250 µm fall with a maximum terminal velocity estimated from the PIV data of 1.3-10.2 × 10^{-3} m/s (Figure 3.9 and Table 3.4). At these velocities and particle sizes, the particle Reynolds number (Re_p, as calculated by Eq. (3.8)) is not in the region in which Stokes' Law is in good agreement with experimental findings ($Re_p < 0.1$) but in the transitional regime ($1 < Re_p < 100$). For all three chamber designs, the experimental velocities, recorded near the base of the chamber, are lower than the terminal velocity expected for a smooth, spherical particles of the same diameters (calculated according to the numerical equation developed by Guo that combines the three classical equations for settling velocity under laminar flow (Stokes' Law), intermediate flow and turbulent flow (Newton's Law) [251]). This is anticipated considering the irregular shape of silica extracted from sand and resulting frictional forces. Zhiyao *et al.* [247] proposed a formula for the terminal velocity of natural sediment that adjusts for the effect of particle shape, however, this does not fully account for the observed decrease in terminal velocity for the larger particles.

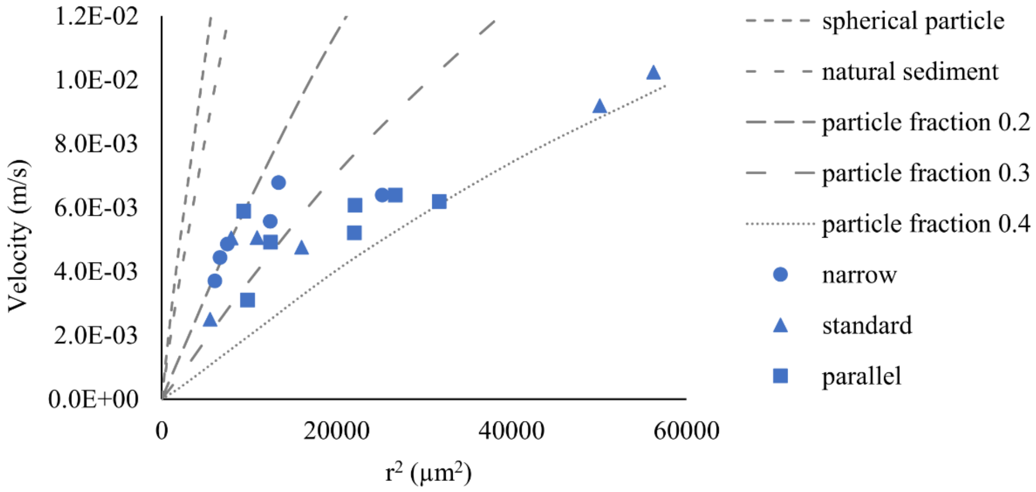

Figure 3.9 Plot of terminal velocity with respect to particle radius showing both (blue points) experimentally observed velocities and (grey curves) theoretical terminal velocities. Predicted velocity for the spherical particle is plotted using the relationship defined by [251] **and that of natural sediment by** [247]**.**

To account for this discrepancy, the action of the fluid displacement is considered during sedimentation. The equations developed by both Guo and Zhiyao *et al.* disregard interactions with other particles or the fluid; however, despite an overall volume fraction of particles in the device < 0.003, the local volume fraction of particles in the plumes is much higher. Immediately after inversion, hindered settling, from the upward motion of the displaced fluid interacting with the particle(s) [252], can thus result in lower velocities. As can be seen from Figure 3.9 and Table 3.4, the experimental data of the particles falling in the initial plumes of r > 50 µm are comparable with an apparent particle fraction of 0.2 - 0.4, as calculated by relationship proposed by Richardson and Zaki [252]. Smaller, more dispersed particles falling after the initial plumes, on the other hand, show less hindered settling and behave more like smaller volume fraction natural sediment. In Table 3.4, light green boxes indicate when the predicted velocities closely match the observed velocities in the first row (in grey). The maximum velocity of the particles (but not particle position along the x-axis) as they cross the indicated location near the base of the device is nearly independent of the design, highlighted in Figure 3.10.

Table 3.4 Calculated and observed parameters for particles.

	particle radius (µm)	**1**	**10**	**50**	**100**	**150**	**200**
Velocities (m/s)	OBSERVED	--	0.20×10^{-3}	1.13×10^{-3}	5.31×10^{-3}	7.02×10^{-3}	1.02×10^{-2}
	spherical particle	2.57×10^{-6}	2.50×10^{-4}	5.79×10^{-3}	1.96×10^{-2}	3.69×10^{-2}	5.49×10^{-6}
	natural sediment	1.91×10^{-6}	1.90×10^{-4}	4.41×10^{-3}	1.49×10^{-2}	2.78×10^{-2}	4.06×10^{-2}
	particle fraction 0.2	6.86×10^{-7}	6.82×10^{-5}	1.60×10^{-3}	6.20×10^{-3}	1.26×10^{-2}	1.90×10^{-2}
	particle fraction 0.3	3.71×10^{-7}	3.69×10^{-5}	8.82×10^{-4}	3.70×10^{-3}	7.81×10^{-3}	1.23×10^{-2}
	particle fraction 0.4	1.83×10^{-7}	1.82×10^{-5}	4.45×10^{-4}	1.99×10^{-3}	4.51×10^{-3}	7.42×10^{-3}

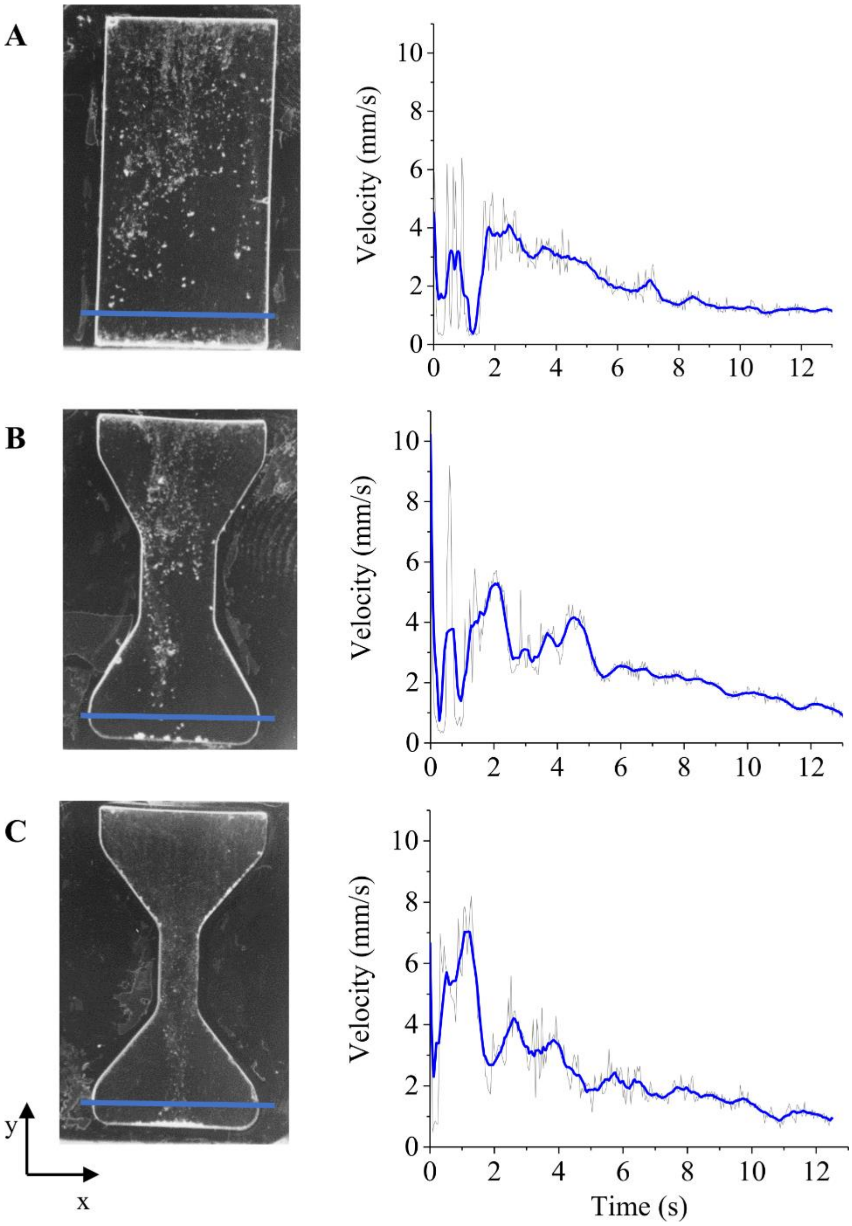

Figure 3.10 Characterization of particle sedimentation for three basic chamber designs of (A) parallel sided, (B) standard waist and (C) narrow waist. Plot of the maximum velocity of the particles over time as they cross the indicated position near the base of each design (blue line), where t = 0 is the time at which the first particle crosses. Bold blue lines show 10 pts moving average while grey shows raw data.

Although terminal velocity of the particles was shown to be nearly independent of chamber design (Figure 3.10), the influence of the funnelling waist on particle trajectory was evident. Overlaying the frames of the video into a single image shows the combined trajectories of the particles through the device, as shown in Figure 3.11. Image thresholding analysis of these trajectories predicts that 80-90 % of the chamber volume is ‘sampled’ on each inversion by particles passing through the chamber. However, this analysis does not consider the fluid movement within the system as a result of the fluid displacement caused by the falling particles, which would likely result in the redistribution of the fluid in the region that appears ‘un-sampled’ back into the path of the particles falling behind the initial plumes. Without additional buoyant tracer particles in the fluid, it is difficult to precisely quantify the impact of this fluid displacement on the overall ‘sampling’ of the volume by the particles. In addition, although the waisted designs have some areas where the passage of particles was limited, especially when compared to the parallel sided design, these trajectories are only for one inversion and the device can be inverted multiple times. The multiple inversion approach also allows for a longer dispersion time of the particles with the sample while keeping device dimensions small and amenable to a POCT. Dispersion of the particles throughout the fluid is often beneficial with respect to the reaction rate for large scale bioreactors [227] and may also be true in this small scale design.

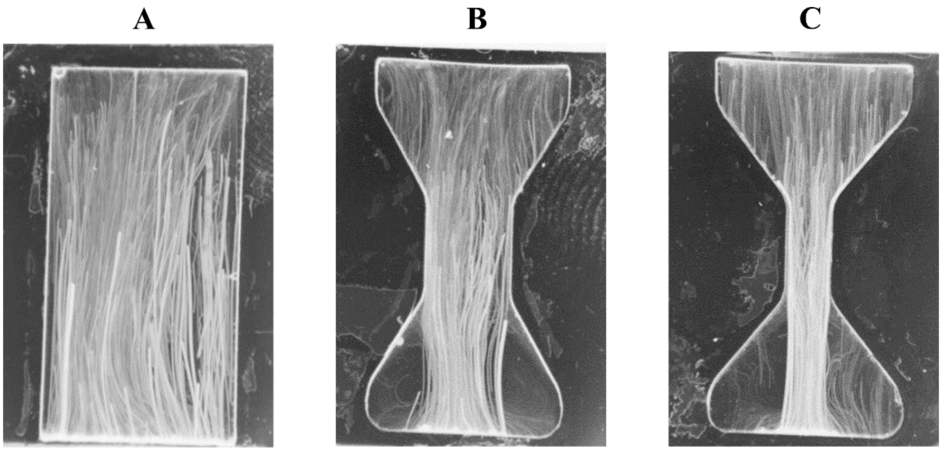

Figure 3.11 Image overlays showing particle trajectories over time for the (A) parallel sided, (B) standard waist and (C) narrow waist design. Images here are compilations of video frames from 2-14 s after inversion.

The waisted nature of the design also had an impact on the final resting position at the end of sedimentation. For all patterns observed above, the device was “flipped” over central horizontal axis; however, the device could easily also be inverted by rotation in plane (“tilt”). The initial movement of the chamber also produces fluid movement in the system, affecting the sedimentation patterns of the particles. Figure 3.12 shows that the positioning of the particles after settling depends on this axis of inversion of the device and on the dimensions of the waist of the chamber. It is seen that by narrowing the waist of the chamber, the bio-functionalised particles are guided to a resting position beneath the central channel, independent of inversion technique. In contrast, the parallel sided and standard waist chambers achieve little focusing of the particle settling. By defining the final position of the particles in a central area irrespective of inversion axis, the narrow waist shape creates a reproducible inversion pattern with the particles always starting from the same location for each inversion. This is not seen in the other designs. Since an enzyme linked assay is a dynamic reaction process, this reproducible sedimentation helps to ensure that a reproducible process occurs and thus the narrow waist chamber design lends itself to a biosensor platform.

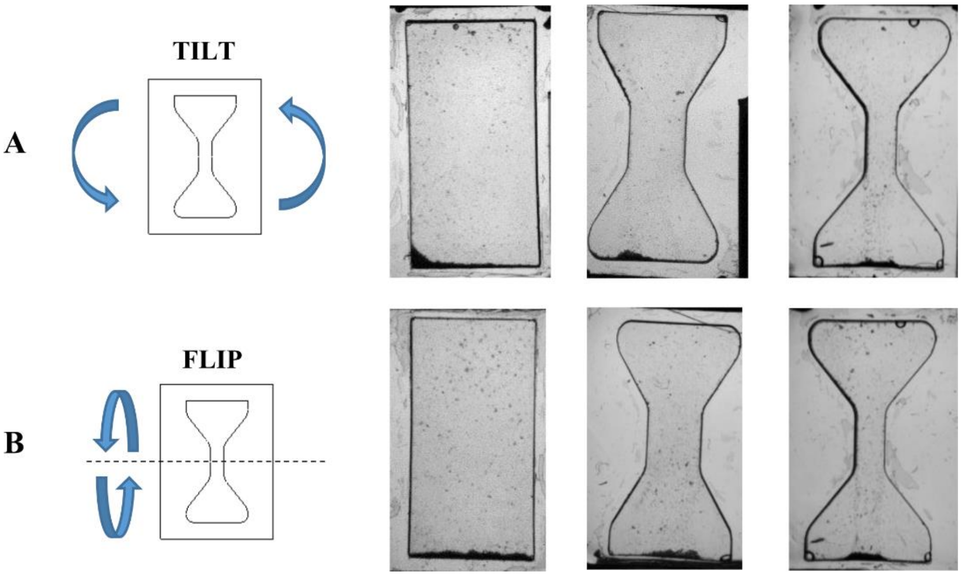

Figure 3.12 Effect of shape and inversion technique on particle sedimentation patterns, showing (A) rotation in plane ("tilt") or (B) "flip" over central axis.

3.3.2 Effect of particle size on falling behaviour

Although additional processing steps to size-select the silica extracted from local sand would increase time and cost, a significant increase in signal generated in a biosensor design could justify the additional steps. For example, assuming constant enzyme coverage per unit surface area and a system under kinetic control, smaller particles would be expected to produce more signal per unit mass. In contrast, a system under mass transport control might favour larger, faster falling particles which increase the turbulence in the system and reduce diffusion restrictions. To investigate the potential effects of size on signal output, an understanding of the effect of size of on settling behaviour in the device is first required. Four discrete size classes of commercial silica gel 60 of were added separately to narrow waisted devices and their behaviour observed: 6-35 µm, 40-63 µm, 63-210 µm and 200-500 µm in diameter. These silica size classes were used previously in Chapter 2 to investigate the effect of particle size on immobilisation efficiency and their particle distributions can be seen in Figure 2.39. Silica nanoparticles produced in house (average diameter of ~250 nm, [239]) were also tested.

For all size classes of commercial silica, particle positioning ability of the narrow waisted design was maintained and they all initially exhibited similar plume falling behaviour to the heterogeneous silica extract (Figure 3.13A), followed by distributed settling of the remaining particles. Size has a clear impact on the speed of settling; as the median diameter of the particle size distribution decreased, it took longer for the first particle or cluster of particles to reach the bottom of the device and the velocity was reduced (Figure 3.14 and Table 3.5). This is expected given the relationships describing particle settling velocity include a component for particle size.

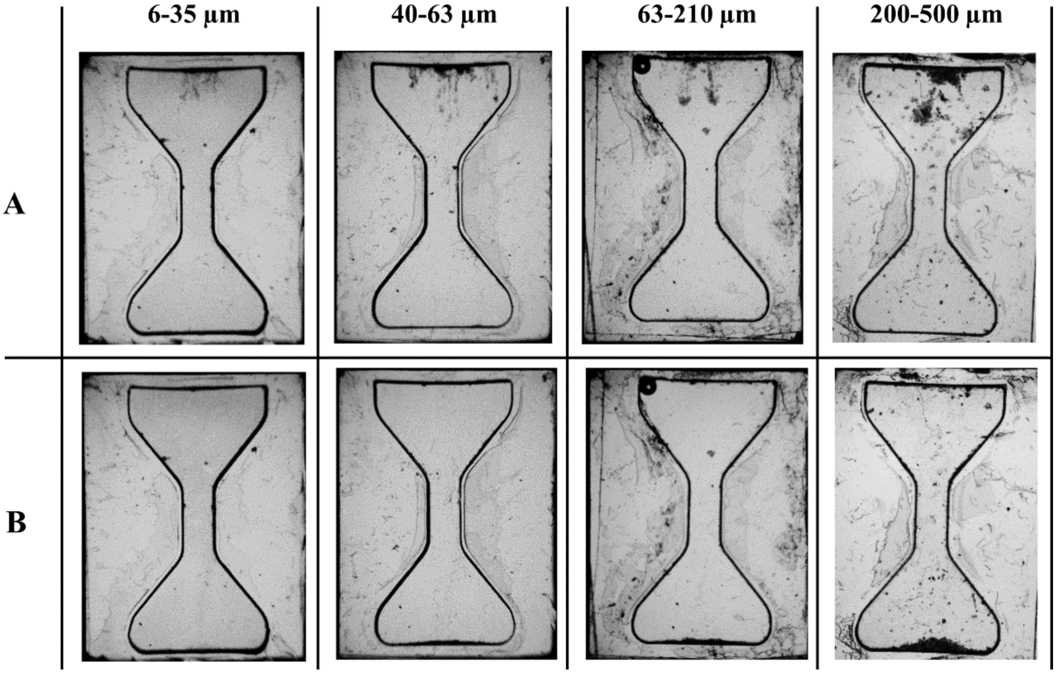

Figure 3.13 Particle sedimentation patterns for various silica gel 60 particle size distributions (6-35, 40-63, 63-210 and 200-500 µm) in the narrow waisted chamber showing images of (A) initial plume behaviour and (B) centralised position of the particles (at 15 s). Images in (A) are selected frames at 2 s, 0.5 s, 0.25 s and 0.5 s, respectively.

For the smaller size distributions (6-35 µm, 40-63 µm and 63-210 µm), settling times for the initial plumes were faster than those predicted by the model by Zhiyao *et al.* for terminal velocity for single natural sediment particles (as calculated for the median diameter of each distribution, Table 3.5). In these cases, the smaller particles were observed to travel in clouds for which an increase in velocity is expected [235]. For the largest silica distribution tested (200-500 µm), the observed initial settling time was slower than the model would predict. This hindered settling behaviour is similar to that observed for the largest particles in the extracted silica. Again, the hindrance of the larger particles is likely a result of the increased local fraction for those first particles and resulting fluid displacement that results in a decreased settling velocity.

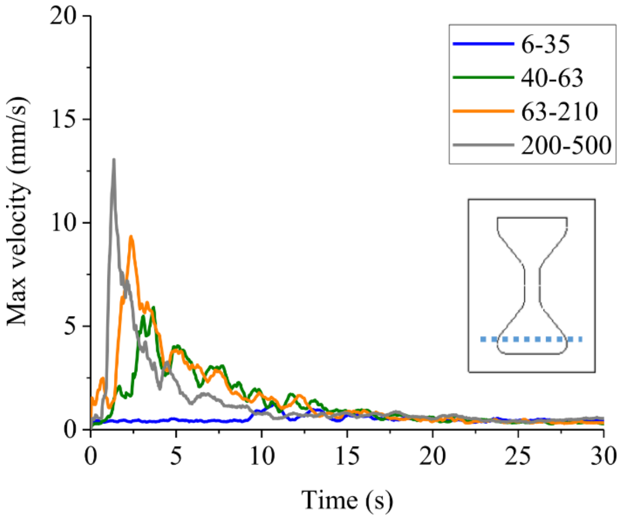

Figure 3.14 Characterization of particle sedimentation for various silica gel 60 particle size distributions (6-35, 40-63, 63-210 and 200-500 µm) in the narrow waisted chamber, showing plots of the maximum velocity of the particles over time as they cross the indicated location the base (blue dashed line) of the chamber. Curves shown are smoothed with 10 pts adjacent averaging.

Table 3.5 Predicted and observed settling times for silica gel 60 size distributions. Green box indicates a faster time than predicted, red indicates a slower time. Median diameter values are drawn from morphology imaging results.

Particle size class (µm)	**6-35**	**40-63**	**63-210**	**200-500**
Median diameter observed (µm)	25	57	73	339
Expected settling time for a single natural particle (Eq. (3.6) from [247]**)**	62	12.3	7.5	0.54
Time of first plume reaching base (s)	🟩 10.88	🟩 2.68	🟩 1.64	🟥 1.36

In addition to changing the settling time of the initial plume, the choice of size distribution also alters the overall time period required for the particles to settle out of solution. Given dispersion is predicted to be beneficial to signal development, a longer settling time is likely desirable. In the case of the commercial silica 60 of 200-500 µm in diameter, the majority of these large particles have fallen in less than 10 s. Although there are some smaller particles in this distribution (likely fragments broken off the larger particles) that continue to fall for the remainder of the 60 s observed, these are few in comparison with the particles that remain falling for an equivalent mass of silica extracted from sand (Figure 3.8). To achieve a level of continued dispersion with the larger commercial particles would require almost constant flipping, making this distribution an impractical choice for the current design of the falling particle biosensor.

With each decrease in particle size class, the length of time for the majority of particles to settle increased (e.g. with the 63-210 µm distribution most of the particles have settled after 25 s). To increase time in suspension, the use of silica nanoparticles (median diameter of 245 ± 49.0 nm) in the falling particle device was explored. The silica nanoparticles were smaller than the resolution of the high-speed imaging set-up, so no PIV analysis was performed on the videos of particle fall. It was observed (Figure 3.15) that although the nanoparticles are suspended in a single fluid, after inversion the sediment laden portion and the remaining portion form pseudo-immiscible fluids, passing each other in separate laminar fronts in the central channel. Here, the upward fluid movement in response to the particle stream is clear. The plumes of the two portions of the fluid follow the evolution of single-mode Raleigh-Taylor instabilities at the interface of a light and heavy fluid in the presence of gravitational acceleration, including the development of mushroom-like shapes at later times caused by secondary Kelvin-Helmholtz instabilities [253]. Here, the sediment laden fluid has an average density higher than that of the surrounding ambient fluid and hence, the driving buoyancy force behind the plumes is the gravity acting on the higher density of the particles temporarily suspended within a fluid. The interface of the two fluid portions is defined by the jump in value of particle concentration. The position of the sediment laden fluid front within the channel is determined by the initial fall of a few clumps of aggregated particles. (It is well known that silica nanoparticles have a tendency to form aggregates [254,255]). This laminar behaviour and lack of mixing of the two portions of the sample would limit the potential of the immobilised enzymes to sample all of the fluid within the chamber. In addition, the smallest particles in this nanoparticle distribution are almost neutrally buoyant and thus, do not settle out in a reasonable amount of time (< 10 min) for a POCT, and could lead to light scattering challenges for detection of the fluorescent product in solution. The settling ability of the particles is also important for the collection of the R5-mCh-Enz coated particles during the previous step of purification from crude lysate, as discussed in Chapter 2. Combined, these characteristics of the silica nanoparticles settling behaviour make them a suboptimal choice for the aims of this work.

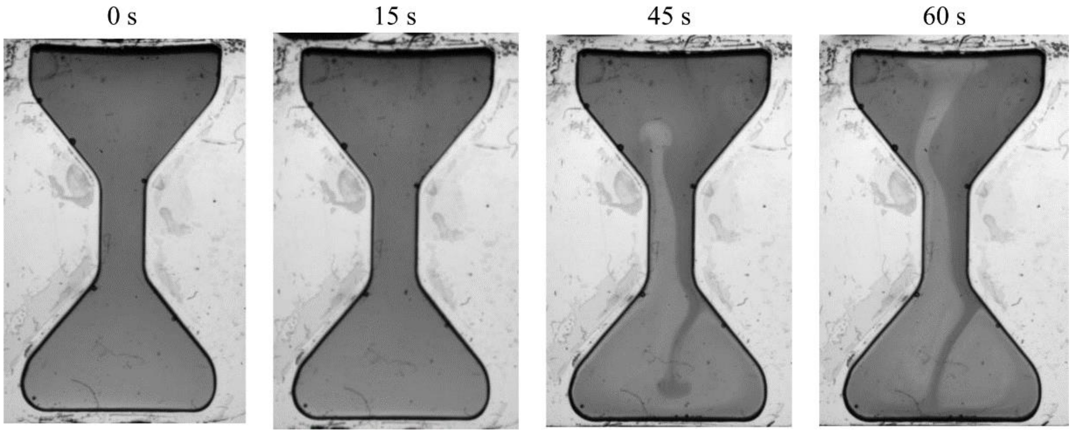

Figure 3.15 Video frames from selected time points for a suspension of silica nanoparticles in the narrow waisted chamber design.

Interestingly, the addition of a few large silica particles (of 200-500 µm in diameter) in with the silica nanoparticles changes these sedimentation patterns (Figure 3.16). The device in Figure 3.16A was loaded only with the silica nanoparticles. Despite a small plume of clustered particles resulting from a higher number of nanoparticle aggregates in this suspension, the pseudo-immiscible fluid behaviour was still observed (as shown in the final image). However, this behaviour was not observed when several larger particles were subsequently added to the same device, indicating a greater degree of mixing in the device in the presence of these larger particles (see the final frame at 48 s in Figure 3.16B). These larger particles also entrain the smaller nanoparticles in their wake, driving faster settling. This effect is evident in the plume of aggregated nanoparticles reaching the base of the device more quickly in the presence of the larger particles (14.8 s instead of 23.8 s) and the correspondingly increased velocity of the nanoparticle plume as it crosses a location near the base of the device (Figure 3.17).

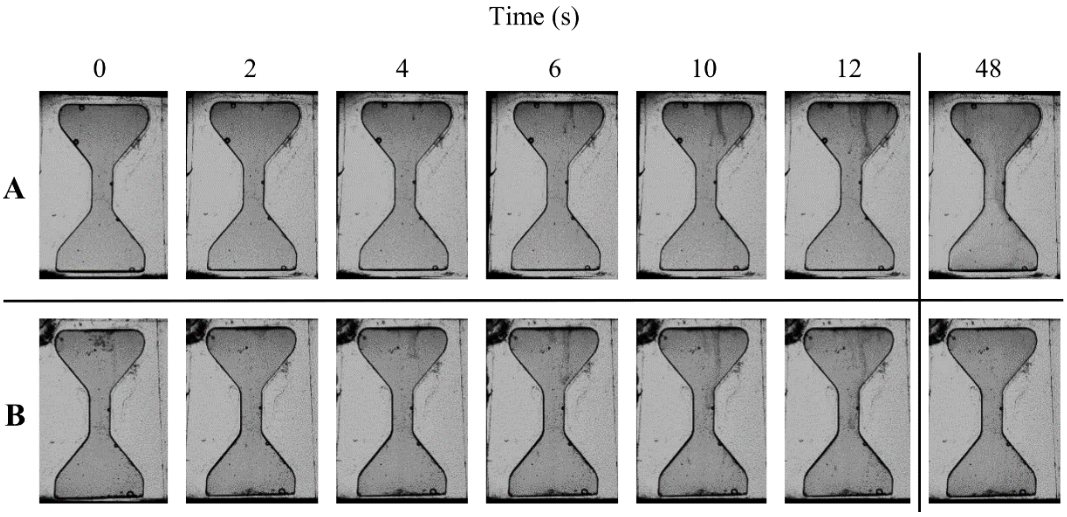

Figure 3.16 Video frames from selected time points for a suspension of silica nanoparticles in the narrow waisted chamber design, (A) without and (B) with a few larger particles (200-500 µm).

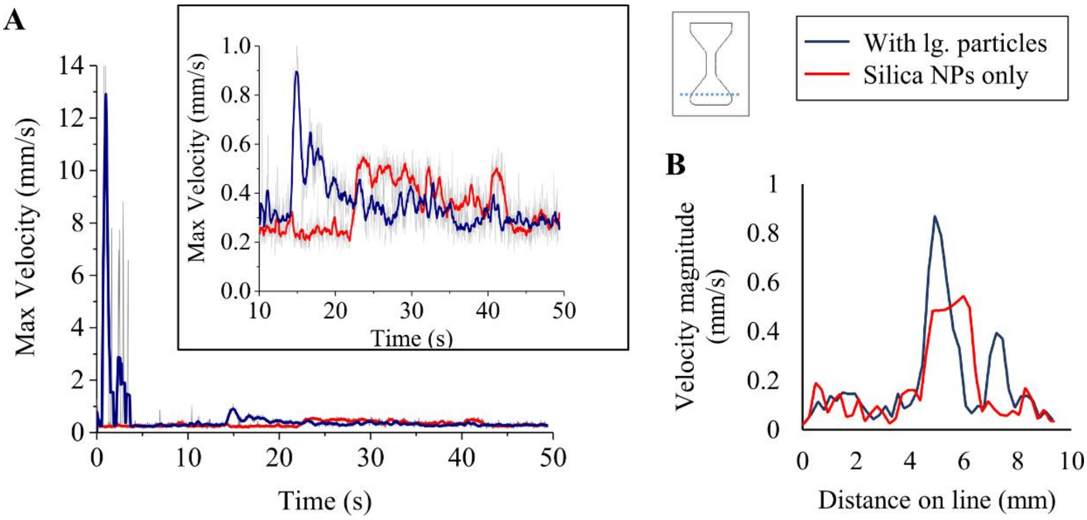

Figure 3.17 Characterization of particle sedimentation patterns for a suspension of silica nanoparticles in the narrow waisted chamber design, with (dark blue) and without (red) a few larger particles added (200-500 µm), showing (A) plot of the maximum velocity of the particles over time as they cross the indicated position near the base of the device (dashed blue line) and (B) the velocity profile across that line when the plume of aggregated particles first crosses (14.8 s and 23.8 s with and without large particles, respectively). Bold lines in (A) show 10 pts moving average while grey shows raw data.

The entrainment of the smaller particles by larger ones is also visible in the settling behaviour of both the silica extracted from sand and the commercial silica gel < 63 µm in diameter, both of which have broad heterogeneous distributions of particle size (see Figure 2.11 for size distributions). Figure 3.18 shows the maximum velocity plots over time for these particles in the narrow waisted device. The commercial silica gel < 63 µm lacks the largest particles observed in the extracted silica. Correspondingly, the maximum velocity observed during the initial period of particle fall (< 10 s) decreased for the commercial silica gel and the time at which the first particle or cluster of particles reached the bottom increased (from 1.1 s to 2.2 s). The remaining particles fall in a dispersed fashion for both silica distributions.

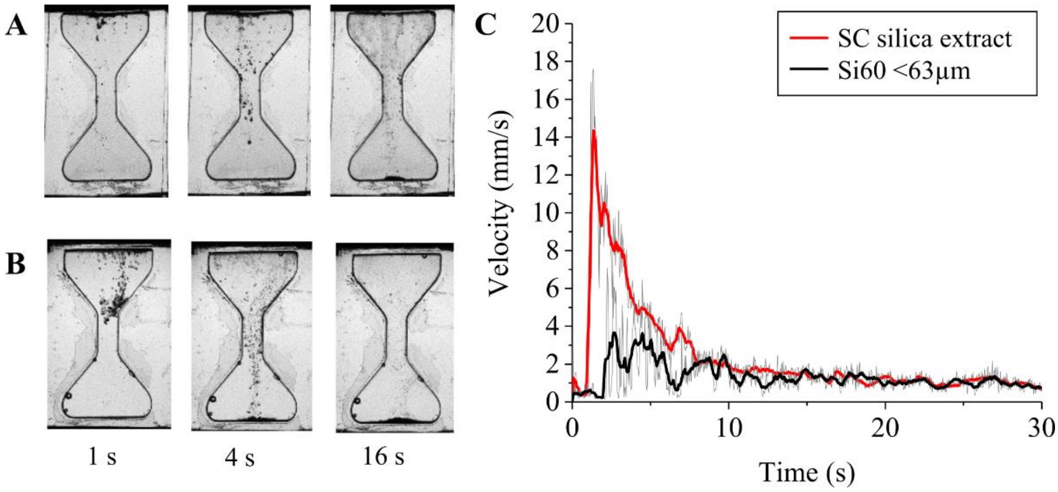

Figure 3.18 Characterization of particle sedimentation for (A) silica gel 60 <63 µm and (B) extracted silica in the narrow waisted chamber, showing images of selected time points during particle sedimentation. (C) Plot of the maximum velocity of the particles over time as they cross near the base of the chamber for (red) silica gel 60 <63 µm and (black) extracted silica. Bold lines show 10 pts moving average while grey shows raw data.

A particle distribution that settles in a reasonable time, enabling purification in the earlier stages of the enzyme production process and removing scattering effects from the final signal processing would be advantageous (unlike the nanoparticles explored above). Moreover, given the particles are intended to be collected by sedimentation in the purification stage, the smallest particles in a mixed distribution that fail to settle would be lost at this stage. On the other hand, very large particles (d > 200 µm) do not remain in suspension for long, and a distribution consisting of only these would require constant flipping to achieve dispersion. Hence, a particle distribution largely within these boundaries is desirable. In addition, the combination of large particles with smaller particles enables high surface area per unit weight from the smaller particles in conjunction with faster settling rates, driven by the larger particles. The increased mixing resulting from these large particles is potentially also an advantage for signal development. While these characteristics potentially enable a more appropriate device from a use perspective, the effect of particle size distribution on rate of product formation by the immobilised enzyme (and thus signal generation) is a critical parameter that must be evaluated before a selection of carrier particle can be made. Understanding this will involve understanding the interplay between kinetic or mass transport rates in a falling particle system.

3.3.3 Modelling product formation by particle-bound enzymes

3.3.3.1 Determining reaction control: kinetic versus mass transport

The reaction efficiency of immobilised enzymes is either controlled primarily by the catalytic activity of the immobilised enzyme (as determined by inherent characteristics of the enzyme and loading capacity of the substrate) or by the mass transport of the substrate to the surface of the particle (Figure 3.19). For a falling particle, the mass transport is affected by the flow conditions around the particle, which is in turn determined by the settling behaviour of the particle. The ratio of the product formation rates for each regime, the Damköhler number, Da, can be used to determine the ratio of catalytic control to mass transport for each falling particle (Eq. (3.15)). When Da << 1, the system is under kinetic control and well-known Michaelis-Menten reaction kinetics for enzyme turnover can be used to calculate rate of product formation. In contrast, when Da >> 1, the formation of product is limited by the rate of mass transport of the substrate to the surface, with all substrate expected to be converted to product by the enzyme immediately upon arrival. Calculating Da provides a first look at the driving forces for product formation by the immobilised enzyme on the falling particles in this system.

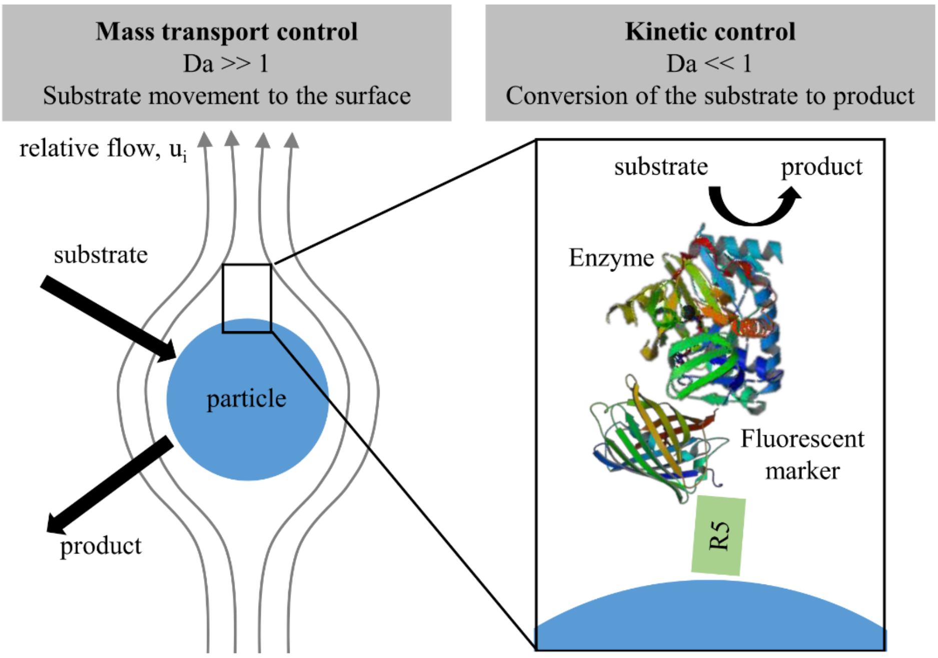

Figure 3.19 Schematic showing the two regimes of reaction control – mass transport and kinetic. (mCh structure 2HQ5 and mSOx 3QSE from RCSB Protein Data Bank).

In chemical engineering, the first Damköhler number is typically reaction rate with respect to convective mass transport rate and the second Damköhler number is with respect to diffusive mass transport rate [244]. In Da described by Eq. (3.15), the convective and diffusive rates are combined to provide a better estimate of the mass transport rate in the transition region where these processes are likely additive (Pe ≈ 1). When either process is dominating, the Da described here becomes equal to the relevant conventional Damköhler number (Figure 3.20).

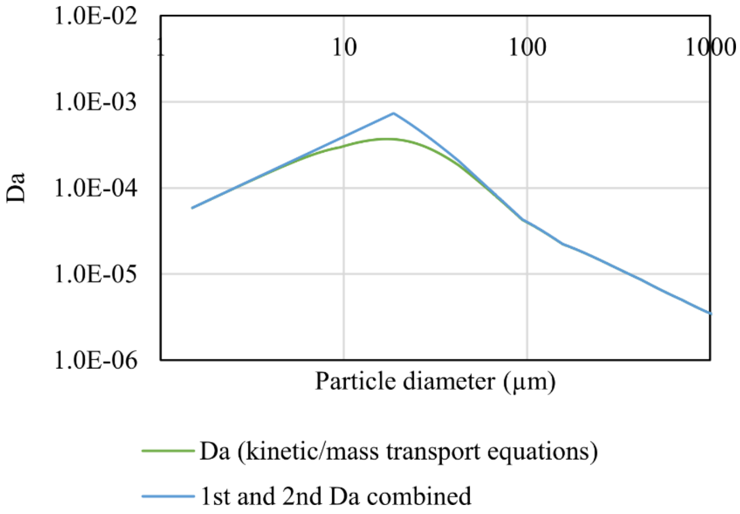

Figure 3.20 Ratio of predicted product formation rates by kinetic and mass transport processes, Da, as determined by Eq. (3.15) (green) and by conventional descriptions of Da (blue). Plotted for silica extracted from sand with R5$_2$-mCh-mSOx-R5-6H and 6 µM sarcosine.

The rates of mass transport are related to hydrodynamic conditions experienced by each particle, which can be approximated by its velocity relative to the surrounding fluid. The experimentally observed particle settling behaviour was combined with theoretical models to assign a velocity to each particle diameter (d) class (discussed in detail in Section 3.2.4). This approach was used for all silica types, given similar settling behaviour was observed (plumes followed by dispersed particles). Figure 3.21A shows the ensuing velocity relationship for each silica type, accounting for their respective densities (as reported in Table 2.4 – 2180 kg/m^3, 2000 kg/m^3 and 1860 kg/m^3 for silica extracted from sand SC, silica gel 60 discrete size classes and silica gel 60 <63 µm, respectively). Terminal velocity increases with an increase in density (Eq. (3.6) and Eq. (3.7)) so the extracted silica is predicted to fall faster for an equivalent diameter particle. At these velocities and particle sizes, $Re_p < 10$ for particles of $d < 500$ µm and $Re_p < 1$ for particles of $d < 200$ µm, indicating that relationships for substrate flux developed under the assumption of low Reynolds number, as described by Eq. (3.11) and Eq. (3.13), still apply for the majority of particles (Figure 3.21B).

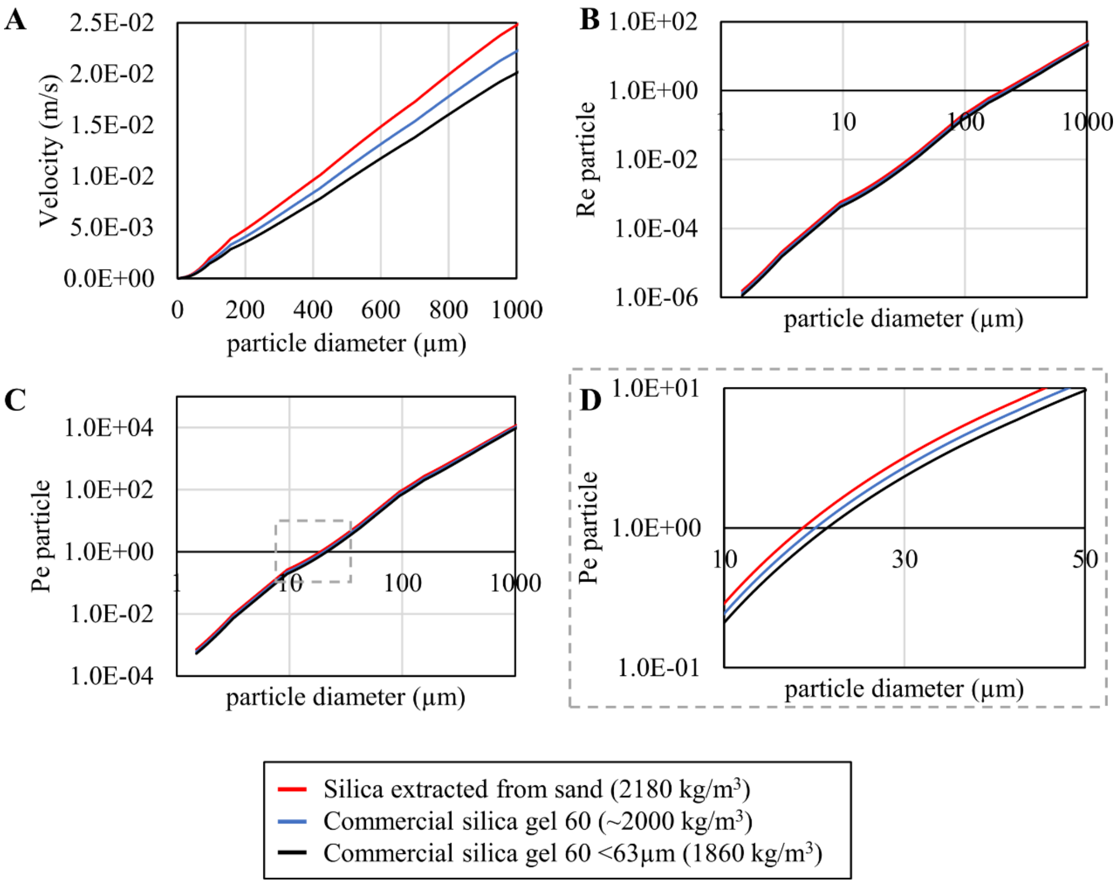

Figure 3.21 Particle velocity and associated dimensionless numbers with respect to particle diameter, showing (A) velocity assigned to each silica type based on experimental data and the corresponding plots of (B) Re_p and (C) Pe. (D) shows the region of (C) where Pe ≈ 1.

Combining these velocities with experimentally determined parameters for R5$_2$-mCh-mSOx-R5-6H on silica (as determined in Chapter 2 and specified in Table 3.3 and Table 3.1), Da << 1 for all particle sizes and silica types (Figure 3.22). This suggests that the system is reaction rate limited by several orders of magnitude. Nonetheless, it is important to test the sensitivity of this result to changes in the assumptions and inputs. Discussion of the changes in Da with silica type will be included in this sensitivity analysis.

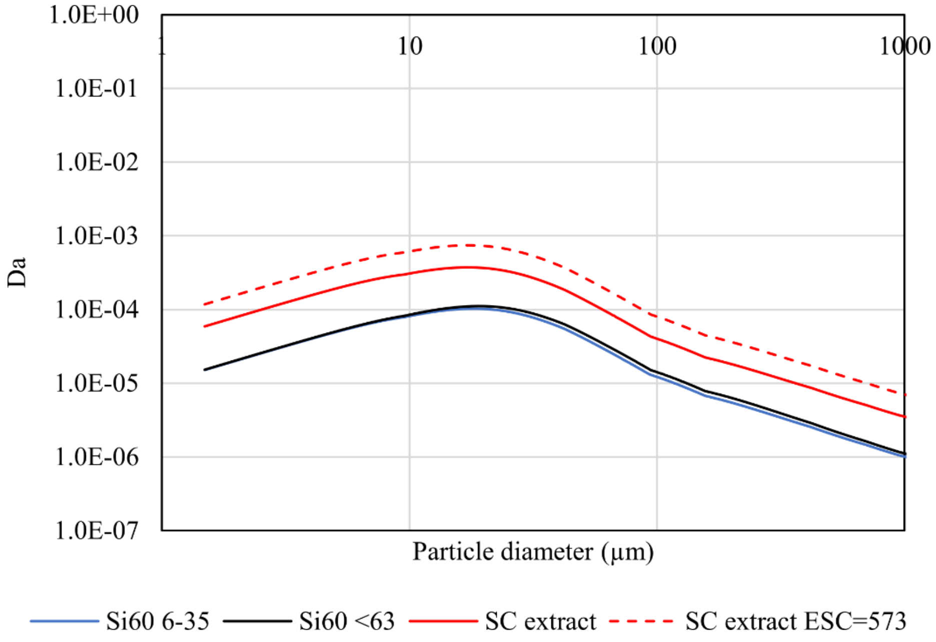

Figure 3.22 Ratio of predicted product formation rates by kinetic and mass transport processes, Da, plotted against particle diameter for the silica types tested in the falling particle biosensor.

Looking at Eq. (3.15), for Da > 1, it would require one or more of the following changes:

- decrease in the flow experienced by the particle (u_i)
- increase in enzyme surface coverage (ESC)
- decrease in the diffusivity of the substrate (D_s)
- increase in specific activity of the enzyme (V_{max})
- increase in affinity of the enzyme for the substrate (corresponding to a decrease in K_m)

All the above components of Da are constant across all particle sizes with the exception of particle velocity, u_i. The falling speed of the particle determines the ratio of advection of the substrate by the flow over diffusion rate driven by gradient, as characterised by Pe (Eq. (3.5)). Higher flow rates are associated with an increased rate of mass transport as flow helps overcome limitations of diffusion by decreasing the effective distance from the surface to the bulk solution (i.e. diffusion boundary layer). Under slow flow or the zero velocity case, the effect of flow on the chemical reaction is limited. Figure 3.21C shows the corresponding Pe for each particle size class. For the smallest particles, Pe < 1 and therefore diffusive flux is the dominant process in mass transport of the substrate and a decrease in flow is unlikely to change Da for these particles. However, for larger particles (d > ~20 µm), Pe > 1 and flow is predicted to increase rate of mass transport, thus making the enzyme on these larger particles more likely to be under kinetic control (Da << 1). The diameter at which diffusion is no longer expected to dominate and flow must be considered ($Pe \approx 1$) shifts slightly for each silica type (Figure 3.21D), as the variance in their density changes the relationship between the particle velocity with respect to diameter (Figure 3.21A). Thus, to probe a change in u_i that could result in $Da > 1$ for those larger particles, one can consider the extreme scenario where the particles are a very slow flow or at zero velocity, such that flow no longer has an effect and the rate of mass transport is determined only by diffusion processes. Indeed, this no flow scenario is reflective of the particles once they have reached the base and are stationary (at least initially before it would be necessary to account for restricted access to the bulk solution and ensuing local depletion of the substrate – as discussed in Section 3.3.3.4). Nonetheless, assuming all other system parameters remain unchanged, even this scenario does not result in $Da > 1$ for the size range of particles studied here (1-1000 µm in diameter, see blue dashed line in Figure 3.23).

The remaining parameters are subject to changes in enzyme characteristics (V_{max}, K_m), substrate properties (D_s) or silica surface-protein interactions (ESC). In the case of V_{max} and ESC, the increase in Da will be proportional. For K_m, the relationship is inversely proportional. The same is true for D_s when $Pe < 1$, i.e. mass transport is diffusion limited. In the system described here with R5-mCh-Enz proteins immobilised on silica, the surface coverage (ESC) is dependent on the ionisation of the silanol groups, the degree of which varies across types of silica [105–109]. The difference in Da for the various silica types in Figure 3.22 is largely a result of this variance in ESC (Table 3.1) rather than the slight variation in particle velocity (Figure 3.21A). Nonetheless, an increase of several orders of magnitude in surface coverage is unlikely as the silica surfaces are close to saturation with the enzyme for the immobilisation conditions explored here (as discussed in Chapter 2, see Figure 2.41 and Figure 2.43).

With respect to substrate diffusivity, a decrease is expected if the substrate is larger in size or the viscosity of the solution increases (assuming operation at a constant temperature). However, a significant change in substrate diffusivity is unlikely even if the system were to be used with other enzymes as many substrates are similar in size to sarcosine and have diffusivities of a similar order of magnitude. With respect to possible changes in viscosity, a switch to a more viscous clinical sample type (e.g. blood serum) over buffer would only be expected to double the viscosity. As observed for glucose in cell culture medium as compared to phosphate buffer, doubling the viscosity produced less than double an increase in the diffusivity [256].

A substantial change in specific activity (V_{max}) or affinity (K_m) is unlikely for any batch to batch variation of the silica-immobilised R5$_2$-mCh-mSOX-R5-6H given the consistency observed experimentally, but a large degree of change is likely when considering the range of other enzymes with which this system could be used. For instance, SOx belongs to the same family of enzymes as the ubiquitous glucose oxidase, which has a specific activity ranging from 172-300 U/mg; however, the specific activity for the one electron process with SOx is known to be an order of magnitude lower in comparison with the two electron oxidation mechanism involving glucose oxidase. This is consistent with the fusion SOx explored here, which has an apparent specific activity of only ~3 U/mg immediately after immobilisation, which decreases to 0.3 U/mg after drying, as used in the falling particle sensor (Table 2.12 and Figure 2.34).

Given the proportionality of Da with respect to the parameters V_{max}, K_m, and ESC, the magnitude of their combined effect on Da can be evaluated by investigating an equivalent magnitude of change in one, as demonstrated in Figure 3.23 with enzyme activity (V_{max}) for both scenarios of flow (solid lines) and no flow (dashed lines). In this analysis of change in V_{max}, the value used for ESC is the highest observed as it was the most likely to support a change in Da (573 mg total protein/m^2 silica surface area for silica extracted from sand, Table 3.1). For particles falling at the speeds observed experimentally for SC extract (solid lines), even when the activity of the enzyme has increased by three orders of magnitude to 300 U/mg (similar to that of glucose oxidase), the system is not predicted to be under mass transport control (solid red line). In the case of slow or no flow when diffusion would dominate the mass transport process (dashed lines), the particle diameter at which the system becomes mass transport limited decreases with the increase in enzyme activity. Where $Da \approx 1$, the system is in the transitional regime so additional simulation would be required to control for the non-valid assumptions, e.g. dilute particles. However, the falling particles under observation here are not in a scenario of limited flow (except once they have reached the base –this will be discussed further in Section 3.3.3.4). Moreover, no significant changes are expected in the values of the remaining parameters for silica functionalised with R5$_2$-mCh-mSOX-R5-6H (V_{max}, K_m, ESC, D_s), so kinetic control is predicted across all particle sizes.

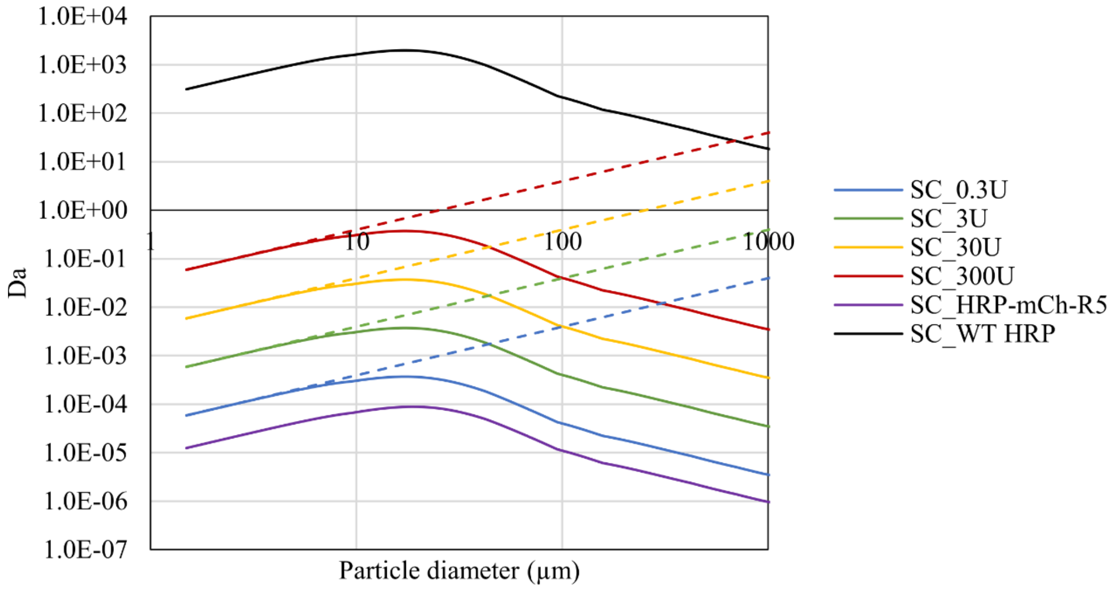

Figure 3.23 Ratio of predicted product formation rates by kinetic and mass transport processes, Da, plotted against particle diameter for a range of enzyme activity values for (solid lines) particles falling at velocities estimated by experimental observation and (dashed lines) particles in a very slow or no flow scenario.

The ratio Da can also be plotted using the experimental parameters for the HRP-mCh-R5-6H construct immobilised on silica extracted from SC sand (where $V_{max} = 0.018$ U/mg, $K_m = 1.6$ mM, as reported in Chapter 2, and $D_s = 1.43 \times 10^{-9}$ m^2/s for H_2O_2 [257]). In this case, the protein was not immobilised at saturation given the low expression level and correspondingly low concentration of the purified protein, so ESC is reduced as compared to immobilisation with R5$_2$-mCh-mSOx-R5-6H (ESC = 128 mg protein/m^2 silica surface area). Under these conditions, particles of all diameters are still predicted to be under kinetic control (purple line in Figure 3.23).

In contrast, plotting Da for WT HRP parameters, as determined for the soluble enzyme ($K_m = 8$ μM and $V_{max} = 386$ U/mg, see Chapter 2), shows that the system is expected to be under diffusion control for all particle sizes (black line in Figure 3.23). This hypothetical case assumes no loss of enzyme activity or substrate affinity due to immobilisation and that immobilisation can be achieved with similar ESC to R5$_2$-mCh-mSOx-R5-6H on SC extract (ESC = 573 mg protein/m^2 silica surface area). The predicted rates of product formation for different silica size classes under this hypothetical case can be compared with the predicted rates for a kinetically controlled system in the next section and both compared against relative ratios of product formed experimentally (Section 3.3.3.3).

3.3.3.2 Predicting product formation for silica particle distributions

Since kinetic control is predicted for particle-bound R5-mCh-Enz across all particle sizes, even while they are settled at the base (barring significant changes in local substrate concentration – see Section 3.3.3.4 for discussion on this), the rate of product formation per particle is described by Eq. (3.3) (assuming steady state Michaelis-Menten reaction kinetics where $S_0 < K_m$). In the hypothetical case of particle-bound WT HRP where diffusion control is predicted, the rate of product formation per particle is described by Eq. (3.14). Figure 3.24 shows the predicted rates of product formation per silica size class based on these relationships and the experimental parameters defined for each of the silica types explored here (including their respective densities (Table 2.4) and enzymatic parameters (Table 3.3)).

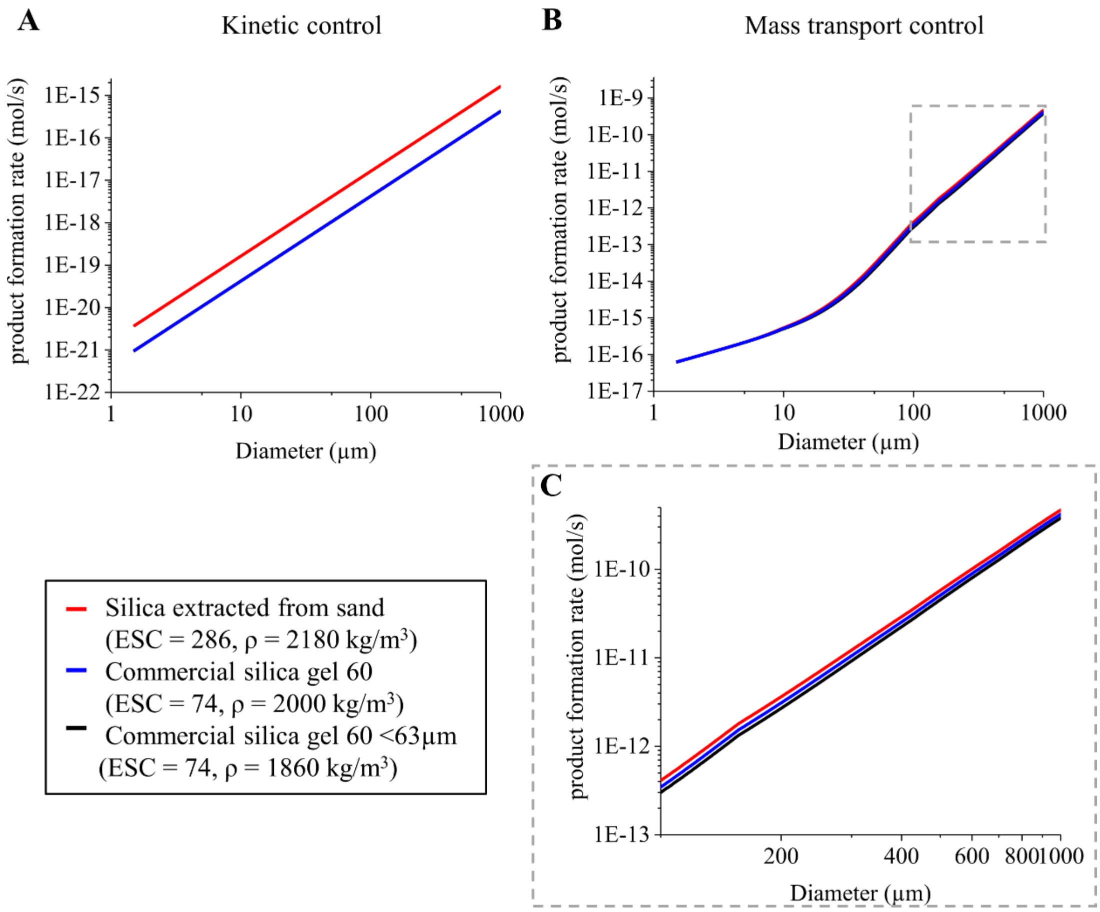

Figure 3.24 Predicted rate of product formation per silica size class for (A) silica functionalised with $R5_2$-mCh-mSOx-R5-6H under kinetic control (parameters in Table 3.3) and for (B) the hypothetical case of mass transport control using WT HRP enzyme parameters (equivalent to parameters in (A) apart from $K_m = 8$ μM and $V_{max} = 386$ U/mg). In both cases, $S_0 = 6$ μM and $D_s = 1.1\times10^{-9}$ m²/s. (C) Region of (B) showing the change in rate as a result of density for larger particles where Pe > 1 and flow affects substrate flux.

Under kinetic control (Figure 3.24A), predicted product formed during an inversion varies with silica type due to the variance in ESC (or lack thereof as in the case of commercial silica gel 60 of 6-35 µm and <63 µm in diameter, see Table 3.1). In contrast, under mass transport control (Figure 3.24B), variance in ESC is no longer a factor and the predicted rate of product formed varies slightly instead with density only for the larger particles (where Pe > 1 and velocity affects substrate flux). Increased relative flow as a result of higher density decreases the thickness of the boundary layer and increases the substrate flux to the surface.

Multiplying either of these predicted reaction rates for a particle by the time between inversions (t_{inver}, i.e. 60 s) produces the expected product formed by the particle during a single inversion. These relationships are plotted with respect to particle diameter in Figure 3.25A and B for commercial silica gels with discrete size ranges (6-35, 40-63 and 63-210 µm). The differences in their ESC and densities are small so the curves appear essentially equivalent.

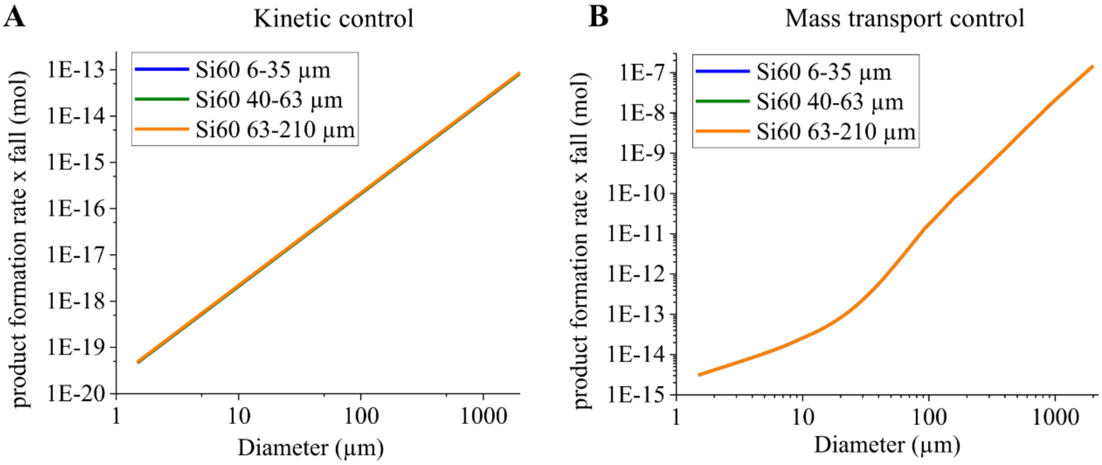

Figure 3.25 Predicted product formed per individual particle during one inversion across particle diameter for commercial silica gel 60 particle distributions (in the presence of 5 µM sarcosine), under (A) kinetic control and (B) mass transport control.

The predicted product formation by individual particles of diameter d_i during one inversion can be multiplied with a size distribution of particles to predict the total product formed by a mass of particles with a known distribution; Figure 3.26 shows the number distributions of the silica types explored here for a known mass (0.875 mg). Valencia *et al.* demonstrated the importance of considering total particle distribution as input rather than considering average particle size in their theoretical model of immobilised enzyme reactor performance [258]. They predicted a lower conversion rate when using the distribution as compared to the average particle size, suggesting that the positive effect of smaller size particles did not compensate for negative effect of particles of larger size. The magnitude of the difference depended on the standard deviation of the distribution, with a wider distribution resulting in a larger decrease in conversion rate when compared to predictions made using average particle size as the input. Thus, silica size distribution rather than average particle size was used to predict product formation in the analysis presented here.

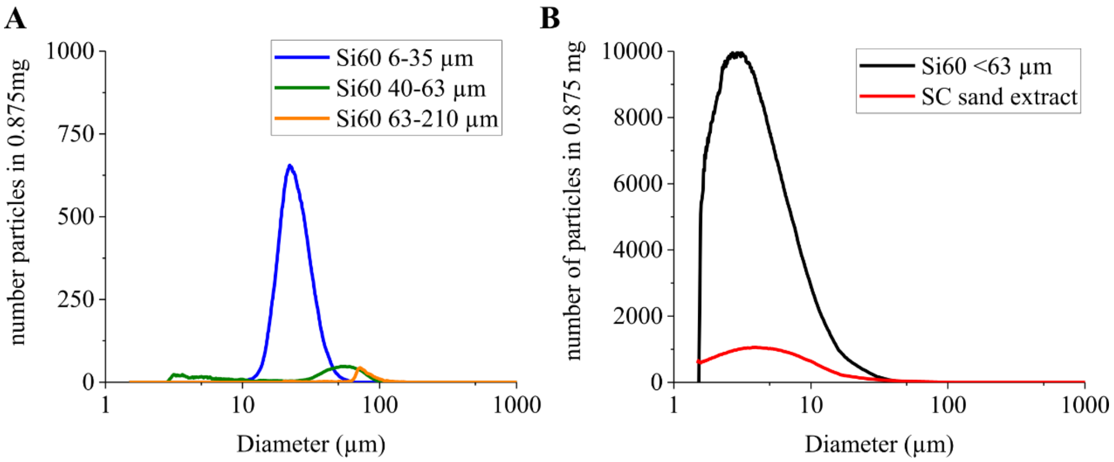

Figure 3.26 Number of particles of each d_i in the distribution for 0.875 mg for (A) discrete size classes of silica gel 60 and (B) heterogeneous silica distributions of commercial silica gel 60 <63 µm and silica extracted from sand.

Figure 3.27 shows the resultant plots from the multiplication of product formation during one inversion (Figure 3.25) and particle distribution (Figure 3.26) for the commercial silica gel with discrete size ranges. The product formation in the hypothetical case of mass transport control is also included. Figure 3.28 shows similar plots of product formation corresponding to the characteristics determined experimentally for silica extracted from sand and commercial silica gel <63 µm. Predicted total product formed during one inversion of the device with the known mass (0.875 mg) and distribution of particles is found by summing the predicted products for each size class d_i as formed by all the particles of that size (approximately equivalent to area under the curve (AUC)). It should be noted that these predictions assume no change in product formation rate by the particles once they have settled to the base, an assumption which will be discussed further in Section 3.3.3.4.

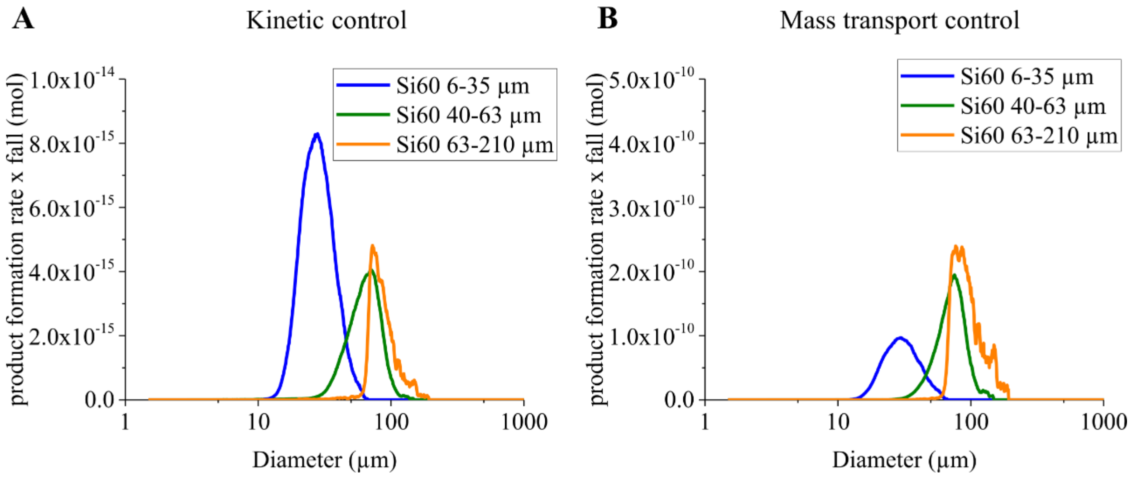

Figure 3.27 Predicted product formed in one inversion by 0.875 mg of commercial silica gel 60 particle distributions (in the presence of 5 μM sarcosine), showing product formation under (A) kinetic control and (B) mass transport control.

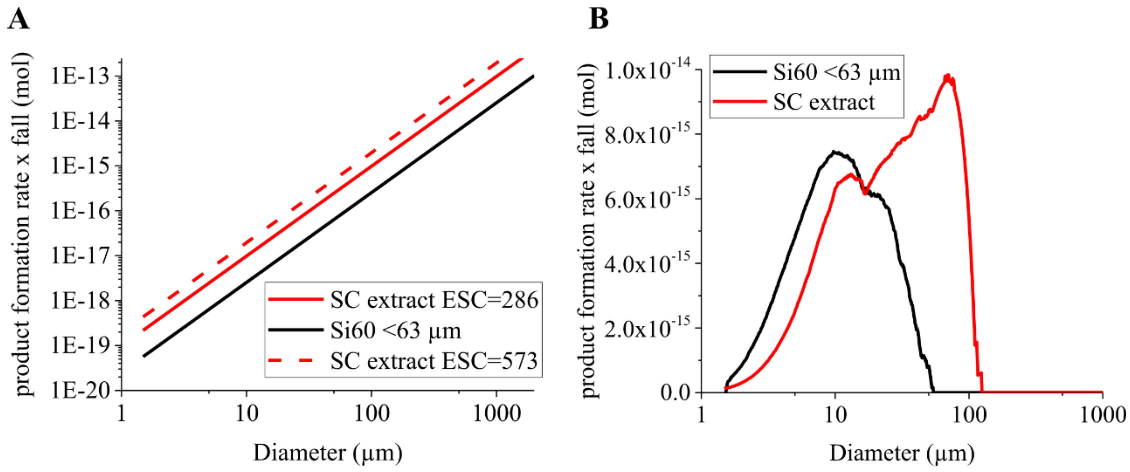

Figure 3.28 Predicted product formation by silica extracted from SC sand and silica gel 60 <63 μm (in the presence of 6 μM sarcosine), showing product formed per (A) individual particle during one inversion across particle diameter and (B) by 0.875 mg of respective distributions.

The total product produced per inversion by the particles (area under the curve) can be multiplied by number of inversions to calculate predicted total product formed after said inversions. Figure 3.30 shows the theoretical product (H_2O_2) produced by the various silica types over time (assuming kinetic controlled system in all cases), plotted as product concentration in the 200 μL assay volume of the narrow waist falling particle chamber. Notably, for SC extract and silica gel 60 <63 μM, product levels are expected to be above the limit of detection for the scanner (Figure 2.4B) after 5 min (in the presence of 6 μM sarcosine). The same is true for the silica gel 60 discrete size ranges when they are allowed to react for longer (~30 min). These predictions of product formed by silica size classes and types were compared to experimental results to determine the validity of the model.

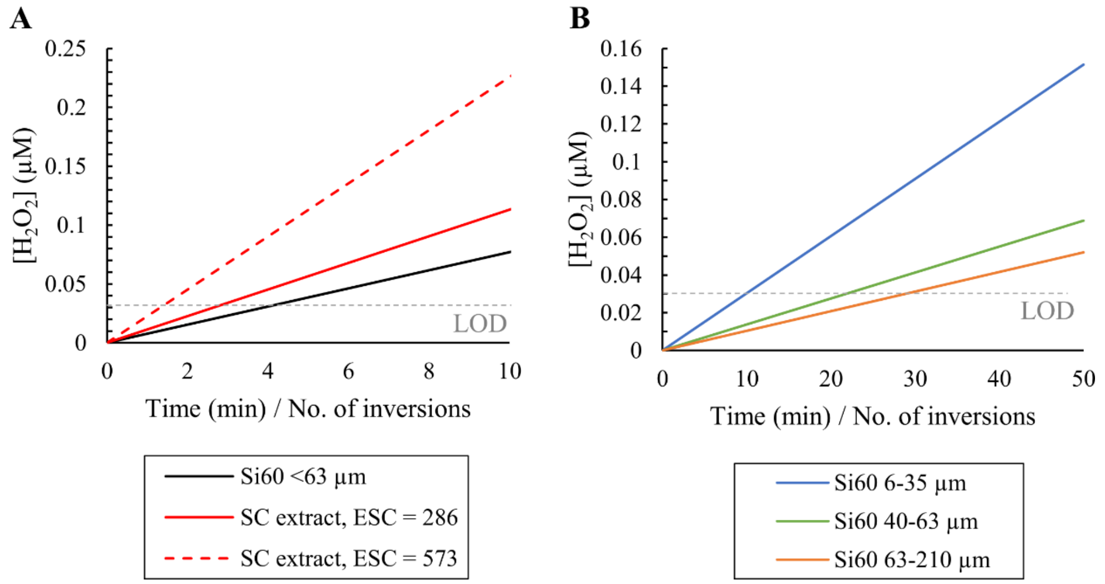

Figure 3.29 Theoretical product produced over time by R5$_2$-mCh-mSOX-R5-6H on (A) silica gel 60 <63 µm and silica extract (with two different loadings) in the presence of 6 µM sarcosine and on (B) silica gel 60 discrete size ranges (6-35, 40-63 and 63-210 µm) in the presence of 5 µM sarcosine (where the device is inverted every 60 s).

3.3.3.3 Comparison of predictions with experimental results

The predicted product formation by the falling particles during one inversion (and correspondingly substrate consumption) is < 0.5 % of the total substrate in the device for all silica variants functionalised with R5$_2$-mCh-mSOx-R5-6H, so the steady state assumption regarding bulk concentration of the substrate should be valid. Figure 3.30 follows the increase in fluorescence with inversions of bio-functionalised silica extracted from sand, revealing a linear relationship with time, even for 30 inversions (= 30 min), and confirming experimentally the steady state assumption.

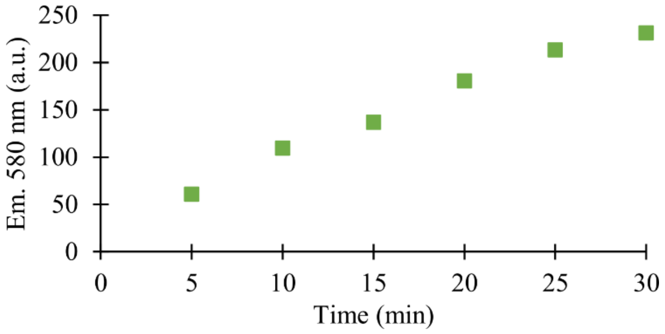

Figure 3.30 Fluorescence increase with device inversions/time in the narrow waisted chamber in the presence of 6 µM sarcosine and R5$_2$-mCh-mSOx-R5-6H immobilised on silica extracted from sand at ESC of 573 mg protein/m^2 silica surface area. Time between inversions was 60 s.

For a kinetically controlled system, one of the driving forces for product formation is the quantity and activity of the enzyme added. In this system, the immobilisation of the R5-mCh-Enz constructs was shown to be largely on the surface of the particles (Chapter 2). In addition, the enzyme coverage on the surface (ESC) is expected to be consistent across particles within a distribution as immobilisation efficiency was shown to be closely related to surface area for silica of the same type under saturated conditions (Figure 2.41). Hence, total enzymatic activity for a distribution of particles should be correlated with total surface area and thus, a mass of smaller particles is expected to produce product at a greater rate than the same mass of larger particles with the same enzyme loading.

These predictions can be tested against experimental results. The same mass (0.875 mg) of three discrete size classes of commercial silica gel with minimal overlap in size ranges, each functionalised with R5$_2$-mCh-mSOx-R5-6H, was added to separate narrow waisted devices with substrate (sarcosine, 5 µM final) and other necessary reagents (AR dye and soluble WT HRP) (Figure 3.31). The number distributions across particle size for each silica mass can be seen in Figure 3.26A. Fluorescent signal was measured at 40 minutes with an inversion every minute. Table 3.6 shows the experimental fluorescence intensity and expected product formation based on the area under the curve (AUC) for either a kinetically or mass transport limited system, all normalized to the result of the 6-35 µm silica. The predicted results for a system under kinetic control match the trends observed experimentally when comparing the different size classes. In contrast, under mass transport limited conditions, the particle distributions of larger size are predicted to perform better, diverging from experimental trends. This is in line with expectations given the system was predicted to be under kinetic control ($Da < 1$) for the experimental conditions of R5$_2$-mCh-mSOx-R5-6H on silica particles and that the mass transport control is a hypothetical case using the enzyme parameters for soluble WT HRP. The predicted results for the kinetic controlled regime are within experimental standard error for the 40-63 µm size class, however, the model predicts slightly higher product formation than observed from the 63-210 µm size class. It was observed during video analysis of particle fall that a small fraction of these particles were sticking to the seal used to create the chamber. This would limit their movement through the sample as well as their accessible surface area (and thus accessible enzyme), which may help explain the difference between experimental and predicted results. This sticking behaviour was not observed for the other size classes tested.

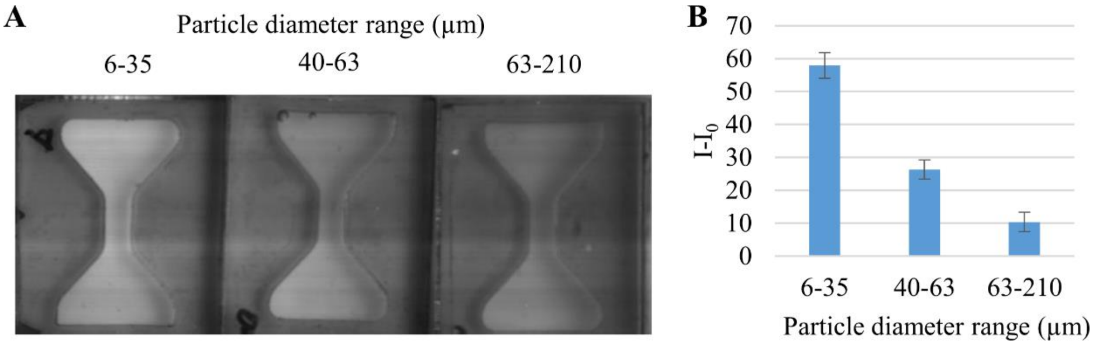

Figure 3.31 Comparison of silica gel 60 size classes in the narrow waisted device for the detection of sarcosine (5 µM) via AR fluorescence, shown (A) visually and (B) by the corresponding change in average signal intensity at 40 minutes.

Table 3.6 Comparison of experimental and predicted results for various silica gel 60 size classes in the narrow waisted device for the detection of sarcosine (5 µM) via AR fluorescence, normalised to 6-35 µm particle size class.

Particle diameter range (µm)	Measured fluorescent signal	Predicted signal (AUC) Kinetic control	Predicted signal (AUC) Mass transport control
6-35	1 ± 0.07	1	1
40-63	0.45 ± 0.06	0.45	1.42
63-210	0.17 ± 0.05	0.34	1.72

While the predictions for narrow size distributions of silica gel 60 were matched well with experimental results, a similar comparison can be done between commercial silica <63 µm in diameter and extracted silica. Like the silica extracted from sand, silica gel 60 <63 µm has a size distribution with higher heterogeneity, albeit without the largest particles observed for the extracted silica. For this comparison, 0.875 mg of each silica was used with 6 µM final sarcosine in the narrow waisted chamber. Reaction time could be decreased from 40 minutes used above to seven minutes as these distributions have more enzyme per unit mass due to the presence of smaller particles and the increased enzyme loading capacity (ESC) of extracted silica (Table 3.1). Both are predicted to be above the LOD for the scanner after reaction for > 5 min (Figure 3.29). Again, the predicted results for a kinetically controlled system reflect the trends observed experimentally; extracted silica produces more signal in the same number of inversions, despite having a distribution shifted towards the larger particles. Given the system is expected to be primarily reaction rate limited, the superior performance of the extracted silica is likely related to its higher loading capacity.

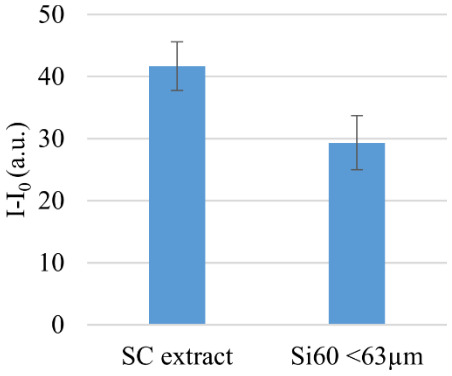

Figure 3.32 Comparison of signal intensity at 7 minutes for silica gel 60 <63 µm and SC extract (ESC = 286 mg protein / m^2 silica surface area) in the narrow waisted device for the detection of sarcosine (6 µM) via AR fluorescence.

Table 3.7 Comparison of experimental and model predicted results silica gel 60 <63 µm and SC extract in the falling particle device for the detection of 6 µM sarcosine via AR fluorescence, normalised to SC extract.

Particles	Measured fluorescent signal	Predicted signal (AUC)
SC extract	1 ± 0.10	1
Si60, <63 µm	0.70 ± 0.10	0.68

It is also possible to compare the best performing across both of narrow and wide particle size distributions: extracted silica versus silica gel 60 6-35 µm. Experimentally, seven inversions of extracted silica produced 72 ± 6.7 % of the signal observed for 40 inversions of the 6-35 µm silica gel 60, compared to 66 % predicted by the model. Again, the predicted results reflect experimental trends. Overall, the match of model predictions with experimental results supports not only the prediction that the system is kinetically controlled for all particle sizes but also supports the use of the model as a tool to help optimise sensor design using a falling particle approach.

3.3.3.4 Limitations of the model

Although the predictions of product formation match well with experimental trends, it should be noted that the model does not fully reflect the behaviour observed in the falling particle devices. For instance, the particles are considered to be in dilute suspension, which does not reflect the situation of those particles the initial plumes. Those particles inside the plumes would experience less relative motion with respect to their surrounding fluid. This decrease in relative velocity could shift the reaction towards diffusion control, and hence the model could again be overestimating their signal contribution. However, given that particle-bound R5-mCh-Enz were still predicted to be under kinetic control in a zero flow condition, this is unlikely. In addition, within the plumes, the local concentration of the substrate is more likely to decrease over time. Given S << K_m and the system is expected to be under kinetic control, local substrate concentration will affect the rate of reaction, which means the product formation rate could be overestimated for these particles. This decrease in local substrate concentration could also occur for those particles falling directly behind another particle. However, the redistribution of fluid caused by the falling particles could help alleviate depletions in local substrate concentration for these particles and is also unaccounted for in the current description of product formation for this system.

Depletion of the local substrate should also be considered with respect to those particles within the bed of settled particles at the base of the device. As mentioned in Section 3.3.3.1, once settled, the particles are essentially in the scenario of slow or no flow. Considering the system is expected to be under kinetic control even in this scenario (see blue dashed line in Figure 3.23), the particles were predicted to consume substrate at the same rate while settled. This assumed minimal changes in the local concentration of the substrate, however, for those particles within the settled bed, substrate from the bulk would be required to diffuse through a porous network to reach the buried enzymes. Thus, depletion should be accounted for when the settled particles are expected to consume a significant portion of the substrate in their immediate vicinity, as access to the bulk is reduced.

The void volume of the settled bed can be used to estimate the local substrate available for consumption. Micro-computed tomography (micro-CT) imaging of packed beds made with the silica extract and the silica gel 60 <63 µm indicated a void fraction, θ_v, of ~25 % (see Chapter 4). With this information, void volume (Vol_{void}) can be calculated using the relationship:

$$Vol_{void} = Vol_{sb}\,\frac{\theta_v}{(1-\theta_v)} \tag{3.16}$$

where Vol_{sb} is the total volume of the particles expected to settle in 60 s and thus, form the settled bed. Vol_{void} can be multiplied by starting concentration of substrate (S_0) to get total molar amount of substrate in the local zone. This can be compared to the predicted product formation by the particles over the time they spend in the settled bed to indicate if it would be necessary to account for a local depletion zone in the modelled rates of product formation.

Predicted product formation by each particle in the settled bed can be estimated by multiplying rate of product formation (Eq. (3.3)) by time spent in the settled bed. For each particle size class, it is possible to estimate their time in the settled bed by subtracting their time of fall from the time between inversions (60 s). The time spent falling for each particle is determined by particle velocity and device dimensions, as described by:

$$\boldsymbol{t_i = h/u_i} \tag{3.17}$$

where h is the height of the chamber (Table 3.3). Those particles not expected to settle within one inversion period have their falling time capped to the time between inversions. Figure 3.33 shows the assigned falling time for each size class.

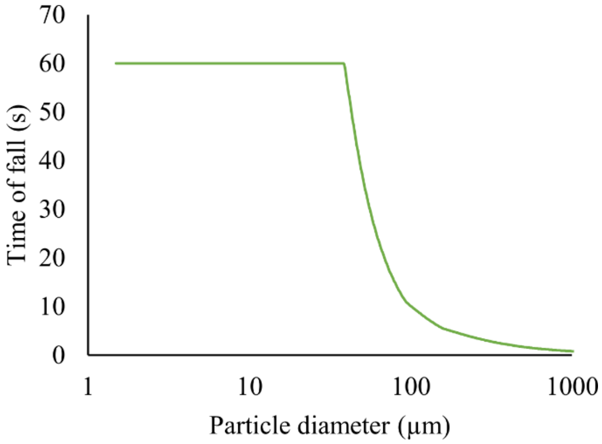

Figure 3.33 Assigned reaction time for each particle size based on estimated velocity, shown here for silica gel 60 size classes with a density of 2000 kg/m^3.

Combining Eq. (3.3) with Eq. (3.17), the quantity of product formed by each particle after settling is described by Eq. (3.18).

$$\boldsymbol{P_i = S_0\left(\frac{V_{max\_SA}}{K_m}\right)(4\pi r_i^2)(60 - t_i)} \tag{3.18}$$

Again, Eq. (3.18) can be multiplied a known particle distribution and area under the curve calculated to estimate predicted total product formed by the settled bed of that silica size distribution. Table 3.8 shows this for each silica class compared with the estimated substrate available for consumption in the void volume (Eq. (3.16) and S_0). Where the predicted product formed is only a small portion of the substrate available in the void, local depletion is not likely to be significant (e.g. silica gel 60 < 63 µm).

In contrast, where the predicted product formed is a significant portion of or greater than the void substrate available, this indicates that a local depletion zone should be taken into consideration when predicting rates of product formation for those particles in the settled bed. This is the case for silica extracted from sand, especially when ESC is increased close to saturation at 573 mg protein / m^2 silica. Under these conditions, the available substrate in the void would be consumed before the next inversion if the particles in the settled bed continued producing product at the initial rate. Thus, for the silica extract, the particles in the settled bed are likely to experience a local depletion zone during the inversion period.

Table 3.8 Void substrate available for consumption compared to expected product formation by the settled particles for a range of silica sizes and experimental conditions.

Silica size class (µm)	ESC	S_0 (µM)	Substrate available in the void (mol)	Product formed by the particles while settled (mol)	Ratio of the predicted product to void substrate
6-35	74	5	1.44×10^{-13}	1.67×10^{-14}	0.12
40-63	74	5	7.07×10^{-13}	1.49×10^{-13}	0.21
63-210	77	5	7.27×10^{-13}	1.57×10^{-13}	0.22
<63	74	6	4.14×10^{-14}	3.49×10^{-15}	0.08
SC extract	286	6	6.52×10^{-13}	5.56×10^{-13}	0.85
SC extract	573	6	6.52×10^{-13}	1.10×10^{-12}	1.69

For those particles within the bed that are likely to face local substrate depletion, their rate of product formation would be expected to decrease accordingly. For example, considering a single particle with its corresponding portion of the void volume (25 % of particle volume), Figure 3.34 shows the estimated decrease in product formation rate as a result of the decrease in local substrate concentration. This clearly indicates that a local depletion zone would reduce the contribution of the settled particles to the total product formation over time.

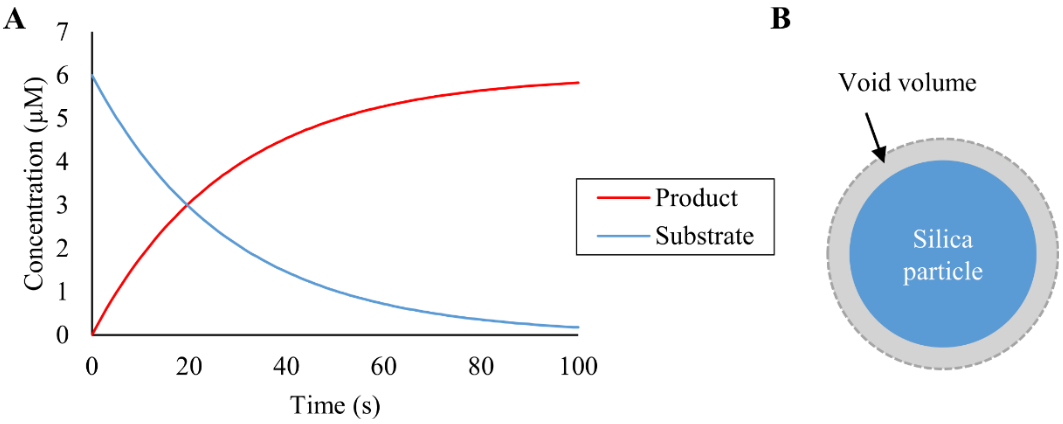

Figure 3.34 Product formation by a single particle (d = 100 µm) over time where S_0 = 6 µM and ESC = 573 mg protein / m^2 silica and V_{max} = 0.3 U/mg, assuming a local depletion zone equal to 25 % particle volume, as shown in (B), that has no access to the bulk solution and continuous redistribution of the substrate in this zone.

This finding is supported by experimental results comparing a change in protocol for inverting the device when loaded with the silica extract at high enzyme loading (ESC = 573 mg protein / m^2 silica). Figure 3.35 compares the result of two different protocols: (A) regular inversions every 60 s (as done for comparison of the various silica classes) and (B) two inversions of the device with 60 s in-between and five minutes of stationary position. In each case the fluorescence is measured at seven minutes from addition of the substrate (6 µM sarcosine), either by measuring average intensity in the top chamber (Figure 3.35B) or by calculating the AUC of a central intensity profile (Figure 3.35C). Assuming the same rate of product formation by both falling and settled particles, the model would predict Protocol B with only two inversions to have 100 % of the signal of Protocol A with seven inversions; however, experimentally Protocol B shows 50 % of the signal from the multi-inversion protocol. This confirms that substrate is being turned over inefficiently by the particles while they are settled at the bottom of the chamber and that the efficiency increases during settling as the particles pass through the fluid. Further simulation and experimental validation could help quantify the contribution to the signal from the settled particles and support the development of a model where particles switch between falling and settled states.

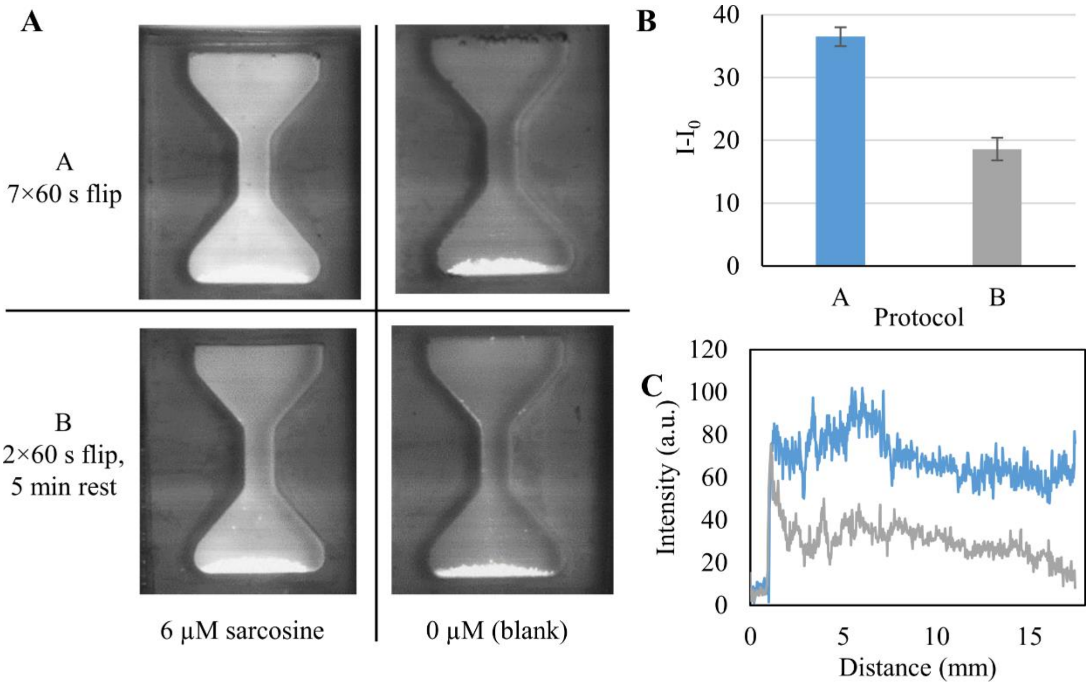

Figure 3.35 Comparison of two flipping protocols for the detection of sarcosine via AR fluorescence in the narrow waist device, shown (A) visually, (B) by the corresponding change in average signal intensity in the top portion of the chamber and (C) by the change in intensity profile throughout the device, plotted along a central line perpendicular to the base. Blank is subtracted for both (B/C).

Overall, a better understanding of not only the settled bed, but also those particles falling in plumes through simulation and experimental validation would help optimize the design of a falling particle chamber and selection of silica size distribution. For instance, the reduced contribution of the settled particles after some time suggests that a more consistent time in suspension per particle by using particles of similar size would be advantageous compared to a distribution where some portion of the particles settles out quickly. However, even with more homogenous size distributions than the extracted silica, the falling behaviour of the initial plumes is complex and has an effect on the overall fluid movement within the system. The design of accurate numerical algorithms for these complex behaviours is challenging. A numerical simulation to account for this complex fluid behaviour by using a discrete description of the individual settling particles, including the hydrodynamic interactions between close neighbours, not to mention the addition of enzyme reaction kinetics, would be computationally expensive to perform. Although the simple mathematical model presented here does not account for all of the complex fluid and particle interactions observed in the falling particle biosensor, it matches well with experimental results for a range of silica types and distributions, providing a first understanding of the driving forces behind product formation in this system. This can be used to inform sensor design with silica-based reagents.

3.3.4 Implications for POCT design using falling particles

First, it should be noted that the predictions of product formation presented above are under the assumption that $S_0 < K_m$. In contrast, when the local concentration of substrate is greater than K_m, the enzyme will act at a constant rate independent of substrate concentration. Thus, to determine the concentration of substrate in a sample using rate of product formation by the immobilised enzyme, the substrate must be the limiting factor and less than K_m.

Given the system is expected to be largely kinetically controlled, any changes in the activity and/or amount of the enzyme present (i.e. V_{max_SA} and/or total SA) are expected to affect the rate of product formation during one inversion and thus affect the rate signal development over time. In conjunction with the calibration curve in Figure 2.4B for known concentrations/amounts of product (H_2O_2) in the fluorescence scanner, the predictions of product formation can be used to estimate the corresponding fluorescent signal produced over the total assay time. Figure 3.36 shows the theoretical fluorescent signal produced by $R5_2$-mCh-mSOX-R5-6H on silica extract after 7 min in the presence of varying sarcosine concentration and demonstrates the effect of a ± 10 % change in V_{max_SA} on the substrate to signal ratio. A change in total enzymatic activity, V_{max_SA} (as determined by both specific activity, V_{max}, and enzyme loading, ESC, see Eq. (3.4)), is predicted to change the total signal proportionally (See Eq. (3.3)). Figure 3.36 shows that for a measured fluorescence intensity, true analyte concentration in the sample would be overestimated with an increase in V_{max_SA} and underestimated with a decrease in V_{max_SA} (e.g. 30 a.u. is the predicted signal output for 4.88 µM sarcosine with 0.3 U/mg activity, however, this signal would be produced by 4.44 µM sarcosine with 0.33 U/mg activity). Such a system could be challenging to use for quantitative detection, as any change in activity would affect the correlation of fluorescent signal with substrate concentration. Nonetheless, this challenge is likely surmountable as enzyme-based biosensors have been successfully developed where the enzyme is under kinetic control by regulating the parameters affecting total enzyme activity in the system and/or including an internal reference. While sensor consistency will need to be established under large-scale production conditions, low batch-to-batch variability with respect to immobilisation levels and enzyme activity was observed over the course of this research. In addition, the stability of the dry reagent over time is promising for sensor shelf-life.

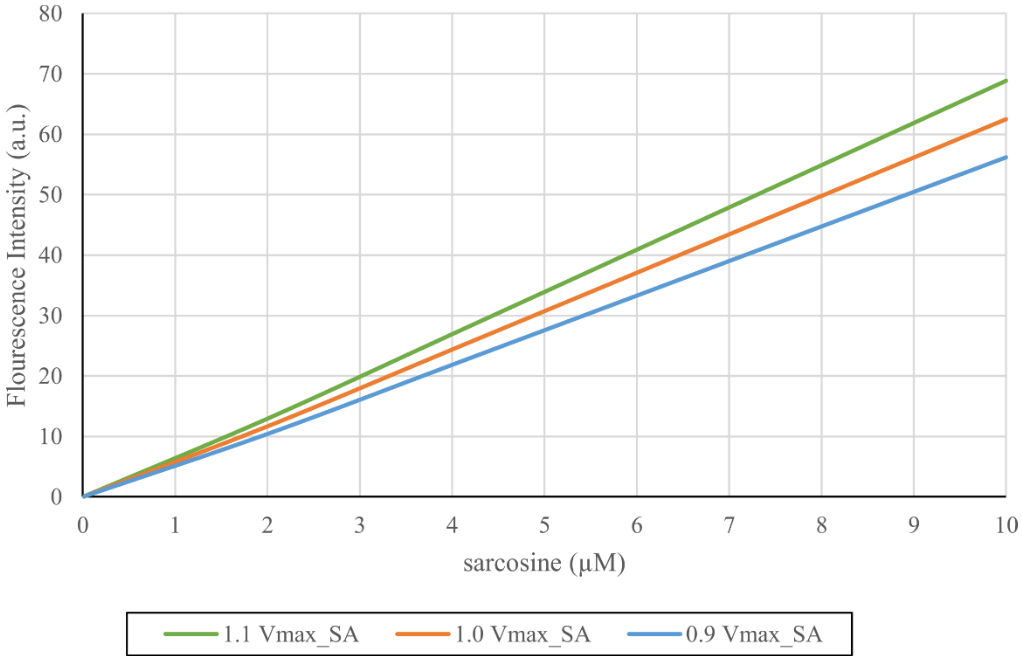

Figure 3.36 Theoretical fluorescent signal produced by R5$_2$-mCh-mSOX-R5-6H on silica extract after 7 min (where ESC = 573 mg protein / m^2 silica surface area and V$_{max}$ = 0.3 U/mg and the device is inverted every 60 s).

Due to the consequent reduction in the effects of sample pH, temperature, presence of inhibitors and variation in enzyme activity on biosensor response, operation under diffusional limitations can be an advantage, and thus an intentional design choice for a biosensor [227]. In some instances, membranes with lower permeability for the substrate have been used to achieve a diffusion limited system [227]; for enzymes with a low K_m, this has the advantage of increasing the dynamic concentration range [154]. However, diffusion limited systems can have their own challenges when it comes to reproducibility. For instance, in thick-film electrochemical biosensors with glucose oxidase, the thickness of the enzyme layer needs to be highly controlled [259], possibly beyond the limits of some commonly used deposition technologies [260]. Moreover, under diffusion conditions the rate of signal development will be reduced as mass transport limitations reduce the apparent catalytic activity of the enzyme [258]. In contrast, under a kinetically controlled system, the particle-bound enzyme is operating at its maximum rate, which potentially allows for a sensitive POCT system despite an enzyme with low activity (such as mSOx).

If, as the results suggest for the parameters explored here, the system is completely kinetically controlled for all particle sizes, then it may be that a benefit of the falling particle biosensor approach is that it enables greater dispersion of the particles. This dispersion results in more enzyme with access to the bulk solution as compared to a settled bed, which likely avoids local substrate depletion. It ultimately leads to higher signals, as observed experimentally with an increase in number of inversions over a defined time period (Figure 3.35).

With respect to the selection of silica distribution for use in the falling particle sensor, although the smaller particles have more surface area per unit mass and thus more enzymatic activity, the behaviour observed for a distribution of nanoparticles suggests particles in this size range may face a limitation in their ability to sample all of the fluid. Nanoparticles also face the challenge of aggregation which would reduce access to the enzymes on their surface. In addition, very small particles are almost neutrally buoyant in the viscosity relevant to clinical sample types and thus, would not settle out in a reasonable amount of time (< 10 min) for a POCT. This would lead to light scattering challenges for fluorescent or colorimetric detection methods and have poor utility for purification by sedimentation. On the other hand, large particles (e.g. 200-500 µm) have significantly reduced enzyme loading per unit volume and have settling rates that would require constant flipping of the device to achieve the benefits of dispersion.

While particle size is important, enzyme surface coverage also has a significant effect. This is clear when considering the performance of silica extracted from sand compared to the commercially available silica gels. Despite its significant fraction of larger particles, silica extracted from sand outperformed all the commercially available silica distributions for the same mass of silica. (Although the signal from 6-35 µm silica gel 60 was higher, it was measured at 40 min of flipping while the signal for the same mass of extracted silica was measured at 7 min). Given the prediction that the system is primarily reaction rate limited, this superior performance is likely related to its higher loading capacity than commercially available silica gel (ESC, Table 3.1). In light of this, the selection of support material for the enzyme must balance both the enzyme loading capacity and particle size distribution.

3.4 Summary

This chapter explored a novel design for a biosensor using silica-immobilised enzymes as the mobile phase. While immobilisation can add stability and simplify processing steps, immobilised enzymes experience different mass transport limitations to soluble enzymes, which can limit their apparent activity. A variety of strategies have been explored in the past to successfully utilize immobilised enzymes by optimising the transport phenomena of substrates and products, including extensive exploration of packed bed approach to biosensors [206,208–216], but there are no examples of gravity-driven dispersion of immobilised enzymes incorporated into a format potentially amenable to a POCT.

In order to optimise the design of a falling particle biosensor, it was necessary to understand the forces controlling the rates of product formation, and thereby signal development, by the particle-bound enzymes in this system. To explore this, it was first necessary to examine the settling behaviour of the particles to determine the relative fluid movement experienced by enzyme on the surface. The particles were observed to fall initially in plumes followed by dispersed smaller particles. These patterns could be harnessed in a design that allowed for a longer suspension time of the particles with the sample while keeping device dimensions small and amenable to POCT through multiple inversions. Use of a chamber design with a narrow waist created reproducible inversion patterns irrespective of inversion technique not seen in the other designs. This reproducible settling is critical to ensure a reproducible process for the enzymatic reaction and hence, the narrow waisted device lends itself to a biosensor platform.

The comparison of kinetic and mass transport rates suggests that the rate of product formation by the falling particles is significantly under kinetic control for the conditions studied here. Although the relative velocity component of the Da is not fully representative of the settling patterns observed in the falling particle device, for a range of silica size distributions, the predicted product formation matched well with experimental results. This suggests that the Da described here and the corresponding rates predicted for product formation could be used alongside experimental results to help select appropriate silica size and enzyme loading for a targeted substrate consumption rate in falling particle devices for other enzyme assays. While the analysis presented is limited to certain situations, it can be extended to support other geometries, enzyme kinetics and reactor configurations.

Given the predicted dependence on enzyme activity for the silica-immobilised R5_2-mCh-mSOx-R5-6H explored here, immobilisation at saturating levels of protein can likely be justified from a process approach, as this would result in the same coverage per mass of silica from crude lysate even with some deviation in expression level. In resource constrained settings, it is not likely to be easy to precisely assess total protein produced in each *E. coli* culture, but consistently adding the same mass of silica to crude lysate could be achievable. With this approach, it will also be important to have consistency of particle size distribution given the correlation between surface area and total enzyme loading. With respect to the selection of particle size, it is clear that this must be balanced with enzyme loading to achieve desired reaction rates.

Working towards a proof-of-concept of a POCT with the falling particle device, silica extracted from sand was selected for further investigation, given its high enzyme loading supported the fastest rate of signal development for the same mass of silica compared to all the commercially available silica distributions tested here. In combination with its settling ability for purification purposes earlier in the production process, likely promoted by the presence of the larger particles, and its potential to be produced on site from local materials, silica extracted from sand could support the local production of a POCT.

As aforementioned, the falling particle biosensor is just one several formats for POCT utilizing particle-bound enzymes, each with their advantages and disadvantages. The performance of the falling particle design will be compared in Chapter 4 against two other formats commonly employed with bio-functionalised particles – (1) simple suspension in a microcentrifuge tube and (2) a packed bed in a microfluidic channel. The narrow waisted chamber design will be used for this comparison in light of its repeatability of inversion patterns and proven ability support the detection of low concentrations of the target substrate, sarcosine. However, future work could progress towards a system that achieves greater particle dispersion, provided additional modelling and simulation confirm that this is an advantage of the falling particle approach.

Finally, for the falling particle system to have clinical utility as a biosensor, it must be able to detect the target substrate within the relevant range for the clinical condition. Figure 3.32 shows the detection of a low concentration of sarcosine within the relevant range for prostate cancer diagnosis (< 10 µM) within a rapid time frame (< 10 min) using silica extracted from sand functionalised with R5$_2$-mCh-mSOx-R5-6H in the narrow waisted chamber. These initial results are promising but the performance of the sensor across the range of relevant concentrations will be explored in Chapter 4.

4 PERFORMANCE OF THE FALLING PARTICLE BIOSENSOR

4.1 Introduction

Chapter 3 explored a novel design for a biosensor with silica-immobilised enzymes where gravitational force is used to drive their movement through the sample. This chapter will evaluate the performance of this design with respect to (A) other assay formats using particle-bound enzymes and (B) its potential to support quantitative or semi-quantitative detection.

Preliminary demonstrations of particle-based biosensors, focusing on the development of the biological or chemical reagents, often use simple suspension in common laboratory consumables, such as well plates and microcentrifuge tubes (as was reported for the initial investigations of the silica-R5-mCh-Enz in Chapter 2). As discussed in Chapter 3, there are alternative assay formats intended for POCTs that utilize particle-bound enzymes, including packed beds in microfluidic channels and magnetic particles manipulated by external magnetic fields. Of those formats utilizing particle-bound enzymes, the packed particle bed is the most commonly reported format. It is also potentially amenable to use with the R5-mCh-Enz functionalised silica particles, whereas the magnetic particle approach requires additional fabrication steps (e.g. creating silica particles with magnetic cores [261]). These additional complex steps would likely be inappropriate for an approach focussed on enabling locally produced materials. Thus, the packed particle bed was selected for comparison with the falling particle design (Figure 4.1). Simple suspension in a microcentrifuge tube was also included in the comparison as a baseline.

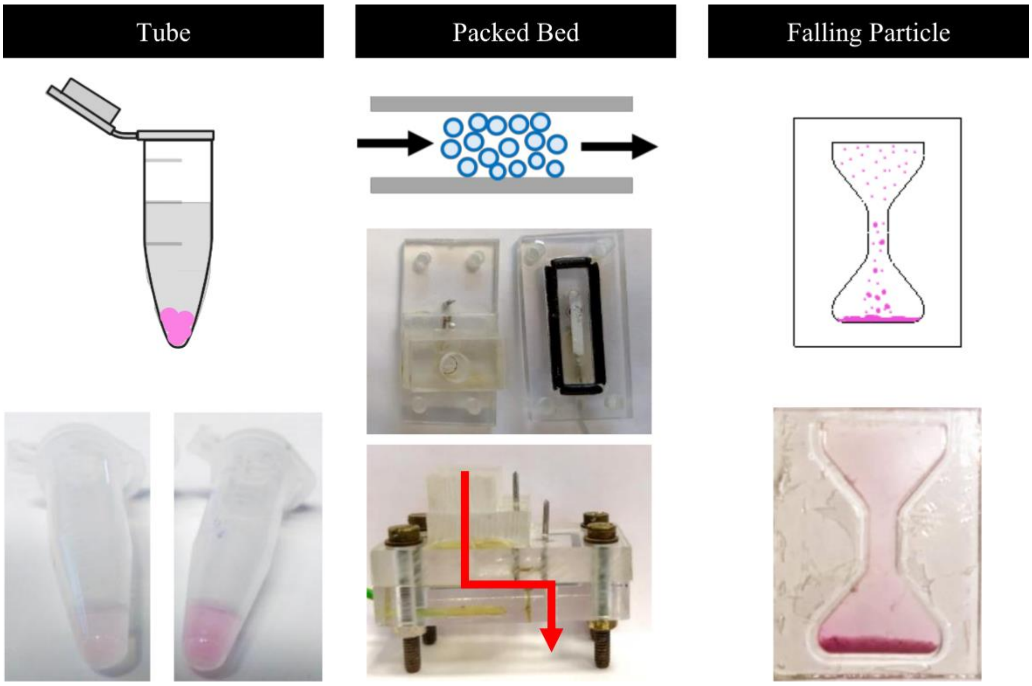

Figure 4.1 Three assay formats used with R5$_2$-mCh-mSOx-R5-6H on silica particles. The red arrow highlights the flow path through the packed bed device.

Regardless of its performance against other assay formats, in order for the falling particle system to have clinical utility as a biosensor, it must support detection of the target analyte within the range relevant to the target disease. The preference for a quantitative result over a semi-quantitative or qualitative result depends on the impact this information would have on the clinical treatment approach. For example, a qualitative lateral flow assay for malaria that shows a positive result will likely prompt treatment with artemisinin-based combination therapy regardless of parasite levels [262]. In contrast, quantitative measurements of glucose are important for diabetic patients, as glucose levels on either side of the acceptable range require distinct interventions. In the case of sarcosine, several studies have found elevated levels in prostate cancer patients compared with healthy patients [158,183,263], but the utility of sarcosine as a biomarker of prostate cancer is still debated [264]. Thus, it is currently unclear how sarcosine levels would be correlated with treatment pathways. One study showed sarcosine levels were significantly different in low grade versus high grade cancers [265], which could suggest that quantitative results could be important for selecting which patients receive nonaggressive therapies. Alternatively, if a threshold can be defined beyond which the likelihood of cancer is high, then a semi-quantitative test could be sufficient as a screening tool to prompt more invasive but confirmatory biopsy. Semi-quantitative tests have been proven as powerful tools to support differential diagnosis at the point-of-care (e.g. [266,267]).

The initial results with the falling particle sensor in Chapter 3 that demonstrate detection of micromolar levels of sarcosine within a rapid time frame (< 10 min) are promising for a POCT. Nonetheless, greater understanding of its performance across the range of relevant concentrations will be necessary to determine its potential towards quantitative or semi-quantitative testing. As the fluorimetric detection scheme requires the coupled enzyme assay of SOx and HRP, fusion proteins for both enzymes will be evaluated in this respect.

4.2 Experimental

4.2.1 Materials

Material sources are described in Chapters 2 and 3 with the addition of the following: polydimethylsiloxane (PDMS, Sylgard® 184, Dowcorning, USA), transparent tape (OfficeDepot, UK).

4.2.2 Construction and characterisation of the packed bed in a channel

The channel system was constructed from two pieces of PMMA with machined inlets and outlets for fluid entry/exit and a channel of $15 \times 2 \times 0.3$ mm^3 engraved in the bottom half, as previously developed by Gooding and Hall [268] and pictured in Figure 4.1. Four corner bolts were used for mating the top plate with the bottom via mechanical pressure and an O-ring around the channel formed the watertight seal.

The bed of bio-functionalised silica particles was created through serial drop casting of a silica slurry in the channel. The same technique was used to create packed beds in PDMS channels for micro-computed tomography imaging (micro-CT, Zeiss Versa 510). (The PMMA channel system was replaced by comparable packed beds in PDMS channels to reduce thickness of the material external to the area of interest (i.e. the packed bed).) The PDMS channel, with a cross-section of 1×0.1 mm^2, was fabricated as described in the author’s parallel publication with collaborators [206]. In brief, PDMS and its curing agent were mixed together in a 10:1 ratio and cured on an in-house fabricated negative aluminium mould for two hours at 80 °C to create the channel structures. The negative mould was designed using 3D modelling software (SolidWorks 2015, Dassault Systems, USA) and manufactured by computer numerical control milling (Department of Chemical Engineering and Biotechnology, University of Cambridge). Prior to curing, the PDMS was degassed under vacuum for 20 min to release any bubbles resulting from mixing and conform the mixture to the surface of the mould. Post-curing, the PDMS channel system was cut out from the aluminium mould, washed once with ethanol and gas dried with nitrogen. Transparent tape was used to seal the PDMS channel system once the silica was deposited in the channel.

In the micro-CT, images were taken 360^0 about the z-axis (Figure 4.2) using settings of 80 kV and 7 W with a pixel size of 2.251 µm, and the resulting tiff stack was rendered in VGstudio (Volume Graphics). A region of interest was defined within the packed bed and greyscale thresholding used to differentiate the void volume from the particles.

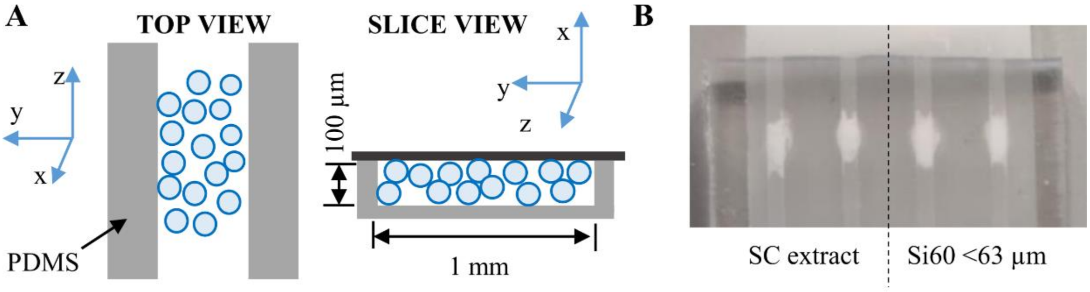

Figure 4.2 Set-up for micro-CT imaging showing (A) schematic of axes orientation relative to channel and (B) PDMS channels filled with silica variants.

4.2.3 Performance evaluation of a range of assay formats

Two assay formats were compared against the custom narrow waisted falling particle chamber presented in Chapter 3 for their rate of conversion of substrate to product: (A) simple suspension in a microcentrifuge tube and (B) a packed bed in a microfluidic channel (Figure 4.1). The falling particle devices were constructed as described in Chapter 3 and the packed bed as described above in Section 4.2.2.

Fusion protein $R5_2$-mCh-mSOx-R5-6H and its corresponding substrate sarcosine were used to compare assay formats. Conversion of sarcosine was detected using the Amplex^{TM} UltraRed (AR) assay with soluble WT HRP as previously described in Chapter 2 and 3 with the following changes. The amount of silica was increased from 0.875 mg to 2.5 mg per assay to enhance detection within short timescales. Final concentration of AR was 25 µM and of sarcosine was 5 µM in all cases.

Residence times of substrate with enzyme were kept equivalent across formats by correlating flow rates through the packed bed system such that 200 µL would pass through the bed in the same time that the falling particle and tube assays of the same volume were allowed to react (Table 4.1). The falling particle chamber was flipped every 60 s throughout the residence time. These flow rates and corresponding residence times were selected based on flow rates observed for capillary flow systems during work by the author with collaborators [206], as equipment free operation (e.g. no syringe pumps) is desirable in low resources settings [18]. However, for the purposes of this comparison, a syringe pump was used to provide consistent flow rates (KDS Model 100, kdScientific), with the tip of the syringe inserted into the entry port of the PMMA channel device.

Table 4.1 Residence times and corresponding flow rates used in device format comparison assays

Residence time (minutes)	Flow rate (mL/hr)
3.5	3.6
14	0.9

4.2.4 Falling particle assays for sarcosine and hydrogen peroxide

Falling particle assays were performed in narrow waisted chambers as described in Chapter 3, with some modifications for each assay depending on the target substrate:

- For the detection of sarcosine, $R5_2$-mCh-mSOx-R5-6H immobilised on silica extracted from SC sand (0.875 mg silica, ~90 µg protein per 1 mg silica) was mixed with AR (4.17 µM), HRP (0.016 mg/mL) and sarcosine (0 µM (blank), 2, 4, 6, 8 µM)) and loaded into the device.

- For the detection of H_2O_2, HRP-mCh-R5-6H immobilised on silica extracted from SC sand (0.5 mg silica, ~20 µg protein per 1 mg silica) was mixed with AR (10.8 µM) and H_2O_2 (0 µM (blank), 21, 42, 84, 126 µM)) and loaded into the device.

- For the detection of sarcosine combining both fusion constructs, $R5_2$-mCh-mSOx-R5-6H immobilised on silica extracted from SC sand (1 mg silica, ~90 µg protein per 1 mg silica) was mixed with AR (10.8 µM), HRP-mCh-R5-6H immobilised on silica extracted from SC sand (1 mg silica, ~20 µg protein per 1 mg silica) and sarcosine (0 µM (blank) to 100 µM)) and loaded into the device.

All of the above were performed using the narrow waisted design with a total volume of 200 µL and all concentrations reported are final concentrations in the assay. As in Chapter 3, the devices were imaged using the fluorescence flatbed scanner and images were analysed for grey scale intensity of the red channel in the chamber area using ImageJ software. Fluorescent signal was determined by measuring the average intensity in the device or by integrating a plot of red channel intensity at right angle from the base along the central line of the chamber.

For the endpoint assay, the reagent concentrations were as described in Chapter 2 for the endpoint assay in well plates. A mini-chamber was designed to accommodate the reduced volume (50 µL) of this assay (Figure 4.10). Given the height of this design is ~50 % of the narrow waisted device, flipping was done every 30 s instead of 60 s using an analogue servo motor (Seeed Studio) and a microcontroller board (Arduino Uno Rev3).

4.3 Results and Discussion

4.3.1 Comparison of assay formats using particle-bound enzymes

As aforementioned, particle-bound enzymes can be utilized in a variety of formats for POCT, each with their advantages and disadvantages. The custom falling particle device presented in Chapter 3 was compared against two other formats commonly employed with particle-bound enzymes: (A) simple suspension in a microcentrifuge tube and (B) a packed bed in a microfluidic channel (Figure 4.1). The degree of interaction of the immobilised bio-recognition element ($R5_2$-mCh-mSOx-R5-6H) with analyte in fluid (sarcosine) in each format was measured by the rate of conversion of substrate to product using fluorescence.

In contrast to most packed bed approaches in the literature that required additional structures to maintain particle position [207,212,213], the packed bed explored here was created through serial drop casting of a silica slurry. This simple manufacturing technique was demonstrated by the author and collaborators for an immunoassay in a packed silica bed and no sign of particle washout was observed after flow [206]. Figure 4.3 and Figure

4.4 show micro-CT images of packed beds in microchannels with the commercial silica gel <63 µm and the silica extracted from SC sand, respectively.

Despite the variation in particle size distributions between the two silica variants and the observable increase in irregularity of packing in the case of the silica extract, analysis of the micro-CT scans using greyscale thresholding to differentiate between particle and void volume returned a void volume of ~25 % for both (indicating a packing fraction of ~75 %). For a packed bed of homogenous spheres in hexagonal close packed arrangement, 26 % is the lowest expected fraction of void space. The silica variants explored here are neither homogenous nor spherical, so their low void volume is likely a result of the smaller particles within the distribution filling the gaps between the largest particles. Although a uniformly sized catalyst is known to reduce the chance and severity of non-ideal behavior in packed bed reactors [136], the silica extract was selected to form the packed bed used in the comparison test to maintain consistency of silica type, and corresponding enzyme loading, across the formats.

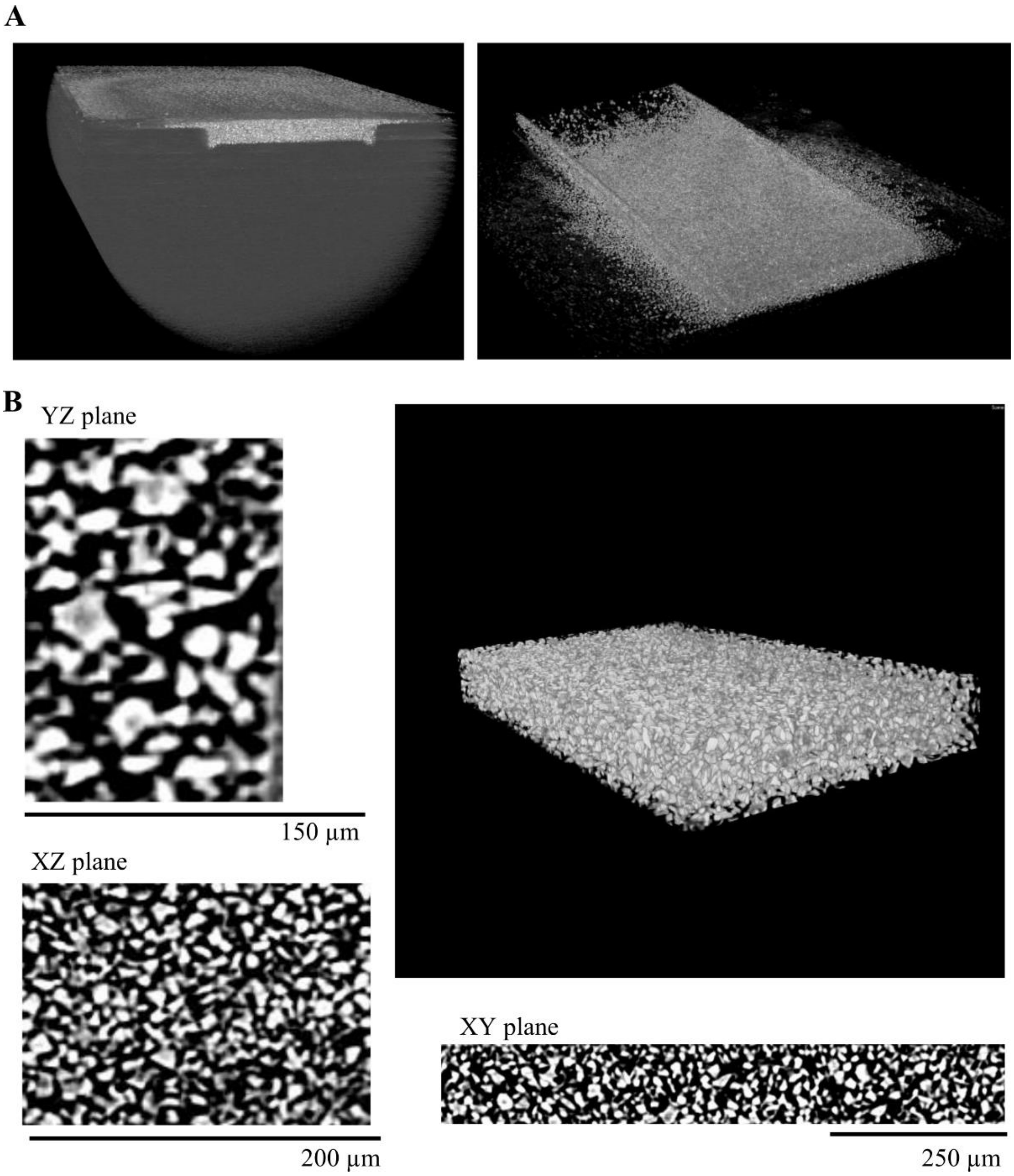

Figure 4.3 Compiled 3D renderings of micro-CT images for PDMS channels filled with commercial silica gel 60 <63 µm, showing (A) overall channel structure and (B) region of interest used for void volume analysis.

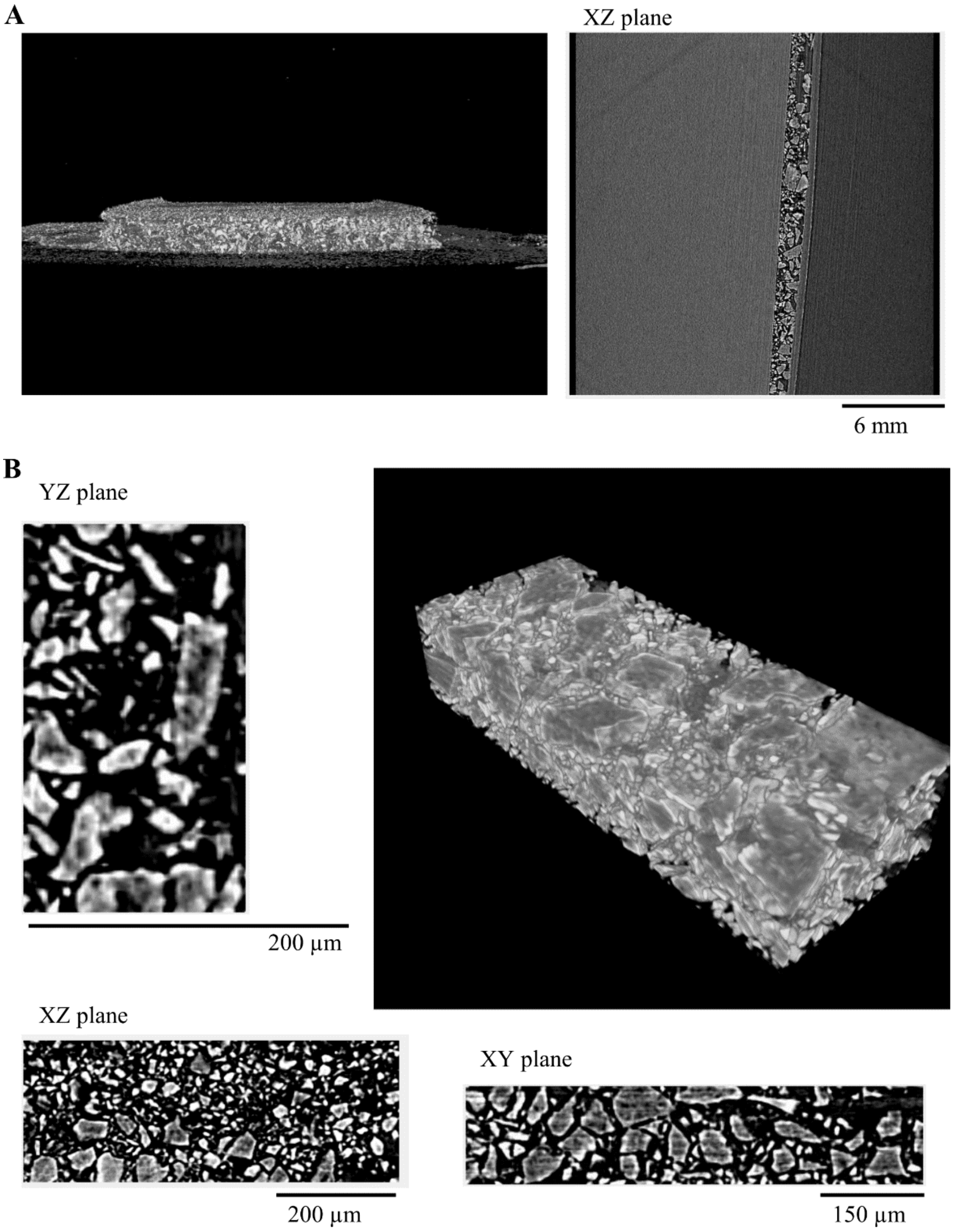

Figure 4.4 Compiled 3D renderings of micro-CT images for PDMS channels filled with silica extracted from SC sand, showing (A) overall channel structure and (B) region of interest used for void volume analysis.

Figure 4.5 shows the signal produced by each assay format for two residence times/flow rates. For all assay formats, increasing residence time of the substrate with the immobilised enzyme (longer reaction time or slower flow rate), increased fluorescence signal. This is expected considering no product inhibition is anticipated and the amount of enzyme added was calculated not to achieve total consumption over even the longest residence time of 14 minutes (endpoint assay showed total consumption only at 40 min with 1.5 times the silica weight used here, see Figure 2.30). In addition, at all flow rates/residence times studied, the fluorescence signal from the falling particle device was greater than the two other formats explored here. An analysis of the expected kinetics by particle-bound enzymes in the packed bed and in simple suspension can help explain the relative performance of the formats.

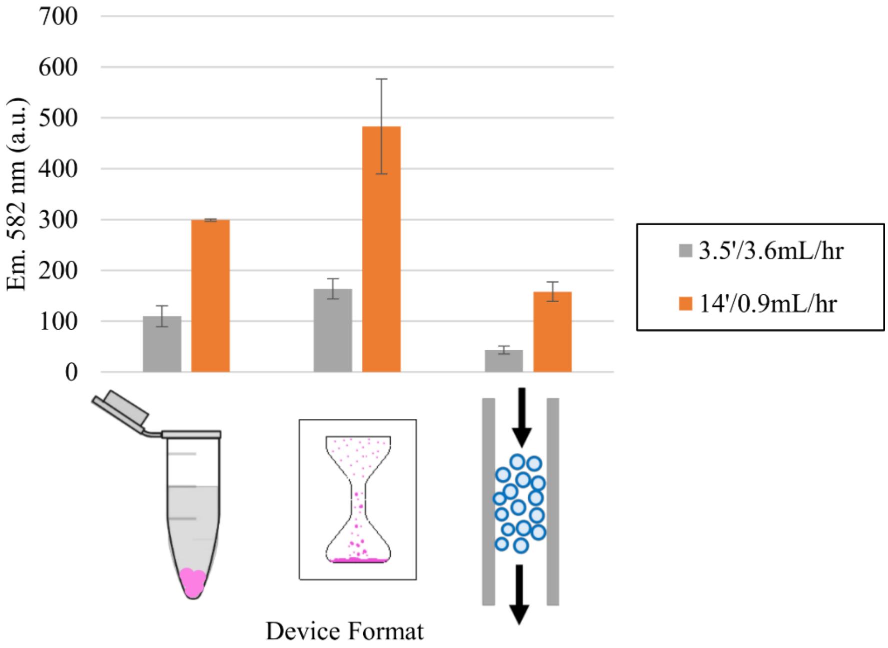

Figure 4.5 Fluorescence signal (ex. 530 nm/ em. 580 nm) in the presence of 5 µM sarcosine for three assay formats (microcentrifuge tube, narrow waisted channel and packed bed) at residence times/flow rates of (grey) 3.5 min / 3.6 mL/hr and (orange) 14 min / 0.9 mL/hr.

A microfluidic channel filled with particles is essentially a small scale version of an industrial packed bed reactor (PBR). Product formation by the immobilised enzyme in a PBR is often described by the plug-flow equation [227,269]:

$$\frac{V_{max}hA}{Q} = [P] + K_m ln\left(\frac{[S]_0}{[S]_0 - [P]}\right) \tag{4.1}$$

where square brackets denote concentration of substrate (S) and product (P), hA is the void volume of the packed bed and Q is the volumetric flow rate applied to the bed. Derived by integrating classic Michaelis-Menten kinetics (Eq. (3.1)) along the length of a packed bed, this relationship accounts for the change in substrate concentration for each volume element along the length; however, this equation neglects the effects of mass transport to and from the surface (assumes $[S]_{surface} = [S]_{bulk}$). In some cases when this equation is used to model dependence of conversion rate on initial substrate concentration, it can result in apparent enzyme parameters being dependent on length of enzyme reactor and/or flow rate [270–273]. As discussed in Chapter 3, the rate of mass transport is related to the flow rate in the system. The Reynolds number for a packed bed (Re_{pb}) can give an indication of the flow regime and is typically expressed as:

$$\boldsymbol{Re_{pb}} = \frac{\boldsymbol{\rho_f * u_s * d}}{\boldsymbol{\eta_f (1 - \theta_v)}} \tag{4.2}$$

where ρ_f is the density of the fluid, η_f is the dynamic viscosity of the fluid, u_s is the superficial velocity of the packed bed, θ_v is the void fraction of the bed and d is the spherical equivalent diameter of the particle (typically mean diameter of the distribution). The superficial velocity, u_s, is the volumetric flowrate, Q, divided by the cross-sectional area of the packed bed channel. As the flow in packed beds is complex, the limits of Re_{pb} for laminar and turbulent regimes are not as well defined as those of the Reynold's number for pipe flow, but it is generally accepted to be laminar flow when $Re_{pb} < 10$. Calculating Re_{pb} for the flow rates used here with the mean diameter and void volume observed for the extracted silica returns $Re_{pb} < 10$ in all cases, indicating that the packed bed is operating under laminar flow. Although it is often suggested in reactor design to operate packed beds under turbulent flow to reduce mass transport limitations [227], the flow rates used for this comparison were selected specifically to mimic those of capillary-driven flow as non-equipment operation is preferable for resource-limited settings [18].

While it is important to consider the effects of mass transport in a biosensor design using a particle bed [269], there may be conditions where the effects are negligible (such as high flow rates leading to efficient mass transfer or low rates of conversion to product due to low enzyme activity or low enzyme loading). Under conditions where the effects of mass transport are negligible, the concentration of product formed is expected to be dependent on residence time with enzyme and hence inversely dependent on flow rate [227,269]. This dependence was observed for the packed bed format explored here (Figure 4.6) and suggests it is under kinetic control. This is unsurprising given the low enzyme activity of the silica-R5$_2$-mCh-mSOx-R5-6H after drying (Chapter 2).

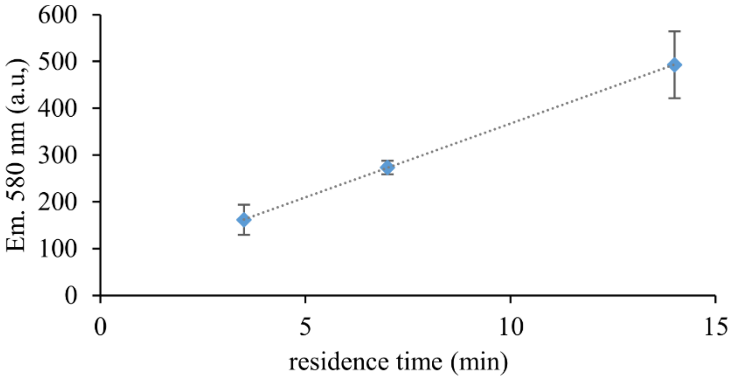

Figure 4.6 Fluorescent signal of outflow against residence time for the packed bed format. The results from Figure 4.5 have been combined with an additional residence time of 7 min corresponding to a flow rate of 1.8 mL/hr.

Given both the falling particle and packed bed formats are expected to be kinetically controlled, the reduced signal observed for the packed bed could be the result of reduced accessible surface area (and thus, enzyme) in this format compared with the surface area exposed during the dispersion observed in the falling particle device. More than point contact of the particles against one another in the packed bed due to the non-spherical nature of the silica could reduce the accessible surface area. While some evidence of this is observed in the micro-CT images of the packed bed in Figure 4.4, the packing observed does not suggest sufficient surface contact to explain the ~70 % reduction in signal observed (Figure 4.5).

The reduction in signal may also be the result of the formation of channels preferential for fluid flow, or channelling, resulting in some of the substrate passing through the channel more rapidly while other areas are stagnant or experience a negligible flow rate. Channelling is known to occur in PBRs and results in deviations from ideal behaviour [227]. For example, Luckarift *et al.* observed that in a small-scale PBR filled with butylrlcholinesterase entrapped in silica nanospheres (formed through co-precipitation with the R5-tag), the conversion rate decreased with time but could be regenerated. The authors did not observe this effect when the same encapsulated enzymes were employed in a fluidized bed format, and proposed that this type of behavior was the result of the formation of channels in the packed silica that lowered the overall retention time [136]. Channels form not only due to an excessive pressure drop or uneven application of the substrate stream, but also due to irregular packing. The latter is likely in the system explored here given the heterogeneity of the extracted silica. This suggests that improvements to avoid the formation of channels could improve the performance packed bed format. Although tightly controlled particle distributions may reduce the risk of channeling, this would add cost and complexity to the production of the silica particles. A change in the method to construct the packed bed could also provide a more uniformly packed bed, however, the incorporation of particles into packed beds on microchips remains a challenge as the classical methods of column preparation in chromatography function poorly at the microscale [274].

In the case of simple suspension of the particles in a microcentrifuge tube, good dispersion of the particles was observed when the sample was initially mixed with the particles. After 1 min, 76.3 ± 0.4 % particle mass had settled, and the remaining settled over the next few minutes of the assay. Once the particles have settled, they can be expected to consume at a similar rate to the settled bed in the falling particle design. For silica extract, the stationary settled bed of particles consumes substrate at a lower rate compared to the dispersed falling particles, as shown experimentally in Figure 3.35. Hence, a larger contribution to the overall signal is expected from the initial period where the particles are dispersed and settling as compared to the contribution from the remainder of the assay where the particles have settled and likely begin experiencing local substrate depletion. If, on the other hand, substrate consumption occurred at a constant rate in this system, the signal would increase linearly with time; thus, a ratio of 25 % would be expected when comparing the signal produced in 3.5 min to that produced in 14 min. In the case of the tube assay, the signal at 3.5 min is ~37 % of the signal at 14 min, which supports the greater contribution of the initial dispersion to the overall signal. The increase in signal from dispersed particles likely also explains the reduced signal of the simple suspension in a tube relative to the falling particle design, as the latter achieves greater dispersion of the particles over the same period of time through repeated flips of the device.

The superior performance of the falling particle format with respect to signal generation as compared with the other two assay formats is encouraging. Nonetheless, its batch format may not be suitable for all enzyme assays, such as those processes involving product inhibition. In these cases, packed beds are the preferred design, all other factors being equal [227]. Packed beds can also avoid potential enzyme inactivation due to shear and abrasion during particle collisions [86]. However, packed beds also face the challenges of clogging resulting in stopped flow, especially with heterogeneous catalyst particles like the silica extracted from sand. In contrast, batch formats, like the falling particle design, have the benefit of simplicity of process development and use, which could be advantageous for a diagnostic platform, especially one intended for production and use in resource-limited settings.

For the falling particle system to have clinical utility as a biosensor, it must support detection of the target substrate within the relevant range for the clinical condition. Given these comparative tests were performed with sarcosine concentration (5 µM) within the clinically relevant range for prostate cancer [157,158] and sufficient fluorescent signal was generated for detection within 5 min, this suggests that falling particle format has the potential to enable a POCT biosensor for sarcosine detection.

4.3.2 Towards a POCT for sarcosine using the falling particle design

Although the detection of sarcosine by fluorescence requires the cascade from SOx to HRP, the performance of the fusion proteins in the falling particle format was initially tested separately for peroxide and sarcosine measurement, using HRP-mCh-R5-(6H)-silica or silica-R5$_2$-mCh-mSOx-R5-6H, respectively (Figure 4.7 and Figure 4.8).

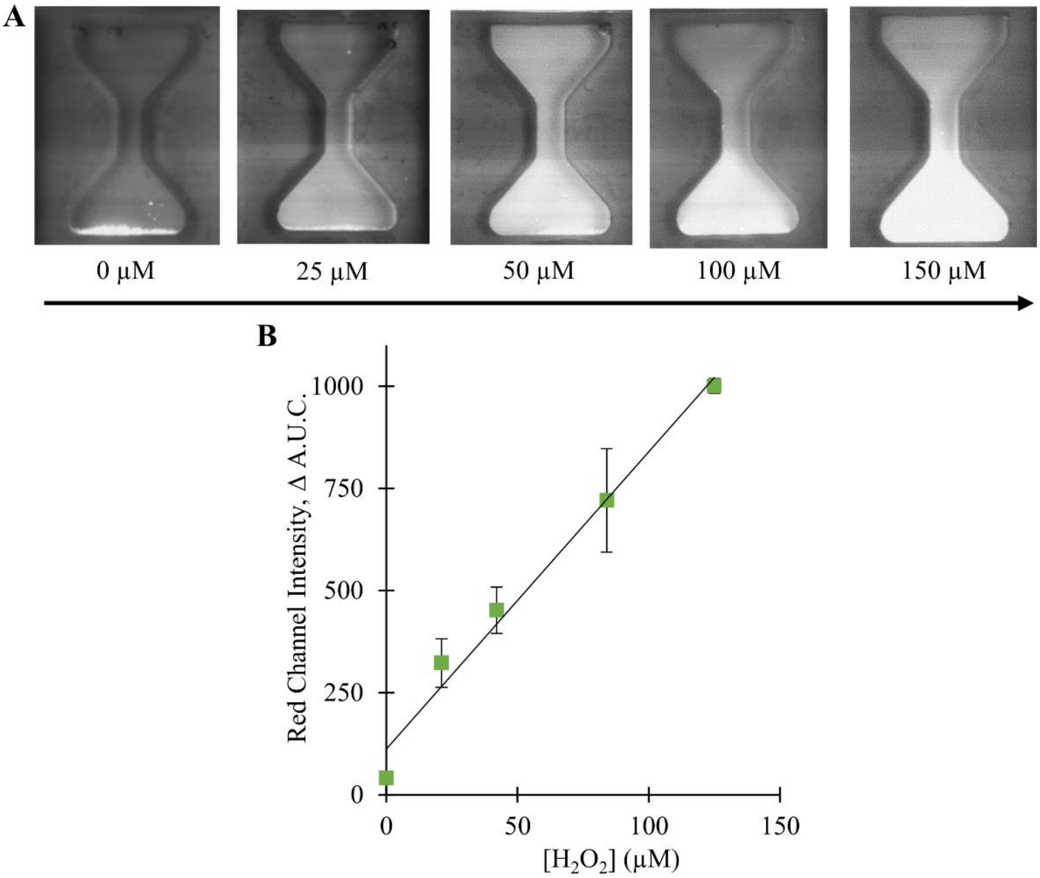

Figure 4.7 Immobilised HRP-mCh-R5-(6H) on silica extracted from sand used in the narrow waisted device for H_2O_2 detection. (A) Images taken following two device inversions with 60 s settling and 5 min stationary signal development. (B) The change in fluorescence over the stationary 5 min, where fluorescence is the AUC of a central line plotted perpendicular to the base.

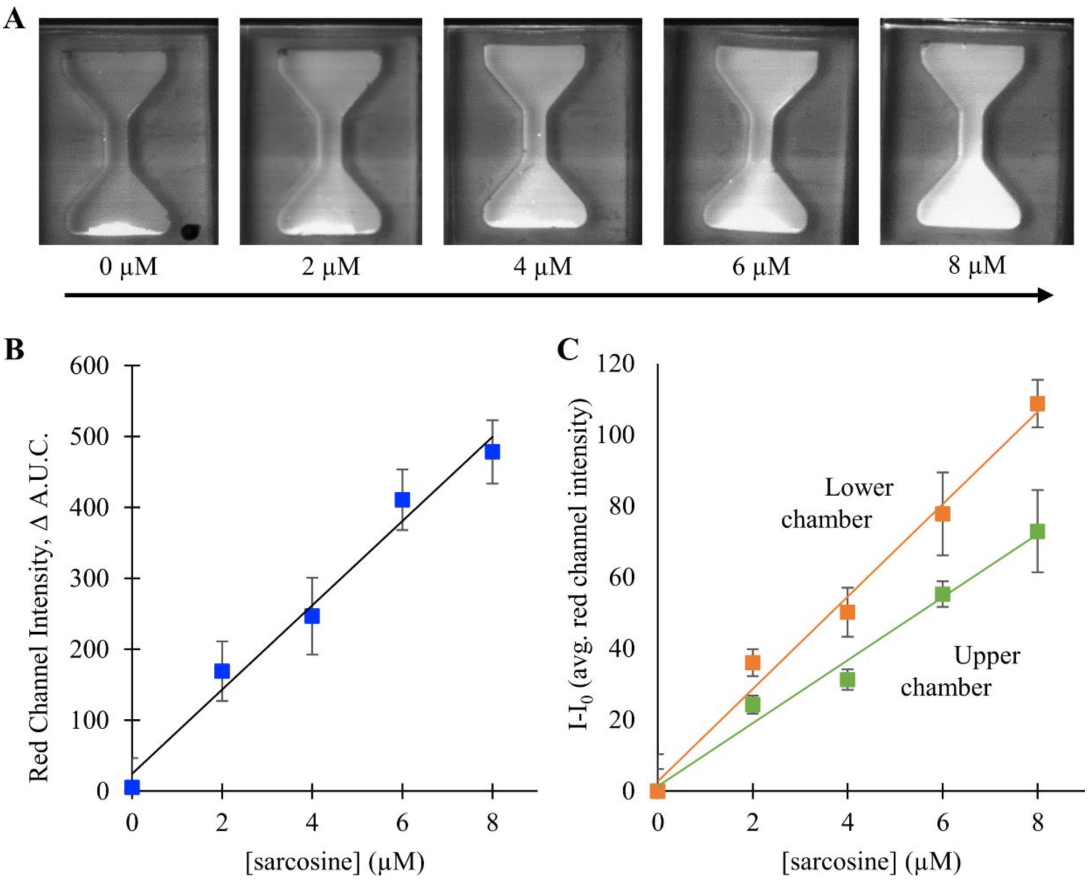

Figure 4.8 Immobilised R5$_2$-mCh-mSOx-R5-6H on silica extracted from sand used in the narrow waisted device for sarcosine detection. (A) Images taken following two device inversions with 60 s settling and 5 min stationary signal development. (B) The change in fluorescence over the stationary 5 min, where fluorescence is the AUC of a central line plotted perpendicular to the base, and (C) average red channel intensity of the upper and lower chamber of the device at 7 min plotted against sarcosine concentration.

Figure 4.7A and Figure 4.8A show visually that the fluorescence increases in the device with concentration of substrate. The fluorescence intensity was measured and the intensity plotted on a trajectory perpendicular to the base through the central line of the chamber. The change in area under the curve (AUC) over 5 min shows a linear relationship ($R^2 > 0.98$, see Table 4.2) with concentration for both hydrogen peroxide and sarcosine (Figure 4.7B and Figure 4.8B, following two inversions). The different concentration ranges measured for these two silica-bound enzymes within the same time period reflect their different activities (Chapter 2).

The plots in Figure 4.7B and Figure 4.8B use the rate of fluorescence signal development from the stationary settled bed after two inversions of the device to determine substrate concentration. As discussed in Chapter 3, flipping the system every 60 s until the signal time point increased the overall rate of signal development in the device (Figure 3.35), and thus could increase the sensitivity of the assay. Figure 4.9 shows the results for the silica-R5$_2$-mCh-mSOx-R5-6H using this approach, both visually and with average intensity results at 7 min. (The performance of the HRP-mCh-R5-6H-silica was not investigated with this protocol given the signal increase observed with the change in protocol (~2-fold) was unlikely to overcome the inherently poor activity of the enzyme to reach the desired range of substrate detection. This will be discussed further with respect to the assay combining both constructs below). Good linearity of average fluorescence intensity with sarcosine concentration ($R^2 > 0.98$) is observed with the multi-inversion approach along with a lower limit of detection (LOD) as compared to using the two inversion technique (Figure 4.9B versus Figure 4.8C, respectively). Comparing the average signal in the top and bottom compartments following the multi-inversion protocol shows consistent distribution of the signal throughout the device; no significant difference is observed in the slopes of the linear regression for the top and bottom chambers (confidence interval (CI) = 95 %, see Table 4.2). In contrast, the upper chamber under the stationary protocol shows reduced intensity (Figure 4.8), as would be expected with conversion of substrate largely by the settled bed. Nonetheless, the dissimilarity in slope is not significantly different (CI = 95 %) between the two chambers.

Table 4.2 Linear regression results, where slope and intercept are reported with 95 % confidence intervals. Protocol A and B refer to 7 inversions or 2 inversions with 5 min stationary, respectively. LOD is calculated based on slope and standard deviation of the blank, as described in Eq. (2.5).

Figure	Enzyme	Protocol	Chamber	Slope	Intercept	R^2	LOD (μM)
Figure 4.7B	HRP	B	-	7.3 ± 1.8	111 ± 128	0.981	11.3
Figure 4.8B	mSOx	B	-	59.4 ± 14.8	24.4 ± 72.8	0.981	3.9
Figure 4.8C	mSOx	B	Upper	8.8 ± 2.3	1.38 ± 11.0	0.985	3.9
Figure 4.8C	mSOx	B	Lower	13.0 ± 2.8	2.7 ± 13.8	0.986	4.5
Figure 4.9B	mSOx	A	Upper	8.2 ± 0.6	-1.0 ± 3.7	0.996	2.7
Figure 4.9B	mSOx	A	Lower	9.1 ± 1.6	0.7 ± 10.0	0.983	2.4

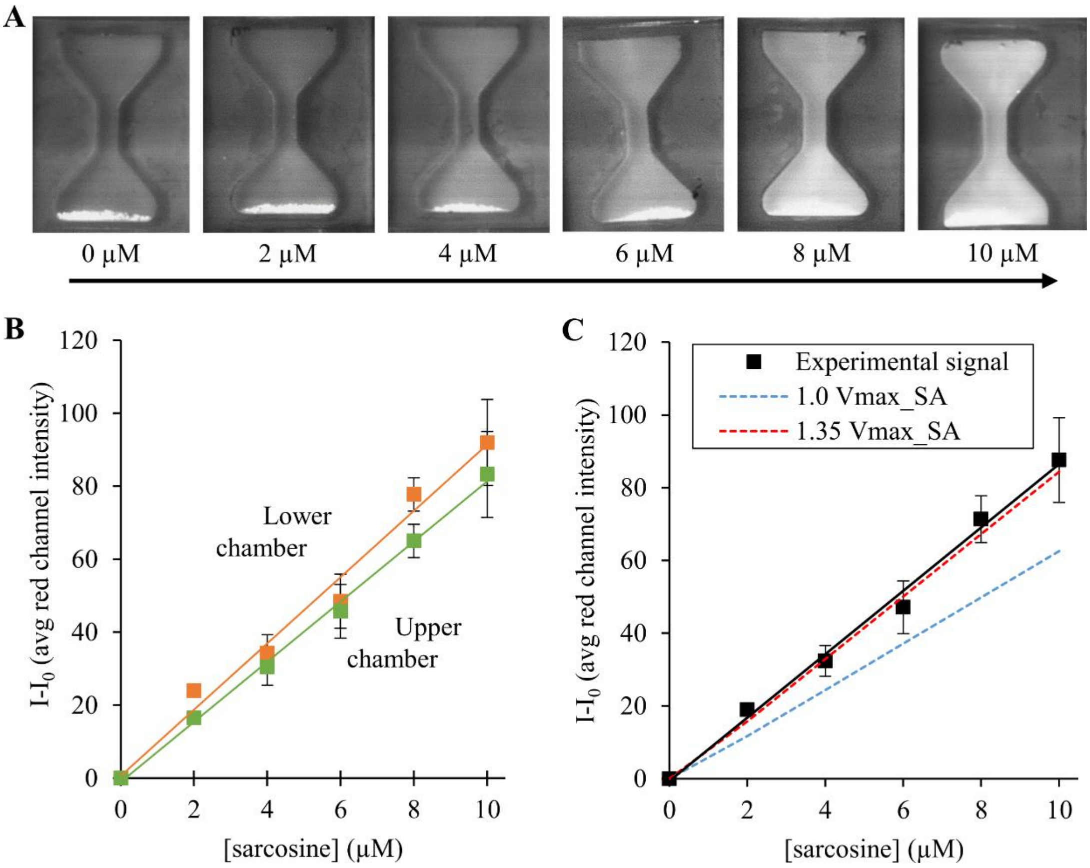

Figure 4.9 Immobilised R5$_2$-mCh-mSOx-R5-6H on silica extracted from sand used in the narrow waisted device for sarcosine detection. (A) Images taken 7 min after sample addition, following device inversions every 60 s. (B) Average red channel intensity of the upper and lower chamber of the device at 7 min plotted against sarcosine concentration. (C) Theoretical fluorescence intensity plotted with experimental results (average of top and bottom chamber).

The experimental results with the multi-inversion protocol can be compared against theoretical signals predicted using the model for product formation presented in Chapter 3 (Figure 4.9C). Predicted concentrations of product formed have been converted into fluorescence signal using the calibration curve for fluorescence in the presence of a known concentration of H_2O_2 (Figure 3.6B). While the experimental results are higher than predictions made with the V_{max_SA} value used in Chapter 3, this difference could be explained by a difference in enzyme activity; only a 35 % increase in V_{max_SA} is required to observe a good fit of the model with experimental results.

The detection range (2.5 to 10 µM) for this assay format corresponds to the range required to detect elevated sarcosine levels in the urine of prostate cancer patients (> 5 µM [157,158,181]). However, the change in fluorescence intensity per micromolar unit of sarcosine concentration (as determined by the slope of the linear regression, Table 4.2) is of the same magnitude as the standard deviation in intensity measurements for discrete concentrations. This suggests that this assay may be suitable for semi-quantitative detection (high/low level of sarcosine) rather than quantitative measurement. Semi-quantitative tests can be powerful tools as POCTs, but in the event that quantitative results are required, controlling total enzyme activity in the system will be particularly important, given the likelihood of kinetic control for this system (as discussed in Section 3.3.3).

In light of the dependence of enzyme activity, it may be desirable to design an endpoint assay where the signal is correlated with total substrate in the sample rather than reaction rate. Thus, provided the detection time point is set based on the lowest activity of the expected range for the enzyme and the signal is stable once developed, an endpoint assay would be largely insensitive to small changes in activity. Following a similar protocol explored in Chapter 2 with the bio-functionalised particles in a well plate, an endpoint assay could be developed by designing a falling particle chamber with a smaller volume; Figure 4.10 shows a 50 µL waisted chamber imaged at 60 min with clear visual distinction between 0, 2 and 10 µM sarcosine as a preliminary example of this approach. The smaller volume also potentially lends itself to assays on clinical sample types where volume is limited and collection is onerous, such as blood. However, achieving an endpoint assay within a reasonable time frame for a POCT requires adding more reagents, which increases the final cost of the test. This would need to be balanced against the cost of achieving consistent activity between batches and throughout storage in order to select an approach for a falling particle POCT using silica-R5$_2$-mCh-mSOx-R5-6H.

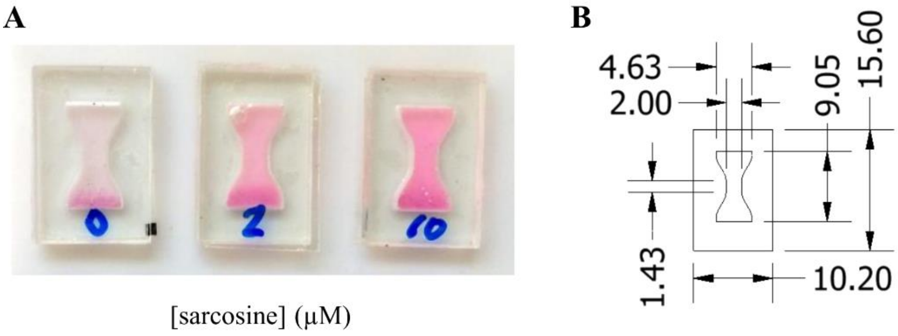

Figure 4.10 Endpoint assay showing (A) visual detection of fluorescence in 50 µL mini-chamber at 60 min and (B) dimensions of the design.

The performance of the separately immobilised fusion constructs suggests that achieving sensitive detection with the multi-enzyme cascade combining separately immobilised HRP-mCh-R5-(6H)-silica and silica-R5$_2$-mCh-mSOx-R5-6H may be challenging. Nonetheless, Figure 4.11 shows an initial proof of concept for multi-enzyme cascades in the falling particle device. The lowest concentration detectable with this 2-enzyme system was 100 µM sarcosine, so an increase in sensitivity would be necessary to make this system applicable to clinically relevant range of sarcosine in urine for prostate cancer detection (< 10 µM) [157,275].

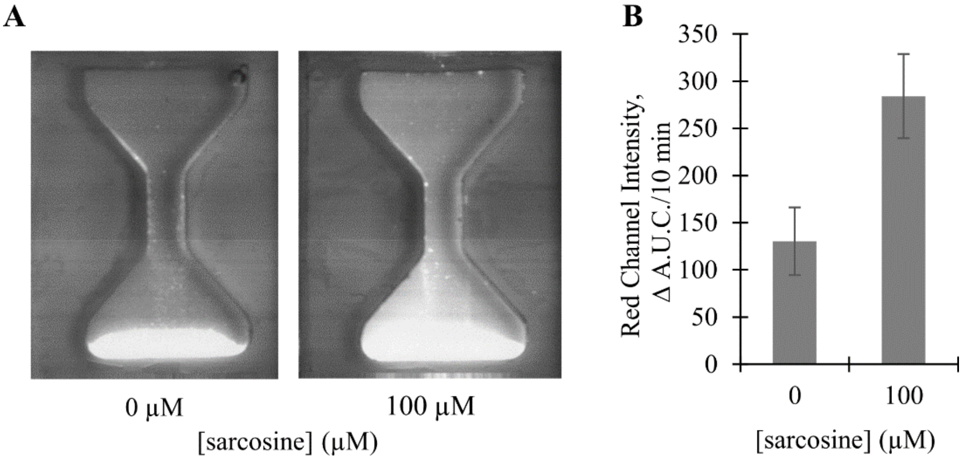

Figure 4.11 Detection of sarcosine via AR fluorescence in the (A) narrow waist design using multi-enzyme cascades combining separately immobilised HRP-mCh-R5-(6H)-silica and silica-R5$_2$-mCh-mSOx-R5-6H, with (B) corresponding change in AUC for red channel intensity plotted on a trajectory perpendicular to the base through the central line of the chamber.

In the design of multi-enzyme cascades for the detection of a target species, the total activity of the downstream enzyme in the system (e.g. HRP) should exceed that of the substrate specific enzyme (e.g. mSOx) such that the rate of reaction is dependent on the species of interest. Generally, the efficiency increases as the ratio of activity of second enzyme compared to the first enzyme increases [276]. However, in this instance, k_{cat}, or turnover rate, for immobilised HRP-mCh-R5-6H is only ~ 6 % of immobilised R5$_2$-mCh-mSOx-R5-6H (based on specific activity after drying, Chapter 2). This suggests the low activity of the HRP-mCh-R5-6H is limiting the sensitivity of the assay and makes optimisation of this assay challenging. A range of strategies could be explored to overcome this limitation, as outlined in Figure 4.12 and discussed below.

An increase in the overall substrate conversion rate in the system could be achieved by increasing the concentration of HRP. With the particle-bound enzymes, increasing the concentration of HRP in the assay would involve increasing the mass of silica added and/or increasing the enzyme surface coverage (ESC) of the silica (Figure 4.12A and B). Using the experimentally determined values of k_{cat} and ESC for silica functionalised with HRP-mCh-R5-6H, it is possible to estimate the mass of silica needed such that the overall turnover rate would be in excess relative to the rate of product formation by the immobilised $R5_2$-mCh-mSOx-R5-6H (assuming kinetic control rather than mass transport). Keeping ESC consistent with experimental conditions above, > 70 mg of silica would be required for the relative turnover rates to be at least 1:1. In the case of HRP-mCh-R5-6H, poor levels of expression resulted in a low concentration used during immobilisation, which corresponded to a ESC below the capacity of the extracted silica (ESC = 128 mg protein / m^2 silica surface area). However, even with an increase in ESC to the loading observed for $R5_2$-mCh-mSOx-R5-6H on the extracted silica (ESC = 573 mg protein / m^2 silica surface area), a 1:1 ratio of turnover rates would still require > 15 mg of silica. This would take up ~10 times more volume in the system (~4 % total volume) and would likely cause a significant change in the behaviour of the falling particle system that would require further investigation.

However, this preliminary demonstration of the 2-enzyme combination on silica in the falling particle sensor has the R5-mCh-Enzs immobilised separately. Alternatively, the enzymes could also either be co-immobilised on the silica or introduced as part of a larger fusion enzyme (Figure 4.12C and D). Both strategies have been shown to improve activity. For the fusion route, it has been previously shown for a multi-enzyme bioluminescence resonance energy transfer pairing [277] that this route is only advantageous if a 1:1 ratio is needed. In addition, the large size of such a fusion protein would likely be a disadvantage for expression in *E. coli* as large proteins require more metabolic energy during overproduction [142]. They also tend to drive the formation inclusion bodies [123], which adds time and complexity to purification and immobilisation.

Dual catalysts (where enzymes are immobilised on the same particle) are generally superior to mixed catalysts (separate particles) when it comes to reaction efficiency [276] and co-assembly of the paired enzymes in close proximity has generally shown several-fold signal enhancement relative to the soluble system [278,279]. However, both theoretical and experimental work show the benefit of proximity only when there is generation of a favourable microenvironment with respect to concentration of the intermediate (e.g. bi-enzyme aggregates perform no better than soluble enzymes [278]). Thus, the facilitated transport of the intermediary product from one enzyme to another owing to proximity is a temporary effect that is only relevant until the concentration of the intermediate substrate becomes significant (i.e. during the lag period of a two-step reaction). A decreased lag phase is observed in the case of co-immobilised enzymes because local concentration of the intermediate within the domain of the particle is higher than in the bulk; thus, the second enzyme sees a more favourable concentration of the rate-limiting intermediate substrate. In contrast, enzymes on separate particles operate in a larger effective volume than the co-immobilised system, so the build-up of intermediate concentration takes longer time, and therefore the lag phase is longer. However, given kinetic control is predicted for the R5-mCh-Enz fusion proteins on silica extract (Chapter 3) and this multi-enzyme system involves a small-molecular intermediate (peroxide) with a high diffusion coefficient, the lack of proximity due to separate immobilisation is unlikely to be the rate limiting step. Instead, the final activity of the cascade is dependent on the slower enzyme, HRP-mCh-R5-6H. Thus, significant improvements in the activity (i.e. turnover rate per reaction site) of the fusion proteins with HRP would be required to achieve a 2-enzyme system using silica-immobilised R5-mCh-Enz in the future.

Further improvements in the activity of the immobilised HRP could come with further modifications to the genetic sequence and/or improvements in the expression. There are over 40 isoenzymes of HRP and they vary in their activity (Figure 4.12E). For example, HRP isoenzyme C1a (as used here) demonstrated a higher activity with the colorimetric substrate 3,3’5,5’-tetramethylbenzidine (TMB) than isoenzyme A but lower activity with another substrate, ABTS [195]. Thus, the choice of the HRP isoenzyme for a diagnostic should be based on the colorimetric substrate to achieve optimal assay sensitivity. With respect to expression, recombinant HRP expressed in *E. coli* has been previously reported with activity similar to the isoenzyme isolated from the plant [160]. However, the challenges in recombinant expression of HRP (as mentioned in Chapter 2) that result in low yields and time-consuming, reagent-heavy re-activation steps may ultimately limit the applicability of the immobilisation approach using recombinant expression with an affinity tag for this protein.

Alternative approaches for immobilisation of plant-extracted WT HRP exist if an entirely particle based sensor is desirable, e.g. glutaraldehyde crosslinking (as shown in a parallel publication by the author with collaborators [181]). Although a loss of activity compared to the soluble form was observed for WT HRP following glutaraldehyde crosslinking (consistent with other reports of reduced activity following glutaraldehyde crosslinking [280]), the immobilised HRP retained sufficient activity to avoid limiting the assay pathway with SOx. However, this alternative immobilisation method is outside the scope of a local production approach that uses molecular biology to produce the biological components and achieve reagent-free immobilisation. To eliminate the need for HRP altogether, an electrochemical approach which detects the peroxide product produced by SOx, akin to the detection approach in the ubiquitous glucose meter, could be explored in place of the fluorimetric approach taken here. Figure 4.12 provides a summary of the strategies discussed above for overcoming the low activity of the HRP fusions with R5-mCh that could be explored in future work.

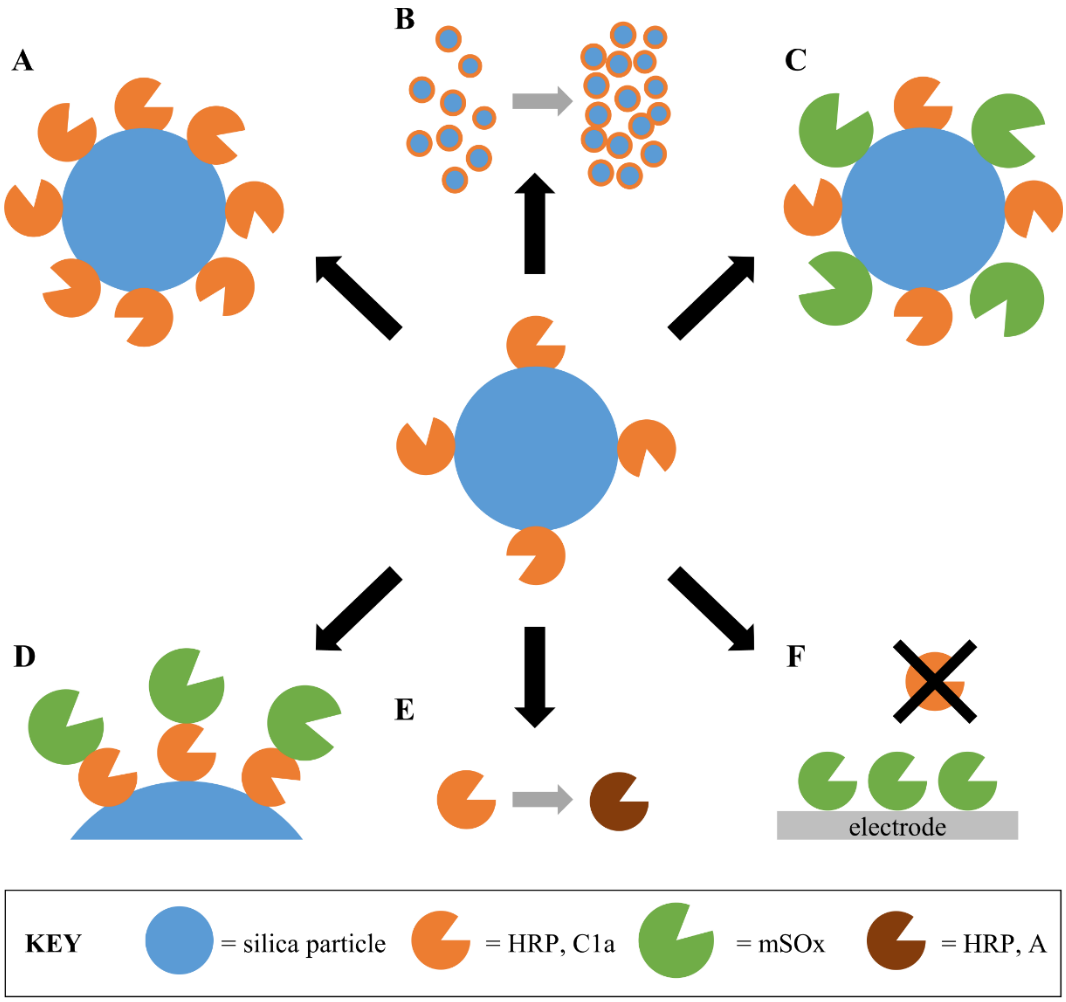

Figure 4.12 Potential strategies for overcoming the limitation of HRP's low activity within a local production approach. One approach is to increase the concentration of HRP in the assay by (A) increasing the enzyme surface coverage (ESC) of the silica and/or (B) by increasing the mass of silica added. Another approach is to decrease the distance that the co-product has to travel between HRP and mSOx by (C) co-immobilisation of separate fusion proteins or (D) design and expression of a larger fusion protein containing both enzymes. Alternative strategies include (E) change of isoenzyme or (F) eliminating the need for HRP altogether with an electrochemical approach. (For simplicity the mCh and R5 subunits have been left out of this diagram.)

4.4 Summary

This chapter explored a range of simple, low-cost designs for a biosensor using the silica-immobilised R5-mCh-Enzymes developed in Chapter 2. The falling particle format explored in depth in Chapter 3 was compared against more classical formats of simple suspension in a microcentrifuge tube and a packed particle bed. The falling particle device outperformed both formats under the conditions studied, likely by achieving good dispersion and thus more enzyme with access to substrate in this kinetically controlled system. However, as discussed in Chapter 3, further simulation of the reaction kinetics in particle clouds and in the settled bed are required in the future to be able to optimise the design of the falling particle system.

Proof of concept was shown for the detection of H_2O_2 with HRP-mCh-R5-(6H)-silica and for sarcosine with silica-$R5_2$-mCh-mSOx-R5-6H across a range of concentrations. The latter showcased an acceptable range of detection for elevated sarcosine levels in the urine of prostate cancer patients (> 5 µM [157,275]) when used with WT HRP. If a fully quantitative result is desired, some improvements in the signal-noise ratio would be required. Nonetheless, the system has potential as a semi-quantitative POCT that could help triage patients by quickly indicating when additional, more invasive tests should be performed.

In addition, further improvements in the activity of R5-mCh-Enz fusion proteins with HRP would be needed for a silica-based reagent system that is capable of the sensitivity required for prostate cancer detection. Alternatively, an electrochemical approach could be explored in the future that would eliminate the need for HRP altogether. This approach will be discussed in the next chapter alongside other improvements which would be necessary to move towards a POCT for sarcosine. Other applications for the falling particle biosensor format and, more generally, for a local production approach through recombinant expression with affinity tags for low-cost materials will also be discussed.

5 CONCLUDING REMARKS

5.1 Summary of findings

With access to diagnostics unaffordable in vulnerable LMICs, there is a need to consider a different approach that doesn't presume the use of expensive off-the-shelf reagents. The overall goal of the research was to explore whether recombinant protein technology in combination with a low-cost support matrix could provide a basis for an inexpensive, simple, and robust production process for the bio-sensing element of a diagnostic. Given its wide-availability and biocompatibility, silica was selected as the low-cost solid support for this work.

The fluorescent protein mCh and the enzymes SOx and HRP were employed as first models of biological reagents. Downstream processing of these reagents was reduced by employing the affinity binding sequence for silica, R5, in fusion with the central assay reagent protein targeting the analyte. The R5 peptide was shown to have affinity for silica comparable to the His-tag affinity for Ni-NTA resin classically used in protein purification ($K_D \approx 1 \times 10^{-6}$ M). Simultaneous isolation and immobilisation onto silica carrier particles was achieved directly from lysate without the use of chemical coupling reagents, with 95 % of the immobilisation occurring in less than 5 minutes. In addition, it was shown that by incorporation of a coloured protein in the fusion construct design the protein production and immobilisation could be followed visually without major infrastructure resources.

Functionality was largely retained in the fusion proteins, before and after immobilisation. The fluorescence emission spectra and lifetime values of the mCh subunits were comparable to expected values for this fluorescent protein, indicating correct folding of the protein. Both HRP constructs were observed to have similar specific activities after refolding in the presence of heme; however, both the soluble and immobilised versions only showed minimal activity when compared to the commercially available WT HRP. This was shown later to be a limitation towards their use in a platform with the fusion SOx for the detection of sarcosine, as HRP should have activity in excess of its oxidase partner in the coupled enzyme assay.

For R5$_2$-mCh-mSOx-R5-6H, specific activity for both soluble form and immobilised was observed to be of a similar order of magnitude as WT SOx. In addition, a comparable limit of detection was achieved with immobilised fusion protein as with the soluble form. Although the drying process should be improved in the future to prevent loss of activity, the dry reagent retained what activity remained for over two months at room temperature, an advantage compared to the soluble reagents. Taken together with the reduced downstream processing achieved by a one-step purification and immobilisation approach, this supports the use of directly immobilised reagents in the development of POCTs.

Sand was investigated as a natural source for silica using a simple extraction process of alkali treatment and subsequent acidification. While not all sands produced sufficient yields of silica, yields of 11.5 ± 1.4 % and 4.7 ± 0.9 % weight were obtained for beach sands from South Carolina (SC) and Ghana (GH), respectively. These sands showed higher Si counts in XRF analysis, which suggests that only sands with high silica content may be suitable as source materials for the production of the low-cost purification matrix.

FTIR spectra of the dried precipitates from this extraction process showed characteristic spectra for Si-O-Si and Si-OH groups, confirming the presence of silica. Comparative TGA with commercially produced silica suggested other inorganic components may be present in the extracted silica and XRF analysis highlighted in which elements differences exist. Nevertheless, all extracted silica supported purification and immobilisation of the fusion proteins, which indicates that these trace elements have limited effect on the binding interaction between the affinity peptide and the silica particles.

Immobilisation was demonstrated to be largely on the surface of the particles for both extracted silica and for silica gel with pore size of 60 Å in spite of an observed difference porosity determined by N_2 adsorption/desorption studies (non-porous / macroporous and mesoporous behaviour, respectively). Increasing the average pore size of commercial silica gel from 60 Å to 150 Å increased the immobilisation efficiency for an equivalent size class of particles, which is in line with the expected size of the fusion proteins. Despite an increased immobilisation efficiency, less activity was observed for the 150 Å pore silica gel. This suggests that the enzymes immobilised in the pore are not as accessible for the reaction with the analyte, and hence, primarily surface immobilisation is desirable. Compared to commercially available silica distributions, silica extracted from sand was shown to have higher enzyme loading capacity per mass of silica. Therefore, silica extract not only supports R5 mediated binding, but is preferred over commercial silica gels when high surface loading is desired.

Silica particles not only make the process of separation and purification simple, but they also function as a versatile protein-silica preparation for many classical assay formats, like microfluidics, as well as more innovative designs, like the novel falling particle biosensor presented here. The sedimentation pattern of the particles in a falling particle approach was studied using PIV, which showed that a chamber shape with a narrow waist gave the best control of particle trajectory, creating reproducible settling position irrespective of inversion technique. Comparative analysis of expected kinetic and mass transport rates suggested that the rate of product formation by the falling particles was considerably under kinetic control for the fusion proteins. The product formation predicted by modelling for the immobilised R5-mCh-Enzymes matched well with experimental trends for a range of silica size distributions, supporting the conclusion that enzyme kinetics are dominating the rate of product formation in this system.

Under such reaction conditions, the increased enzyme loading capacity per mass of silica for the extracted silica corresponded to the fastest rate of signal development in the falling particle device. In combination with its settling ability for purification purposes earlier in the production process, and its potential to be produced on site from local materials, silica extracted from sand could support the in-country production of a POCT.

The performance of the falling particle design was compared against two other formats commonly employed with bio-functionalised particles: (A) simple suspension in a microcentrifuge tube and (B) a packed bed in a microfluidic channel. The falling particle device outperformed both formats under the conditions studied (~ 150 % and ~ 325 % signal increase, respectively), likely by achieving good dispersion and thus, more accessible enzyme in this kinetically controlled system. Proof-of-concept was shown for the detection of H_2O_2 with HRP-mCh-R5-(6H)-silica and for sarcosine with silica-R5$_2$-mCh-mSOx-R5-6H across a range of concentrations in the falling particle device. The latter showcased acceptable detection in the clinically useful range in urine for prostate cancer [157,275]. However, further improvements in the activity of R5-mCh-Enz fusion proteins with HRP would be necessary for a silica-based reagent system that is capable of the sensitivity required for prostate cancer detection.

Nevertheless, this research has demonstrated a proof-of-concept for a “gene to diagnostic” pathway, highlighting the use of silica as a protein carrier and presenting a novel biosensor format for utilizing particle-bound enzymes. It is the hope that this research provides a first step towards reducing the hurdles to local production of biosensors in LMICs.

5.2 Suggested future work

In light of the findings from this research, a few key areas were identified in which further work would be required to progress towards a locally-produced POCT – (1) stability of the reagent, including greater retention of activity during the drying process, (2) further development of assay formats with silica-immobilised reagents to optimise signal output, and (3) development of a handheld imaging system for interpretation of the fluorescence results. This section will describe some promising avenues for the next stages of research into these areas.

5.2.1 Stability of the reagent

This work explored the use of immobilised reagents stored in a dry form. Once dried, silica-immobilised R5$_2$-mCh-mSOx-R5-6H was shown to largely retain its activity when stored at room temperature for over two months. This stability without refrigeration would be an advantage for the use of these reagents in remote areas as refrigeration is often lacking [26] and the expense of cold-chain distribution can account for large portion of the cost [40]. However, there was a significant loss of activity during drying, which indicates the need for further improvements in this step of the process.

Lyophilisation, or freeze-drying, is one of the oldest methods for post-treatment of an immobilised enzyme aimed at improving their storage stability [281]. This process involves quickly freezing the product and placing it under extremely low pressure to induce sublimation of water content from the material. However, the cost of the specialised equipment to perform lyophilisation can be substantial, and may be prohibitive towards a local production process.

Enzyme stability during dehydration can also be improved by the addition of sugars [203,282]. Sugars are common additives during the lyophilisation process [281] but they can also protect enzymes even when dried under ambient or even higher temperatures (e.g. 37 ^{0}C [283]). They are hypothesized to protect proteins by (i) preventing molecular mobility (vitrification hypothesis) and/or (ii) preventing changes in protein structure by replacing hydrogen bonds between the protein and water (water replacement hypothesis). Ideal sugars are thought to be relatively small with a relatively high glass transition temperature [282], e.g. trehalose [283] and sucrose. Interestingly, sarcosine was shown to increase the thermal stability of enzymes co-precipitated with the R5 peptide [136], however, this strategy would clearly not be suitable for a SOx-based biosensor. Future work should look to compare the stabilising capacity of different sugars during drying of silica-immobilised R5-mCh-Enz proteins, varying the protein-sugar ratio and the drying regime to find the optimum conditions.

5.2.2 Optimisation of assay formats with functionalised particles

Although the falling particle design explored in this work enabled signal production at a faster rate than either the packed bed or simple suspension approach, the design parameter space for this approach has yet to be fully explored. Design changes could include varying the particle volume fraction as well as optimisation of the aspect ratio, including not only height and width of the chamber but also depth (transitioning from a largely 2D design to 3D space). On the condition that further modelling and simulation confirms that particle dispersion is the advantage of the falling particle approach, designs should be considered that increase the time particles spend in suspension. Figure 5.1 provides a diagram of some of the design options discussed below.

Adding mechanical mixing or flow-driven dispersion (akin to stirred tank and fluidised bed reactors in classical reactor design [227,284–286]) would add cost and complexity, making such approaches impractical for the design of a disposable device. Instead, as mentioned in Chapter 3, magnetisation could be considered to induce particle movement via an external component (Figure 5.1A). This could be accomplished either by inclusion of additional magnetic particles in the system or by incorporating the magnetic component into the bio-functionalised particles (e.g. silica shell particles with magnetic cores [261] for use with the R5 peptide or a change of peptide sequence to one with affinity for bare magnetic nanoparticles [287–290]). If incorporated as part of the affinity matrix for the biological reagent, the magnetic nature could be also utilized in purification. However, the addition of magnetic particles would add cost and complexity to the production process.

Alternatively, a system of neutrally buoyant particles could be considered where dispersion would be maintained without requiring intervention beyond the initial shaking to distribute the particles throughout the fluid (Figure 5.1B). This could be achieved by increasing fluid density to match that of silica or more likely (because the fluid is determined by the nature of the sample), decreasing particle density by changing material. For instance, the polystyrene or polyethylene microspheres typically used in PIV analysis of flows (with densities near to 1 g/cm^3) could be coated with a silica shell before functionalisation with R5-mCh-Enz. Although neutrally buoyant particles would be advantageous for dispersion, they would have limited utility during the earlier purification stage. Moreover, the additional synthesis steps required for coupling R5-tagged proteins with such particles would again add cost and complexity to the production process.

Without transitioning from silica particles, chamber shapes can be considered that contribute to increased dispersion time. For instance, a helical channel creates an extended settling length without drastically increasing the overall length of the device (Figure 5.1C); however, this geometry is known to lead to the size segregation of particles through the simultaneous application of gravitational and centripetal forces on the particles [291]. In addition, the particles in a helical design would require a steep helix angle to avoid collecting the smallest particles on the inclined surface. Alternatively, a rotating drum or torus could be used to provide continuous movement of the particles relative to the fluid, achieving dispersion over time rather than space (Figure 5.1D). The rotational speed could be tuned to ensure the particles become suspended without being stuck to the outer wall by the centrifugal force. Similar to the optimisation of rotational speed for a drum or torus, the time between inversions of the falling particle device could be adjusted to achieve maximum dispersion and, correspondingly, signal output (Figure 5.1E). Decreasing the time between inversions should increase overall time of dispersion and preliminary results have shown an increase in signal. Nevertheless, this requires further experimentation to tune the timing of inversions with relation to particle size.

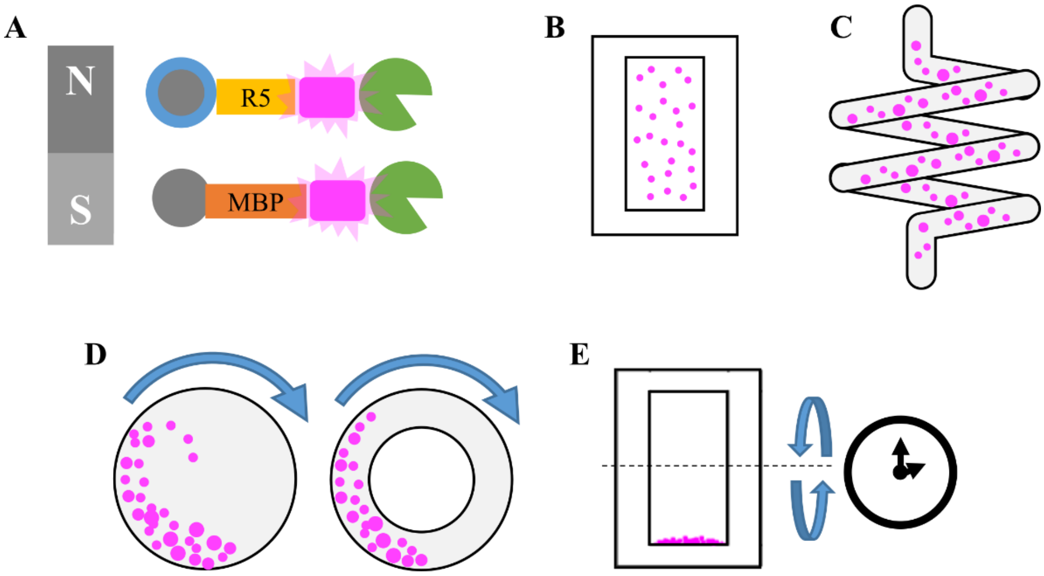

Figure 5.1 Potential approaches to achieving dispersion of particle-bound enzymes. (A) Particle movement driven by an external magnet, showing options of magnetic-core silica-shell particles for use with the R5 peptide or bare magnetic particles for use with a magnetic binding protein (MBP) incorporated with a fluorescent protein and the functional enzyme. (B) A suspension of neutrally buoyant particles in a chamber device. (C) A helix design for increased duration of particle sedimentation. (D) Rotating drum or torus. (E) Optimising the time between inversions of the falling particle chamber.

With a falling particle approach, the dispersion of the particles is also dependent on the size distribution of the particles. A narrower size distribution would achieve a more uniform settling time (excluding any initial particle plumes), which would reduce the time spent by particles in the inefficient settled bed at the base of the device. Despite its broad size distribution, the performance of the silica extracted from sand with respect to enzyme loading capacity and ultimately signal development was clearly superior to the commercial silica gel. Nonetheless, size selection could be used to further optimise its behaviour in the falling particle device. Particles should be small to maximise the enzymatic activity per unit mass and to achieve long settling times without lengthy reactor chambers, but not so small that the sediment laden portion of the fluid becomes a pseudo-immiscible fluid with the rest of the sample (as in the case of the silica nanoparticles). However, the time and cost of achieving a narrower distribution from the locally produced silica will need to be balanced against the benefit in assay performance.

Although the falling particle approach was the clear frontrunner in the comparison conducted in this thesis, there are applications for which the packed particle bed is better suited (e.g. in the presence of product inhibition or in assay protocols with multiple wash steps). The packed bed format would also likely be improved by narrowing the size distribution of the particles, as this is known to reduce the risk of channelling behaviour [136]. Upgrading from simple drop-casting to more advanced particle loading techniques, such as flowing the particle slurry into a channel fitted with a filter plug, could also be used to improve the structure of the packed bed and thus, improve signal development with this format.

Regardless of assay format, the final design will ultimately need to take manufacturability into consideration so that the device can be efficiently produced at the scale and price required to meet the demands of a healthcare system.

5.2.3 Development of handheld imaging

Signal processing of the biological reaction to the target analyte is a key element in any biosensor and an additional functionality required for the falling particle system to move towards POCT applications. While the custom-built fluorescence scanner used in this work provided spatial information about signal development patterns, supporting analysis of reaction kinetics, ultimately, a smaller, handheld instrument would be desirable for a POCT.

Mobile phones are an attractive platform for signal analysis given the high mobile phone penetration (including an increasing adoption of smartphones) and rapidly growing telecommunications infrastructure in emerging markets [42,249,292,293]. Multiple reports have testified that mobile phones hold the power to not only transform diagnostic technologies for low resource settings but to more broadly strengthen healthcare systems, with mHealth platforms covering range of applications in clinical medicine [294–296].

Smartphones, in particular, contain all the necessary components for a portable diagnostic reader (e.g. screen for display and control, image collection (camera), data processing and data communication). It should be noted that the audio jack in mobile phones can also be harnessed for both bi-directional signal (data transfer) and power, supporting external peripherals such as LEDs, photodiodes and other sensors [297–299]. With regards to image capture, phone cameras typically contain CMOS (complementary metal-oxide semiconductor) sensors, capable of taking high-quality images/videos [300]. The circuitry behind each pixel of the CMOS sensor converts photon counts to Red (R), Green (G), and Blue (B) channel values, which can then be described in a variety of colour spaces for analysis [249,301]. Thus, it is advantageous to select an appropriate indicator dye based on spectral properties that align well with the RGB sensitivities of common cell phone camera sensors [302,303].

Smartphones can be harnessed to not only perform automatic interpretation of the results, but also to support the administration of POCTs through in context assistance to users [293], to integrate with medical record systems that are currently in use in developing countries and to enable data collection for public health monitoring. They have been used for the analysis of commercially available rapid diagnostic tests (lateral flow assays, e.g.[293,304]), as well as custom built microfluidic chips (e.g. [298,302]) and paper-based analytical devices (e.g.[31,305]) .

While they are a potentially powerful platform, camera phones typically have integrated colour balancing functions optimised for photography in ambient light. These make the collected images more pleasing to the eye, but skew measurements and make standardisation challenging [301,302]. Several groups have addressed the variability of ambient lighting conditions and other challenges associated with using smartphone cameras for detection (e.g. user positioning, shadows, focal distance [305]) with phone holders and adapters. These are often 3D-printed forms and typically include additional components to aid in image capture such as lenses, plastic colour bandpass filters, LEDs, and/or batteries (e.g. [304,306,307]). Although these solutions are successful in alleviating ambient light challenges, this approach requires additional, often phone-specific components, which would face some of the same challenges as dedicated readers (e.g. maintenance/repair). Other have addressed this challenge through calibration with reference images (test assays/colour cards) [308,309], but again this requires additional components unless these reference points can be built in to the test. An attractive alternative is to get behind the image processing algorithms and extract the raw sensory data from the scanner, an approach advocated for by several publications [303,306,310]. However, this approach may be challenging with fully integrated smartphone cameras without support from the manufacturer of the sensor and/or smartphone. Ultimately, surmounting these technical hurdles towards the use of smartphone for POCT analysis will need to be balanced against the cost of developing specialised handheld reader alternatives.

5.3 Outlook and opportunities

The research presented in this thesis provides an initial validation of a production process, including the downstream integration into an assay format that could enable in-country manufacture of affordable POCTs by combining molecular biology and a low-cost support material for simultaneous purification and immobilisation. This section will discuss a potential application for the silica-based reagents developed in this work as well as future opportunities for the expansion of this approach with other materials and other IVD assays. As mentioned in Chapter 2, the coupled enzyme system (SOx and HRP) explored here as a first model has potential application in prostate cancer diagnosis (Section 5.3.1). While this work focused on silica, other materials with known affinity tags could be investigated in the future for their potential as a low-cost support material (Section 5.3.1). Finally, the local production approach could be also be applied to other IVD assays (Section 5.3.3).

5.3.1 Towards a diagnostic for prostate cancer

Prostate cancer is one of the leading causes of cancer death among men globally [12,13]. Although elevated levels of prostate specific antigen (PSA) are now widely used in connection with prostate cancer screening, PSA was originally intended only as a marker of disease progression in already diagnosed patients. Its wider use and resulting ambiguity in the result (including false-positives and overdiagnosis of clinically insignificant cancers [311]) is now driving the search for better biomarkers and subsequently IVDs [312,313]. Molecular biomarkers (metabolite, gene and protein based) are being identified that collectively may lead to better diagnostics and treatment management [314], one of which is sarcosine [183].

Significantly elevated levels of sarcosine in urine of prostate cancer patients have been recorded in some studies [183,263]. While the possible role of sarcosine as a biomarker for prostate cancer is still debated [158], some of the discrepancy in reports may be due to the variation in assay methods, as discussed with respect to the original conflicting studies that both measured sarcosine levels using mass spectrometry (MS) techniques [170,183,198,315]. One of the challenges in detecting sarcosine via MS is differentiating it from its isomer, alanine, which is present in urine at 1000 fold higher levels [170]. Several methods have been developed to separate the two isomers that may make MS approaches still viable [316,317], however, the MS technique requires considerable skill and specialized equipment not amenable to POCTs, especially in LMICs.

Currently available laboratory test kits for sarcosine primarily use an oxidase-linked chromogenic assay (akin to the system presented in this thesis) [265]. Unlike MS techniques, enzymatic assays show excellent selectivity for sarcosine. Nevertheless, although these kits are suitable for use in plasma and serum, interference in measurements made in urine is typically reported, producing erroneous results. It is well known that some substances in urine such as glucose, ascorbic acid, bilirubin, as well as uric acid often affect enzymatic methods that utilize peroxidase [152].

Some attention has been given to overcoming this interference, with strategies including the use of nanoparticles with pseudo-peroxidase activity instead of HRP [157,318] and the detection the other co-product (formaldehyde) via a pH change associated with its conversion to formic acid [153]. However, these methods required significant laboratory processing steps that would make the design of a near patient diagnostic with these approaches complex and thus, the interference of the measurement of sarcosine in urine remains a challenge for a POCT.

Alternatively, a simple system using silica-based reagents has shown potential to overcome the interference in urine in work performed with collaborators at the University of Valencia [181]. This study used the silica-immobilised enzyme construct R5$_2$-mCh-SOx-R5-6H in conjunction with WT HRP immobilised via glutaraldehyde crosslinking and AR dye encapsulated using a sol-gel technique as a layer on the surface of silica particles. In contrast to the commercial kit using soluble reagents, the silica-based reagents were shown to be less affected by the interferents in human urine and provided greater sensitivity in the concentration range relevant to prostate cancer detection (0-10 µM) [157,158]. In a preliminary study, the system was able to differentiate between urine from healthy and from prostate cancer patients. While this approach was successful in overcoming interference in urine, to move away from classical cross-linking methods (i.e. glutaraldehyde) and towards the local production approach presented in this thesis, significant improvements in the activity of R5-mCh-Enz constructs with HRP would be required (as discussed in Chapters 3 and 4). In addition, it would be necessary show that they also are not affected by urine interferents. Alternatively, it could be advantageous to move from a chromogenic agent to an electrochemical approach that doesn’t rely on HRP (as discussed briefly in Chapter 2).

Electrochemical biosensors are one of the most common biosensor techniques, including the very successful glucose biosensor (~ 50 % of the biosensor market [319]). Typically, the redox enzyme is immobilised on the surface of the working electrode and the product monitored amperometrically. With an electrochemical approach, it is generally advantageous to have peptide affinity tags that bind directly to inorganic surfaces to minimize the distance between the active site of the enzyme and the electrode surface [56]. To enable binding with the R5 peptide fusions presented in this thesis, the electrode surface could be modified with silicalite [320], a microporous material which has silanol groups [321] that could interact with positive residues of the affinity tag. Alternatively, the presence of the R5 peptide could be used to drive silica sol gel encapsulation on the electrode surface, as previously shown for the fusion construct mSOx-R5-6H [159].

While these strategies enable immobilisation of the R5-tagged fusions on the electrode surface, the addition of the silica layer would likely impede diffusion of the mediator and could have a deleterious effect on sensitivity by increasing background noise. Thus, it may be beneficial to switch the R5-tag for another polypeptide tag with affinity for common electrode materials. Polypeptide sequences exist for a variety of common electrode materials (Ag, Au, Pt, etc.) [56]; however, this switch of affinity peptide would require corresponding changes in the purification matrix which may be unfavourable for a local production approach. Alternatively, silica particles pre-immobilised with enzyme could be deposited around the working electrode. While this could reduce the speed of the response by increasing the distance the mediator has to travel, it could be more amenable to direct integration with the one-step purification and immobilisation process presented in this thesis.

In summary, new detection strategies are required that can accurately detect the presence of sarcosine among the interferents in urine in order to, in the first instance, establish if sarcosine is a valid marker for prostate cancer, and second, if this is the case, to provide a POCT for its measurement. An electrochemical approach with $R5_2$-mCh-mSOx-R5-6H could be one potential option for this POCT.

5.3.2 Alternate low-cost, local materials as the support matrix

Since the R5-tag promotes affinity for negatively charged surfaces, it can likely be used with other materials having anionic surfaces. For example, R5-tagged proteins have previously shown affinity for microbubbles synthesised with natural polymer surface coatings (alginate and lignosulfonate) [141]. Another SBP, Car9, was originally identified for its affinity for carbonaceous substrates [71,127]. Given the interaction is thought to be mediated by similar electrostatic forces to those involved in R5 affinity for silica, R5 may also have affinity for this class of materials.

As mentioned above, other affinity peptides have also been identified for a wide range of substrates [56] including materials like cellulose and lignin, indicating that this approach has broad applicability to abundant, naturally occurring materials. Cellulose-binding modules (CBMs) are particularly attractive given the wealth of research developing advanced paper-based diagnostic tests for resource-limited settings. Paper is proposed to be a good fit with A.S.S.U.R.E.D. principles for the development of POCTs, with cited advantages including passive transport of fluids through wicking behaviour, compatibility with biological samples, disposal by incineration, and scalable for manufacture (as described in recent reviews [31,322–324]).

CBM-tagged proteins can be easily integrated into microfluidic paper-based analytical devices (e.g. [325]). In addition, a number of publications have demonstrated affinity purification with CBMs for a variety of expression hosts using both microcrystalline and amorphous cellulose and filter paper [58,326–330]. Pardee *et al.* have estimated using regenerated amorphous cellulose could result in a cost reduction of five orders of magnitude compared to Ni-NTA resin [40]. CBMs typically contain aromatic/hydrophobic and polar amino acids and their binding to cellulose can be attributed, at least in part, to their hydrophobic surface [329]. It should be noted that addition of these hydrophobic regions can decrease fusion protein solubility and in some cases, lead to formation of inclusion bodies. Interestingly, Nahalka and Nidetzky proposed an approach for biocatalyst formation that capitalised on the inter-molecular aggregation of CBMs due to their hydrophobic nature. Insoluble enzyme aggregates were produced without prior isolation of the protein and retained 40 % activity of the highly purified form [331]. Despite their tendency towards insolubility, CBMs still offer a promising alternative option to SBPs for affinity driven immobilisation on low-cost and locally available materials.

5.3.3 Application of the local production approach to other diagnostic targets

Depending on the choice of functional enzyme, the silica-R5-protein constructs can be adapted for other types of IVD assays (e.g. small molecule, nucleic acid, immunoassay), all of which have utility at different points in the patient care pathway. For example, immunoassays and nucleic acids are particularly relevant to the detection of infectious diseases which are leading causes of mortality and morbidity in LMICs [8,332]. Most rapid diagnostic tests typically used in resource-limited settings are based on lateral flow immunoassay technology [293,333,334]. Immunoassays employ antibodies and/or antigens as the biological reagents, but the recombinant production of antibodies is made challenging by their large size, structural complexity, disulphide bonds, and post-translational modification requirements [40]. Nevertheless, directed evolution and other engineering techniques have created designer binding proteins, which maintain the high affinity and specificity of the antibody-antigen interaction but are smaller in size and have been successfully produced in *E. coli* hosts [40,335]. These antibody mimetics or single chain antibodies could be designed for the analyte of choice and fused with silica-R5-protein constructs for detection. Irrespective of antibody mimetic selected, the sequential wash steps required by immunoassay protocols would likely make the packed bed assay format preferable to the batch-reactor approach of the falling particle design.

Nucleic acid amplification (NAA) is an alternate diagnostic method to immunoassay which detects the molecular signature of the pathogen, i.e. DNA/RNA. This approach potentially offers greater sensitivity, especially in the early stages of a disease when the body's immune system is just beginning to respond to the presence of the pathogen antibody concentrations are low [336]. The laboratory standard for NAA is polymerase chain reaction (PCR), which requires thermocycling patterns for denaturation of the double-stranded target, annealing of the primers to the target sequence and extension by the polymerase (95 °C, 50 °C, 72 °C, respectively). R5 fusion proteins have been developed with a variant of the Taq polymerase (Klentaq [337], in collaboration with Dr. David Bailey), but, due to PCRs high temperature step, these constructs required a change in the fluorescent protein to a thermostable variant (thermal green protein [338]). Nonetheless, initial tests have shown both good immobilisation from lysate and successful amplification of template sequences with silica-immobilised fusion polymerase (Appendix E). However, these fusion constructs require further optimisation as they lost all their activity upon drying.

Recently, isothermal NAA techniques (e.g. loop isothermal amplification, LAMP [339,340]) have risen in popularity, especially for use in resource-limited settings, as they eliminate the need for complex thermocyclers. A R5-mCh-Enz fusion containing the polymerase for the LAMP approach (Bst) has also been developed (by Dushanth Seevratnam) and preliminary tests have shown amplification by the silica-based reagent in the falling particle device (done in collaboration, see Appendix E). The 50 µL chamber design was used for this proof-of-concept but further work will be required to move towards a design that could support the small-scale reaction volumes typically used for LAMP (12.5 - 25 µL). In the optimisation of this design, it will be necessary to consider the reaction kinetics of this assay and what mass transport limitations exist, if any. The diffusivity of DNA will be dependent on its size [341], but it is generally expected to be slower than the small molecules discussed in this work (sarcosine and peroxide). This could mean the system is more likely to be under diffusion control, however, this will depend on the kinetic activity of the fusion Bst (measured by rate of nucleotide incorporation [342]). It will also be necessary to consider the potential electrostatic repulsion effects, given the negative charge at the silica surface [103] and the negative charge of DNA, and the influence this would have on diffusion to the particle surface. The modelling approach presented in Chapter 3 could be adapted to incorporate these parameters and determine the rate limiting step for the LAMP assay with the fusion construct on silica particles.

While still in the initial stages of development and optimisation, these fusions demonstrate the potential of the local production approach for a range of biological reagents which would be applicable to the development of a diverse set of diagnostic tools. It is the hope that this approach can not only increase access to quality diagnostics in LMICs but also provide a more self-sustaining healthcare system and support the development of the local economy.

APPENDICES

A. Experimental details regarding recombinant protein design

B. Details of video submissions

C. MATLAB code for particle settling analysis

D. Technical specifications for the FFEI fluorescence flatbed scanner

E. Experimental details and preliminary results for nucleic acid amplification assays with silica-based reagents

APPENDIX A: EXPERIMENTAL DETAILS REGARDING RECOMBINANT PROTEIN DESIGN

A.1 mCh-6H, R5-mCh-6H, R5$_3$-mCh-6H, R5$_2$-mCh-mSOx-R5-6H

E. coli glycerol stock with mCh-6H, R5-mCh-6H, R5$_3$-mCh-6H constructs in pET24a expression vector were prepared previously in-house as described in [141]. The pET24a vector encoding mSOx-R5-6H (prepared as described in [159]) was used as a template for R5$_2$-mCherry-mSOx-R5-6H fusion protein construction by Elizabeth Pumford. The vector was subjected to site directed mutagenesis aimed to add two restriction sites of NdeI and BamHI for insertion of the mSOx-R5 gene, while the stop codon was placed at the end of the sequence. Chemically competent NovaBlue Singles *E. coli* cells (*endA1 hsdR17 (*r_{K12-} m_{K12+}*) supE44 thi-1 recA1 gyrA96 relA1 lacF'[proA+B+lacI*^{q}*ZΔ M15::Tn10*] (Tet^{R})) were used for transformation and plasmid propagation and were cultured in LB medium supplemented with 5 µg/ml kanamycin at 37 °C.

PCR was performed using Q5 Hot Start High-Fidelity Polymerase following the manufacturer's instructions (New England Biolabs, UK) using a thermocycler (Mastercycler, Eppendorf). PCR product was purified by using QIAquick DNA purification kit and stored at -20 °C. Primers were designed by using ApE plasmid editor and purchased from the Sigma Aldrich Custom DNA Oligo Service. The primers were re-suspended in water (100 µM stock solution) and stored at -20 °C. Transformed *E. coli* colonies were screened by colony PCR using Q5 Hot Start High-Fidelity Polymerase.

Transformation was completed using a standard heat shock method. Plasmid DNA was purified from transformant *E. coli* using the QIAprep Spin miniprep kit and stored at -20 °C for further use. Validation of plasmid DNA was confirmed by DNA sequencing services (Department of Biochemistry, University of Cambridge). DNA size was checked by agarose gel electrophoresis, 1 % (w/v).

A.2 HRP-mCh-R5-6H and 6H-R5-mCh-HRP

The HRP sequences (isoenzyme C1a, RCSB Protein Data Bank 1ATJ) were ordered from GeneArtTM Gene Synthesis. The genes were cloned into pAK plasmid. The constructs were assembled in NEB Turbo cells using the Klenow Assembly Method. PCR, transformation and DNA sequencing were completed as aforementioned.

APPENDIX B: DETAILS OF VIDEO SUBMISSIONS

Sample videos have been provided on a USB drive to provide additional context for the results and discussion in Chapter 3. Table B.1 provides a list of the videos along with experimental details.

Table B.1 Experimental details for videos of particle sedimentation patterns.

File name	Silica	Shape	Rotation
SCextract_narrow_flip	SC extract	narrow waist	flip
SCextract_narrow_flip_long	SC extract	narrow waist	flip
SCextract_narrow_tilt	SC extract	narrow waist	tilt
SCextract_parallel_flip	SC extract	parallel sided	flip
SCextract_parallel_tilt	SC extract	parallel sided	tilt
SCextract_standard_flip	SC extract	standard waist	flip
SCextract_standard_tilt	SC extract	standard waist	tilt
Si60_6-35_narrow_flip	Si60 6-35 µm	narrow waist	flip
Si60_40-63_narrow_flip	Si60 40-63 µm	narrow waist	flip
Si60_63-210_narrow_flip	Si60 63-210 µm	narrow waist	flip
Si60_200-500_narrow_flip	Si60 200-500 µm	narrow waist	flip
Si60_less63_narrow_flip	Si60 <63 µm	narrow waist	flip
SiNPs_narrow_flip_1	Nanoparticles	narrow waist	flip
SiNPs_narrow_flip_2	Nanoparticles	narrow waist	flip
SiNPs+LGparticles_narrow_flip	Nanoparticles with 200-500 µm	narrow waist	flip

APPENDIX C: MATLAB CODE FOR PARTICLE SETTLING ANALYSIS

The supplementary code used in addition to PIVlab [242] for analysis of particle settling behaviour using MATLAB is provided below.

C.1 Function for image conversion to inverse grayscale

Description of key functions:

- rgb2gray converts RGB values to grayscale values (I) by forming a weighted sum of the *R*, *G*, and *B* components using Eq. (C.1).

$$I = \mathbf{0.2989 \times R + 0.5870 \times G + 0.1140 \times B} \tag{C.1}$$

- Imcomplement computes the complement of the image, where each pixel value is subtracted from the maximum pixel value supported by the class (e.g. 255). The difference is used as the pixel value in the output image. In the output image, dark areas become lighter and light areas become darker.

The following script was used with the imageBatchProcessor application in MATLAB.

```
function results = myimfcn(im)
% IM      - Input image.
% RESULTS - A scalar structure with the processing
results.
if(size(im,3)==3)
    % Convert RGB to grayscale
    imgray = rgb2gray(im);
else
    imgray = im;
end
reverseIM=imcomplement(imgray);
results.reverse = reverseIM;
```

C.2 Function for extraction of maximum velocity from PIV analysis frames

The following script was used to extract maximum velocity values and position on the x-axis from .csv output files for each frame (image pair) from PIV analysis.

```
%% Max velocity over all frames in PIV
```

```
allfiles=dir('C:\foldername’)
size(allfiles)
sz=1234 %number of last files to extract from

%% Loop containing import and output for each frame
for i=3:sz

pathf=strcat(allfiles(i).folder,"\",allfiles(i).name);
%recombine filename and path
    [maxvel(i), maxposn(i)] =
importoutputmaxvelposn(pathf, 2, 2000); %call function
to return maximum velocity and position along the line
at which that occurs
    clear pathf
    splitname=strsplit(allfiles(i).name,["_",".txt"])
%split up the filename to find the number of the frame
    frame(i)=str2num(cell2mat(splitname(4))) %convert
the frame number from text to a number
end

scatter(frame,maxvel)%plot frame vs maxvel to check
splitname=strsplit(allfiles(5).folder,["\"])%split
path name to name csv file based on the 5th file in
the list
csvfilename=strcat(splitname(10),"_csv.csv")%name csv
file
csvwrite(csvfilename,[frame',maxvel',maxposn'])%popula
tes csv
```

where `importoutputmaxvelposn` is described by:

```
function [maxvel, maxposn] =
importoutputmaxvelposn(filename, startRow, endRow)

%% Initialize variables.
delimiter = ',';
if nargin<=2
    startRow = 2;
    endRow = inf;
end

%% Format for each line of text:
%   column1: double (%f)
%   column2: double (%f)
% For more information, see the TEXTSCAN
documentation.
formatSpec = '%f%f%[^\n\r]';
```

```
%% Open the text file.
fileID = fopen(filename,'r');

%% Read columns of data according to the format.
dataArray = textscan(fileID, formatSpec, endRow(1)-
startRow(1)+1, 'Delimiter', delimiter, 'TextType',
'string', 'EmptyValue', NaN, 'HeaderLines',
startRow(1)-1, 'ReturnOnError', false, 'EndOfLine',
'\r\n');
for block=2:length(startRow)
    frewind(fileID);
    dataArrayBlock = textscan(fileID, formatSpec,
endRow(block)-startRow(block)+1, 'Delimiter',
delimiter, 'TextType', 'string', 'EmptyValue', NaN,
'HeaderLines', startRow(block)-1, 'ReturnOnError',
false, 'EndOfLine', '\r\n');
    for col=1:length(dataArray)
        dataArray{col} =
[dataArray{col};dataArrayBlock{col}];
    end
end

%% Close the text file.
fclose(fileID);

%% Allocate imported array to column variable names
Distanceonlinem = dataArray{:, 1};
Velocitymagnitudems = dataArray{:, 2};

%% Find maximum velocity and output with position
[maxvel indmaxvel] = max(Velocitymagnitudems)
maxposn=Distanceonlinem(indmaxvel)

end
```

APPENDIX D: TECHNICAL SPECIFICATIONS FOR THE FFEI FLUORESCENCE FLATBED SCANNER

The custom fluorescence scanner was developed by FFEI as part of EU funded BiognostiX project. Figure D.1 shows the LED emission spectra and CCD spectral response from the user manual provided by FFEI. Illumination by LEDs was double-sided 47.5 degrees from the horizontal plane with a shortpass filter (cut-off 505 nm). The CCD detector is positioned parallel to the horizontal sample tray (See Figure 3.5) with a longpass filter (cut-off of 580 nm).

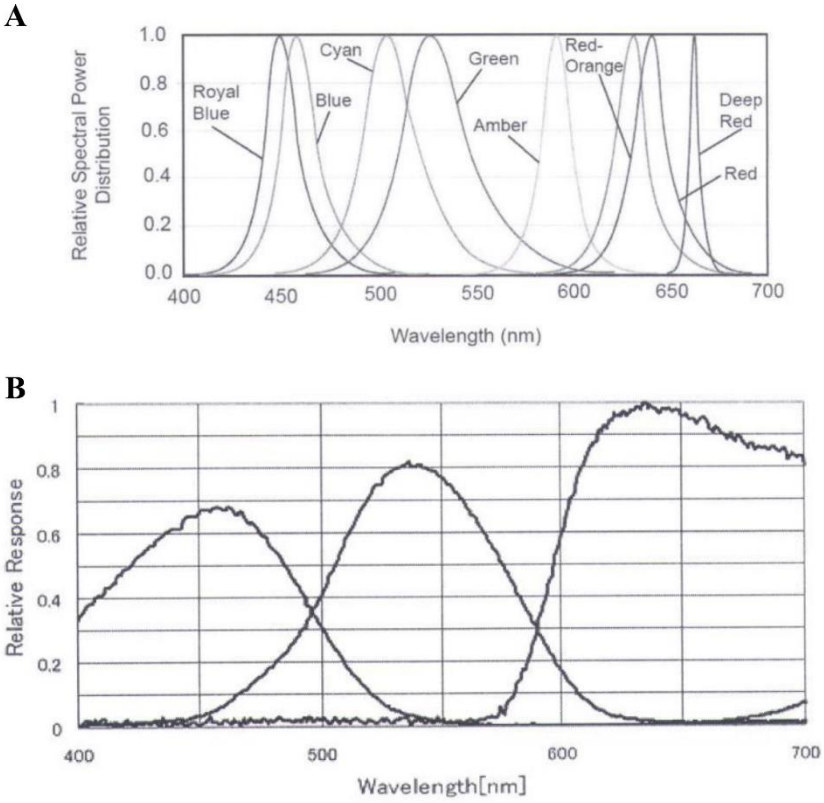

Figure D.1 Technical specifications for the custom scanner as specified in the user manual provided by FFEI, showing (A) LED emission spectra (Cyan) and (B) CCD spectral response.

APPENDIX E: EXPERIMENTAL DETAILS AND PRELIMINARY RESULTS FOR NUCLEIC ACID AMPLIFICATION ASSAYS WITH SILICA-BASED REAGENTS

This section contains the experimental methods and preliminary results for nucleic acid amplification (NAA) assays using silica-based reagents, as mentioned in Chapter 5. Two approaches are under development: loop-isothermal amplification (LAMP) and more traditional polymerase chain reaction (PCR). Fusion proteins were designed, transformed and expressed by Dushanth Seevaratnam (R5-mCh-Bst-6H) and Dr. David Bailey ($R5_5$-TGP-10H-Klentaq) with the appropriate polymerase for LAMP and PCR, respectively. In the case of the Klentaq variant, mCh is replaced by thermal green protein (TGP) [338] as mCh was observed to denature under the high temperature step of PCR. Sequences for these proteins are provided in Section E.3 and Section E.4. Immobilisation onto silica was completed following the protocol outlined in Chapter 2, with Ni-purified protein and silica gel 60 <63 µm for R5-mCh-Bst-6H and direct from lysate with silica extracted from sand for $R5_5$-TGP-10H-Klentaq. Experimental details for amplification assays and results are described below.

E.1 Loop-mediated isothermal amplification (LAMP)

The LAMP tests were performed in PCR tubes using 25 µL reaction volume or in mini-chambers using 50 µL reaction volumes in collaboration with Dushanth Seevaratnam. The primers were designed by Dr. Hui Yee Chee (Universiti Putra Malaysia) against the secY gene of *Leptospira interrogans* (bacterial pathogen causing leptospirosis [343]) . Each reaction mixture contained 40 pmol of FIP and BIP, 20 pmol of LF and LB, 5 pmol of F3 and B3 primers (sequences in Table E.1), 1.4 mM deoxyribonucleotide triphosphate (dNTP), 100 mmol $MgSO_4$, 0.2X Isothermal Amplification Buffer II (New England Biolabs), 1 mM $MnCl_2$, 0.964 ng/µL of template DNA, and 0.4 µg/µL silica-R5-mCh-Bst-6H DNA Polymerase (~ 0.1 mg R5-mCh-Bst-6H per 1 mg silica).

Table E.1 Primer sequences for LAMP assay

Primer label	Sequence
FIP	5’-TTCCGTGCCGGTAGACCAGAACCGTAATTCTTTGTGCG-3’
BIP	5’-CTTGAGCCTGCGCGTTACAATGAGAAGAACGGTTCCG-3’
LF	5’-GCGAGTTGGATCACTGCTA-3’
LB	5’-CCGGGCTTAATCAATTCTTCTG-3’
F3	5’-CTTGTTCCTGCCCTTCAAA-3’
B3	5’-TTCGGTGATCTGTTCTCCT-3’

Falling particle chambers were laser cut from PMMA using the 50 µL mini-chamber design described in Chapter 4 for an endpoint assay (Figure 4.10) and sealed with thin-film plastic coated with a pressure sensitive adhesive (AR90349, Adhesive Research Inc.). Control studies where strips of plastic were added to PCR tube reactions showed AR90349 resulted in minimal inhibition, unlike the PCR plate seal used in the rest of this thesis. The solution was incubated in the chambers on Peltier (19.6 W, Farnell) at a constant 65 °C for 90 min. The Peltier temperature was controlled by a proportional-integral-derivative function on a microprocessor (Arduino) with temperature input from a thermistor (10 kΩ, B57551G1 Series, EPCOS) and voltage output by DC voltage generator (thandar, 30 V – 2 A) (See Figure E.1 for experimental set-up). Function constants were $K_p = 5$, $K_i = 0.2$, and $K_d = 1$ when temperature input was within +/- 2 °C from set-point; otherwise, $K_p = 50$, $K_i=1$, and $K_d = 2$. The Peltier control circuit was built in collaboration with Andrew Stretton and Sebastian Cosnefroy. The amplification products were stained and analysed with a 1 % w/v agarose gel containing ethidium bromide; Figure E.1B shows successful amplification in the presence of the template (positive) and no amplification without the template (negative). In LAMP, amplification produces a heterogeneous distribution of polymers which are not distinguished as a single individual band for a positive signal [340].

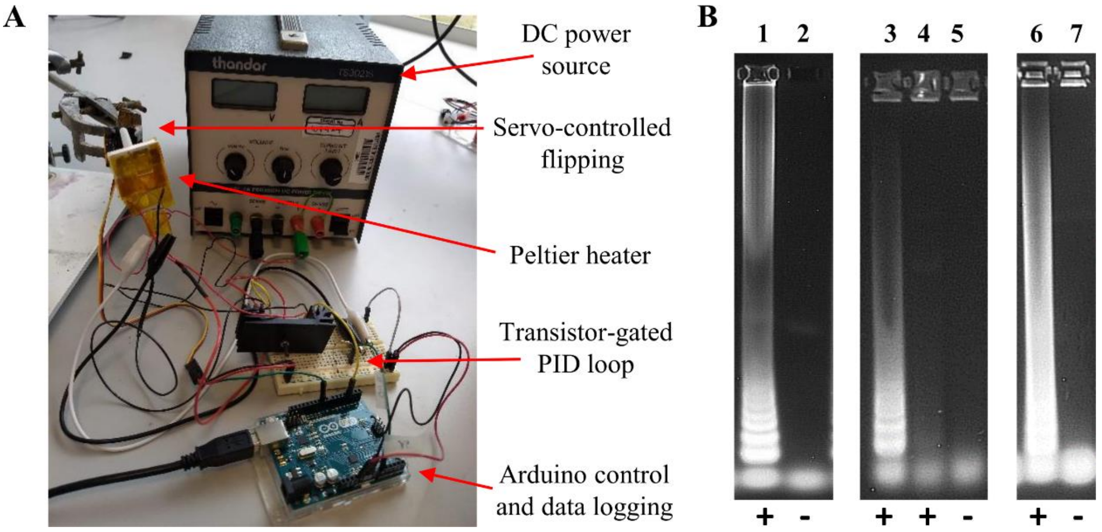

Figure E.1 (A) Experimental set-up for providing heat to LAMP reaction in the mini-chamber. (B) agarose gel image showing DNA amplification by soluble R5-mCh-Bst-6H (1 - positive, 2 - negative), on silica (3 - positive, 4 - positive without $MnCl_2$, 5 - negative) and on silica in the mini-chamber (6 - positive, 7 - negative), in the presence of the template (positive) and without the template (negative).

E.2 Polymerase chain reaction (PCR)

The PCR tests were performed in PCR tubes with 25 µL reaction volume using the fusion protein $R5_5$-10H-TGP-Klentaq. A 2X master mix was prepared with 50 µL ThermoPol buffer, 10 µL dNTPs (200 µM final concentration), 1 µL of each primer stock and 2 µL of 135 bp target to a total volume of 250 µL with H_2O. For each reaction, 12.5 µL of 2X master mix was added to 12.5 µL H_2O and 0.5-1.0 µL of lysate or protein immobilised on silica extract. Immobilised proteins were re-suspended in 150 µL of H_2O per 5 mg of silica in order to compare activity with crude lysate (as 150 µL of lysate was added to 5 mg of silica extract). PCR was performed using 2 min at 94 °C at the start, then 25 cycles of 5 s at 94 °C, 5 s at 55 °C, 60 s at 74 °C, and finally 2 min at 74 °C as final extension. Amplification was assessed by gel electrophoresis in 1 % w/v agarose gel run for 20 min at 90 V.

Figure E.2 shows the retention of both fluorescent and polymerase functionality by the fusion protein $R5_5$-TGP-10H-Klentaq. The fluorescence spectra of the construct showed no observable difference between the soluble and immobilised protein (Figure E.2C); both match well with literature reported peaks for green fluorescent proteins (ex. 480 nm / em. 510 nm). Good immobilisation of the fusion protein was observed on silica extracted from SC sand (Figure E.2B). Based on a reported value of 8000 U/mg for commercial

Taq, R5$_5$-TGP-10H-Klentaq was estimated to be 120 times less active per mg protein than commercial (when used from crude lysate). Nonetheless, similar levels of amplification were observed for soluble and immobilised protein (Figure E.2D).

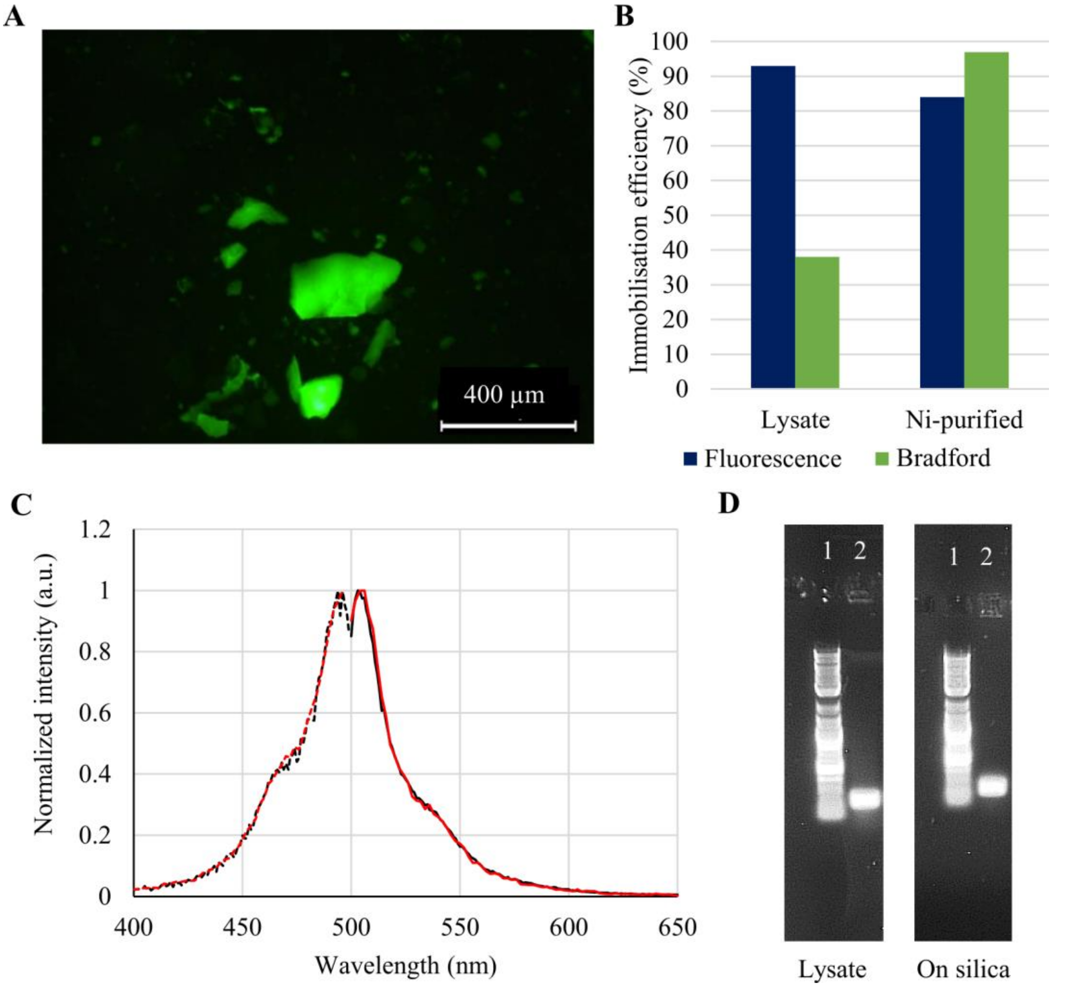

Figure E.2 Characterisation of the R5$_5$-TGP-10H-Klentaq fusion protein. (A) Fluorescence microscopy of immobilised protein on silica extract (from lysate) and (C) emission (solid) and excitation (dots) spectra of the soluble (black) and immobilised (red) protein, showing no observable difference. (B) Efficiency of immobilisation as assessed by fluorescence intensity for target protein (navy) and Bradford assay for total protein (green). (D) Gel electrophoresis result of PCR products produced by the fusion polymerase, showing similar levels of amplification with the silica-bound protein as the soluble form. In both cases, lane 1 is a 2log ladder and lane 2 is the amplification product.

E.3 DNA sequences for fusion polymerases

***R5*-mCh-Bst-6H:**

atg*TCCTCTAAAAAGTCTGGTTCCTACTCTGGTAGCAAAGGCTCCAAACGTCGCAT*
*CCTG*GTGAGCAAGGGCGAGGAGGATAACATGGCCATCATCAAGGAGTTCAT

GCGCTTCAAGGTGCACATGGAGGGCTCCGTGAACGGCCACGAGTTCGAGAT
CGAGGGCGAGGGCGAGGGCCGCCCCTACGAGGGCACCCAGACCGCCAAGC
TGAAGGTGACCAAGGGTGGCCCCCTGCCCTTCGCCTGGGACATCCTGTCCCC
TCAGTTCATGTACGGCTCCAAGGCCTACGTGAAGCACCCCGCCGACATCCCC
GACTACTTGAAGCTGTCCTTCCCCGAGGGCTTCAAGTGGGAGCGCGTGATG
AACTTCGAGGACGGCGGCGTGGTGACCGTGACCCAGGACTCCTCCCTGCAG
GACGGCGAGTTCATCTACAATGTGAAGCTGCGCGGCACCAACTTCCCCTCC
GACGGCCCCGTAATGCAGAAGAAGACCATGGGCTGGGAGGCCTCCTCCGAG
CGGATGTACCCCGAGGACGGCGCCCTGAAGGGCGAGATCAAGCAGAGGCT
GAAGCTGAAGGACGGCGGCCACTACGACGCTGAGGTCAAGACCACCTACA
AGGCCAAGAAGCCCGTGCAGCTGCCCGGCGCCTACAACGTCAACATCAAGT
TGGACATCACCTCCCACAACGAGGACTACACCATCGTGGAACAGTACGAAC
GCGCCGAGGGCCGCCACTCCACCGGCGGCATGGACGAGCTGTACAAGGGAT
CCGAGCTCGCCGAAGGGGAGAAACCGCTTGAGGAGATGGAGTTTGCCATCG
TTGACGTCATTACCGAAGAGATGCTTGCCGACAAGGCAGCGCTTGTCGTTG
AGGTGATGGAAGAAAACTACCACGATGCCCCGATTGTCGGAATCGCACTAG
TGAACGAGCATGGGCGATTTGCCATGCGCCCGGAGACCGCGCTGGCTGATT
CGCAATTTTTAGCATGGCTTGCCGATGAAACGAAGAAAAAAAGCATGTTTG
ACGCCAAGCGGGCAGTCGTTGCCTTAAAGTGGAAAGGAATTGAGCTTCGCG
GCGTCGCCTTTGATTTATTGCTCGCTGCCTATTTGCTCAATCCGGCTCAAGAT
GCCGGCGATATCGCTGCGGTGGCGAAAATGAAACAATATGAAGCGGTGCGG
TCGGATGAAGCGGTCTATGGCAAAGGCGTCAAGCGGTCGCTGCCGGACGAA
CAGACGCTTGCTGAGCATCTCGTTCGCAAAGCGGCAGCCATTTGGGCGCTTG
AGCAGCCGTTTATGGACGATTTGCGGAACAACGAACAAGATCAACAATTGT
TATTAACGAAGCTTGAGCAGCCGCTGGCGGCGATTTTGGCTGAAATGGAAT
TCACTGGGGTGAACGTGGATACAAAGCGGCTTGAACAGATGGGTTCGGAGC
TGGCCGAACAACTGCGTGCCATCGAGCAGCGCATTTACGAGCTAGCCGGCC
AAGAGTTCAACATTAACTCACCAAAACAGCTCGGAGTCATTTTATTTGAAA
AGCTGCAGCTACCGGTGCTGAAGAAGACGAAAACAGGCTATTCGACTTCGG
CTGATGTGCTTGAGAAGCTTGCGCCGCATCATGAAATCGTCGAAAACATTTT
GCATTACCGCCAGCTTGGCAAACTGCAATCAACGTATATTGAAGGATTGTTG
AAAGTTGTGCGCCCTGATACCGGCAAAGTGCATACGATGTTCAACCAAGCG
CTGACGCAAACTGGGCGGCTCAGCTCGGCCGAGCCGAACTTGCAAAACATT
CCGATTCGGCTCGAAGAGGGGCGGAAAATCCGCCAAGCGTTCGTCCCGTCA
GAGCCGGACTGGCTCATTTTCGCCGCCGATTACTCACAAATTGAATTGCGCG

TCCTCGCCCATATCGCCGATGACGACAATCTAATTGAAGCGTTCCAACGCGA
TTTGGATATTCACACAAAAACGGCGATGGACATTTTCCATGTGAGCGAAGA
GGAAGTCACGGCCAACATGCGCCGCCAGGCAAAGGCCGTTAACTTCGGTAT
CGTTTACGGAATTAGCGATTACGGATTGGCGCAAAACTTGAACATTACGCG
CAAAGAAGCTGCCGAATTTATCGAACGTTACTTCGCCAGCTTTCCGGGCGTA
AAGCAGTATATGGAAAACATTGTGCAAGAAGCGAAACAGAAAGGATATGT
GACAACGCTGTTGCATCGGCGCCGCTATTTGCCTGATATTACAAGCCGCAAT
TTCAACGTCCGCAGTTTTGCAGAGCGGACGGCCATGAACACGCCAATTCAA
GGAAGCGCCGCTGACATTATTAAAAAAGCGATGATTGATTTAGCGGCACGG
CTGAAAGAAGAGCAGCTTCAGGCTCGTCTTTTGCTGCAAGTGCATGACGAA
CTCATTTTGGAAGCGCCAAAAGAGGAAATTGAGCGATTATGTGAGCTTGTT
CCGGAAGTGATGGAGCAGGCCGTTACGCTCCGCGTGCCGCTGAAAGTCGAC
TACCATTACGGCCCAACATGGTATGATGCCAAAGGATCAGCAGGTCTCGAG
CATCATCATCATCATCATtaa

***R5*$_5$-TGP-10H-Klentaq:**

ATGGGATCCTCCTCTAAAAAGTCTGGTTCCTACTCTGGTAGCAAAGGCTCCA
AACGTCGCATCCTGTCCTCTAAAAAGTCTGGTTCCTACTCTGGTAGCAAAGG
CTCCAAACGTCGCATCCTGTCCTCTAAAAAGTCTGGTTCCTACTCTGGTAGC
AAAGGCTCCAAACGTCGCATCCTGTCCTCTAAAAAGTCTGGTTCCTACTCTG
GTAGCAAAGGCTCCAAACGTCGCATCCTGTCCTCTAAAAAGTCTGGTTCCTA
CTCTGGTAGCAAAGGCTCCAAACGTCGCATCCTGAATTTATCAGTAATTAAA
CCGGAAATGAAAATTAAATTGCGTATGGAAGGTGCCGTTAACGGCCATAAA
TTTGTAATTGAAGGAGAAGGAATAGGCAAACCATACGAAGGAACCCAGAC
CCTGGATTTAACCGTAGAAGAAGGCGCACCTCTCCCTTTCTCGTACGACATC
CTCACCCCAGCCTTCCAATACGGCAATCGCGCTTTCACCAAATACCCAGAAG
ATATTCCAGACTATTTTAAACAAGCATTCCCCGAAGGCTATTCTTGGGAACG
CTCTATGACCTATGAAGATCAAGGAATTTGTATCGCTACCTCCGACATTACT
ATGGAAGGAGACTGTTTTTTTTATGAAATTCGCTTTGATGGAACTAACTTCC
CCCCGAACGGCCCTGTAATGCAAAAGAAGACCTTAAAATGGGAACCTAGCA
CCGAAAAAATGTATGTAGAAGACGGAGTTCTTAAGGGTGACGTAGAAATGG
CACTTCTGCTCGAAGGAGGTGGACACTACCGCTGCGATTTTAAAACCACTTA
TAAAGCCAAAAAAGATGTTCGTCTTCCAGATGCACACGAGGTGGACCACCG
CATTGAAATCCTGAGCCACGATAAAGATTATAATAAAGTTAGACTCTATGA

ACACGCCGAAGCCCGCTATTCTGGCGGAGGCAGCGGAGGCGGTAGCCACCA
CCATCATCACCATCACCATCACCACGGAGGTGGCTCGGGTCTCCTCCACGAG
TTCGGCCTTCTGGAAAGCCCCAAGGCCCTGGAGGAGGCCCCCTGGCCCCCG
CCGGAAGGGGCCTTCGTGGGCTTTGTGCTTTCCCGCAAGGAGCCCATGTGG
GCCGATCTTCTGGCCCTGGCCGCCGCCAGGGGGGGCCGGGTCCACCGGGCC
CCCGAGCCTTATAAAGCCCTCAGGGACCTGAAGGAGGCGCGGGGGCTTCTC
GCCAAAGACCTGAGCGTTCTGGCCCTGAGGGAAGGCCTTGGCCTCCCGCCC
GGCGACGACCCCATGCTCCTCGCCTACCTCCTGGACCCTTCCAACACCACCC
CCGAGGGGGTGGCCCGGCGCTACGGCGGGGAGTGGACGGAGGAGGCGGGG
GAGCGGGCCGCCCTTTCCGAGAGGCTCTTCGCCAACCTGTGGGGGAGGCTT
GAGGGGGAGGAGAGGCTCCTTTGGCTTTACCGGGAGGTGGAGAGGCCCCTT
TCCGCTGTCCTGGCCCACATGGAGGCCACGGGGGTGCGCCTGGACGTGGCC
TATCTCAGGGCCTTGTCCCTGGAGGTGGCCGAGGAGATCGCCCGCCTCGAG
GCCGAGGTCTTCCGCCTGGCCGGCCACCCCTTCAACCTCAACTCCCGGGACC
AGCTGGAAAGGGTCCTCTTTGACGAGCTAGGGCTTCCCGCCATCGGCAAGA
CGGAGAAGACCGGCAAGCGCTCCACCAGCGCCGCCGTCCTGGAGGCCCTCC
GCGAGGCCCACCCCATCGTGGAGAAGATCCTGCAGTACCGGGAGCTCACCA
AGCTGAAGAGCACCTACATTGACCCCTTGCCGGACCTCATCCACCCCAGGA
CGGGCCGCCTCCACACCCGCTTCAACCAGACGGCCACGGCCACGGGCAGGC
TAAGTAGCTCCGATCCCAACCTCCAGAACATCCCCGTCCGCACCCCGCTTGG
GCAGAGGATCCGCCGGGCCTTCATCGCCGAGGAGGGGTGGCTATTGGTGGC
CCTGGACTATAGCCAGATAGAGCTCAGGGTGCTGGCCCACCTCTCCGGCGA
CGAGAACCTGATCCGGGTCTTCCAGGAGGGGCGGGACATCCACACGGAGAC
CGCCAGCTGGATGTTCGGCGTCCCCCGGGAGGCCGTGGACCCCCTGATGCG
CCGGGCGGCCAAGACCATCAACTTCGGGGTCCTCTACGGCATGTCGGCCCA
CCGCCTCTCCCAGGAGCTAGCCATCCCTTACGAGGAGGCCCAGGCCTTCATT
GAGCGCTACTTTCAGAGCTTCCCCAAGGTGCGGGCCTGGATTGAGAAGACC
CTGGAGGAGGGCAGGAGGCGGGGGTACGTGGAGACCCTCTTCGGCCGCCGC
CGCTACGTGCCAGACCTAGAGGCCCGGGTGAAGAGCGTGCGGGAGGCGGC
CGAGCGCATGGCCTTCAACATGCCCGTCCAGGGCACCGCCGCCGACCTCAT
GAAGCTGGCTATGGTGAAGCTCTTCCCCAGGCTGGAGGAAATGGGGGCCAG
GATGCTCCTTCAGGTCCACGACGAGCTGGTCCTCGAGGCCCCAAAAGAGAG
GGCGGAGGCCGTGGCCCGGCTGGCCAAGGAGGTCATGGAGGGGGTGTATCC
CCTGGCCGTGCCCCTGGAGGTGGAGGTGGGGATAGGGGAGGACTGGCTCTC
CGCCAAGGAGtaa

E.4 Amino acid sequences for fusion polymerases

***R5*-mCh-Bst-6H:**

M*SSKKSGSYSGSKGSKRRIL*VSKGEEDNMAIIKEFMRFKVHMEGSVNGHEFEIEGEGEGRPYEGTQTAKLKVTKGGPLPFAWDILSPQFMYGSKAYVKHPADIPDYLKLSFPEGFKWERVMNFEDGGVVTVTQDSSLQDGEFIYNVKLRGTNFPSDGPVMQKKTMGWEASSERMYPEDGALKGEIKQRLKLKDGGHYDAEVKTTYKAKKPVQLPGAYNVNIKLDITSHNEDYTIVEQYERAEGRHSTGGMDELYKGSELAEGEKPLEEMEFAIVDVITEEMLADKAALVVEVMEENYHDAPIVGIALVNEHGRFAMRPETALADSQFLAWLADETKKKSMFDAKRAVVALKWKGIELRGVAFDLLLAAYLLNPAQDAGDIAAVAKMKQYEAVRSDEAVYGKGVKRSLPDEQTLAEHLVRKAAAIWALEQPFMDDLRNNEQDQQLLLTKLEQPLAAILAEMEFTGVNVDTKRLEQMGSELAEQLRAIEQRIYELAGQEFNINSPKQLGVILFEKLQLPVLKKTKTGYSTSADVLEKLAPHHEIVENILHYRQLGKLQSTYIEGLLKVVRPDTGKVHTMFNQALTQTGRLSSAEPNLQNIPIRLEEGRKIRQAFVPSEPDWLIFAADYSQIELRVLAHIADDDNLIEAFQRDLDIHTKTAMDIFHVSEEEVTANMRRQAKAVNFGIVYGISDYGLAQNLNITRKEAAEFIERYFASFPGVKQYMENIVQEAKQKGYVTTLLHRRRYLPDITSRNFNVRSFAERTAMNTPIQGSAADIIKKAMIDLAARLKEEQLQARLLLQVHDELILEAPKEEIERLCELVPEVMEQAVTLRVPLKVDYHYGPTWYDAKGSAGLEHHHHHH

$R5_5$-TGP-10H-Klentaq:

MGS*SSKKSGSYSGSKGSKRRILSSKKSGSYSGSKGSKRRILSSKKSGSYSGSKGSKRRILSSKKSGSYSGSKGSKRRILSSKKSGSYSGSKGSKRRIL*NLSVIKPEMKIKLRMEGAVNGHKFVIEGEGIGKPYEGTQTLDLTVEEGAPLPFSYDILTPAFQYGNRAFTKYPEDIPDYFKQAFPEGYSWERSMTYEDQGICIATSDITMEGDCFFYEIRFDGTNFPPNGPVMQKKTLKWEPSTEKMYVEDGVLKGDVEMALLLEGGGHYRCDFKTTYKAKKDVRLPDAHEVDHRIEILSHDKDYNKVRLYEHAEARYSGGGSGGGSHHHHHHHHHHGGGSGLLHEFGLLESPKALEEAPWPPPEGAFVGFVLSRKEPMWADLLALAAARGGRVHRAPEPYKALRDLKEARGLLAKDLSVLALREGLGLPPGDDPMLLAYLLDPSNTTPEGVARRYGGEWTEEAGERAALSERLFANLWGRLEGEERLLWLYREVERPLSAVLAHMEATGVRLDVAYLRALSLEVAEEIARLEAEVFRLAGHPFNLNSRDQLERVLFDELGLPAIGKTEKTGKRSTSAAVLEALREAHPIVEKILQYRELTKLKSTYIDPLPDLIHPRTGRLHTRFNQTATATGRLSSSDPNLQNIPVRTPLGQRIRRAFIAEEGWLLVALDYSQIELRVLAHLSGDENLIRVFQEGRDIHTETASWMF

GVPREAVDPLMRRAAKTINFGVLYGMSAHRLSQELAIPYEEAQAFIERYFQSFPKVRAWIEKTLEEGRRRGYVETLFGRRRYVPDLEARVKSVREAAERMAFNMPVQGTAADLMKLAMVKLFPRLEEMGARMLLQVHDELVLEAPKERAEAVARLAKEVMEGVYPLAVPLEVEVGIGEDWLSAKE

REFERENCES

[1] R. Peeling, R. McNerney, Increasing Access to Diagnostics Through Technology Transfer and Local Production, Geneva, 2011.

[2] L.M. Bebell, A.N. Muiru, Antibiotic use and emerging resistance: How can resource-limited countries turn the tide?, Glob. Heart. 9 (2014) 347–358. doi:10.1016/j.gheart.2014.08.009.

[3] A. Zumla, J.A. Al-Tawfiq, V.I. Enne, M. Kidd, C. Drosten, J. Breuer, M.A. Muller, D. Hui, M. Maeurer, M. Bates, P. Mwaba, R. Al-Hakeem, G. Gray, P. Gautret, A.A. Al-Rabeeah, Z.A. Memish, V. Gant, Rapid point of care diagnostic tests for viral and bacterial respiratory tract infections-needs, advances, and future prospects, Lancet Infect. Dis. 14 (2014) 1123–1135. doi:10.1016/S1473-3099(14)70827-8.

[4] M.S. Dryden, J. Cooke, P. Davey, Antibiotic stewardship-more education and regulation not more availability?, J. Antimicrob. Chemother. 64 (2009) 885–888. doi:10.1093/jac/dkp481.

[5] I.N. Okeke, R.W. Peeling, H. Goossens, R. Auckenthaler, S.S. Olmsted, J.F. De Lavison, B.L. Zimmer, M.D. Perkins, K. Nordqvist, Diagnostics as essential tools for containing antibacterial resistance, Drug Resist. Updat. 14 (2011) 95–106. doi:10.1016/j.drup.2011.02.002.

[6] S.H. Habib, S. Saha, Burden of non-communicable disease: Global overview, Diabetes Metab. Syndr. Clin. Res. Rev. 4 (2010) 41–47. doi:10.1016/j.dsx.2008.04.005.

[7] D. Beran, J.S. Yudkin, M. De Courten, Access to care for patients with insulin-requiring diabetes in developing countries: Case studies of Mozambique and Zambia, Diabetes Care. 28 (2005) 2136–2140. doi:10.2337/diacare.28.9.2136.

[8] C.D. Mathers, D. Loncar, Projections of Global Mortality and Burden of Disease from 2002 to 2030, PLoS Med. 3 (2006) 2011–2030. doi:10.1371/journal.pmed.0030442.

[9] G.D.L. Lopes, J.A. de Souza, C. Barrios, Access to cancer medications in low- and

middle-income countries, Nat. Rev. Clin. Oncol. 10 (2013) 314–322. doi:10.1038/nrclinonc.2013.55.

[10] K. Haney, P. Tandon, R. Divi, M.R. Ossandon, H. Baker, P.C. Pearlman, The Role of Affordable, Point-of-Care Technologies for Cancer Care in Low- and Middle-Income Countries: A Review and Commentary, IEEE J. Transl. Eng. Heal. Med. 5 (2017) e1-14. doi:10.1109/JTEHM.2017.2761764.

[11] M. Plummer, C. de Martel, J. Vignat, J. Ferlay, F. Bray, S. Franceschi, Global burden of cancers attributable to infections in 2012: a synthetic analysis, Lancet Glob. Heal. 4 (2016) e609–e616. doi:10.1016/S2214-109X(16)30143-7.

[12] J. Cuzick, M.A. Thorat, G. Andriole, O.W. Brawley, P.H. Brown, Z. Culig, R.A. Eeles, L.G. Ford, F.C. Hamdy, L. Holmberg, D. Ilic, T.J. Key, C. La Vecchia, H. Lilja, M. Marberger, F.L. Meyskens, L.M. Minasian, C. Parker, H.L. Parnes, S. Perner, H. Rittenhouse, J. Schalken, H.P. Schmid, B.J. Schmitz-Dräger, F.H. Schröder, A. Stenzl, B. Tombal, T.J. Wilt, A. Wolk, Prevention and early detection of prostate cancer, Lancet Oncol. 15 (2014) e484–e492. doi:10.1016/S1470-2045(14)70211-6.

[13] A. Jemal, F. Bray, M.M. Center, J. Ferlay, E. Ward, D. Forman, Global Cancer Statistics, CA Cancer J Clin. 61 (2011) 69–90. doi:10.3322/caac.20107.

[14] N. Howlader, A. Noone, M. Krapcho, D. Miller, K. Bishop, C. Kosary, M. Yu, J. Ruhl, Z. Tatalovich, A. Mariotto, D. Lewis, H. Chen, E. Feuer, K. Cronin, SEER Cancer Statistics Review, 1975-2014, Bethesda, MD, 2017.

[15] E.P. Hyle, I. V. Jani, J. Lehe, A.E. Su, R. Wood, J. Quevedo, E. Losina, I. V. Bassett, P.P. Pei, A.D. Paltiel, S. Resch, K.A. Freedberg, T. Peter, R.P. Walensky, The Clinical and Economic Impact of Point-of-Care CD4 Testing in Mozambique and Other Resource-Limited Settings: A Cost-Effectiveness Analysis, PLoS Med. 11 (2014) e1001725. doi:10.1371/journal.pmed.1001725.

[16] A. Vassall, S. van Kampen, H. Sohn, J.S. Michael, K.R. John, S. den Boon, J.L. Davis, A. Whitelaw, M.P. Nicol, M.T. Gler, A. Khaliqov, C. Zamudio, M.D. Perkins, C.C. Boehme, F. Cobelens, Rapid diagnosis of tuberculosis with the Xpert MTB/RIF assay in high burden countries: A cost-effectiveness analysis, PLoS

Med. 8 (2011) e1001120. doi:10.1371/journal.pmed.1001120.

[17] J.-P. Allain, O. Opare-Sem, Screening and diagnosis of HBV in low-income and middle-income countries, Nat. Rev. Gastroenterol. Hepatol. 13 (2016) 643–653. doi:10.1038/nrgastro.2016.138.

[18] R.W. Peeling, D. Mabey, Point-of-care tests for diagnosing infections in the developing world., Clin. Microbiol. Infect. 16 (2010) 1062–9. doi:10.1111/j.1469-0691.2010.03279.x.

[19] W. Jung, J. Han, J.-W. Choi, C.H. Ahn, Point-of-care testing (POCT) diagnostic systems using microfluidic lab-on-a-chip technologies, Microelectron. Eng. 132 (2015) 46–57. doi:10.1016/j.mee.2014.09.024.

[20] A. Van den Berg, L. Segerink, eds., Microfluidics for medical applications, Royal Society of Chemistry, 2015.

[21] N.P. Pai, C. Vadnais, C. Denkinger, N. Engel, M. Pai, Point-of-Care Testing for Infectious Diseases: Diversity, Complexity, and Barriers in Low- And Middle-Income Countries, PLoS Med. 9 (2012) e1001306. doi:10.1371/journal.pmed.1001306.

[22] M. Urdea, L.A. Penny, S.S. Olmsted, M.Y. Giovanni, P. Kaspar, A. Shepherd, P. Wilson, C.A. Dahl, S. Buchsbaum, G. Moeller, D.C. Hay Burgess, Requirements for high impact diagnostics in the developing world, Nature. 444 (2006) 73–79.

[23] N. Singh, D. Abrol, Challenge of In-vitro Diagnostics for Resource Poor Settings: An Assessment, New Delhi, 2014.

[24] L. Perry, R. Malkin, Effectiveness of medical equipment donations to improve health systems: How much medical equipment is broken in the developing world?, Med. Biol. Eng. Comput. 49 (2011) 719–722. doi:10.1007/s11517-011-0786-3.

[25] P. Yadav, Health Product Supply Chains in Developing Countries: Diagnosis of the Root Causes of Underperformance and an Agenda for Reform, Heal. Syst. Reform. 1 (2015) 142–154. doi:10.4161/23288604.2014.968005.

[26] S. Sharma, J. Zapatero-Rodríguez, P. Estrela, R. O'Kennedy, Point-of-Care Diagnostics in Low Resource Settings: Present Status and Future Role of

Microfluidics, Biosensors. 5 (2015) 577–601. doi:10.3390/bios5030577.

[27] Global Burden of Disease Health Financing Collaborators Network, Evolution and patterns of global health financing 1995 – 2014 : development assistance for health, and government, prepaid private, and out-of-pocket health spending in 184 countries, Lancet. 389 (2017) 1981–2004. doi:10.1016/S0140-6736(17)30874-7.

[28] D. Mabey, R.W. Peeling, A. Ustianowski, M.D. Perkins, Diagnostics for the developing world, Nat. Rev. Microbiol. 2 (2004) 231–240. doi:10.1038/nrmicro841.

[29] W.K. Tomazelli Coltro, C.M. Cheng, E. Carrilho, D.P. de Jesus, Recent advances in low-cost microfluidic platforms for diagnostic applications, Electrophoresis. 35 (2014) 2309–2324. doi:10.1002/elps.201400006.

[30] S. Byrnes, G. Thiessen, E. Fu, Progress in the development of paper-based diagnostics for low-resource point-of-care settings, Bioanalysis. 5 (2013) 2821–2836. doi:10.4155/bio.13.243.

[31] A.W. Martinez, S.T. Phillips, G.M. Whitesides, E. Carrilho, Diagnostics for the developing world: Microfluidic paper-based analytical devices, Anal. Chem. 82 (2010) 3–10. doi:10.1021/ac9013989.

[32] M.T. Novak, C.N. Kotanen, S. Carrara, A. Guiseppi-Elie, F.G. Moussy, Diagnostic tools and technologies for infectious and non-communicable diseases in low-and-middle-income countries, Health Technol. (Berl). 3 (2013) 271–281. doi:10.1007/s12553-013-0060-9.

[33] M.S. Cordray, R.R. Richards-Kortum, Review: Emerging nucleic acid-based tests for point-of-care detection of malaria, Am. J. Trop. Med. Hyg. 87 (2012) 223–230. doi:10.4269/ajtmh.2012.11-0685.

[34] K.D. Koirala, L. van Niekerk, P.J. Garcia, R. Peeling, N. Kumar, A. Vyas, S. Witek-McManus, E. Chambert, J.-F. de Lavison, J. Sommerfeld, F.G. Moussy, Improving Access to Quality Diagnostic Tools in Low and Middle Income Countries (LMICs) Through Social Innovation-Lessons Learnt, Int. J. Public Heal. Saf. 2 (2017) 123.

[35] S. Horton, R. Sullivan, J. Flanigan, K.A. Fleming, M.A. Kuti, L.M. Looi, S.A. Pai, M. Lawler, Delivering modern, high-quality, affordable pathology and laboratory medicine to low-income and middle-income countries: a call to action, Lancet. 391 (2018) 1953–1964. doi:10.1016/S0140-6736(18)30460-4.

[36] A.M. Taylor, M.P. Taylor, The Purchasing Power Parity Debate, J Econ. Perspect. 18 (2004) 135–158.

[37] C.J. Henderson, E. Pumford, D.J. Seevaratnam, R. Daly, E.A.H. Hall, Gene to diagnostic : Self immobilizing protein for silica microparticle biosensor, modelled with sarcosine oxidase, Biomaterials. 193 (2019) 58–70. doi:10.1016/j.biomaterials.2018.12.003.

[38] N. Singh, D. Abrol, In-vitro diagnostics (IVDs) innovations for resource-poor settings: The Indian experience, African J. Sci. Technol. Innov. Dev. 9 (2017) 617–636. doi:10.1080/20421338.2017.1359465.

[39] K.S. Boles, K. Kannan, J. Gill, M. Felderman, H. Gouvis, B. Hubby, K.I. Kamrud, J.C. Venter, D.G. Gibson, Digital-to-biological converter for on-demand production of biologics, Nat. Biotechnol. 35 (2017) 672–675. doi:10.1038/nbt.3859.

[40] K. Pardee, S. Slomovic, P.Q. Nguyen, J.W. Lee, N. Donghia, D. Burrill, T. Ferrante, F.R. McSorley, Y. Furuta, A. Vernet, M. Lewandowski, C.N. Boddy, N.S. Joshi, J.J. Collins, Portable, On-Demand Biomolecular Manufacturing, Cell. 167 (2016) 248–259. doi:10.1016/j.cell.2016.09.013.

[41] R. McNerney, Diagnostics for Developing Countries, Diagnostics. 5 (2015) 200–209. doi:10.3390/diagnostics5020200.

[42] A.K. Yetisen, M.S. Akram, C.R. Lowe, Paper-based microfluidic point-of-care diagnostic devices., Lab Chip. 13 (2013) 2210–51. doi:10.1039/c3lc50169h.

[43] D. Headon, G. Walsh, The industrial production of enzymes, Biotehcnology Adv. 12 (1994) 635–646.

[44] P. Perez-Pinera, N. Han, S. Cleto, J. Cao, O. Purcell, K.A. Shah, K. Lee, R. Ram, T.K. Lu, Synthetic biology and microbioreactor platforms for programmable

production of biologics at the point-of-care, Nat. Commun. 7 (2016) e1-10. doi:10.1038/ncomms12211.

[45] L.J. Millet, J.D. Lucheon, R.F. Standaert, S.T. Retterer, M.J. Doktycz, Modular microfluidics for point-of-care protein purifications, Lab Chip. 15 (2015) 1799–1811. doi:10.1039/c5lc00094g.

[46] C. Xu, K. Xu, H. Gu, X. Zhong, Z. Guo, R. Zheng, X. Zhang, B. Xu, Nitrilotriacetic acid-modified magnetic nanoparticles as a general agent to bind histidine-tagged proteins, J. Am. Chem. Soc. 126 (2004) 3392–3393. doi:10.1021/ja031776d.

[47] Y. Zhang, Y. Yang, W. Ma, J. Guo, Y. Lin, C. Wang, Uniform Magnetic Core/Shell Microspheres Functionalized with Ni 2+ −Iminodiacetic Acid for One Step Purification and Immobilization of His-Tagged Enzymes, Appl. Mater. Interfaces. 5 (2013) 2626–2633. doi:10.1021/am4006786.

[48] F. Xu, J.H. Geiger, G.L. Baker, M.L. Bruening, Polymer Brush-Modified Magnetic Nanoparticles for His-tagged protein purification, Langmuir. 27 (2011) 3106–3112. doi:10.1021/la1050404.

[49] K. Pardee, A.A. Green, T. Ferrante, D.E. Cameron, A. Daleykeyser, P. Yin, J.J. Collins, Paper-Based Synthetic Gene Networks, Cell. 159 (2014) 940–954. doi:10.1016/j.cell.2014.10.004.

[50] K. Pardee, A.A. Green, M.K. Takahashi, D.H.O. Connor, L. Gehrke, J.J. Collins, Rapid, Low-Cost Detection of Zika Virus Using Programmable Biomolecular Components, Cell. 165 (2016) 1255–1266. doi:10.1016/j.cell.2016.04.059.

[51] Y. Kwon, M.C. Jewett, High-throughput preparation methods of crude extract for robust cell-free protein synthesis, Sci. Rep. 5 (2015) e1-8. doi:10.1038/srep08663.

[52] O.W. Ogonah, K.M. Polizzi, D.G. Bracewell, Cell free protein synthesis: a viable option for stratified medicines manufacturing?, Curr. Opin. Chem. Eng. 18 (2017) 77–83. doi:10.1016/j.coche.2017.10.003.

[53] N. Krinsky, M. Kaduri, J. Shainsky-Roitman, M. Goldfeder, E. Ivanir, I. Benhar, Y. Shoham, A. Schroeder, A simple and rapid method for preparing a cell-free bacterial lysate for protein synthesis, PLoS One. 11 (2016) e0165137.

doi:10.1371/journal.pone.0165137.

[54] J. Peccoud, Synthetic Biology: fostering the cyber-biological revolution, Synth. Biol. 1 (2016) e1-7. doi:10.1093/synbio/ysw001.

[55] J.J. Lichty, J.L. Malecki, H.D. Agnew, D.J. Michelson-Horowitz, S. Tan, Comparison of affinity tags for protein purification, Protein Expr. Purif. 41 (2005) 98–105. doi:10.1016/j.pep.2005.01.019.

[56] E.A.H. Hall, S. Chen, J. Chun, Y. Du, Z. Zhao, A molecular biology approach to protein coupling at a biosensor interface, Trends Anal. Chem. 79 (2016) 247–256. doi:10.1016/j.trac.2016.01.024.

[57] S. Wang, E.S. Humphreys, S.Y. Chung, D.F. Delduco, S.R. Lustig, H. Wang, K.N. Parker, N.W. Rizzo, S. Subramoney, Y.M. Chiang, A. Jagota, Peptides with selective affinity for carbon nanotubes, Nat. Mater. 2 (2003) 196–200. doi:10.1038/nmat833.

[58] N. Sugimoto, K. Igarashi, M. Samejima, Cellulose affinity purification of fusion proteins tagged with fungal family 1 cellulose-binding domain, Protein Expr. Purif. 82 (2012) 290–296. doi:10.1016/j.pep.2012.01.007.

[59] C. Tamerler, E.E. Oren, M. Duman, E. Venkatasubramanian, M. Sarikaya, Adsorption kinetics of an engineered gold binding peptide by surface plasmon resonance spectroscopy and a quartz crystal microbalance, Langmuir. 22 (2006) 7712–7718. doi:10.1021/la0606897.

[60] S. Ko, T.J. Park, H.S. Kim, J.H. Kim, Y.J. Cho, Directed self-assembly of gold binding polypeptide-protein A fusion proteins for development of gold nanoparticle-based SPR immunosensors, Biosens. Bioelectron. 24 (2009) 2592–2597. doi:10.1016/j.bios.2009.01.030.

[61] N. Soh, T. Tokuda, T. Watanabe, K. Mishima, T. Imato, T. Masadome, Y. Asano, S. Okutani, O. Niwa, S. Brown, A surface plasmon resonance immunosensor for detecting a dioxin precursor using a gold binding polypeptide, Talanta. 60 (2003) 733–745. doi:10.1016/S0039-9140(03)00139-5.

[62] R.R. Naik, S.J. Stringer, G. Agarwal, S.E. Jones, M.O. Stone, Biomimetic

synthesis and patterning of silver nanoparticles, Nat. Mater. 1 (2002) 169–172. doi:10.1038/nmat758.

[63] Z. Xu, Y. Peng, Y. Wantai, C. Jinchun, The bio-inspired approach to controllable biomimetic synthesis of silver nanoparticles in organic matrix of chitosan and silver-binding peptide (NPSSLFRYLPSD), Mater. Sci. Eng. C. 28 (2008) 237–242. doi:10.1016/j.msec.2006.12.007.

[64] K.I. Sano, K. Shiba, A Hexapeptide Motif that Electrostatically Binds to the Surface of Titanium, J. Am. Chem. Soc. 125 (2003) 14234–14235. doi:10.1021/ja038414q.

[65] H. Nishida, T. Kajisa, Y. Miyazawa, Y. Tabuse, T. Yoda, H. Takeyama, H. Kambara, T. Sakata, Self-oriented immobilization of DNA polymerase tagged by titanium-binding peptide motif, Langmuir. 31 (2015) 732–740. doi:10.1021/la503094k.

[66] M. Umetsu, M. Mizuta, K. Tsumoto, S. Ohara, S. Takami, H. Watanabe, I. Kumagai, T. Adschiri, Bioassisted room-temperature immobilization and mineralization of zinc oxide - The structural ordering of ZnO nanoparticles into a flower-type morphology, Adv. Mater. 17 (2005) 2571–2575. doi:10.1002/adma.200500863.

[67] N. Yokoo, T. Togashi, M. Umetsu, K. Tsumoto, T. Hattori, T. Nakanishi, S. Ohara, S. Takami, T. Naka, H. Abe, I. Kumagai, T. Adschiri, Direct and selective immobilization of proteins by means of an inorganic material-binding peptide: Discussion on functionalization in the elongation to material-binding peptide, J. Phys. Chem. B. 114 (2010) 480–486. doi:10.1021/jp907731b.

[68] H. Dai, W.S. Choe, C.K. Thai, M. Sarikaya, B.A. Traxler, F. Baneyx, D.T. Schwartz, Nonequilibrium synthesis and assembly of hybrid inorganic-protein nanostructures using an engineered DNA binding protein, J. Am. Chem. Soc. 127 (2005) 15637–15643. doi:10.1021/ja055499h.

[69] C.C. Lechner, C.F.W. Becker, Immobilising proteins on silica with site-specifically attached modified silaffin peptides, Biomater. Sci. 3 (2015) 288–297. doi:10.1039/c4bm00310a.

[70] I.E. Pamirsky, K.S. Golokhvast, Silaffins of diatoms: From applied biotechnology to biomedicine, Mar. Drugs. 11 (2013) 3155–3167. doi:10.3390/md11093155.

[71] B.L. Coyle, F. Baneyx, A cleavable silica-binding affinity tag for rapid and inexpensive protein purification, Biotechnol. Bioeng. 111 (2014) 2019–2026. doi:10.1002/bit.25257.

[72] O. Choi, B.C. Kim, J.H. An, K. Min, Y.H. Kim, Y. Um, M.K. Oh, B.I. Sang, A biosensor based on the self-entrapment of glucose oxidase within biomimetic silica nanoparticles induced by a fusion enzyme, Enzyme Microb. Technol. 49 (2011) 441–445. doi:10.1016/j.enzmictec.2011.07.005.

[73] C.C. Chen, J.S. Do, Y. Gu, Immobilization of HRP in mesoporous silica and its application for the construction of polyaniline modified hydrogen peroxide biosensor, Sensors. 9 (2009) 4635–4648. doi:10.3390/s90604635.

[74] E. Eteshola, L.J. Brillson, S.C. Lee, Selection and characteristics of peptides that bind thermally grown silicon dioxide films, Biomol. Eng. 22 (2005) 201–204. doi:10.1016/j.bioeng.2005.09.004.

[75] Z. Munasir, T. Triwikantoro, M. Zainuri, D. Darminto, Synthesis of SiO2 nanopowders containing quartz and cristobalite phases from silica sands, Mater. Sci. 33 (2015) 47–55. doi:10.1515/msp-2015-0008.

[76] S. Arunmetha, A. Karthik, S.R. Srither, M. Vinoth, R. Suriyaprabha, P. Manivasakan, V. Rajendran, Size-dependent physicochemical properties of mesoporous nanosilica produced from natural quartz sand using three different methods, RSC Adv. 5 (2015) 47390–47397. doi:10.1039/c5ra07074k.

[77] V. Vaibhav, U. Vijayalakshmi, S.M. Roopan, Agricultural waste as a source for the production of silica nanoparticles, Spectrochim. Acta - Part A Mol. Biomol. Spectrosc. 139 (2015) 515–520. doi:10.1016/j.saa.2014.12.083.

[78] J. Chun, S. An, J. Lee, Highly mesoporous silicon derived from waste iron slag for high performance lithium ion battery anodes, J. Mater. Chem. A. 3 (2015) 21899–21905. doi:10.1039/c5ta04693a.

[79] C. Garcia-Galan, Á. Berenguer-Murcia, R. Fernandez-Lafuente, R.C. Rodrigues,

Potential of different enzyme immobilization strategies to improve enzyme performance, Adv. Synth. Catal. 353 (2011) 2885–2904. doi:10.1002/adsc.201100534.

[80] R.K. Singh, M.K. Tiwari, R. Singh, J.K. Lee, From protein engineering to immobilization: Promising strategies for the upgrade of industrial enzymes, Int. J. Mol. Sci. 14 (2013) 1232–1277. doi:10.3390/ijms14011232.

[81] H.R. Luckarift, G.R. Johnson, J.C. Spain, Silica-immobilized enzyme reactors; application to cholinesterase-inhibition studies, J. Chromatogr. B. 843 (2006) 310–316. doi:10.1016/j.jchromb.2006.06.036.

[82] A.I. Benítez-Mateos, I. Llarena, A. Sánchez-Iglesias, F. López-Gallego, Expanding One-Pot Cell-Free Protein Synthesis and Immobilization for On-Demand Manufacturing of Biomaterials, ACS Synth. Biol. 7 (2018) 875–884. doi:10.1021/acssynbio.7b00383.

[83] N.R. Mohamad, N.H.C. Marzuki, N.A. Buang, F. Huyop, R.A. Wahab, An overview of technologies for immobilization of enzymes and surface analysis techniques for immobilized enzymes, Biotechnol. Biotechnol. Equip. 29 (2015) 205–220. doi:10.1080/13102818.2015.1008192.

[84] D.M. Liu, J. Chen, Y.P. Shi, Advances on methods and easy separated support materials for enzymes immobilization, Trends Anal. Chem. 102 (2018) 332–342. doi:10.1016/j.trac.2018.03.011.

[85] U. Guzik, K. Hupert-Kocurek, D. Wojcieszynska, Immobilization as a strategy for improving enzyme properties- Application to oxidoreductases, Molecules. 19 (2014) 8995–9018. doi:10.3390/molecules19078995.

[86] A. Liese, L. Hilterhaus, Evaluation of immobilized enzymes for industrial applications, Chem. Soc. Rev. 42 (2013) 6236–6249. doi:10.1039/c3cs35511j.

[87] M. Saleemuddin, Bioaffinity Based Immobilization of Enzymes, Adv. Biochem. Eng. Biotech. 64 (1999) 203–226.

[88] M. Yang, B.G. Choi, T.J. Park, N.S. Heo, W.H. Hong, S.Y. Lee, Site-specific immobilization of gold binding polypeptide on gold nanoparticle-coated graphene

sheet for biosensor application, Nanoscale. 3 (2011) 2950–2956. doi:10.1039/c1nr10197h.

[89] S. Ghose, T.M. McNerney, B. Hubbard, Preparative protein purification on underivatized silica, Biotechnol. Bioeng. 87 (2004) 413–423. doi:10.1002/bit.20125.

[90] D.H. Reifsnyder, C. V. Olson, T. Etcheverry, H. Prashad, S.E. Builder, Purification of insulin-like growth factor-I and related proteins using underivatized silica, J. Chromatogr. A. 753 (1996) 73–80. doi:10.1016/S0021-9673(96)00549-3.

[91] J. Nawrocki, The silanol group and its role in liquid chromatography, J Chromatogr. A. 779 (1997) 29–71.

[92] E.D.E.R. Hyde, A. Seyfaee, F. Neville, R. Moreno-Atanasio, Colloidal Silica Particle Synthesis and Future Industrial Manufacturing Pathways: A Review, Ind. Eng. Chem. Res. 55 (2016) 8891–8913. doi:10.1021/acs.iecr.6b01839.

[93] W. Stober, A. Fink, E. Bohn, Controlled Growth of Monodisperse Silica Spheres in the Micron Size Range, J. Colloid Interface Sci. 26 (1968) 62–69. doi:10.1109/ICOSP.2006.345929.

[94] R.R. Naik, M.M. Tomczak, H.R. Luckarift, J.C. Spain, M.O. Stone, Entrapment of enzymes and nanoparticles using biomimetically synthesized silica, ChemComm. 298 (2004) 1684–1685. doi:10.1039/b404586f.

[95] C.C. Lechner, C.F.W. Becker, Modified silaffin R5 peptides enable encapsulation and release of cargo molecules from biomimetic silica particles, Bioorganic Med. Chem. 21 (2013) 3533–3541. doi:10.1016/j.bmc.2013.04.006.

[96] K. Lazaar, W. Hajjaji, R.C. Pullar, J.A. Labrincha, F. Rocha, F. Jamoussi, Production of silica gel from Tunisian sands and its adsorptive properties, J. African Earth Sci. 130 (2017) 238–251. doi:10.1016/j.jafrearsci.2017.03.017.

[97] C.O. Ayegba, T. Makinde, P. Obigwa, J. Orijajogun, Production of Silica Gel from Clay, Int. J. Mater. Chem. 5 (2015) 123–126. doi:10.5923/j.ijmc.20150506.01.

[98] W.A.A. Sudjarwo, M.M.F. Bee, Synthesis of silica gel from waste glass bottles and its application for the reduction of free fatty acid (FFA) on waste cooking oil,

AIP Conf. Proc. 1855 (2017) 020019. doi:10.1063/1.4985464.

[99] V. Puddu, C.C. Perry, Interactions at the silica-peptide interface: The influence of particle size and surface functionality, Langmuir. 30 (2014) 227–233. doi:10.1021/la403242f.

[100] S. V. Patwardhan, F.S. Emami, R.J. Berry, S.E. Jones, R.R. Naik, O. Deschaume, H. Heinz, C.C. Perry, Chemistry of Aqueous Silica Nanoparticle Surfaces and the Mechanism of Selective Peptide Adsorption, J. Am. Chem. Soc. 134 (2012) 6244–6256. doi:10.1021/ja211307u.

[101] K.K. Unger, Porous silica, Elsevier Science Ltd, Amsterdam, 1979.

[102] V. Puddu, C.C. Perry, Peptide adsorption on silica nanoparticles: Evidence of hydrophobic interactions, ACS Nano. 6 (2012) 6356–6363. doi:10.1021/nn301866q.

[103] K.R. Iler, The Chemistry of Silica: Solubility, Polymerization, Colloid and Surface Properties, and Biochemistry, John Wiley & Sons, New York, 1979.

[104] P.A. Ciullo, Industrial Minerals and Their Uses: A Handbook and Formulary, Noyes Publishing, 1996.

[105] G.H. Bolt, Determination of the charge density of silica sols, J. Phys. Chem. 61 (1957) 1166–1169. doi:10.1021/j150555a007.

[106] R. Zerrouk, A. Foissy, R. Mercier, Y. Chevallier, J.C. Morawski, Study of Ca2+-induced silica coagulation by small angle scattering, J. Colloid Interface Sci. 139 (1990) 20–29. doi:10.1016/0021-9797(90)90441-P.

[107] S.K. Milonjić, Determination of surface ionization and complexation constants at colloidal silica/electrolyte interface, Colloids and Surfaces. 23 (1987) 301–312. doi:10.1016/0166-6622(87)80273-1.

[108] D.E. Yates, T.W. Healy, The structure of the silica/electrolyte interface, J. Colloid Interface Sci. 55 (1976) 9–19. doi:10.1016/0021-9797(76)90003-5.

[109] T.F. Tadros, J. Lyklema, Adsorption of potential-determining ions at the silica-aqueous electrolyte interface and the role of some cations, J. Electroanal. Chem.

Interfacial Electrochem. 17 (1968) 267–275.

[110] R.R. Naik, L. Brott, S. Clarson, M.O. Stone, Silica-precipitating peptides isolated from a combinatorial phage display peptide library, J. Nanosci Nanotechnol. 2 (2002) 95–100.

[111] E.E. Oren, C. Tamerler, D. Sahin, M. Hnilova, U.O.S. Seker, M. Sarikaya, R. Samudrala, A novel knowledge-based approach to design inorganic-binding peptides, Bioinformatics. 23 (2007) 2816–2822. doi:10.1093/bioinformatics/btm436.

[112] A.C. McUmber, T.W. Randolph, D.K. Schwartz, Electrostatic Interactions Influence Protein Adsorption (but Not Desorption) at the Silica-Aqueous Interface, J. Phys. Chem. Lett. 6 (2015) 2583–2587. doi:10.1021/acs.jpclett.5b00933.

[113] S. Salgin, U. Salgin, S. Bahadir, Zeta Potentials and Isoelectric points of biomolecules: The effects of ion types and ionic strengths, Int. J. Electrochem. Sci. 7 (2012) 12404–12414. doi:10.1016/S0040-4039(00)98708-2.

[114] R. Hogg, T.W. Healy, D.W. Fuerstenau, Mutual coagulation of colloidal dispersions, Trans. Faraday Soc. 62 (1966) 1638–1651. doi:10.1039/tf9666201638.

[115] B. V Derjaguin, L.D. Landua, Theory of the Stability of Strongly Charged Lyophobic Sols and of the Adhesion of Strongly Charged Particles in Solutions of Electrolytes, Acta Physiochim. URSS. 14 (1941) 633–662.

[116] E.J.W. Verwey, J.T.G. Overbeek, Theory of the Stability of Lyophobic Colloids, Elsevier, Amsterdam, 1948.

[117] J.J. Valle-Delgado, J.A. Molina-Bolívar, F. Galisteo-González, M.J. Gálvez-Ruiz, A. Feiler, M.W. Rutland, Hydration forces between silica surfaces: Experimental data and predictions from different theories, J. Chem. Phys. 123 (2005) e034708. doi:10.1063/1.1954747.

[118] H. Yotsumoto, R.-H. Yoon, Application of Extended DLVO theory: II. Stability of silica suspensions, J. Colloid Interface Sci. 157 (1993) 434–441.

[119] J.K. Luey, J. McGuire, R.D. Sproull, The effect of pH and NaCl concentration on

adsorption of β-lactoglobulin at hydrophilic and hydrophobic silicon surfaces, J. Colloid Interface Sci. 143 (1991) 489–500. doi:10.1016/0021-9797(91)90282-D.

[120] S.K. Parida, S. Dash, S. Patel, B.K. Mishra, Adsorption of organic molecules on silica surface, Adv. Colloid Interface Sci. 121 (2006) 77–110. doi:10.1016/j.cis.2006.05.028.

[121] A.A. Vertegel, R.W. Siegel, J.S. Dordick, Silica nanoparticle size influences the structure and enzymatic activity of adsorbed lysozyme, Langmuir. 20 (2004) 6800–6807. doi:10.1021/la0497200.

[122] K. Taniguchi, K. Nomura, Y. Hata, T. Nishimura, Y. Asami, A. Kuroda, The Si-tag for immobilizing proteins on a silica surface, Biotechnol. Bioeng. 96 (2007) 1023–1029. doi:10.1002/bit.21208.

[123] M.A.A. Abdelhamid, K. Motomura, T. Ikeda, T. Ishida, R. Hirota, A. Kuroda, Affinity purification of recombinant proteins using a novel silica-binding peptide as a fusion tag, Appl. Microbiol. Biotechnol. 98 (2014) 5677–5684. doi:10.1007/s00253-014-5754-z.

[124] N. Kröger, R. Deutzmann, M. Sumper, Polycationic peptides from diatom biosilica that direct silica nanosphere formation, Science (80-.). 286 (1999) 1129–1132. doi:10.1126/science.286.5442.1129.

[125] M. Hnilova, D. Khatayevich, A. Carlson, E.E. Oren, C. Gresswell, S. Zheng, F. Ohuchi, M. Sarikay, C. Tamerler, Single-step fabrication of patterned gold film array by an engineered multi-functional peptide, J. Colloid Interface Sci. 365 (2012) 97–102. doi:10.1016/j.jcis.2011.09.006.

[126] H.M. Sassenfeld, S.J. Brewer, A polypeptide fusion designed for the purification of recombinant proteins, Nat. Biotechnol. 2 (1984) 76–81.

[127] B.L. Coyle, M. Rolandi, F. Baneyx, Carbon-binding designer proteins that discriminate between sp2- and sp3-hybridized carbon surfaces, Langmuir. 29 (2013) 4839–4846. doi:10.1021/la4000846.

[128] S.M. Fuchs, R.T. Raines, Polyarginine as a multifunctional fusion tag, Protein Sci. 14 (2005) 1538–1544. doi:10.1110/ps.051393805.

[129] J. Soto-Rodríguez, B.L. Coyle, A. Samuelson, K. Aravagiri, F. Baneyx, Affinity purification of Car9-tagged proteins on silica matrices: Optimization of a rapid and inexpensive protein purification technology, Protein Expr. Purif. 135 (2017) 70–77. doi:10.1016/j.pep.2017.05.003.

[130] C. Lechner, Functional analysis and biotechnological applications of silaffin peptides, Technische Universitat Munchen, 2013.

[131] K. Watanabe, M. Kimura, Location of the binding region for 23S ribosomal RNA on ribosomal protein L2 from Bacillus stearothermophilus, Eur J Biochem. 153 (1985) 299–304.

[132] T. Ikeda, K. ichi Ninomiya, R. Hirota, A. Kuroda, Single-step affinity purification of recombinant proteins using the silica-binding Si-tag as a fusion partner, Protein Expr. Purif. 71 (2010) 91–95. doi:10.1016/j.pep.2009.12.009.

[133] T. Ikeda, K. Motomura, Y. Agou, T. Ishida, R. Hirota, A. Kuroda, The silica-binding Si-tag functions as an affinity tag even under denaturing conditions, Protein Expr. Purif. 77 (2011) 173–177. doi:10.1016/j.pep.2011.01.012.

[134] B.L. Coyle, F. Baneyx, Direct and reversible immobilization and microcontact printing of functional proteins on glass using a genetically appended silica-binding tag, Chem. Commun. 52 (2016) 7001–7004. doi:10.1039/c6cc02660e.

[135] W. Yang, B. Hellner, F. Baneyx, Self-Immobilization of Car9 Fusion Proteins within High Surface Area Silica Sol-Gels and Dynamic Control of Protein Release, Bioconjug. Chem. 27 (2016) 2450–2459. doi:10.1021/acs.bioconjchem.6b00406.

[136] H.R. Luckarift, J.C. Spain, R.R. Naik, M.O. Stone, Enzyme immobilization in a biomimetic silica support, Nat. Biotechnol. 22 (2004) 211–213. doi:10.1038/nbt931.

[137] R.R. Naik, P.W. Whitlock, F. Rodriguez, L.L. Brott, D.D. Glawe, S.J. Clarson, M.O. Stone, Controlled formation of biosilica structures in vitro, Chem. Commun. 9 (2003) 238–239. doi:10.1039/b210635c.

[138] W.D. Marner, A.S. Shaikh, S.J. Muller, J.D. Keasling, Enzyme immobilization via silaffin-mediated autoencapsulation in a biosilica support, Biotechnol. Prog. 25

(2009) 417–423. doi:10.1002/btpr.136.

[139] D.H. Nam, K. Won, Y.H. Kim, B.I. Sang, A novel route for immobilization of proteins to silica particles incorporating silaffin domains, Biotechnol. Prog. 25 (2009) 1643–1649. doi:10.1002/btpr.261.

[140] T.T. Olmez, E. Yuca, E. Eyupoglu, H.B. Catalak, O. Sahin, U.O.S. Seker, Autonomous synthesis of fluorescent silica biodots using engineered fusion proteins, ACS Omega. 3 (2018) 585–594. doi:10.1021/acsomega.7b01769.

[141] S.R. Abbas, Preliminary investigation of natural materials for use in Ultrasound contrast agents, University of Cambridge, 2014.

[142] D.S. Waugh, Making the most of affinity tags, Trends Biotechnol. 23 (2005) 316–320. doi:10.1016/j.tibtech.2005.03.012.

[143] M.R. Knecht, D.W. Wright, Functional analysis of the biomimetric silica precipitation activity of the R5 peptide from Cylindrotheca fusiformis, Chem. Commun. (2003) 3038–3039. doi:10.1039/b309074d.

[144] C.C. Lechner, C.F.W. Becker, A sequence-function analysis of the silica precipitating silaffin R5 peptide, J. Pept. Sci. 20 (2014) 152–158. doi:10.1002/psc.2577.

[145] N.C. Shaner, R.E. Campbell, P.A. Steinbach, B.N.G. Giepmans, A.E. Palmer, R.Y. Tsien, Improved monomeric red, orange and yellow fluorescent proteins derived from Discosoma sp. red fluorescent protein, Nat. Biotechnol. 22 (2004) 1567–1572. doi:10.1038/nbt1037.

[146] K.B. Bravaya, O.M. Subach, N. Korovina, V. V Verkhusha, A.I. Krylov, Insight into the Common Mechanism of the Chromophore Formation in the Red Fluorescent Proteins: The Elusive Blue Intermediate Revealed, J. Am. Chem. Soc. 134 (2012) 2807–2814. doi:10.1021/ja2114568.

[147] R.N. Day, Fluorescent protein tools for studying protein dynamics in living cells: a review, J. Biomed. Opt. 13 (2019) e031202. doi:10.1117/1.2939093.

[148] A.D. Laurent, V.A. Mironov, P.P. Chapagain, A. V. Nemukhin, A.I. Krylov, Exploring Structural and Optical Properties of Fluorescent Proteins by Squeezing:

Modeling High-Pressure Effects on the mStrawberry and mCherry Red Fluorescent Proteins, J. Phys. Chem. B. 116 (2012) 12426–12440. doi:10.1021/jp3060944.Exploring.

[149] X. Shu, N.C. Shaner, C.A. Yarbrough, R.Y. Tsien, S.J. Remington, Novel Chromophores and Buried Charges Control Color in mFruits, Biochemistry. 45 (2006) 9639–9647. doi:10.1021/bi060773l.

[150] C. Chen, Q. Xie, D. Yang, H. Xiao, Y. Fu, Y. Tan, S. Yao, Recent advances in electrochemical glucose biosensors: A review, RSC Adv. 3 (2013) 4473–4491. doi:10.1039/C2RA22351A.

[151] J. Wang, Electrochemical Glucose Biosensors, Chem. Rev. 108 (2008) 814–825.

[152] V. Yamkamon, B. Phakdee, S. Yainoy, T. Suksrichawalit, T. Tatanandana, P. Sangkum, W. Eiamphungporn, Development of sarcosine quantification in urine based on enzyme-coupled colorimetric method for prostate cancer diagnosis, EXCLI J. 17 (2018) 467–478. doi:10.17179/excli2018-1245 This.

[153] C. Burton, S. Gamagedara, Y. Ma, A novel enzymatic technique for determination of sarcosine in urine samples, Anal. Methods. 4 (2012) 141–146. doi:10.1039/c1ay05541k.

[154] D. Grieshaber, R. MacKenzie, J. Voros, E. Reimhult, Electrochemical biosensors - Sensor principles and architectures, Sensors. 8 (2008) 1400–1458. doi:10.3390/s80314000.

[155] T.S.C.R. Rebelo, C.M. Pereira, M.G.F. Sales, J.P. Noronha, J. Costa-Rodrigues, F. Silva, M.H. Fernandes, Sarcosine oxidase composite screen-printed electrode for sarcosine determination in biological samples, Anal. Chim. Acta. 850 (2014) 26–32. doi:10.1016/j.aca.2014.08.005.

[156] T.P. Nguy, T. Van Phi, D.T.N. Tram, K. Eersels, P. Wagner, T.T.N. Lien, Development of an impedimetric sensor for the label-free detection of the amino acid sarcosine with molecularly imprinted polymer receptors, Sensors Actuators, B Chem. 246 (2017) 461–470. doi:10.1016/j.snb.2017.02.101.

[157] J. Lan, W. Xu, Q. Wan, X. Zhang, J. Lin, J. Chen, J. Chen, Colorimetric

determination of sarcosine in urine samples of prostatic carcinoma by mimic enzyme palladium nanoparticles, Anal. Chim. Acta. 825 (2014) 63–68. doi:10.1016/j.aca.2014.03.040.

[158] N. Cernei, Z. Heger, J. Gumulec, O. Zitka, M. Masarik, Sarcosine as a Potential Prostate Cancer Biomarker — A Review, Int. J. Mol. Sci. 14 (2013) 13893–13908. doi:10.3390/ijms140713893.

[159] S. Chen, Bio-inspired immobilisation, University of Cambridge, 2016.

[160] V. Grigorenko, T. Chubar, Y. Kapeliuch, T. Börchers, F. Spener, A. Egorova, New Approaches for Functional Expression of Recombinant Horseradish Peroxidase C In Escherichia Coli, Biocatal. Biotransformation. 17 (1999) 359–379. doi:10.3109/10242429909015236.

[161] Y. Xue, X. Li, H. Li, W. Zhang, Quantifying thiol-gold interactions towards the efficient strength control, Nat. Commun. 5 (2014) e1-9. doi:10.1038/ncomms5348.

[162] B. Arkles, J.R. Steinmetz, J. Zazyczny, P. Mehta, Factors contributing to the stability of alkoxysilanes in aqueos solution, in: K.L. Mittal (Ed.), Silanes and Other Coupling Agents, VSP, Amsterdam, 1992: pp. 91–104.

[163] J. Wu, L. Ling, J. Xie, G. Ma, B. Wang, Surface modification of nanosilica with 3-mercaptopropyl trimethoxysilane: Experimental and theoretical study on the surface interaction, Chem. Phys. Lett. 591 (2014) 227–232. doi:10.1016/j.cplett.2013.11.043.

[164] G.T. Hermanson, Silane coupling agents, in: Bioconjugate Tech., Elsevier, Amsterdam, 2008.

[165] S. Hauck, S. Drost, E. Prohaska, H. Wolf, S. Dubel, Analysis of Protein-Interactions Using a Quartz Crystal Microbalance Biosensor, in: Protein-Protein Interact. A Mol. Cloning Man., Cold Spring Harbor Laboratory Press, New York, 2002: pp. 273–284.

[166] K.A. Marx, Quartz crystal microbalance: A useful tool for studying thin polymer films and complex biomolecular systems at the solution-surface interface, Biomacromolecules. 4 (2003) 1099–1120. doi:10.1021/bm020116i.

[167] J.E. Sohna Sohna, M.A. Cooper, Does the Sauerbrey equation hold true for binding of peptides and globular proteins to a QCM? A systematic study of mass dependence of peptide and protein binding with a piezoelectric sensor., Sens. Bio-Sensing Res. 11 (2016) 71–77. doi:10.1016/j.sbsr.2016.07.001.

[168] G. Sauerbrey, Use of quartz crystals for weighing thin layers and for microwieghing, Mag. Phys. 155 (1959) 206–222. doi:10.1007/BF01337937.

[169] D.B. Barr, L.C. Wilder, S.P. Caudill, A.J. Gonzalez, L.L. Needham, J.L. Pirkle, Urinary creatinine concentrations in the U.S. population: Implications for urinary biologic monitoring measurements, Environ. Health Perspect. 113 (2005) 192–200. doi:10.1289/ehp.7337.

[170] A. Hewavitharana, Re: Florian Jentzmik, Carsten Stephan, Kurt Miller, et al. Sarcosine in Urine after Digital Rectal Examination Fails as a Marker in Prostate Cancer Detection and Identification of Aggressive Tumours. Eur Urol. In press. doi:10.1016/j.eururo.2010.01.035, Eur Urol. 58 (2010) e39–e40. doi:S0302-2838(10)00430-6 [pii]\r10.1016/j.eururo.2010.05.003.

[171] Classification of soils for engineering purposes: Annual Book of ASTM Standards D 2487-83 04.08, 1985.

[172] G.J. Weltje, R. Tjallingii, Calibration of XRF core scanners for quantitative geochemical logging of sediment cores: Theory and application, Earth Planet. Sci. Lett. 274 (2008) 423–438. doi:10.1016/j.epsl.2008.07.054.

[173] R. Tjallingii, U. Röhl, M. Kölling, T. Bickert, Influence of the water content on X-ray fluorescence corescanning measurements in soft marine sediments, Geochemistry, Geophys. Geosystems. 8 (2007) e1-12. doi:10.1029/2006GC001393.

[174] R.P.W. Scott, S. Traiman, Solute-solvent interactions on the surface of silica gel: III. Multilayer adsorption of water on the surface of silica gel, J. Chromatogr. 196 (1980) 193–205. doi:10.1016/S0021-9673(00)80439-2.

[175] M. Sumper, N. Kröger, Silica formation in diatoms: the function of long-chain polyamines and silaffins, J. Mater. Chem. 14 (2004) 2059–2065. doi:10.1039/B401028K.

[176] L. Senior, M.P. Crump, C. Williams, P.J. Booth, S. Mann, A.W. Perriman, P. Curnow, Structure and function of the silicifying peptide R5, J. Mater. Chem. B. 3 (2015) 2607–2614. doi:10.1039/C4TB01679C.

[177] C.C. Lechner, C.F.W. Becker, Silaffins in silica biomineralization and biomimetic silica precipitation, Mar. Drugs. 13 (2015) 5297–5333. doi:10.3390/md13085297.

[178] E. Gasteiger, C. Hoogland, A. Gattiker, S. Duvaud, M.R. Wilkins, R.D. Appel, A. Bairoch, Protein Identification and Analysis Tools on the ExPASy Server, in: J.M. Walker (Ed.), Proteomics Protoc. Handb., 2005: pp. 571–607.

[179] M. Soumbo, A. Pugliara, M.-C. Monje, C. Roques, B. Despax, C. Bonafos, R. Carles, A. Mlayah, K. Makasheva, Physico-Chemical Characterization of the Interaction of Red Fluorescent Protein—DsRed With Silica Layers, IEEE Trans. Nanobioscience. 15 (2016) 412–417. doi:10.1109/TNB.2016.2547895.

[180] L. Nieba, S. Nieba-Axmann, A. Persson, M. Hämäläinen, F. Edebratt, A. Hansson, J. Lidholm, K. Magnusson, A. Karlsson, A. Plückthun, BIACORE analysis of histidine-tagged proteins using a chelating NTA sensor chip, Anal. Biochem. 252 (1997) 217–228. doi:10.1016/S0735-1097(84)80242-9.

[181] N. Jornet-Martínez, E.A.H. Hall, C.J. Henderson, P. Campíns-Falcó, R. Daly, Towards sarcosine determination in urine for prostatic carcinoma detection, Sensors Actuators B. Chem. 287 (2019) 380–389. doi:10.1016/j.snb.2019.02.061.

[182] B. Seefeldt, R. Kasper, T. Seidel, P. Tinnefeld, K.-J. Dietz, M. Heilemann, M. Sauer, Fluorescent proteins for single-molecule fluorescence applications, J. Biophotonics. 1 (2008) 74–82. doi:10.1002/jbio.200710024.

[183] A. Sreekumar, L. Poisson, T. Rajendiran, A. Khan, Q. Cao, J. Yu, B. Laxman, R. Mehra, R. Lonigro, Y. Li, M. Nyati, A. Ahsan, S. Kalyana-Sundaram, B. Han, X. Cao, J. Byun, G. Omenn, D. Ghosh, S. Pennathur, D. Alexander, A. Berger, J. Shuster, J. Wei, S. Varambally, C. Beecher, A. Chinnaiyan, Metabolomic Profiles Delineate Potential Role for Sarcosine in Prostate Cancer Progression, Nature. 457 (2009) 910–914. doi:10.1038/nature07762.

[184] V.G. Grigorenko, I.P. Andreeva, M.Y. Rubtsova, A.M. Egorov, Recombinant horseradish peroxidase: Production and analytical applications, Biochem. 80

(2015) 408–416. doi:10.1134/S0006297915040033.

[185] S. Asad, B. Dabirmanesh, N. Ghaemi, S.M. Etezad, K. Khajeh, Studies on the refolding process of recombinant horseradish peroxidase, Mol. Biotechnol. 54 (2013) 484–492. doi:10.1007/s12033-012-9588-6.

[186] T. Gundinger, O. Spadiut, A comparative approach to recombinantly produce the plant enzyme horseradish peroxidase in Escherichia coli, J. Biotechnol. 248 (2017) 15–24. doi:10.1016/j.jbiotec.2017.03.003.

[187] N. Schultz, G. Metreveli, M. Franzreb, F.H. Frimmel, C. Syldatk, Zeta potential measurement as a diagnostic tool in enzyme immobilisation, Colloids Surfaces B Biointerfaces. 66 (2008) 39–44. doi:10.1016/j.colsurfb.2008.05.004.

[188] A.A. Tsyganenko, P.P. Mardilovich, Structure of alumina surfaces, J. Chem. Soc. Faraday Trans. 92 (1996) 4843–4852. doi:10.1039/ft9969204843.

[189] C. Wu, L. Wang, D. Harbottle, J. Masliyah, Z. Xu, Studying bubble-particle interactions by zeta potential distribution analysis, J. Colloid Interface Sci. 449 (2015) 399–408. doi:10.1016/j.jcis.2015.01.040.

[190] K. Rezwan, L.P. Meier, L.J. Gauckler, Lysozyme and bovine serum albumin adsorption on uncoated silica and AlOOH-coated silica particles: The influence of positively and negatively charged oxide surface coatings, Biomaterials. 26 (2005) 4351–4357. doi:10.1016/j.biomaterials.2004.11.017.

[191] D. Myśliwiec, M. Chylińska, M. Szymańska-Chargot, S. Chibowski, A. Zdunek, Revision of adsorption models of xyloglucan on microcrystalline cellulose, Cellulose. 23 (2016) 2819–2829. doi:10.1007/s10570-016-0995-x.

[192] H. Orelma, I. Filpponen, L.-S. Johansson, J. Laine, O.J. Rojas, Modification of cellulose films by adsorption of CMC and chitosan for controlled attachment of biomolecules, Biomacromolecules. 12 (2011) 4311–4318. doi:10.1021/bm201236a.

[193] G. Tarì, J.M.F. Ferreira, Colloidal Processing of Calcium Carbonate, Ceram. Int. 24 (1998) 527–532. doi:10.1016/S0272-8842(97)00052-7.

[194] F. Meder, T. Daberkow, L. Treccani, M. Wilhelm, M. Schowalter, A. Rosenauer,

L. Mädler, K. Rezwan, Protein adsorption on colloidal alumina particles functionalized with amino, carboxyl, sulfonate and phosphate groups, Acta Biomater. 8 (2012) 1221–1229. doi:10.1016/j.actbio.2011.09.014.

[195] F.W. Krainer, R. Pletzenauer, L. Rossetti, C. Herwig, A. Glieder, O. Spadiut, Purification and basic biochemical characterization of 19 recombinant plant peroxidase isoenzymes produced in Pichia pastoris, Protein Expr. Purif. 95 (2014) 104–112. doi:10.1016/j.pep.2013.12.003.

[196] Y. Nishiya, S. Nakano, K. Kawamura, Y. Abe, Monomeric sarcosine oxidase acts on both L- and D-substrates, J. Anal. Bio-Science. 35 (2012) 426–430.

[197] M.A. Wagner, M.S. Jorns, Monomeric sarcosine oxidase: 2. Kinetic studies with sarcosine, alternate substrates, and a substrate analogue, Biochemistry. 39 (2000) 8825–8829. doi:10.1021/bi000350y.

[198] F. Jentzmik, C. Stephan, K. Miller, M. Schrader, A. Erbersdobler, G. Kristiansen, M. Lein, K. Jung, Sarcosine in Urine after Digital Rectal Examination Fails as a Marker in Prostate Cancer Detection and Identification of Aggressive Tumours, Eur. Urol. 58 (2010) 12–18. doi:10.1016/j.eururo.2010.01.035.

[199] S. Chairam, P. Buddhalee, M. Amatatongchai, A Novel Hydrogen Peroxide Biosensor Based on Horseradish Peroxidase Immobilized on Poly(aniline-co-o-aminobenzoic acid) Modified Glassy Carbon Electrode Coated with Chitosan Film, Int. J. Electrochem. Sci. 8 (2013) 10250–10264.

[200] M. Zhang, Q. Lv, N. Yue, H. Wang, Study of fluorescence quenching mechanism between quercetin and tyrosine-H2O2-enzyme catalyzed product, Spectrochim. Acta Part A Mol. Biomol. Spectrosc. 72 (2009) 572–576. doi:10.1016/j.saa.2008.10.045.

[201] Y. Nishiya, T. Imanaka, Alteration of substrate specificity and optimum pH of sarcosine oxidase by random and site-directed mutagenesis, Appl. Environ. Microbiol. 60 (1994) 4213–4215.

[202] Y. Matsuda, H. Hoshika, Y. Inouye, S. Ikuta, K. Matsuura, S. Nakamura, Purification and Characterization of Sarcosine Oxidase of Bacillus origin, Chem. Pharm. Bull. 35 (1987) 711–717.

[203] J.D. Brennan, D. Benjamin, E. DiBattista, M.D. Gulcev, Using sugar and amino acid additives to stabilize enzymes within sol-gel derived silica, Chem. Mater. 15 (2003) 737–745. doi:10.1021/cm020768d.

[204] A.C. Pierre, The sol-gel encapsulation of enzymes, Biocatal. Biotransformation. 22 (2004) 145–170. doi:10.1080/10242420412331283314.

[205] J. Zhang, Q. Chi, S. Dong, E. Wang, In situ electrochemical scanning tunnelling microscopy investigation of structure for horseradish peroxidase and its electricatalytic property, Bioelectrochemistry Bioenerg. 39 (1996) 267–274. doi:http://dx.doi.org/10.1016/0302-4598(95)01893-X.

[206] J.F. Engels, C.J. Henderson, R. Daly, R. Renneberg, E.A.H. Hall, A lateral flow channel immunoassay combining a particle binding zone geometry with nanoparticle labelling amplification, Sensors Actuators B. Chem. 262 (2018) 1–8. doi:10.1016/j.snb.2018.01.213.

[207] E. Verpoorte, Beads and chips: new recipes for analysis, Lab a Chip Focus. 3 (2003) 60N-68N. doi:10.1039/b313217j.

[208] T. Buranda, J. Huang, V.H. Perez-Luna, B. Schreyer, L.A. Sklar, G.P. Lopez, Biomolecular recognition on well-characterized beads packed in microfluidic channels, Anal. Chem. 74 (2002) 1149–1156. doi:10.1021/ac0109624.

[209] S. Senapati, A.R. Mahon, J. Gordon, C. Nowak, S. Sengupta, T.H.Q. Powell, J. Feder, D.M. Lodge, H.C. Chang, Rapid on-chip genetic detection microfluidic platform for real world applications, Biomicrofluidics. 3 (2009) e1–e7. doi:10.1063/1.3127142.

[210] J. Křenková, F. Foret, Immobilized microfluidic enzymatic reactors, Electrophoresis. 25 (2004) 3550–3563. doi:10.1002/elps.200406096.

[211] K. Sato, M. Yamanaka, H. Takahashi, M. Tokeshi, H. Kimura, T. Kitamori, Microchip-based immunoassay system with branching multichannels for simultaneous determination of interferon-gamma, Electrophoresis. 23 (2002) 734–739. doi:10.1002/1522-2683(200203)23:5<734::AID-ELPS734>3.0.CO;2-W.

[212] K. Sato, M. Tokeshi, T. Odake, H. Kimura, T. Ooi, M. Nakao, T. Kitamori,

Integration of an immunosorbent assay system: Analysis of secretory human immunoglobulin A on polystyrene beads in a microchip, Anal. Chem. 72 (2000) 1144–1147. doi:10.1021/ac991151r.

[213] G.H. Seong, R.M. Crooks, Efficient mixing and reactions within microfluidic channels using microbead-supported catalysts, J. Am. Chem. Soc. 124 (2002) 13360–13361. doi:10.1021/ja020932y.

[214] D.N. Kim, Y. Lee, W.G. Koh, Fabrication of microfluidic devices incorporating bead-based reaction and microarray-based detection system for enzymatic assay, Sensors Actuators B Chem. 137 (2009) 305–312. doi:10.1016/j.snb.2008.12.042.

[215] T. Ito, M. Kunimatsu, S. Kaneko, S. Ohya, K. Suzuki, Microfluidic device for the detection of glucose using a micro direct methanol fuel cell as an amperometric detection power source, Anal. Chem. 79 (2007) 1725–1730. doi:10.1021/ac0618167.

[216] L. Blanes, M.F. Mora, C.L. Do Lago, A. Ayon, C.D. García, Lab-on-a-chip biosensor for glucose based on a packed immobilized enzyme reactor, Electroanalysis. 19 (2007) 2451–2456. doi:10.1002/elan.200704001.

[217] D. Kim, A.E. Herr, Protein immobilization techniques for microfluidic assays., Biomicrofluidics. 7 (2013) e41501. doi:10.1063/1.4816934.

[218] A. Van Reenen, A.M. De Jong, J.M.J. Den Toonder, M.W.J. Prins, Integrated lab-on-chip biosensing systems based on magnetic particle actuation - a comprehensive review, Lab Chip. 14 (2014) 1966–1986. doi:10.1039/c3lc51454d.

[219] C.-H. Wang, K.-Y. Lien, T.-Y. Wang, T.-Y. Chen, G.-B. Lee, An integrated microfluidic loop-mediated-isothermal-amplification system for rapid sample pre-treatment and detection of viruses, Biosens. Bioelectron. 26 (2011) 2045–52. doi:10.1016/j.bios.2010.08.083.

[220] H. Bordelon, N.M. Adams, A.S. Klemm, P.K. Russ, J. V Williams, H.K. Talbot, D.W. Wright, F.R. Haselton, Development of a Low-Resource RNA Extraction Cassette Based on Surface Tension Valves, Appl. Mater. Interfaces. 3 (2011) 2161–2168. doi:10.1021/am2004009.

[221] K.M. Davis, J.D. Swartz, F.R. Haselton, D.W. Wright, Low-resource method for extracting the malarial biomarker histidine-rich protein II to enhance diagnostic test performance, Anal. Chem. 84 (2012) 6136–6142. doi:10.1021/ac301030m.

[222] N.M. Adams, A.E. Creecy, C.E. Majors, B.A. Wariso, P.A. Short, D.W. Wright, F.R. Haselton, Design criteria for developing low-resource magnetic bead assays using surface tension valves, Biomicrofluidics. 7 (2013) e014104. doi:10.1063/1.4788922.

[223] N.M. Adams, K.K.A. Wang, A.C. Caprioli, L.C. Thomas, B. Kankia, F.R. Haselton, D.W. Wright, Quadruplex priming amplification for the detection of mRNA from surrogate patient samples, Analyst. 139 (2014) 1644–1652. doi:10.1039/c3an02261g.

[224] A. Creecy, P.K. Russ, F. Solinas, D.W. Wright, F.R. Haselton, Tuberculosis Biomarker Extraction and Isothermal Amplification in an Integrated Diagnostic Device, PLoS One. 10 (2015) e0130260. doi:10.1371/journal.pone.0130260.

[225] G. Xu, H. Zhao, J.M. Cooper, J. Reboud, A capillary-based multiplexed isothermal nucleic acid-based test for sexually transmitted diseases in patients, Chem. Commun. 52 (2016) 12187–12190. doi:10.1039/c6cc05679b.

[226] T.G. Kang, M.A. Hulsen, P.D. Anderson, J.M.J. Den Toonder, H.E.H. Meijer, Chaotic mixing induced by a magnetic chain in a rotating magnetic field, Phys. Rev. E. 76 (2007) e066303. doi:10.1103/PhysRevE.76.066303.

[227] M.F. Chaplin, C. Bucke, Enzyme Technology, Cambridge University Press, Cambridge, 1990.

[228] A.G. Marangoni, Enzyme kinetics: a modern approach, Wiley-Interscience, Hoboken, NJ, 2003.

[229] Y.T. Shih, D. Gidaspow, D.T. Wasan, Hydrodynamics of sedimentation of multisized particles, Powder Technol. 50 (1987) 201–215. doi:10.1016/0032-5910(87)80065-7.

[230] M. Hartman, O. Trnka, K. Svoboda, Free Settling of Nonspherical Particles, Ind. Eng. Chem. Res. 33 (1994) 1979–1983. doi:10.1021/ie00032a012.

[231] J.G. Yates, Fundamentals of Fluidized-Bed Processes, Butterworths, London, 1983.

[232] G.G. Stokes, Mathematical and physical papers, Cambridge University Press, Cambridge, 1901.

[233] J.S. McNown, J. Malaika, Effects of particle shape on settling velocity at low reynolds numbers, EOS Trans. 31 (1950) 74–82. doi:10.1029/TR031i001p00074.

[234] S. Alabrudziński, M.L. Ekiel-Jeżewska, D. Chehata-Gómez, T.A. Kowalewski, M.L. Ekiel-Jezewska, D. Chehata-Gómez, T.A. Kowalewski, Particle clusters settling under gravity in a viscous fluid, Phys. Fluids. 21 (2009) e073302. doi:10.1063/1.3168615.

[235] É. Guazzelli, J.F. Morris, A Physical Introduction to Suspension Dynamics, Cambridge University Press, Cambridge, 2011.

[236] J.F. Richardson, W.N. Zaki, Sedimentation and fluidisation: Part I, Trans. Inst. Chem. Eng. 32 (1954) S82–S100. doi:10.1016/S0263-8762(97)80006-8.

[237] S. Mirza, J.F. Richardson, Sedimentation of suspensions of particles of two or more sizes, Chem. Eng. Sci. 34 (1979) 447–454.

[238] M.J. Lockett, K.S. Basson, Sedimentation of binary particle mixtures, Powder Technol. 24 (1979) 1–7.

[239] Y. Du, Particle-modified Surface Plasmon Resonance Biosensor, University of Cambridge, 2019.

[240] C.A. Schneider, W.S. Rasband, K.W. Eliceiri, C. Instrumentation, NIH Image to ImageJ : 25 years of Image Analysis, Nat. Methods. 9 (2012) 671–675.

[241] The MathWorks Inc., MATLAB Release 2017a, (2017).

[242] W. Thielicke, E.J. Stamhuis, PIVlab – Towards User-friendly , Affordable and Accurate Digital Particle Image Velocimetry in MATLAB, J. Open Res. Softw. 2 (2014) e30. doi:http://dx.doi.org/10.5334/jors.bl.

[243] E.L. Cussler, Diffusion: Mass transfer in fluid systems, 3rd ed., Cambridge University Press, Cambridge, 2009.

[244] T. Gervais, K.F. Jensen, Mass transport and surface reactions in microfluidic systems, Chem. Eng. Sci. 61 (2006) 1102–1121. doi:10.1016/j.ces.2005.06.024.

[245] Y. Ma, C. Zhu, P. Ma, K.T. Yu, Studies on the diffusion coefficients of amino acids in aqueous solutions, J. Chem. Eng. Data. 50 (2005) 1192–1196. doi:10.1021/je049582g.

[246] A.D. Polyanin, A.M. Kutepov, D.A. Kazenin, A. V Vyazmin, Hydrodynamics, Mass and Heat Transfer in Chemical Engineering, CRC press, Boca Raton, FL, 2001.

[247] S. Zhiyao, W. Tingting, X. Fumin, L. Ruijie, A simple formula for predicting settling velocity of sediment particles, Water Sci. Eng. 1 (2008) 37–43. doi:10.1016/S1674-2370(15)30017-X.

[248] M.J. Rhodes, Introduction to Particle Technology, 2nd ed., John Wiley & Sons, Chichester, 2008.

[249] K. Grudpan, S.D. Kolev, S. Lapanantnopakhun, I.D. McKelvie, W. Wongwilai, Applications of everyday IT and communications devices in modern analytical chemistry: A review, Talanta. 136 (2015) 84–94. doi:10.1016/j.talanta.2014.12.042.

[250] N. Reis, A.P. Harvey, M.R. Mackley, A.A. Vincente, J.A. Teixeira, Fluid mechanics and design aspects of a novel oscillatory flow screening mesoreactor, Chem. Eng. Res. Des. 83 (2005) 357–371. doi:10.1205/cherd.03401.

[251] J. Guo, Logarithmic matching and its applications in computational hydraulics and sediment transport, J. Hydraul. Res. 40 (2002) 555–565. doi:10.1080/00221680209499900.

[252] J.F. Richardson, W.N. Zaki, The sedimentation of a suspension of uniform spheres under conditions of viscous flow, Chem. Eng. Sci. 3 (1954) 65–73. doi:10.1016/0009-2509(54)85015-9.

[253] I. Sagert, W. Bauer, D. Colbry, J. Howell, A. Stavber, T. Strother, Kinetic Simulations of Rayleigh-Taylor Instabilities, J. Phys Conf. Ser. 535 (2014) 012032. doi:10.1088/1742-6596/535/1/012032.

[254] M. Kobayashi, F. Juillerat, P. Galletto, P. Bowen, M. Borkovec, Aggregation and charging of colloidal silica particles: Effect of particle size, Langmuir. 21 (2005) 5761–5769. doi:10.1021/la046829z.

[255] L. Liu, Aggregation of Silica Nanoparticles in an Aqueous Suspension, AIChE J. 56 (2015) 2136–2146. doi:10.1002/aic.1483.

[256] S. Wang, H. Suhaimi, D.B. Das, Glucose diffusivity in cell culture medium used in tissue engineering bioreactor, in: Present. 6th APS Int. PharmSci 2015, 7th-9th Sept. 2015, Univ. Nottingham., 2015.

[257] F.M. Stroe-Biezen, van, S. A. M., Everaerts, L.J.J. Janssen, R.A. Tacken, Diffusion coefficients of oxygen, hydrogen peroxide and glucose in a hydrogel, Anal. Chim. Acta. 273 (1993) 553–560. doi:10.1016/0003-2670(93)80202-V.

[258] P. Valencia, S. Flores, L. Wilson, A. Illanes, Effect of particle size distribution on the simulation of immobilized enzyme reactor performance, Biochem. Eng. J. 49 (2010) 256–263. doi:10.1016/j.bej.2010.01.002.

[259] J.J. Gooding, E.A.H. Hall, D.B. Hibbert, From Thick Films to Monolayer Recognition Layers in Amperometric Enzyme Electrodes, Electroanalysis. 10 (1998) 1130–1136. doi:10.1002/(SICI)1521-4109(199811)10:16<1130::AID-ELAN1130>3.0.CO;2-6.

[260] E.A.H. Hall, J.J. Gooding, C.E. Hall, Redox enzyme linked electrochemical sensors: Theory meets practice, Mikrochim. Acta. 121 (1995) 119–145. doi:10.1007/BF01248246.

[261] Q. Yue, J. Li, W. Luo, Y. Zhang, A.A. Elzatahry, X. Wang, C. Wang, W. Li, X. Cheng, A. Alghamdi, A.M. Abdullah, Y. Deng, D. Zhao, An Interface Coassembly in Biliquid Phase: Toward Core-Shell Magnetic Mesoporous Silica Microspheres with Tunable Pore Size, J. Am. Chem. Soc. 137 (2015) 13282–13289. doi:10.1021/jacs.5b05619.

[262] F. Nosten, N.J. White, Artemisinin-Based Combination Treatment of Falciparum Malaria, Am. J. Trop. Med. Hyg. 77 (2007) 181–192.

[263] Y. Jiang, X. Cheng, C. Wang, Y. Ma, Quantitative Determination of Sarcosine and

Related Compounds in Urinary Samples by Liquid Chromatography with Tandem Mass Spectrometry, Anal Chem. 82 (2010) 9022–9027. doi:10.1021/ac1019914.

[264] H.J. Issaq, T.D. Veenstra, Is sarcosine a biomarker for prostate cancer?, J. Sep. Sci. 34 (2011) 3619–3621. doi:10.1002/jssc.201100572.

[265] G. Lucarelli, M. Fanelli, A. Maria, V. Larocca, C.A. Germinario, M. Rutigliano, A. Vavallo, F.P. Selvaggi, C. Bettocchi, M. Battaglia, P. Ditonno, Serum Sarcosine Increases the Accuracy of Prostate Cancer Detection in Patients With Total Serum PSA LessThan 4.0 ng/mL, Prostate. 72 (2012) 1611–1621. doi:10.1002/pros.22514.

[266] H.J. Kwon, J. Lee, H. Il Park, K. Han, Evaluation of a novel point-of-care test kit, ABSOGEN ^{TM} PCT, in semi-quantitative measurement of procalcitonin in whole blood, J. Clin. Lab. Anal. 31 (2017) e22111. doi:10.1002/jcla.22111.

[267] A. V. Ritchie, I. Ushiro-Lumb, D. Edemaga, H.A. Joshi, A. De Ruiter, E. Szumilin, I. Jendrulek, M. McGuire, N. Goel, P.I. Sharma, J.P. Allain, H.H. Lee, SAMBA HIV semiquantitative test, a new point-of-care viral-load-monitoring assay for resource-limited settings, J. Clin. Microbiol. 52 (2014) 3377–3383. doi:10.1128/JCM.00593-14.

[268] J.J. Gooding, E.A.H. Hall, A Fill-and-Flow Biosensor, Anal Chem. 70 (1998) 3131–3136.

[269] S. Hatz, E.A.H. Hall, The “free-flow” biosensor in enzyme inhibition assay, Sensors Actuators B Chem. 113 (2006) 700–710. doi:10.1016/j.snb.2005.07.020.

[270] H. Miyakawa, F. Shiraishi, A Film Diffusional Effect on the Apparent Kinetic Parameters in Packed-Bed Immobilized Enzyme Reactors, J. Chem. Tech. Biotechnol. 69 (1997) 456–462.

[271] J. Marcos, A. Rios, M. Valcircel, Automatic determination of Michaelis-Menten by the variable flow-rate technique, Anal. Chim. Acta. 283 (1993) 429–438.

[272] P. Richter, B.L. Ruiz, M. Sánchez-Cabezudo, H.A. Mottola, Immobilized enzyme reactors. Diffusion/convection, kinetics, and a comparison of packed-column and rotating bioreactors for use in continuous-flow systems, Anal. Chem. 68 (1996)

1701–1705. doi:10.1021/ac950910c.

[273] A.R. Ozdural, D. Tanyolac, Z. Demircan, I.H. Boyacib, M. Mutlub, C. Webb, A new method for determination of apparent kinetics parameters in recirculating packed-bed immobilized enzyme reactors, Chem. Eng. Sci. 56 (2001) 3483–3490.

[274] A. Kecskemeti, A. Gaspar, Particle-based immobilized enzymatic reactors in microfluidic chips, Talanta. 180 (2018) 211–228. doi:10.1016/j.talanta.2017.12.043.

[275] Z. Heger, N. Cernei, S. Krizkova, M. Masarik, P. Kopel, P. Hodek, O. Zitka, V. Adam, R. Kizek, Paramagnetic nanoparticles as a platform for FRET-based sarcosine picomolar detection, Sci. Rep. 5 (2015) e08868. doi:10.1038/srep08868.

[276] J.C. Bouin, M.T. Atallah, H.O. Hultin, Relative efficiencies of a soluble and immobilized two-enzyme system of glucose oxidase and catalase, Biochim. Biophys. Acta. 438 (1976) 23–36.

[277] G. Borghei, E.A.H. Hall, BRET-linked ATP assay with luciferase, Analyst. 139 (2014) 4185–4192. doi:10.1039/C4AN00436A.

[278] Y. Zhang, S. Tsitkov, H. Hess, Proximity does not contribute to activity enhancement in the glucose oxidase-horseradish peroxidase cascade, Nat. Commun. 7 (2016) e13982. doi:10.1038/ncomms13982.

[279] B. Mosbach, Klaus, Mattiasson, Matrix-bound Enzymes, Acta Chim. Scand. 24 (1970) 2084–2100.

[280] H. Ashraf, Q. Husain, Stabilization of DEAE cellulose adsorbed and glutaraldehyde crosslinked white radish (Raphanus sativus) peroxidase, J. Sci. Ind. Res. 69 (2010) 613–620.

[281] L. Cao, Carrier-bound Immobilized Enzymes: Principles, Application and Design, Wiley-VCH, Weinham, 2006.

[282] M.A. Mensink, H.W. Frijlink, K. van der Voort Maarschalk, W.L.J. Hinrichs, How sugars protect proteins in the solid state and during drying (review): Mechanisms of stabilization in relation to stress conditions, Eur. J. Pharm. Biopharm. 114 (2017) 288–295. doi:10.1016/j.ejpb.2017.01.024.

[283] C. Colaco, S. Sen, M. Thangavelu, S. Pinder, B. Roser, Extraordinary stability of eznymes dried in trehalose: simplified molecular biology, Nat. Biotechnol. 10 (1992) 1007–1011.

[284] R. Baronas, J. Kulys, L. Petkevičius, Computational modeling of batch stirred tank reactor based on spherical catalyst particles, J. Math. Chem. (2018) e1-16. doi:10.1007/s10910-018-0954-x.

[285] A. Bódalo, J.L. Gómez, E. Gómez, J. Bastida, M.F. Máximo, Fluidized bed reactors operating with immobilized enzyme systems: Design model and its experimental verification, Enzyme Microb. Technol. 17 (1995) 915–922. doi:10.1016/0141-0229(94)00125-B.

[286] L.E. Freed, G. V. Vunjak-Novakovic, P.A. Drinker, R. Langer, Bioreactor Based on Suspended Particles of Immobilized Enzyme, Ann. Biomed. Eng. 21 (1993) 57–65.

[287] S.A. Blank-Shim, S.P. Schwaminger, M. Borkowska-Panek, P. Anand, P. Yamin, P. Fraga-García, K. Fink, W. Wenzel, S. Berensmeier, Binding patterns of homo-peptides on bare magnetic nanoparticles: Insights into environmental dependence, Sci. Rep. 7 (2017) e14047. doi:10.1038/s41598-017-13928-6.

[288] S.P. Schwaminger, S.A. Blank-Shim, I. Scheifele, P. Fraga-García, S. Berensmeier, Peptide binding to metal oxide nanoparticles, Faraday Discuss. 204 (2017) 233–250. doi:10.1039/c7fd00105c.

[289] S.P. Schwaminger, P. Fraga-García, S.A. Blank-Shim, T. Straub, M. Haslbeck, F. Muraca, K.A. Dawson, S. Berensmeier, Magnetic one-step purification of his-tagged protein by bare iron oxide nanoparticles, ACS Omega. 4 (2019) 3790–3799. doi:10.1021/acsomega.8b03348.

[290] S.P. Schwaminger, S.A. Blank-Shim, I. Scheifele, V. Pipich, P. Fraga-García, S. Berensmeier, Design of Interactions Between Nanomaterials and Proteins: A Highly Affine Peptide Tag to Bare Iron Oxide Nanoparticles for Magnetic Protein Separation, Biotechnol. J. 14 (2019) e1800055. doi:10.1002/biot.201800055.

[291] S. Lee, Y. Stokes, A.L. Bertozzi, Behavior of a particle-laden flow in a spiral channel, Phys. Fluids. 26 (2014) e043302. doi:10.1063/1.4872035.

[292] International Telecommunications Union, Millenium Development Goals, Targets and Indicators, (2019).

[293] N. Dell, G. Borriello, Mobile tools for point-of-care diagnostics in the developing world, Proc. 3rd ACM Symp. Comput. Dev. (2013) e1-4. doi:10.1145/2442882.2442894.

[294] C. Doukas, P. Stagkopoulos, I. Maglogiannis, Mobile Health Technologies: Methods and Protocols, 2015. doi:10.1007/978-1-4939-2172-0_29.

[295] T. Hampton, Recent advances in mobile technology benefit global health, research and care, JAMA. 307 (2012) 2013–2014.

[296] G. Kayingo, Transforming global health with mobile technologies and social enterprises, Yale J. Biol. Med. 85 (2012) 425–427.

[297] Y.-S. Kuo, S. Verma, T. Schmid, P. Dutta, Hijacking power and bandwidth from the mobile phone's audio interface, in: Proc. First ACM Symp. Comput. Dev., ACM Press, New York, New York, USA, 2010: pp. e1-10. doi:10.1145/1926180.1926210.

[298] T. Laksanasopin, T.W. Guo, S. Nayak, A. a Sridhara, S. Xie, O.O. Olowookere, P. Cadinu, F. Meng, N.H. Chee, J. Kim, C.D. Chin, E. Munyazesa, P. Mugwaneza, A.J. Rai, V. Mugisha, A.R. Castro, D. Steinmiller, V. Linder, J.E. Justman, S. Nsanzimana, S.K. Sia, A smartphone dongle for diagnosis of infectious diseases at the point of care., Sci. Transl. Med. 7 (2015) 273re1. doi:10.1126/scitranslmed.aaa0056.

[299] A. Nemiroski, D.C. Christodouleas, J.W. Hennek, A. a Kumar, E.J. Maxwell, M.T. Fernández-abedul, G.M. Whitesides, Universal mobile electrochemical detector designed for use in resource-limited applications, Proc. Natl. Acad. Sci. 111 (2014) 11984–11989. doi:10.1073/pnas.1405679111.

[300] A.W. Martinez, S.T. Phillips, E. Carrilho, S.W. Thomas, H. Sindi, G.M. Whitesides, Simple Telemedicine for Developing Regions: Camera Phones and Paper-Based Microfluidic Devices for Real-Time, Off-Site Diagnosis, Anal. Chem. 80 (2008) 3699–3707. doi:10.1021/ac800112r.

[301] L. Shen, J.A. Hagen, I. Papautsky, Point-of-care colorimetric detection with a smartphone, Lab Chip. 12 (2012) 4240–4243. doi:10.1039/c2lc40741h.

[302] J. Rodriguez-Manzano, M.A. Karymov, S. Begolo, D.A. Selck, D. V. Zhukov, E. Jue, R.F. Ismagilov, Reading Out Single-Molecule Digital RNA and DNA Isothermal Amplification in Nanoliter Volumes with Unmodified Camera Phones, ACS Nano. 10 (2016) 3102–3113. doi:10.1021/acsnano.5b07338.

[303] C.A. de Villiers, M.C. Lapsley, E.A.H. Hall, A step towards Mobile Arsenic measurement for surface waters, Analyst. 140 (2015) 2644–2655. doi:10.1039/C4AN02368D.

[304] O. Mudanyali, S. Dimitrov, U. Sikora, S. Padmanabhan, I. Navruz, A. Ozcan, Integrated rapid-diagnostic-test reader platform on a cellphone, Lab Chip. 12 (2012) 2678–2686. doi:10.1039/c2lc40235a.

[305] G.G. Morbioli, T. Mazzu-Nascimento, A.M. Stockton, E. Carrilho, Technical aspects and challenges of colorimetric detection with microfluidic paper-based analytical devices (μPADs) - A review, Anal. Chim. Acta. 970 (2017) 1–22. doi:10.1016/j.aca.2017.03.037.

[306] V.M. Ugaz, A. Priye, Smartphone-Enabled Detection strategies for portable PCR-based diagnostics, in: A. Rasooly, B. Prickril (Eds.), Biosens. Biodetection Methods Protoc. Vol. 1 Opt. Detect., Springer, 2017: pp. 251–266. doi:10.1007/978-1-4939-6848-0.

[307] H.N. Chan, Y. Shu, B. Xiong, Y. Chen, Y. Chen, Q. Tian, S.A. Michael, B. Shen, H. Wu, Simple, Cost-Effective 3D Printed Microfluidic Components for Disposable, Point-of-Care Colorimetric Analysis, ACS Sensors. 1 (2016) 227–234. doi:10.1021/acssensors.5b00100.

[308] A.K. Yetisen, J.L. Martinez-Hurtado, A. Garcia-Melendrez, F. Da Cruz Vasconcellos, C.R. Lowe, A smartphone algorithm with inter-phone repeatability for the analysis of colorimetric tests, Sensors Actuators B Chem. 196 (2014) 156–160. doi:10.1016/j.snb.2014.01.077.

[309] W. Shen, X. Zhang, Q. Huang, Q. Xu, W. Song, Preparation of solid silver nanoparticles for inkjet printed flexible electronics with high conductivity.,

Nanoscale. 6 (2014) 1622–8. doi:10.1039/c3nr05479a.

[310] Z. Göröcs, A. Ozcan, Biomedical imaging and sensing using flatbed scanners, Lab Chip. 14 (2014) 3248–3257. doi:10.1039/c4lc00530a.

[311] C. Parker, D. Muston, J. Melia, S. Moss, D. Dearnaley, A model of the natural history of screen-detected prostate cancer, and the effect of radical treatment on overall survival, Br. J. Cancer. 94 (2006) 1361–1368. doi:10.1038/sj.bjc.6603105.

[312] M. Rigau, J. Morote, M.C. Mir, C. Ballesteros, M. Garcia, A. Ruiz, I. Ortega, A. Sanchez, E. Cola, A. Doll, M. Abal, J. Planas, J. Revento, PSGR and PCA3 as Biomarkers for the Detection of Prostate Cancer in Urine, Prostate. 70 (2010) 1760–1767. doi:10.1002/pros.21211.

[313] D. Cao, D. Ye, H. Zhang, Y. Zhu, Y. Wang, X. Yao, A Multiplex Model of Combining Gene-Based, Protein-Based, and Metabolite-Based With Positive and Negative Markers in Urine for the Early Diagnosis of Prostate Cancer, Prostate. 71 (2011) 700–710. doi:10.1002/pros.21286.

[314] A.J. Armstrong, M.A. Eisenberger, S. Halabi, S. Oudard, D.M. Nanus, D.P. Petrylak, A.O. Sartor, H.I. Scher, Biomarkers in the Management and Treatment of Men with Metastatic Castration-Resistant Prostate Cancer, Eur. Urol. 61 (2012) 549–559. doi:10.1016/j.eururo.2011.11.009.

[315] E.A. Struys, A.C. Heijboer, J. van Moorselaar, C. Jakobs, M.A. Blankenstein, Serum sarcosine is not a marker, Ann. Clin. Biochem. 47 (2010) 282.

[316] T.E. Meyer, S.D. Fox, H.J. Issaq, X. Xu, L.W. Chu, T.D. Veenstra, A.W. Hsing, A reproducible and high-throughput HPLC/MS method to separate sarcosine from alpha- and beta-Alanine and to quantify sarcosine in human serum and urine, Anal. Chem. 83 (2011) 5735–5740. doi:10.1021/ac201003r.

[317] Y. Gao, X. Xu, G. Song, Y. Hu, H. Cheng, A novel derivatization method for separation of sarcosine from isobaric L-alanine in human urine by GC-MS, Chromatographia. 76 (2013) 1181–1186. doi:10.1007/s10337-013-2523-6.

[318] D. Uhlirova, M. Stankova, M. Docekalova, B. Hosnedlova, M. Kepinska, B. Ruttkay-Nedecky, J. Ruzicka, C. Fernandez, H. Milnerowicz, R. Kizek, A Rapid

Method for the Detection of Sarcosine Using SPIONs/Au/CS/SOX/NPs for Prostate Cancer Sensing, Int. J. Mol. Sci. 19 (2018) 3722. doi:10.3390/ijms19123722.

[319] E. Yoo, S. Lee, Glucose Biosensors: An Overview of Use in Clinical Practice, Sensors. 10 (2010) 4558–4576. doi:10.3390/s100504558.

[320] O.Y. Dudchenko, V.M. Pyeshkova, O.O. Soldatkin, B. Akata, B.O. Kasap, A.P. Soldatkin, S. V. Dzyadevych, Development of Silicalite/Glucose Oxidase-Based Biosensor and Its Application for Glucose Determination in Juices and Nectars, Nanoscale Res. Lett. 11 (2016) e1-7. doi:10.1186/s11671-016-1275-2.

[321] S. Ashtekar, J.J. Hastings, P.J. Barrie, L.F. Gladden, Quantification of the number of silanol groups in silicalite and mesoporous MCM-41: Use of FT-Raman spectroscopy, Spectrosc. Lett. 33 (2000) 569–584. doi:10.1080/00387010009350140.

[322] M.M. Gong, D. Sinton, Turning the Page: Advancing Paper-Based Microfluidics for Broad Diagnostic Application, Chem. Rev. 117 (2017) 8447–8480. doi:10.1021/acs.chemrev.7b00024.

[323] J. Hu, S. Wang, L. Wang, F. Li, B. Pingguan-Murphy, T.J. Lu, F. Xu, Advances in paper-based point-of-care diagnostics, Biosens. Bioelectron. 54 (2014) 585–597. doi:10.1016/j.bios.2013.10.075.

[324] M.S. Akram, R. Daly, F.C. Vasconcellos, A.K. Yetisen, I. Hutchings, E.A.H. Hall, Chapter 7 - Applications of Paper-Based Diagnostics, in: J. Castillo-Leon, W.E. Svendsen (Eds.), Lab-on-a-Chip Devices Micro-Total Anal. Syst., Springer, 2015. doi:10.1007/978-3-319-08687-3.

[325] E.A. Miller, S. Baniya, D. Osorio, Y.J. Al Maalouf, H.D. Sikes, Paper-based diagnostics in the antigen-depletion regime: High-density immobilization of rcSso7d-cellulose-binding domain fusion proteins for efficient target capture, Biosens. Bioelectron. 102 (2018) 456–463. doi:10.1016/j.bios.2017.11.050.

[326] W. Wan, D. Wang, X. Gao, J. Hong, Expression of family 3 cellulose-binding module (CBM3) as an affinity tag for recombinant proteins in yeast, Appl. Microbiol. Biotechnol. 91 (2011) 789–798. doi:10.1007/s00253-011-3373-5.

[327] M. Kavoosi, J. Meijer, E. Kwan, A.L. Creagh, D.G. Kilburn, C.A. Haynes, Inexpensive one-step purification of polypeptides expressed in Escherichia coli as fusions with the family 9 carbohydrate-binding module of xylanase 10A from T. maritima, J. Chromatogr. B. 807 (2004) 87–94. doi:10.1016/j.jchromb.2004.03.031.

[328] J. Hong, Y. Wang, X. Ye, Y.H.P. Zhang, Simple protein purification through affinity adsorption on regenerated amorphous cellulose followed by intein self-cleavage, J. Chromatogr. A. 1194 (2008) 150–154. doi:10.1016/j.chroma.2008.04.048.

[329] O. Shoseyov, Z. Shani, I. Levy, Carbohydrate Binding Modules: Biochemical Properties and Novel Applications, Microbiol. Mol. Biol. Rev. 70 (2006) 283–295. doi:10.1128/MMBR.00028-05.

[330] B. Rodriguez, M. Kavoosi, J. Koska, A.L. Creagh, D.G. Kilburn, C.A. Haynes, Inexpensive and generic affinity purification of recombinant proteins using a family 2a CBM fusion tag, Biotechnol. Prog. 20 (2004) 1479–1489. doi:10.1021/bp0341904.

[331] J. Nahalka, B. Nidetzky, Fusion to a Pull-Down Domain : A Novel Approach of Producing Trigonopsis variabilis D-Amino Acid Oxidase as Insoluble Enzyme Aggregates, Biotechnol. Bioeng. 97 (2007) 454–461. doi:10.1002/bit.

[332] Institute for Health Metrics and Evaluation, The Global Burden of Disease: Generating Evidence, Guiding Policy, (2013).

[333] M.G.A. Goris, M.M.G. Leeflang, M. Loden, J.F.P. Wagenaar, P.R. Klatser, R.A. Hartskeerl, K.R. Boer, Prospective evaluation of three rapid diagnostic tests for diagnosis of human leptospirosis, PLoS Negl. Trop. Dis. 7 (2013) e2290. doi:10.1371/journal.pntd.0002290.

[334] L. Lafleur, J.D. Bishop, E.K. Heiniger, R.P. Gallagher, M.D. Wheeler, P.C. Kauffman, X. Zhang, E. Kline, J. Buser, S. Ramachandran, S. Byrnes, N. Vermeulen, N. Scarr, Y. Belousov, W. Mahoney, B.J. Toley, P.D. Ladd, B. Lutz, P. Yager, A rapid, instrument-free, sample-to-result nucleic acid amplification test, Lab Chip. 52 (2016) 3377–3383. doi:10.1039/C6LC00677A.

[335] X. Yu, Y.-P. Yang, E. Dikici, S.K. Deo, S. Daunert, Beyond Antibodies as Binding Partners: The Role of Antibody Mimetics in Bioanalysis, Annu. Rev. Anal. Chem. 10 (2017) 293–320. doi:10.1146/annurev-anchem-061516-045205.

[336] D.A. Haake, P.N. Levett, Leptospirosis in humans., Curr. Top. Microbiol. Immunol. 387 (2015) 65–97. doi:10.1007/978-3-662-45059-8_5.

[337] W.M. Barnes, The fidelity of Taq polymerase catalyzig PCR is imporved by an N-terminal deletion, Gene. 112 (1992) 29–35.

[338] D.W. Close, C.D. Paul, P.S. Langan, M.C.J. Wilce, D.A.K. Traore, R. Halfmann, R.C. Rocha, G.S. Waldo, R.J. Payne, J.B. Rucker, M. Prescott, A.R.M. Bradbury, TGP, an extremely stable, non-aggregating fluorescent protein created by structure-guided surface engineering, Proteins. 83 (2015) 1225–1237. doi:10.1002/prot.24699.

[339] Y. Mori, K. Nagamine, N. Tomita, T. Notomi, Detection of loop-mediated isothermal amplification reaction by turbidity derived from magnesium pyrophosphate formation, Biochem. Biophys. Res. Commun. 289 (2001) 150–154. doi:10.1006/bbrc.2001.5921.

[340] T. Notomi, H. Okayama, H. Masubuchi, T. Yonekawa, K. Watanabe, N. Amino, T. Hase, Loop-mediated isothermal amplification of DNA, Nucleic Acids Res. 28 (2000) E63.

[341] G.L. Lukacs, P. Haggie, O. Seksek, D. Lechardeur, N. Freedman, A.S. Verkman, Size-dependent DNA Mobility in Cytoplasm and Nucleus, J. Biol. Chem. 275 (2000) 1625–1629. doi:10.1074/jbc.275.3.1625.

[342] D.R. Zweitzig, N.M. Riccardello, B.I. Sodowich, S.M. O’Hara, Characterization of a novel DNA polymerase activity assay enabling sensitive, quantitative and universal detection of viable microbes, Nucleic Acids Res. 40 (2012) e109. doi:10.1093/nar/gks316.

[343] P.N. Levett, Leptospirosis, Clin. Microbiol. Rev. 14 (2001) 296–326. doi:10.1128/CMR.14.2.296.